Effects of free-stream turbulence intensity on laminar separation bubbles

by

Mark Istvan

A thesis
presented to the University of Waterloo
in fulfillment of the
thesis requirement for the degree of
Master of Applied Science
in
Mechanical and Mechatronics Engineering

Waterloo, Ontario, Canada, 2017

I hereby declare that I am the sole author of this thesis. This is a true copy of the thesis, including any required final revisions, as accepted by my examiners.

I understand that my thesis may be made electronically available to the public.

Abstract

The effects of free-stream turbulence intensity on the flow over a NACA 0018 airfoil are studied experimentally in a wind tunnel facility. A parametric study is performed over a range of chord Reynolds numbers from 100 000 to 200 000, angles of attack from 0° to 20°, and free-stream turbulence intensities from 0.09% to 2.03% in order to unravel the effects of each parameter on suction side laminar separation bubble topology and the resulting changes in airfoil lift. In order to investigate the effects of free-stream turbulence intensity on the streamwise and spanwise flow development within a separation bubble, flow field measurements are made using planar Particle Image Velocimetry for an angle of attack of 4°, chord Reynolds numbers of 80 000 and 125 000, and free-stream turbulence intensities between 0.10% and 1.94%.

The results show that increasing the level of free-stream turbulence intensity leads to a reduction in the length of the separation bubble formed over the suction side of the airfoil. The reduction in bubble length is a result of a downstream shift in mean separation as well as an upstream shift in mean transition and, consequently, mean reattachment. At low angles of attack, the reduction in separation bubble length leads to a slight reduction in airfoil lift, while at pre-stall angles of attack the reduction in separation bubble length alleviates the loss of suction at the location of the suction peak, thereby increasing lift, and can delay stall. While the effects of turbulence intensity and chord Reynolds number on the mean flow are shown to be similar, their effects on transition are shown to be notably different. The upstream shift in mean transition with increasing turbulence intensity is shown to be the result of disturbances reaching higher amplitudes earlier upstream as the level of turbulence intensity is increased, despite increased bubble stability. This result suggests that the increased initial perturbation amplitude at elevated turbulence intensity levels is solely responsible for the upstream shift in mean transition. In contrast, the upstream shift in mean transition with increasing Reynolds number is a result of decreased bubble stability.

Wavenumber-frequency spectra of velocity fluctuations in the separated shear layer show that disturbances become more broadband in both time and space with increasing turbulence intensity. In addition, the results show that as the level of free-stream turbulence intensity is increased, the spanwise coherence of shear layer rollers decreases at the location of roll-up, leading to earlier vortex breakdown. At elevated levels of turbulence intensity, streamwise streaks of low speed fluid are observed, and originate in the boundary layer upstream of the separation bubble. These streaks form as a result of the onset of bypass transition, leading to significant changes in bubble dynamics, particularly at the highest level of turbulence intensity investigated. The results suggest that the transition mechanism in the separation bubble at the highest level of turbulence intensity investigated is altered.

Acknowledgements

First and foremost, I would like to thank my supervisor, Professor Serhiy Yarusevych, for his guidance, patience, and support over the past two years. Your attention to detail, knowledge, and passion for fluid mechanics foster an invaluable environment for academic success.

The friendship and camaraderie within the research group surely went a long way in keeping my morale high during the many long days and weeks of this work. John Kurelek, Supun Pieris, Jeff McClure, Andrew Lambert, Eugene Zivkov, Winston Hu, Erik Marble, Ajith Airody, Jonathan Deng, Caddie Zhang, Laura Haya, and Burak Tuna, thank you all for your support and willingness to help. The many games of squash and softball we played were particularly enjoyable. Special thanks are certainly owed to John, whose help with experimental setups, numerous discussions, and MATLAB and LaTeX expertise went far beyond any help I could have expected, to Burak, who helped me with my PIV experiments and image processing, and to Supun, who helped me through coursework.

I would also like to thank the following technical staff members from whom I had help with various aspects of this work: Jason Benninger, Rob Kraemer, Mark Kuntz, Neil Griffett, and Richard Gordon. In particular, I would like to thank Jason and Rob for their help in fabricating the turbulence generating grids, and Neil Griffett for fixing the airfoil microphone array and helping John to develop the microphone breadboard unit.

The love and support of my family and friends outside of my academic world are also owed many thanks. Firstly, to my parents Stewart and Jennifer for their love and financial support which has enabled me to pursue a higher education, and to my brother Ian and sister Abby who kept my mindset on my studies light. To the rest of my family and friends, many of whom knew of my work as studying 'bubbles', thank you for supporting me each step of the way and encouraging me, it went further than many of you likely know. Specifically to my grandparents Don, Arlene, Edward, and Christa who have always had a keen interest in my engineering studies, and my uncle Peter and aunt Sarah who could sympathize with some of the struggles of graduate studies. I'd like to give a special thank you to Alie Thompson, whose friendship and many lunchtime discussions helped me through some of my most difficult times over the last two years. Finally, I want to thank my girlfriend Ellen James, your love, support, and encouragement ensured the timely completion of this thesis, I truly appreciate all of your help.

Financial support of this work was provided by the Natural Sciences and Engineering Research Council of Canada (NSERC) and Bombardier Aerospace. Thanks are extended to Guillaume Malaval and Stephen Colavincenzo for their supervision and guidance over the course of my Industrial Postgraduate Scholarship placement.

Table of Contents

List of Tables

List of Figures

Nomenclature

Dimensionless Numbers

Symbol	Description	Definition
ΔSt	non-dimensionalized unstable frequency band	$\Delta f c/U_0$
Re_c	Reynolds number	$U_0 c/\nu$
St	Strouhal number based on airfoil chord length	fc/U_0
St_0	Strouhal number of central shear layer disturbance frequency	$f_0 c/U_0$
C_l	sectional lift coefficient	$\int_0^1 (C_{P,pressure} - C_{P,suction}) dx/c$
C_P	surface pressure coefficient	$(P - P_0)/q_0$
H	boundary layer shape factor	δ^*/θ

Roman Symbols

Symbol	Description	Units
Δf	unstable frequency band	Hz
ΔP_c	static pressure drop across tunnel contraction	Pa
ℓ	separation bubble length; $x_R - x_S$	m
ℓ_b	chordwise separation bubble length; $X_R - X_S$	m
PSD	power spectral density of $a^{(n)}$	-
$\overline{U_X}$	average chordwise velocity	ms^{-1}
$\overline{U}$	average streamwise velocity	ms^{-1}
p'_{max}	maximum of p'	Pa
Tu	free-stream turbulence intensity; u'/U_0	-
A	wind tunnel calibration constant	-
$a^{(n)}$	POD mode temporal coefficient	-
B	wind tunnel calibration constant	-
c	airfoil chord length	m
$C_{l,max}$	maximum of C_l	-
d	turbulence generating grid element size	m
E_c	cumulative relative POD modal energy	-
E_r	relative POD modal energy	-
E_{pp}	energy spectrum of p	Pa^2
E_{uu}	energy spectrum of u	$m^2\ s^{-2}$
E_{vv}	energy spectrum of v	$m^2\ s^{-2}$
f	frequency	Hz

f_0	central disturbance frequency	Hz
k_x	streamwise wavenumber	m
L	streamwise coordinate relative to turbulence generating grids	m
l	spanwise coherence length	m
M	turbulence generating grid mesh size	m
n	POD mode number	-
P	mean surface pressure	Pa
p	fluctuating component of P	Pa
p'	root-mean-square of p	Pa
P_0	mean free-stream static pressure	Pa
q_0	mean free-stream dynamic pressure; $0.5\rho U_0^2$	Pa
t	time	s
U	instantaneous streamwise velocity	ms^{-1}
u	fluctuating component of U	ms^{-1}
u'	root-mean-square of u	ms^{-1}
U_0	mean free-stream velocity	ms^{-1}
U_c	average convective velocity of disturbances	ms^{-1}
U_e	boundary layer edge velocity	ms^{-1}
U_X	instantaneous chordwise velocity	ms^{-1}
u_X	fluctuating component of U_X	ms^{-1}
u'_X	root-mean-square of u_X	ms^{-1}
W	instantaneous spanwise velocity	ms^{-1}

w	fluctuating component of W	ms^{-1}
X	chord aligned coordinate	m
x	surface attached streamwise coordinate	m
X_R	chordwise location of mean reattachment	m
x_R	surface attached location of mean reattachment	m
X_S	chordwise location of mean separation	m
x_S	surface attached location of mean separation	m
X_T	chordwise location of mean transition	m
x_T	surface attached location of mean transition	m
y	surface-normal coordinate	m
z	spanwise coordinate relative to airfoil midspan	m

Greek Symbols

Symbol	Description	Units
α	airfoil angle of attack	degrees (°)
β	turbulence generating grid porosity; $(1 - d/m)^2$	-
δ^*	boundary layer displacement thickness	m
Δu_ϵ	uncertainty estimate of quantity ϵ	-
ϵ	quantity of interest in uncertainty calculations	-
Λ	free-stream integral length scale	m
ν	kinematic viscosity of air	m^2 s
$\psi^{(n)}$	Eigenfunction of POD mode number n	-
ρ	density of air	kgm^{-3}
$\sigma_{p'}$	spatial amplification rate; $\sigma_{p'} = \frac{\Delta \ln(p'/q_0)}{\Delta X/c}$	-
$\sigma_{u'}$	spatial amplification rate; $\sigma_{u'} = \frac{\Delta \ln(u'/U_0)}{\Delta x/c}$	-
$\sigma_{v'}$	spatial amplification rate; $\sigma_{v'} = \frac{\Delta \ln(v'/U_0)}{\Delta x/c}$	-
$\sigma_{p',max}$	maximum of $\sigma_{p'}$	-
$\sigma_{u',max}$	maximum of $\sigma_{u'}$	-
$\sigma_{v',max}$	maximum of $\sigma_{v'}$	-
θ	boundary layer momentum thickness	m

Chapter 1

Introduction

Airfoils are important to numerous engineering applications, and can be found in sizes ranging from the wings of Unmanned Aerial Vehicles and the blades of wind turbines, to the wings of large commercial aircraft. Further, airfoils operate over a range of speeds from slow gliders to supersonic military aircraft. This large design space over which airfoils are employed presents a significant challenge to engineers in terms of required airfoil performance, thus numerous airfoil designs exist and have been thoroughly characterized [1, 2]. The important non-dimensional parameter characterizing this broad range of operating conditions is the Reynolds number based on the airfoil chord length. One of the most challenging design ranges of chord Reynolds numbers occurs below approximately 700 000 [3], where performance is reduced as compared to that achieved at higher chord Reynolds numbers [4]. The decrease in airfoil performance is a largely due to laminar boundary layer separation over the suction side of the airfoil.

At low chord Reynolds numbers, $50\,000 \lesssim Re_c \lesssim 700\,000$ depending on specific airfoil geometry, the flow over the suction side of the airfoil is prone to laminar separation downstream of the suction peak in the presence of an adverse pressure gradient [3, 4]. The flow in the separated shear layer then undergoes transition to turbulence and may reattach to the surface of the airfoil downstream. The region of fluid between the mean separation and mean reattachment locations, which flows upstream in the mean sense, is termed the laminar separation bubble and is the focus of this investigation. At higher chord Reynolds numbers, above approximately 700 000, separation bubbles may still form but are so small as to be nearly inconsequential to the mean surface pressure distribution [3]. Maintaining laminar flow over as much of the airfoil surface as possible becomes the challenge in this flow regime, as laminar boundary layers are characterized by lower skin friction drag than turbulent boundary layers. At very low chord Reynolds numbers, below

approximately 50 000, the flow over the suction side of the airfoil is prone to separation without reattachment, since the transition process in the separated shear layer occurs more slowly. This leaves the airfoil in a stalled state and, as a result, maintaining attached flow is of interest in this regime.

One of the first studies of laminar separation bubbles formed over airfoils was performed by Owen and Klanfer [5], though credit for the term 'laminar separation bubble' lies in the later works of Tani [6], Gaster [7], and Horton [8]. The presence of a separation bubble can be identified by reverse flow or by a region of nearly constant surface pressure downstream of the suction peak [6, 7, 9, 10]. Separation bubbles can be classified as either long or short, depending on their effect on the airfoil's mean surface pressure distribution [5–7]. Long bubbles are typically found on thin airfoils and were originally classified as 'thin airfoil stall' [11]. For this type of bubble, the separation point remains relatively close to the suction peak while the reattachment point gradually shifts downstream with increasing angle of attack until the bubble bursts [5, 7], resulting in a fully stalled airfoil. Short bubbles are more typical for thicker airfoils and may form anywhere over the length of the airfoil depending on the flow conditions [10]. For short bubbles, the size of a laminar separation bubble generally decreases with increasing angle of attack or Reynolds number, though the angle of attack effect is greater [9, 10]. At large angles of attack, the bubble eventually bursts [5, 7] and the airfoil is left in a stalled state. While the accepted time-averaged topology of the laminar separation bubble has not changed significantly since it was sketched by Horton [8], our understanding of the unsteadiness of the bubble has improved significantly.

When the flow over the suction side of the airfoil separates, the transition process in the separated shear layer determines if the flow will reattach downstream. The transition process begins with the amplification of small amplitude perturbations originating upstream through the receptivity process [12]. The initial growth of these disturbances is primarily two-dimensional and nearly exponential, and can be modelled by linear stability theory [13–15]. As the disturbances continue to grow, non-linear interactions begin to occur, and the shear layer rolls up into coherent spanwise oriented vortices [16–18]. As these vortices convect downstream, the enhanced momentum exchange with the free-stream enables mean flow reattachment [17, 18]. The vortices eventually breakdown to smaller scales downstream of mean flow reattachment, and a turbulent boundary layer develops [15, 17, 18].

The sensitivity of the transition process in the separated shear layer to the amplitude and frequency of the initial disturbances has offered an opportunity to utilize active flow control to improve airfoil performance. A variety of active control techniques have been used to promote the transition process in the separated shear layer, and include acoustic excitation [19, 20], plasma actuation [21–24], and synthetic jet actuation [25]. These techniques work by introducing disturbances into the flow upstream of separation, and are then amplified in

the separated shear layer. Typically, these disturbances are introduced at the most unstable frequency of the unperturbed separation bubble, where growth rates are the largest. The net effect is that transition occurs further upstream and can thus be used to reattach the flow of a stalled airfoil [26] or to reduce the size of formed separation bubbles [18, 23, 24], thereby improving overall airfoil performance.

Transition is sensitive to the test section environment, and in particular, to incoming flow perturbations [27, 28]. As a result, conflicting descriptions of the transition process in laminar separation bubbles have been reported in the literature. For example, some investigations report that roll-up of the shear layer is periodic and coherent in the spanwise direction [18, 29, 30], while others observe little spanwise coherence [31, 32]. Further, Ol *et al.* [33] conducted a comparison of mean separation bubble topology measured for nominally identical experiments performed in three different facilities and reported significant differences. One of the contributions to the observed changes in both of these examples is a variation in the level of free-stream turbulence intensity in the research facilities. Free-stream turbulence intensity is a measure of the amplitude of velocity fluctuations in the free-stream about the mean value, and is computed as the root-mean-square of the fluctuations divided by the mean free-stream velocity, typically reported as a percentage value. Higher free-stream turbulence intensity levels therefore represent higher disturbance environments, and can have a significant influence on experiments [9, 27, 28, 33].

In the context of wind tunnels and transitional studies, low free-stream turbulence intensities are on the order of 0.1% [18, 27, 34] and high levels on the order of 1% [31], whereas in turbomachines, turbulence intensities can be as high as 5% to 10% [35–37]. While some investigations have looked at the effects of free-stream turbulence intensity on separation bubble topology [9, 34, 38] and airfoil performance [28, 39], its effects on the transition process in the separated shear layer remain to be fully addressed. In addition, studies measuring the effects of increased free-stream turbulence intensity on airfoil lift and formed laminar separation bubbles simultaneously are limited, and thus any relationship has yet to be fully addressed. Any link between the effects of free-stream turbulence intensity on separation bubbles and airfoil lift is important to understand for applications in which airfoils are employed in elevated levels of free-stream turbulence intensity, such as in downstream wind turbines in a wind farm and turbo-machines.

1.1 Study Objectives

The goal of this study is to experimentally investigate the effects of free-stream turbulence intensity on the flow over a NACA 0018 airfoil at low Reynolds numbers. Specifically, the study aims to shed light on the effects of free-stream turbulence intensity on mean laminar separation bubble topology, the transition process within the separated shear layer, and any attendant changes to airfoil lift. Therefore, the main objectives are as follows:

1. Characterize the effects of free-stream turbulence intensity on the mean flow by
   (a) describing changes in mean separation bubble topology, and
   (b) relating the observed changes to the sectional lift coefficient.
2. Investigate the effects of free-stream turbulence intensity on the transition process by
   (a) evaluating the streamwise and spanwise flow development of formed laminar separation bubbles, and
   (b) characterizing disturbance development within the separated shear layer.

Chapter 2

Background

Airfoils operating at low Reynolds numbers can be found in several engineering applications, including small aircraft, such as unmanned aerial vehicles, and small to medium sized wind turbines [4]. Over the past several decades, significant research efforts have been invested into better understanding the decrease in airfoil performance at low Reynolds numbers as compared to that achieved at higher Reynolds numbers [3, 4]. The most significant issue facing airfoils operating at low Reynolds numbers is laminar boundary layer separation, particularly over the suction side of the airfoil, leading to the formation of a laminar separation bubble. Reviewing the current understanding of laminar separation bubbles, as well as the laminar-to-turbulent transition process in the separated shear layer are the focuses of this chapter. First, an overview of separation bubbles formed over low Reynolds number airfoils will be presented. Then, the transition processes in attached boundary layers and free-shear layers are reviewed in order to draw comparisons with separated shear layer transition in laminar separation bubbles. Finally, previous investigations of the effects of free-stream turbulence intensity (FSTI) on the flow over low Reynolds number airfoils as well as on laminar separation bubbles are considered.

2.1 Laminar Separation Bubbles Formed over an Airfoil at Low Reynolds Numbers

The low Reynolds number regime for airfoils is typically characterized by chord Reynolds numbers below approximately 700 000 [3]. Generally speaking, the performance of an airfoil is decreased in this regime as compared to that at higher Reynolds numbers, and is attributed to the presence of a suction side Laminar Separation Bubble (LSB) [4]. While

there are numerous airfoil sections whose characteristics vary greatly for different flow conditions [1], the LSB is a challenge faced by all airfoils operating in the low Reynolds number regime. At low speeds, the boundary layer formed over the fore portion of the airfoil remains laminar, and is thus prone to separation since it carries less momentum near the wall as compared to a turbulent boundary layer. Downstream of the suction peak, the flow faces an adverse pressure gradient which may cause the flow to separate [3–5, 11]. The resulting separated shear layer undergoes transition to turbulence, and the enhanced momentum exchange with the free-stream can result in mean flow reattachment. The region of fluid between the mean separation and reattachment points is re-circulating in the mean sense, and has been termed a laminar separation bubble [6–8]. A time-averaged sketch of an LSB is shown by the shaded grey region in Fig. 2.1.

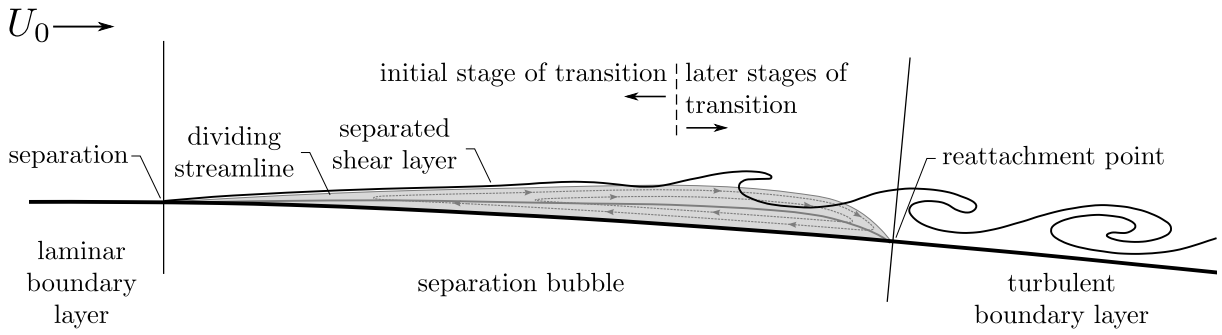

Figure 2.1: Sketch of a laminar separation bubble, from Kurelek [20]. The shaded grey region represents the time-averaged bubble topology.

Laminar separation bubbles formed over airfoils have been studied experimentally [9, 18, 31, 32, 40, 41] as well as numerically [17, 42–45]. Separation bubbles can also be induced on a flat plate with imposed adverse pressure gradients both experimentally [7, 46, 47] and numerically [30, 43, 48, 49]. While both geometries yield similarly behaved LSBs, by studying separation bubbles over a flat plate an experimentalist benefits from being able to make measurements over a much simpler geometry. Separation bubbles also form in other geometries, such a backward facing steps and humps [50], but this chapter will focus on the airfoil and flat plate geometries. Over an airfoil, separation bubbles may be either short or long depending on their effect on the mean surface pressure distribution [5, 7, 11]. Long bubbles are typically found on thinner airfoils where the separation point is near the leading edge, and was thus originally characterized as thin airfoil stall [11]. For this type of bubble, as the angle of attack is increased, the reattachment point shifts downstream until the bubble 'bursts' [5, 7], stalling the airfoil. In the case of short bubbles,

the bubble typically forms further downstream from the leading edge at low angles of attack [10]. As the angle of attack is increased, the bubble decreases in length and also shifts upstream [10, 11]. Beyond the stall angle of the airfoil, the enhanced momentum exchange in the transitioning separated shear layer can no longer sustain flow reattachment and the bubble bursts, leaving the airfoil in a fully stalled state. This dependence of mean flow reattachment on the transition process in the separated shear layer highlights the importance of transition to the overall flow development of LSBs.

While the accepted time-averaged topology of the separation bubble as shown in Fig. 2.1 has remained essentially unchanged since the early descriptions of Gaster [7] and Horton [8], significant progress related to the understanding of the unsteady nature of the bubble has been made in the last two decades [13, 18, 32, 46, 51, 52]. In the initial stages of transition (see Fig. 2.1), small perturbations which originate upstream through the receptivity process [12] are amplified in the separated shear layer. The amplification of these perturbations is initially two-dimensional and nearly exponential, and is well modelled by linear stability theory [13, 15, 42]. Further downstream in the later stages of transition (see Fig. 2.1), non-linear interactions begin to occur and the shear layer is observed to roll-up into spanwise oriented vortices [16, 18, 31] which are shed at the most amplified frequency of the separation bubble [17, 18, 26]. The enhanced momentum exchange with the free-stream induced by these vortices enables mean flow reattachment [18].

Spectra of velocity fluctuations in the separated shear layer exhibit strong peaks at the frequency of vortex shedding [10, 17, 18, 26], but can have additional peaks at low frequencies which are associated with bubble 'flapping' [32, 48, 50, 53, 54], and/or peaks at the subharmonic of the shedding frequency which are associated with vortex merging [17, 20, 55]. Bubble flapping is associated with fluctuations within the separation bubble that are not related to the shedding of shear layer vortices [17], and result in an unsteady up and down motion of the separated shear layer [31, 48]. This behaviour results in a mean flow deformation, when viewed from the higher frequency instabilities of the separated shear layer, and thus alters the stability characteristics of the bubble [43]. By exciting a bubble experiencing low-frequency oscillations with acoustic waves near the natural frequency of the bubble, Zaman *et al.* [56] were able to suppress the low-frequency oscillations. Vortex merging involves the coalescence of two consecutive vortices shed from the separated shear layer. Merging results from minor variations in the roll-up process, and more specifically in the relative strength and/or position of consecutive rollers [55]. In a merging event, these minor variations result in an upstream vortex convecting downstream faster than the vortex directly downstream of it. As the upstream vortex approaches the downstream one, the vortices begin to orbit and eventually coalesce, doubling the streamwise wavelength [55]. When merging occurs frequently enough, this doubling of the streamwise wavelength

of the vortices leads to the subharmonic frequency peak noted in experiments [17, 20, 55]. Merging is associated with subharmonic instabilities in the separated shear layer [50] and also occurs in free-shear layers [57–61]. By acoustically forcing a separation bubble at the subharmonic frequency of its natural shedding frequency, Kurelek [20] was able to promote the merging process and observe a significant increase in the number of merging events in the separated shear layer as compared to when the bubble was left unforced.

As the shear layer rollers convect downstream, a secondary instability is amplified and results in spanwise undulations in the vortex filaments [17, 18, 32]. The amplitude of bulges in a vortex filament are amplified as the roller convects downstream, leading to a re-orientation of spanwise vorticity into the streamwise direction [18]. The arms of the vortex filament adjacent to a downstream bulge in a vortex filament induce a wall normal velocity which causes the leading edge of the bulge to lift up into higher velocity fluid in the upper part of the boundary layer. As a result, the streamwise oriented vorticity is stretched and the structure begins to resemble Λ-structures observed in attached boundary layers [62–65]. Further downstream, the vortices break up into smaller scales as the flow transitions to turbulence, and a turbulent boundary layer develops [18].

The separated shear layer transition process is highly sensitive to the amplitude of the initial perturbations, and thus to the upstream flow conditions from which disturbances originate via a receptivity process [12]. This sensitivity has led researchers to explore active flow control as a means to reduce the size of formed LSBs. Applying acoustic excitation at a frequency at which the bubble amplifies has been shown to lead to mean reattachment of the flow for a stalled airfoil [26], as well as to reduce the size of formed separation bubbles [20]. Further, roll-up of the separated shear layer and the shedding of vortices becomes more periodic and coherent across the span of the airfoil [20]. Similar findings have also been reported using plasma actuation to introduce disturbances upstream of separation bubbles [22–24], as well as in numerical simulations in which periodic disturbances are introduced upstream of separation [43, 44, 66]. Some flow disturbances however originate from the research facility itself and have led to difficulties in comparing results obtained in different facilities using identical experimental conditions. The extent of the challenge was elucidated by Ol *et al.* [33] who compared results for nominally identical experimental conditions performed in three facilities. They noted significant differences in mean bubble topology and attributed the differences, in part, to different levels of FSTI in the facilities. The effects of FSTI on separation bubbles was shown further by Olson *et al.* [34] who increased the level of FSTI in their facility and saw a downstream shift in the location of mean separation as well as an upstream shift in mean reattachment. A brief review of the effects of FSTI on transition is provided in Section 2.2.3, while Section 2.3 reviews the effects of FSTI on separation bubbles and airfoil lift.

2.2 Transition to Turbulence and the Effects of Free-Stream Turbulence Intensity

Since the early experiments of transition in a pipe conducted by Reynolds [67], researchers have been studying the laminar-to-turbulent transition process in a number of flows in an attempt to understand and predict the process. A number of factors are known to affect transition, including model roughness, acoustic environment, and the free-stream turbulence intensity [28, 33, 68], with the later being the focus of this thesis. The purpose of this section is to review the transition process in the separated shear layer of LSBs, as well as boundary layers and free-shear layers, in order to compare and contrast the flows. Where available, literature documenting the effects of free-stream turbulence intensity on each of these transition processes is reviewed.

2.2.1 Boundary Layers

The concept of the boundary layer was put forth by Prandtl [69] in an effort to describe fluid motion over a surface between the no-slip condition at a wall, and the free-stream velocity away from the wall. For the flow over a flat plate with zero pressure gradient, a laminar boundary layer initially forms from the leading edge, with a velocity profile that is well described by a Blasius profile [70]. At some distance downstream, the boundary layer profile resembles that of a turbulent profile. Over some range between these locations, the flow is in a transitional state. This transition from a laminar boundary layer to a turbulent on is depicted in Fig. 2.2. Transition begins with the amplification of small amplitude perturbations in the boundary layer that originate from sources such as surface roughness, acoustic waves in a research facility, or small velocity fluctuations in the free-stream, to name a few [12, 65]. In low disturbance environments where the initial perturbations have small amplitudes and are two-dimensional, their growth or decay can be modelled by superimposing them onto the linearized Navier-Stokes equations describing the mean boundary layer flow. This treatment is the foundation of linear stability theory which was mentioned in Section 2.1 in describing the transition process in LSBs. By modelling the disturbances as waves with a given frequency and wavelength, they will grow or decay based on solutions to the Orr-Sommerfeld equation, named as such after the stability calculations of laminar flows by Orr [71] and independently by Sommerfeld [72]. For a given pair of disturbance wavelength and local Reynolds number, Tollmien [73] solved the Orr-Sommerfeld equation and developed a neutral stability curve for flat plate boundary layers. Growth rates of disturbances within this curve were later calculated by Schlichting [74]. Below a given value of the local Reynolds number, the flow is stable to all disturbance

wavelengths provided that their amplitude is small. This value of this Reynolds number is called the indifference Reynolds number, above which the boundary layer will amplify disturbances with certian wavelengths based on the flow's stability curve [65].

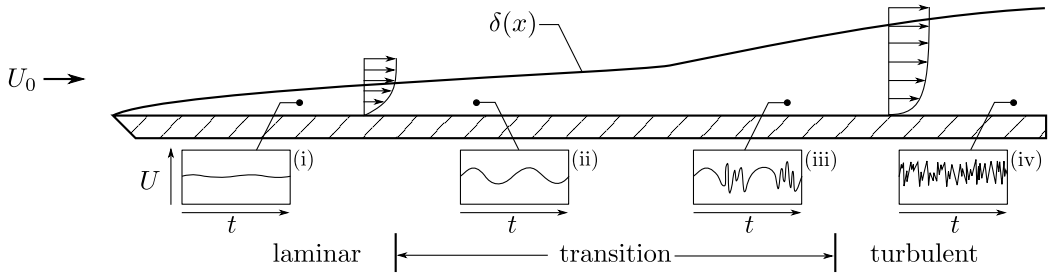

Figure 2.2: Side view of simplified flat plate boundary layer transition, after Kurelek [20] and Schlichting and Gersten [65].

Since these disturbances originate from very small amplitude perturbations (*i.e.*, the velocity time trace (i) in Fig. 2.2), the so-called Tollmien-Schlichting (TS) waves leading to transition over a flat plate weren't measured until the experiments of Schubauer and Skramstad [27] in a wind tunnel with carefully controlled free-stream disturbance levels. In their study, Schubauer and Skramstad [27] also showed that these waves could be artificially excited using a vibrating ribbon across the span of the flow, facilitating measurements of their streamwise development. As the TS waves convect downstream, they are amplified based on the stability curve [65] (*i.e.*, the velocity time trace (ii) in Fig. 2.2), but also develop a spanwise unsteadiness, namely peaks in the streamwise velocity fluctuation amplitudes across the span, as was revealed in early flow visualization work [62, 75]. This three-dimensionality of the waves was controlled and studied experimentally by Klebanoff *et al.* [63], who used an experimental set-up similar to that of Schubauer and Skramstad [27] but with spacers under the vibrating ribbon in order to induce a fixed spanwise wavelength in the initial perturbations. Measurements of spanwise velocity fluctuations taken across the span of the flow revealed distinct pairs of peaks in the fluctuation amplitudes. These pairs were centered at the spanwise location corresponding to the peaks in the streamwise velocity fluctuations, such that one peak in the spanwise velocity fluctuations was on either side of the peak in streamwise velocity fluctuations. These peaks were therefore taken to be evidence of a longitudinal eddy system [63]. The structures were termed vortex loops by Hama *et al.* [75], 'hairpin' eddies by Klebanoff *et al.* [63], and more recently are often called Λ-structures [64, 76]. The difference in terminology is largely attributed to the local Reynolds number and the spanwise extent of the vortices [77]. The development of

disturbances from the two-dimensional TS waves to Λ-structures is depicted in Fig. 2.3.

Primary instability calculations breakdown when the amplitudes of disturbances reach approximately 1% of the mean free-stream velocity, and can no longer be considered small. Since the observed Λ structures typically form downstream of where the TS wave amplitude is above this level, their development must be described by a secondary instability [64, 78]. The solutions to the primary instability of the mean flow are used as the new base flow in a coordinate system which moves along with the phase speed of the TS waves, and is thus quasi-steady and periodic [65]. A three-dimensional pertubation is then superimposed onto this new base flow [65, 78], and the solution then describes motions which are periodic in both the streamwise and spanwise directions. Based on the phase speed of the disturbance, the solutions are classified as one of three modes: harmonic, subharmonic, or detuned modes [78]. For the harmonic mode, the phases, and thus wavelengths, of the streamwise and spanwise disturbances are the same. For the subharmonic mode, the disturbances are perfectly out of phase and the streamwise wavelength is twice the spanwise wavelength. The detuned mode has a phase speed which falls between these two modes [78]. In all cases, the growth rate of the secondary instability is significantly higher than that of the TS wave, justifying the quasi-steady assumption of the primary instability flow used in the derivation of the secondary instability [78, 79]. Numerous terms have been used in the literature to describe the arrangement of the Λ-structures forming as a result of either the harmonic or subharmonic oscillations. In short, K-type refers to the aligned Λ-structures observed by Klebanoff *et al.* [63] (Fig. 2.3a) that form as a result of fundamental modes, while H-type refers to staggered Λ-structures (Fig. 2.3b) that form as a result of subharmonic modes and named after Herbert [64]. Subharmonic modes are more unstable than the fundamental modes [78, 80], and therefore the staggered Λ-structure will emerge if transition is left to natural paths and the growth of the TS wave is slow. On the other hand, the fundamental mode will dominate for larger TS waves as is the case when they are forced [63]. This distinction is seen in the flow visualizations of Knapp and Roache [81], where the staggered pattern is observed for natural transition, while the aligned pattern was observed when acoustic excitation was used. An adverse pressure gradient also increased the occurrence of the aligned structures, leading the authors to conclude that the aligned structure pattern was more likely to form for cases where development of the TS waves was faster.

As the three-dimensional structures convect downstream, they are stretched by the large wall-normal gradient in the mean streamwise flow. Eventually, they begin to break apart and turbulent spots are observed near the top of the boundary layer (Fig. 2.3), often at the tips of the Λ-structures [75]. These spots were first observed in water table experiments by Emmons [83], and appear at random locations across the span of a flow, dependent on where the Λ-structures form [84]. Once formed, these spots spread in all three directions,

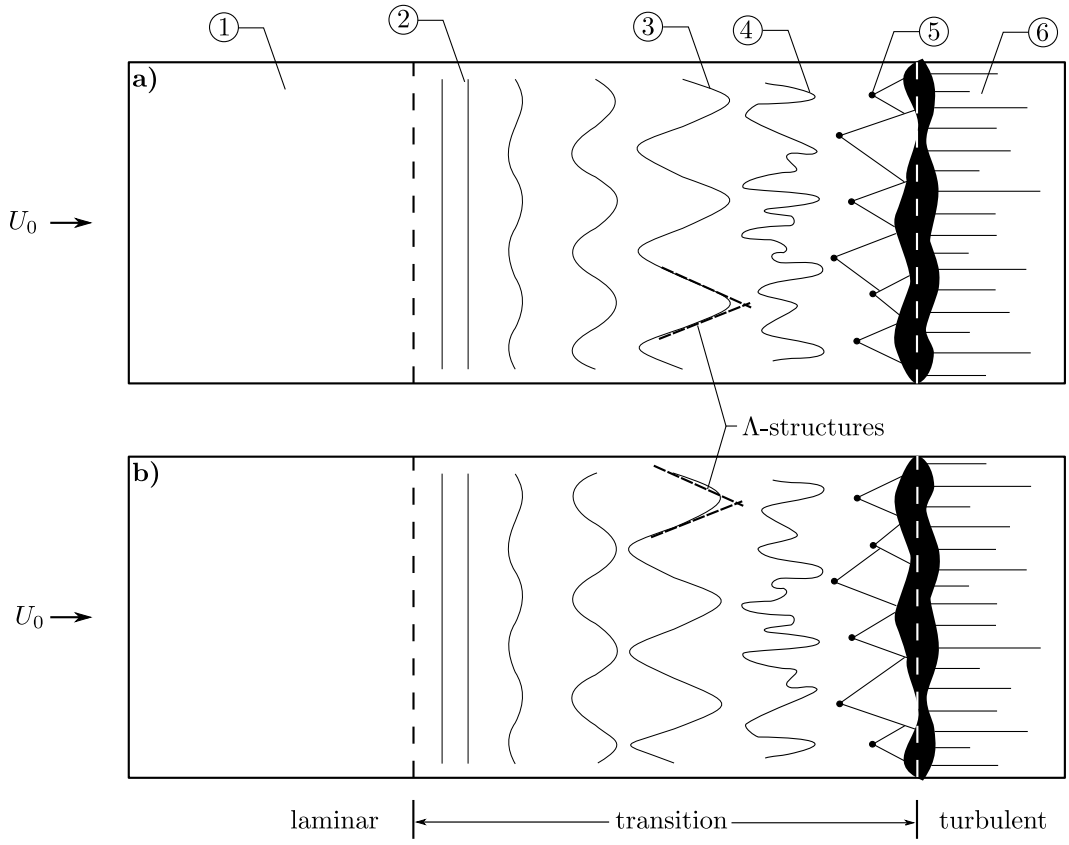

Figure 2.3: Top view of simplified flat plate boundary layer transition with (a) harmonic and (b) subharmonic oscillations resulting in the aligned and staggered Λ-structure formations, respectively. Sketched after Kurelek [20], Schlichting and Gersten [65], and Bertolotti [82]. ① Laminar flow; ② TS waves; ③ three-dimensional waves and Λ-structure formation; ④ vortex breakdown; ⑤ turbulent spot formation; ⑥ turbulent flow.

at a rate faster than diffusion [84], until they merge with neighbouring spots and the entire boundary layer becomes turbulent (*i.e.*, location 6 in Fig. 2.3). In experiments of transition in boundary layers which are excited by a vibrating ribbon, the formation of Λ-structures, and hence turbulent spots, beomes more regular as they form at regular spanwise locations [27, 63, 84]. This makes the spots easier to measure and also typically results in a shorter transitional length as more spots form than when the boundary layer is left unforced.

The experiments of Schubauer and Skramstad [27] elucidated the sensitivity of transition to FSTI. In fact, Taylor [85] proposed that free-stream turbulence was responsible for

transition (albeit by a mechanism which was later disproved) since evidence of TS waves could not be found until the experiments of Schubauer and Skramstad [27]. At large levels of FSTI, the typical transition mechanism may be bypassed [12, 86]. Although it is meant to indicate any change to the natural transition path, the term bypass transition has become associated with transition under high levels of FSTI, typically above about 1% [87, 88]. At these levels of turbulence intensity, streamwise streaks have been observed in boundary layers both numerically [16, 87–91] and experimentally [92–96]. These streaks have been called Klebanoff modes [88, 97], and are not to be confused with the aforementioned K-type Λ-structures observed in natural boundary layer transition. The spanwise extent of the streaks is on the order of the boundary layer thickness, while their streamwise extent is significantly larger [94]. These streaks do not induce significant spanwise velocity fluctuations, but bring low speed fluid to the top of the boundary layer and high speed fluid towards the wall [89, 97], resulting in streamwise velocity fluctuations between 10% and 20% of the mean free-stream velocity [87, 90, 91, 94]. The mechanism by which FSTI leads to these streaks is complex [98], and therefore for the purposes of this discussion it is sufficient to say that streaks are formed at high levels of FSTI.

The progression of streamwise streaks to turbulence is not well described by theory [12, 97], but Direct Numerical Simulations (DNS) have led to some understanding of their breakdown [87–89, 95, 97]. In simulations, FSTI must be modelled, and one common method is that proposed by Jacobs and Durbin [87]. Details will be discussed further in Section 2.3.3 but the method relies on a Fourier expansion of the disturbance velocities at the domain inlet. In the wall-normal direction, investigators typically model the disturbance quantities with continuous modes of the Orr-Somerfeld equation [88–90, 99, 100], as they model travelling wave perturbations that naturally decay towards the wall in the boundary layer, replicating FSTI in experiments. These modes are a set of complementary solutions to the discrete modes of the Orr-Sommerfeld equation, and were shown to exist in unbounded flows by Grosch and Salwen [101]. The reader is referred to the work of Grosch and Salwen [101] for details of these continuous modes, but the important aspect here is that, in simulations, FSTI is modelled as a superposition of periodic modes onto the mean flow. The formation of streaks in simulations has been shown to depend on the local Reynolds number as well as the wall-normal frequency of the prescribed modes used to model FSTI [88–90]. Interestingly, streaks do not necessarily lead to transition on their own, but, will actually decay as a result of viscous effects if left unperturbed [89], even in the presence of adverse pressure gradients [90]. In simulations where FSTI was described by a simple superposition of two modes at the domain inlet, Zaki and Durbin [89] showed that for transition to occur, one mode must be low-frequency and the other high-frequency. The lower frequency mode forms the streaks in the boundary layer as it can penetrate further into the boundary layer,

while the higher frequency mode remains in the free-stream. The induced velocity from the streaks causes them to lift up towards the boundary layer edge, where they interact with the high frequency mode which remains in the free-stream [89]. At this interface, a secondary instability resembling that of a Kelvin-Helmholtz instability arises, and the formed vortices grow in amplitude with increasing streamwise distance until they break up into a turbulent spot [89]. Brandt and Henningson [102] showed that the streaks may also break down as a result of a sinuous instability, which leads to a streamwise waviness in the streak. Even when streamwise streaks are present, TS waves may also amplify and interact with the streaks [88, 93]. In simulations where discrete and continuous Orr-Sommerfeld modes are prescribed at the domain inlet, generating TS waves and streaks respectively, the interaction of these two modes has been shown to lead to transition [88, 96]. In this case, the formed streaks destabilize the TS waves and lead to a secondary instability that locks onto the streak width, forming similar structures to those observed in natural transition, *i.e.*, Λ-structures [88].

2.2.2 Free Shear Layers

Free shear layers, or mixing layers, are formed between two parallel streams of fluid which may be either co-flowing or opposing. In the case of co-flowing streams, free shear layers are often studied downstream of a splitter plate because of the simplicity of the geometry [103]. In this case, the free shear layer is characterized by the velocity ratio of the two streams,

$$R = \frac{U_1 - U_2}{2\overline{U}}$$

where $\overline{U}$ is the average velocity of the two streams. For the limiting cases, when $R = 0$ the streams are of equal velocity and there is no shear between them, while for $R = 1$ only one stream is present and therefore behaves similarly to a free jet.

Downstream of a splitter plate with $0 < R < 1$, the free shear layer is unstable via an inviscid Kelvin-Helmholtz intstability since the velocity profile contains an inflection point [57, 103, 104]. Disturbance waves in the shear layer grow with downstream distance until the shear layer rolls-up into periodic, spanwise oriented vortices [58, 105–107] which convect downstream at the average velocity of the two streams [103]. The growth rate of the structures with streamwise distance increases with increasing velocity difference between the two streams. In the region of roll-up, the spreading rate of the shear layer is approximately linear with downstream distance [58, 59]. Similarly to boundary layers, linear stability analysis has proven useful in describing the initial amplification of disturbances in a free shear layer [57, 108]. In order to perform these stability calculations, a hyperbolic

tangent velocity profile is often assumed [103, 104, 109, 110]. Through a series of detailed stability calculations, Monkewitz and Huerre [110] showed that by increasing R from 0 to 1 the maximum spatial growth rate of disturbances in the free shear layer grows by about 20% while the frequency of the most amplified wave decreases by only approximately 5%.

Merging of consecutive vortices is observed downstream of the initial roll-up location [57–61]. Subsequent merging events continue for large distances downstream [59], resulting in increasing streamwise spacing between vortices with increasing streamwise distance. Vortex merging results from the amplification of disturbances at the subharmmonic frequency of the initial Kelvin-Helmholtz instability [104, 111, 112]. The first merging event typically occurs at approximately twice the streamwise distance from the splitter plate as the location of initial roll-up [60, 113]. The dynamics of the merging process depend on the phase difference between the fundamental and subharmonic modes [61, 103, 114], while the rate at which the vortices merge increases with increasing vorticity concentration of the rollers as well as increasing vertical offset of the cores [59, 61]. When the subharmonic mode is in phase with the fundamental mode, consecutive vortices are displaced upwards and downwards respectively, resulting in a net vertical displacement between the vortices [61, 104]. The difference in the mean flow velocities at the locations of the vortex cores then induces a relative velocity between the vortices. When the vortices approach, they begin to rotate about each other and eventually coalesce [57, 59, 61, 103]. Even though the vortices are observed to merge, simulations show that the two vortices maintain their identity [103], an effect that is smeared out in flow visualizations [115]. The merging process has been suggested to be associated with increased fluid entrainment [59, 61, 103], however, Hernan and Jimenez [116] suggest that most entrainment takes place during the initial growth of the vortices rather than during merging. When the subharmonic mode is perfectly out of phase from the fundamental mode, consecutive vortices are displaced in the same direction [61, 104] and thus the merging process is supressed. In this case, a vortex from the fundamental mode is caught between the nodes of the subharmonic mode and is shredded away [103, 114]. In both cases of the subharmonic and fundamental modes being perfectly in or out of phase, the subharmonic mode becomes dominant [57, 59, 60, 117]. Instead of consecutive rollers merging simultaneously across the entire span of a flow, merging can occur locally and is termed 'helical pairing' [104, 118]. This type of merging occurs when the subharmonic mode is three-dimensional and thus has a dominant spanwise wavelength [104]. Although the subharmonic mode is most unstable in a two-dimensional form [104], if it is three-dimensional the spanwise wavelength leads to the localized merging of the spanwise oriented vortices [58, 104, 107, 118].

Similarly to boundary layers, as the rollers convect downstream three-dimensional structures are observed, but are different from the 'helical pairing' three-dimensionality.

Instead of developing from the rollers themselves as in boundary layers, in free-shear layers streamwise counter-rotating vortices superimposed onto the large scale spanwise rollers are observed [104, 112, 117, 119, 120]. Following a similar method to the theoretical analysis of Benney and Lin [121], Pierrehumbert and Widnall [104] numerically investigated the interaction of a two-dimensional wave superimposed with a three-dimensional wave having the same streamwise wavelength. They determined that this instability, termed a translative mode [104, 111], leads to the secondary counter-rotating vortices superimposed onto the rollers, which are observed in simulations [104, 122] as well as experiments [112, 120, 123, 124]. This instability is most unstable when the spanwise wavelength is equal to two-thirds of the fundamental wavelength; in good agreement with experimental observations [117, 120]. The three-dimensional waves grow more slowly than the two-dimensional ones [112, 125], and are thus typically observed downstream of the location of the first vortex merging events [117, 119]. Corcos and Lin [111] showed that the growth rate of the three-dimensional instability is relatively constant through the initial shear layer roll-up, however, the formation of streamwise oriented structures is delayed by vortex merging [112, 113].

Transition to turbulence begins with the appearance of small-scale eddies that lead to the breakdown of the large spanwise oriented vortices [103]. Flow visualizations conducted by Konrad [126] suggested that these eddies originated in the cores of the spanwise oriented vortices, but were later shown by Huang and Ho [113] to originate in the streamwise oriented vortices. The progression of transition in a free-shear layer is often measured as the degree of 'mixedness' of the shear layer which is a different measure than the amount of fluid entrained by the shear layer [103, 113]. Different conditions for the begining of the turbulent regime have been proposed. Bradshaw [127] proposed the location of the peak in the turbulence level, which typically occurs around the streamwise location of the first vortex merging event [103]. Jimenez *et al.* [128] suggested the location at which the roll-off exponent of the spectra of velocity fluctuations reached $-5/3$, indicative of a turbulent flow. This value was shown by Huang and Ho [113] to consistently occur between the second and third merging locations for varying values of R. Finally, transition has been suggested to occur where the level of mixing rapidly grows [119, 126], and was shown by Ho and Huerre [103] to agree well with the third merging location. Since all of these findings suggest that transition typically occurs downstream of merging, it is speculated that the merging process is responsible for the production of the small-scale eddies, shifting energy to the higher frequencies, leading to turbulent breakdown [103, 113]. While the small eddies form via an inviscid instability and are not Reynolds number dependent [113], in order to maintain the small scale motion leading to transition, the local Reynolds number must be $3000 < Re < 5000$ based on the momentum thickness [103, 126] or $13\,000 < Re < 19\,000$ based on vorticity thickness [113]. Theoretical models of transition are limited, but Lin and

Corcos [122] relate shear layer mixing to the dynamics of the three-dimensional structures in the braid region while Huang and Ho [113] relate mixing to the production of small-scale eddies in the merging process.

The transition process is very sensitive to experimental conditions such as the initial boundary layer parameters, the acoustics in a research facility, and, of interest to this thesis, FSTI [103]. The effects of turbulence intensity on free-shear flows were investigated by Wygnanski *et al.* [129], who inserted a turbulence generating grid in one of the streams upstream of the trailing edge of a splitter plate. The authors found that roll-up of the shear layer persisted with the increase in FSTI, despite previous hypotheses and results suggesting that free-stream turbulence intensity inhibits two-dimensional roll-up, and rather leads directly to a three-dimensional flow [118]. Elevated turbulence intensity has been shown to not significantly alter the mean velocity profile for a given velocity ratio [130], but does significantly increase shear layer growth [130, 131], especially if the same relative amount turbulence intensity is added to the higher velocity stream. This finding is intuitive as the same relative turbulence intensity in the higher velocity stream produces a larger initial amount of turbulent kinetic energy in the flow as compared to if the turbulence is added to the lower velocity stream.

2.2.3 Laminar Separation Bubbles

As discussed in Section 2.1, the transition process in the separated shear layer is one of the key aspects of the laminar separation bubble as it determines whether or not the flow will reattach to the airfoil surface. The transition process in separated shear layers shares similarities with free shear layers (Section 2.2.2) and boundary layers (Section 2.2.1) [50]. At and downstream of separation, the separated shear layer contains an inflection point, making it inviscidly unstable [65] as in free-shear layers. However, the presence of the wall increases viscous effects, similar to boundary layer transition [50]. As a result, flow structures in separated shear layers are similar to those in both boundary layers and free-shear layers, and growth rates of disturbances are larger than in boundary layers but smaller than in free-shear layers.

The sketch of an LSB shown in Fig. 2.1 highlights that while the bubble has a well defined mean topology, it is highly unsteady if observed instantaneously. In the fore portion of the bubble, disturbances are small and almost undetectable. However, over a relatively short streamwise distance, fluctuations become large and dominate the flow in the aft portion of the bubble. This laminar-to-turbulent transition process has been the focus of numerous experimental [15, 18, 24, 31, 32, 46, 47, 132, 133] and numerical [14, 17, 29, 30, 42, 43, 49, 134] investigations. More recent studies of the transition process have benefited greatly from

more powerful experimental techniques and computational capabilities.

The transition process begins with the amplification of small amplitude perurbations which originate upstream in the laminar boundary layer. These small perturbations are generated by background conditions in a research facility as a result of the receptivity process (*e.g.*, Ref. [12]). Provided that the initial disturbances are small, these perturbations convect into the separated shear layer where their ensuing amplification has been shown to be primarily two-dimensional [13, 30] and nearly exponential [13, 15, 50, 132], and is well modeled by linear stability theory [15, 43, 47, 51, 135]. In this region of the separation bubble (*i.e.*, the intial stages of transition marked in Fig. 2.1), growth rates are generally lower than those measured in free-shear layers but larger than those in boundary layers [50]. This is a result of the damping effect on growth rates imposed by the presence of the wall [24, 50].

As the disturbances continue to grow, non-linear interactions occur and different unstable modes begin to interact [13, 50]. These interactions typically occur when oscillations reach an amplitude of approximately 1% of the free-stream velocity [50]. Further downstream, disturbance amplitudes saturate, and the shear layer rolls-up into spanwise oriented vortices as a result of an instability that resembles that of a Kelvin-Helmholtz instability [13, 29, 134]. Diwan and Ramesh [132] argue that the origin of the perturbations that lead to roll-up is upstream of the mean separation location, in the laminar boundary layer. They also show that these perturbations grow rapidly once the inflection point of the velocity profile is displaced sufficiently far from the the wall, where growth rates are higher [50]. Recently, using linear stability analysis, Yarusevych and Kotsonis [24] showed that indeed the stability spectrum is continuous across the separation point, but disturbances propagating from the attached portion of the boundary layer experience significantly higher growth rates. Shear layer roll-up occurs in the vicinity of the maximum bubble height [13, 132, 133, 136], and the formed vortices are then shed at the frequency of the most amplified disturbance in the separated shear layer [18, 24, 26]. The observed shedding frequency of a given separation bubble is decreased when controlled disturbances are introduced into the flow, resulting in a decrease in separation bubble size, as shown by Yarusevych and Kotsonis [24]. By normalizing the convection speed of the shear layer rollers by the edge velocity at separation [26], or the shedding frequency by the momentum thickness and edge velocity [29], the shedding characteristics of the bubble have a small dependence on Reynolds number, though do not represent true universal scalings of the shedding phenomenon. If the level of reverse flow within the separation bubble exceeds 15-20% of the mean free-stream velocity, the separation bubble becomes absolutely unstable [134].

Initially, roll-up of the shear layer is two-dimensional and the structures are coherent across the span of the flow [16, 18, 44, 133]. Downstream, the structures break-up as a result of a secondary instability of the shear layer rollers [17, 42]. One of the secondary

instabilities is elliptic [42], resulting in a spanwise deformation of the shear layer rollers, and has been observed in several investigations [17, 18, 42, 47, 134]. This spanwise deformation grows with increasing streamwise distance and has a wavelength that is typically 2-3 times that of the streamwise wavelength of the shear layer rollers [17, 18, 137]. Using spacers under an oscillating wire to induce a three-dimensional disturbance, Lang *et al.* [47] show that deformations in the spanwise rollers lead to a pair of counter-rotating streamwise oriented vortices. This deformation in the rollers is also seen in the resuls of Burgmann and Schröder [31] as a re-orientation of the spanwise vorticity into the streamwise direction. This re-orientation results in the leading edges of the bulges to be lifted away from the wall. As a result of the large velocity gradient across the boundary layer, streamwise stretching of the structures occurs and they begin to resemble the Λ-structures characteristic of boundary layers [18, 31, 134]. Further stretching of these structures leads to their break-up into smaller scales. A second type of secondary instability can occur within the braid region between two consecutive rollers and with a wavelength that is smaller than that of the shear layer rollers [17, 42]. In this case, the instability generates streamwise vorticity in the braid region which convects upstream in the near wall region due to large instantaneous reverse flow velocities [42]. This vorticity is then fed into the upstream forming vortex and the process continues. As a result, the shear layer roll-up then operates as an oscillator and causes the shear layer rollers to break-up within a short streamwise distance. This behaviour was oberved in the simulations of Jones *et al.* [42], but only when three-dimensional forcing being applied to a separation bubble was subsequently switched off. Flow development within the separation bubble has been studied numerically using both two- and three-dimensional simulations and it is not suprising that investigators have concluded that two-dimensional simulations are inadequate in describing the breakdown to turbulence, or even mean separation bubble topology [17, 30, 134].

At moderately increased levels of FSTI (less than approximately 1%), the transition process in the separated shear layer is promoted, with transition occuring further upstream [9, 16, 38, 138, 139]. The results from Lamballais *et al.* [139] show that earlier shear layer breakdown and mean reattachment is observed for increases in the level of FSTI from 0% to 0.1% and 1%, but the transition process remains qualitatively similar. Associated with the earlier breakdown is an increase in the number of smaller scale vortical structures [138]. However, at increased levels of FSTI, the spanwise coherence of shear layer rollers at the roll-up location is decreased notably [31, 32], as compared to experiments performed in low disturbance environments [18, 133] or simulations [16]. At high levels of FSTI (greater than approximately 1-2%), notable streamwise velocity fluctuations are detected upstream of separation [140]. These fluctuations are indicative of bypass transition and, more specifically, are evidence of streamwise oriented streaks forming in the laminar boundary layer upstream

of mean separation [16, 37, 133]. The streaks are similar to those that form in boundary layers at high levels of FSTI as discussed in Section 2.2.1. These structures then interact with the separated flow, creating a roll-up process which is three-dimensional [16]. A more detailed discussion of the effects of FSTI on transition in a separation bubble and the resulting effects on mean topology is contained in Section 2.3.2.

2.3 Effects of Free-stream Turbulence Intensity on Airfoil Performance and Separation Bubbles

Investigations of the effects of free-stream turbulence intensity on low Reynolds number flows over airfoils have generally focused on either the performance of the airfoil, or mean laminar separation bubble topology. Airfoil performance studies are typically conducted using relatively large test matrices with force balance measurements and thus neglect flow measurements, while studies on separation bubbles are generally limited to small parameter spaces. This section reviews past investigations of the effects of free-stream turbulence intensity on the lift and drag forces generated by an airfoil, as well as laminar separation bubbles formed over airfoils and flat plates. Additionally, a brief review of the generation of free-stream turbulence intensity in both experiments and simulations is provided.

2.3.1 Low Reynolds Number Airfoil Performance

At low Reynolds numbers and turbulence intensities, airfoils can exhibit significant hysteresis near their stall angle [28, 39, 141]. For increasing angles of attack, the lift produced by the airfoil increases until the airfoil stalls and a significant decrease in lift is observed. The angle of attack must then be decreased to well below the stall angle of attack before the lift recovers to its pre-stall magnitude. As the level of FSTI is increased, the size of this hysteresis loop can be reduced or eliminated altogether [28, 141, 142]. Further, increases in the stall angle and maximum lift coefficient are observed as the level of FSTI is increased [28, 39]. Some investigations at low chord Reynolds numbers have noted an increase in drag at elevated levels of FSTI [28, 39, 141], while at higher chord Reynolds numbers, where the baseline separation bubble is smaller [10], there is very little change in drag with increasing FSTI [141]. Since studies of airfoil performance do not typically make detailed flow measurements, the observed reduction in airfoil lift hysteresis was hypothesized to be a result of transition over the airfoil being promoted, and more specifically the separation bubble size decreasing [28]. This decrease in separation bubble size will be discussed in detail in Section 2.3.2.

In addition to the effects of FSTI on airfoil performance, Cao *et al.* [39] also investigated the effects of the turbulence integral length scale on the lift and drag of an S1223 airfoil. For a constant integral length scale, increasing the level of FSTI led to a small decrease in lift at pre-stall angles of attack, but with a much more gradual ('softer') stall behaviour, consistent with the findings of Yap *et al.* [141]. The decrease in lift is in agreement with the results of Mueller *et al.* [28], but in disagreement with the results of Yap *et al.* [141] who noted an increase in lift. The conflicting observations of the effects of free-stream turbulence intensity on airfoil lift seem to be the result of the different airfoils used by the researchers. For a constant FSTI, smaller integral length scales tend to result in higher stall angles, while the larger turbulent scales tend to result in larger lift values at large angles of attack [39]. For a given free-stream condition, as the chord Reynolds number is increased, the effects of both turbulence intensity and integral length scale are decreased [39].

Using a combination of oil flow visualizations and force balance measurements, Hoffmann [142] investigated the effects of Reynolds number and FSTI on the separation bubble formed over the suction side of a NACA 0015 airfoil, as well as the attending changes in airfoil lift. At the baseline level of turbulence intensity, a small separation bubble was observed, and was completely eliminated and replaced by a turbulent boundary layer when the turbulence intensity was increased from 0.25% to 9%. Despite the change in flow over the airfoil, there was no notable change in the lift or drag of the airfoil at a given angle of attack, likely as a result of the small separation bubble that formed at the baseline level of turbulence intensity. However, Hoffmann [142] did note an increase of 30% in the maximum lift coefficient, attributed solely to the delayed stall angle of the airfoil at the elevated level of FSTI. In a study of the effects of FSTI on the flow over a NACA 66_3-018 airfoil, O'Meara and Mueller [9] show that at high angles of attack, increasing FSTI results in an increase in the magnitude of the suction peak, likely increasing lift though the authors did not report this value. The authors also report a decrease in mean separation bubble length with increasing FSTI, thereby indicating that the observed changes in airfoil performance in other studies is likely a result of FSTI influencing the suction side laminar separation bubble.

2.3.2 Laminar Separation Bubbles

A number of investigations have examined the effects of FSTI on mean laminar separation bubble topology [9, 33, 34, 53, 138, 143, 144]. While the effects of FSTI on the transition process in the laminar separation bubble were discussed briefly at the end of Section 2.2.3, its effects specifically on mean separation bubble topology are reviewed here. Some of the earliest work on the effects of FSTI on separation bubbles was performed over the corner of

blunt flat plates placed parallel with the free-stream [53, 143]. In this configuration, the flow separates over the corner of the plate, forming a separated shear layer, then transitions to turbulence and reattaches to the plate downstream. By increasing the level of FSTI, the transition process in the separated shear layer is promoted, leading to earlier mean flow reattachment [53, 143] and thus a reduction in the size of the separation bubble. This finding has been confirmed more recently by Lamballais *et al.* [138, 139] who simulated the flow over a blunt flat plate with rounded corners using DNS, as well as by Langari and Yang [140] who simulated the flow over a blunt nosed flat plate using Large Eddy Simulations (LES). Lamballais *et al.* [139] showed that the reduction in separation bubble length is more significant for larger corner radii of the plate since a larger separation bubble initially forms at low FSTI, and thus the observed reduction at elevated FSTI is more significant. The decrease in separation bubble length was shown by Kiya and Sasaki [143] to result in an increase in the magnitude of the negative mean surface pressure over the corner of the plate, which the authors attributed to higher acceleration around the corner as a result of the decreased separation bubble height.

One of the first studies of the effects of FSTI on the separation bubble formed over an airfoil was performed by O'Meara and Mueller [9]. Using mean surface pressure measurements, the authors showed that the length of formed separation bubbles was reduced as the level of FSTI was increased. The magnitude of the suction peak increased as a result of the decrease in separation bubble length, similar to the results found over the corner of a blunt flat plate [143]. More recently, planar Particle Image Velocimetry (PIV) has been used to examine mean separation bubble topology on the suction side of airfoils [31, 33, 34]. Similar reductions in the length of formed separation bubbles with increasing FSTI have been observed in these studies. The importance of documenting a facility's free-stream conditions was elucidated by Ol *et al.* [33] who compared experimental results from three facilities for nominally identical experimental conditions. The authors noted that the locations of mean separation, transition, and reattachment varied by 15%, 10%, and 5%, respectively, which they attributed in part to the effects of FSTI which varied by approximately 0.1% between the facilities. In a study of the effects of increasing FSTI on a bubble formed in the same facility, Olson *et al.* [34] showed that the decrease in separation bubble length was the result of a downstream shift in mean separation as well as an upstream shift in mean reattachment, a result consistent with the findings of Hain *et al.* [32]. By improving the flow conditioning in their facility and reducing the free-stream turbulence inensity from 1.5% to 1.0%, Burgmann and Schröder [31] observed a significant increase in the size of the formed separation bubble on the suction side of an airfoil. However, despite the reduction in FSTI, Burgmann and Schröder [31] observed little spanwise coherence of the shear layer rollers which are largely two-dimensional in low disturbance environments

[17, 18, 133]. Instead, they observed three-dimensional 'c-shaped' structures at roll-up, similar to the findings of Hain *et al.* [32] also in a higher disturbance environment, which rapidly deformed into structures resembling Λ-structures before breaking down to smaller scales.

The effects of integral length scale have been studied experimentally for the flow past the corner of a blunt flat plate [53] as well as over the suction side of an airfoil [144]. The integral length scale has been found to have a negligible effect on the flow transition location and thus separation bubble length [53, 144]. However, smaller scales are associated with increased stagnation point heat transfer [144] while larger scales are associated with larger surface pressure fluctuations [53], findings which may be important for heat transfer and unsteady aerodynamics, respectively.

Researchers have also studied the effects of FSTI on separation bubbles induced on flat plates [37, 38]. Using planar PIV, Simoni *et al.* [38] showed that the length of formed separation bubbles decreases with increasing FSTI as a result of an upstream shift in mean reattachment, with no significant change in the location of mean separation. Using DNS, McAuliffe and Yaras [16] found that the location of mean separation shifted downstream slightly while there was a more significant upstream shift in the location of mean reattachment. The relative insensitivity of the mean separation location on flat plates to increases in FSTI, even in simulations with high spatial resolution, is in qualitative disagreement with the PIV measurements of Olson *et al.* [34] over an airfoil, as Olson *et al.* [34] note a significant downstream shift in the location of mean separation when FSTI is increased. This difference is also observed in the LES performed by Lardeau *et al.* [37] over both a flat plate and a compressor blade. While no shift in the location of mean separation was noted for the flat plate with increases to FSTI, a slight downstream shift in the location of mean separation was observed over the compressor blade. These results indicate that changes in the location of mean separation in response to changes in bubble size may be dependent on the flow geometry as well as the level of FSTI. In the work of Simoni *et al.* [38], a doubling of the Reynolds number (for constant FSTI) also results in no significant change in the location of mean separation, which is in contradiction to the well established upstream shift shown to exist over airfoils for increasing chord Reynolds numbers, *e.g.*, Ref. [10].

At large levels of FSTI (approximately 1%), the topology of the separation bubble is affected by the condition of the boundary layer upstream of separation, most notably by streamwise oriented streaks similar to those associated with bypass transition [87, 91, 94], as discussed at the end of Section 2.2.1. In low Reynolds number airfoil studies, these streaks have been observed in simulations [16, 37, 133], and are also speculated by Simoni *et al.* [38] and Lengani and Simoni [133] to be present in the experiments. At elevated levels of FSTI, the separation bubble is significantly smaller than that formed at lower turbulence intensity

levels [37, 38], and the roll-up process of the separated shear layer is highly three-dimensional [16, 133]. This three-dimensionality is observed as spanwise deformations in Q-critereon [145, 146] contours presented by Langari and Yang [140]. Lardeau *et al.* [37] showed, using LES of a separation bubble induced on a flat plate, that at elevated levels of FSTI a spanwise variation in the locations of mean separation and reattachment exists as a result of streamwise streaks formed in the boundary layer upstream of separation. In their study at high levels of FSTI, Lengani and Simoni [133] found that the separation bubble formed over an airfoil is eliminated, and POD results from wall-parallel measurements show structures with large streamwise wavelengths. Simoni *et al.* [38] investigated a separation bubble imposed on a flat plate at high levels of FSTI, observing large streamwise wavelengths in POD modes computed from wall-normal measurements. The authors speculated that this was a result of streamwise streaks but did not perform wall-parallel measurements to confirm this assertion. In some experiments at high levels of FSTI, streamwise oriented streaks are not detected [31, 32]. The observation [16, 37, 133] or absence [31, 32, 138, 140, 144] of streamwise oriented streaks at elevated levels of FSTI is curious, but the formation of these streaks is dependent upon the receptivity of the specific flow and is a complex process [12, 91, 98]. In a study over an airfoil, Butler *et al.* [144] found that at very high FSTI ($\approx 10\%$), boundary layer separation was suppressed as the flow transitioned to turbulence very close to the leading edge of an airfoil.

2.3.3 Generation of Free-stream Turbulence Intensity

Throughout Sections 2.2, 2.3.1, and 2.3.2, the effects of FSTI on experiments and simulations was discussed and it is therefore worthwhile to briefly discuss how FSTI is typically generated in both experiments and numerical simulations. Generally speaking, the quality of a research facility used for transitional studies is based in part on the magnitude of the FSTI in the test section. Low levels of FSTI are desirable in order to observe 'natural' transition. In order to increase the level of FSTI in experiments, woven wire mesh screens are inserted upstream of the test-section in an attempt to generate homogeneous and nearly isotropic turbulence [147–149].

To quantify the free-stream turbulence, it is necessary to measure the magnitude of velocity fluctuations as well as their spectral content. Further, it is often of interest to compute a characteristic length scale of the fluctuations, typically the integral length scale. The root-mean-square of the velocity fluctuations in the streamwise direction divided by the mean flow velocity is usually used to define FSTI. The integral length scale is typically computed by employing Taylor's frozen turbulence theory [85]. Taylor's theory states that when the velocity induced by turbulent eddies is small compared to that of the mean

velocity, one can assume that the fluctuations measured at a single point are the result of a pattern of consecutive turbulent eddies [85]. Therefore, by integrating the autocorrelation function of the velocity signal at a given point, the length scale associated with the turbulent fluctuations, the integral length scale, may be computed. Finally, computing the spectra of the velocity fluctuations ensures that no dominant frequency is introduced into the flow by the grids which could have additional forcing effects on the transition process of interest.

In numerical simulations, the velocity fluctuations at the domain inlet are zero to within numerical round-off errors. Since investigators often try to make comparisons with experimental data where FSTI is notably higher, some artificial perturbations must be defined at the computation domain inlet. A method proposed by Jacobs and Durbin [87] and used by other investigators [91] is to superimpose a series of Fourier modes with random amplitudes onto the inlet velocity profile. In addition, specific discrete or continuous [101] modes of the Orr-Sommerfeld equation may be defined at the domain inlet in order to promote either natural (*i.e.*, TS wave) or bypass [87–90, 95] transition, respectively.

Chapter 3

Experimental Methodology

The effects of free-stream turbulence intensity on the low Reynolds number flow over an airfoil were studied experimentally in a wind tunnel facility. A number of measurement techniques were employed in this investigation in order to investigate the time-averaged and spatio-temporal flow development over a NACA 0018 airfoil. The airfoil model was developed within the research group by Gerakopulos [150] and has been used previously in the studies of Kurelek [20], Boutilier [151], Kirk [152], and Lambert [153]. In all, these investigations have examined the aerodynamic characteristics of the airfoil, as well as the transition process within laminar separation bubbles formed over its suction surface. This study is comprised of two experimental campaigns: 1) a parametric study which aims to unravel the interdependence of angle of attack, chord Reynolds number, and free-stream turbulence intensity effects on suction side separation bubble mean topology, separated shear layer transition characteristics, and airfoil lift by measuring mean and fluctuating surface pressure distributions; and 2) a more detailed study using planar Particle Image Velocimetry (PIV) in two configurations to examine the effects of free-stream turbulence intensity on the spatio-temporal flow development within laminar separation bubbles. For the parametric study, angles of attack between 0° and 20°, chord Reynolds numbers between 100 000 and 200 000, and free-stream turbulence intensities between 0.09% and 2.03% were investigated. In the PIV study, a single angle of attack of 4° was investigated for two chord Reynolds numbers and four free-stream turbulence intensities.

This chapter provides details about the experimental facility, the airfoil model, and the measurement techniques employed in this investigation.

3.1 Experimental Setup

All experiments were performed in the closed-loop wind tunnel located in the Fluid Mechanics Research Laboratory at the University of Waterloo, sketched in Fig. 3.1. Measurements were made over an aluminum NACA 0018 airfoil model designed by Gerakopulos [150]. The following subsections provide further details about the wind tunnel facility, experimental conditions, and the airfoil model.

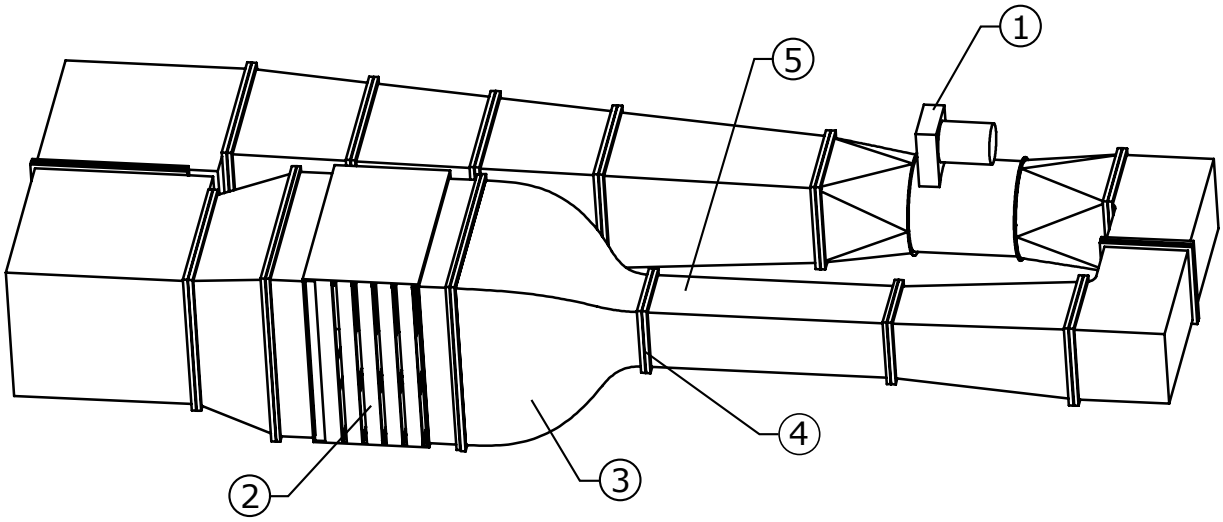

Figure 3.1: Sketch of the closed-loop wind tunnel in the Fluid Mechanics Research Laboratory. Labelled components are as follows: ① fan motor, ② settling chamber, ③ contraction, ④ turbulence generating grid location, and ⑤ test section. After Kurelek [20].

3.1.1 Wind Tunnel Facility

The closed-loop wind tunnel features a test section that is 0.61 m wide by 0.61 m high and 2.4 m long. The test section has walls which are constructed from Lexan, offering full optical access to the installed model. Further, the closed-loop nature of the tunnel allows for good control of flow seeding, which is critical for the particle-based flow diagnostics used in this investigation and detailed in Section 3.2.2. Flow in the wind tunnel is driven by a 6-blade axial fan and conditioned by an aluminum honeycomb structure and a set of five turbulence reducing screens upstream of a 9:1 contraction leading into the test section.

The resulting free-stream turbulence intensity is approximately 0.1% over the range of free-stream velocities studied in this investigation. The flow uniformity in the test section was assesed by Kurelek [20] for a chord Reynolds number of 125 000 and was found to be within ±0.4% across both the spanwise and vertical directions. In order to increase the level of free-stream turbulence intensity, turbulence generating grids were placed just upstream of the test section, at the location shown in Fig. 3.1. A summary of the geometry of the grids is provided in Table 3.1, with additional details about the fabrication and installation of the grids provided in Appendix C. With or without a turbulence generating grid installed, the free-stream velocity in the test section was set based on the static pressure drop across the contraction, calibrated against a Pitot-static tube placed in the empty test section at the streamwise location of the airfoil. Since the grids result in an additional pressure drop upstream of the test section, the calibration between the static pressure drop across the contraction and the test section velocity was established for each grid, with the details provided in Appendix B. In all cases, the associated uncertainty in the free-stream velocity is less than 2% for all Reynolds numbers investigated.

Table 3.1: Summary of the turbulence generating grid geometry.

	Grid geometry		
Case	d [mm]	M [mm]	β [%]
i) No screen	-	-	-
ii) Finest screen	0.11	0.67	70
iii) Medium screen	0.26	1.48	68
iv) Coarse screen	0.48	2.19	61
v) Grid	1.72	14.32	77

The free-stream conditions in the test section for all investigated chord Reynolds numbers were characterized by means of hot-wire anemometry. Measurements were conducted using a normal Dantec 55P15 probe, operated with a Dantec Streamline Constant Temperature Anemometry unit. All measurements were made in an empty test section at the location corresponding to the midspan of the leading edge of the airfoil at zero angle of attack. The hot-wire probe was calibrated in-situ against a Pitot-static probe placed approximately 3 cm below it. All hot-wire data acquisitions were performed on the same day as the calibration so as to maintain an accurate calibration. The voltage supplied to the hot-wire was sampled at 100 kHz, and low-pass filtered at 50 kHz, for a total of 2^{23} samples using a National Instruments PCI-4472 data acquisition card. Turbulence intensities were computed as the

root-mean-square of the velocity fluctuations divided by the mean free-stream velocity. Integral length scales were computed by first integrating an exponential curve fit to the auto-correlation function of the fluctuating velocity, then, applying Taylor's hypothesis [85], the result was multiplied by the mean free-stream velocity. A summary of all investigated flow conditions is provided in Table 3.2 with additional details of the hot-wire calibration procedure and determination of the flow conditions provided in Appendix B.

Table 3.2: Investigated flow conditions.

	PIV experiments				Parametric study experiments					
	$Re_c = 80\,000$		125 000		100 000		150 000		200 000	
Case	Tu [%]	Λ [mm]	Tu	Λ	Tu	Λ	Tu	Λ	Tu	Λ
i)	0.11	64.54	0.10	74.93	0.10	74.33	0.10	88.31	0.09	95.51
ii)	0.22	4.13	0.25	2.64	0.24	2.88	0.25	2.47	0.26	1.91
iii)	-	-	-	-	0.37	3.30	0.37	2.61	0.35	2.21
iv)	0.50	4.14	0.53	3.24	0.51	3.61	0.54	2.96	0.60	2.69
v)	1.92	6.54	1.94	5.69	1.94	6.03	1.90	5.23	2.03	4.73

A close-up view of the test section arrangement is shown in Fig. 3.2, and shows that the turbulence generating grids are 0.55 m upstream of the airfoil leading edge. In considering the downstream distance of the airfoil leading edge from the grids, L, relative to the characteristic mesh size, M, Batchelor and Townsend [154] suggest that the region of developing turbulence behind a grid is located within $L/M \leq 20$. In their review, Laws and Livesey [149] suggest that this region extends to $L/M = 40$ before homogeneous and near isotropic turbulence is measured. For the present investigation, the airfoil leading edge is located within $38 \lesssim L/M \lesssim 820$, depending on the grid, and is thus assumed to be subjected to nearly homogeneous and isotropic free-stream turbulence.

It is also imformative to compute the frequency spectra of the free-stream velocity fluctuations. Spectra of the velocity fluctuations were computed using Welch's method [155], and have a resulting frequency resolution of 0.8 Hz. Spectra for all grids, and the case where no grid is installed, for the three Reynolds numbers of the parametric study (Table 3.2) and are shown in Fig. 3.3. The results show that no dominant frequencies are introduced into the flow by the grids, and that the free-stream turbulence intensity is increased as a result of an increase in energy over a broad range of frequencies. There are slight peaks around $St \approx 0.8$ which are associated with the fan blade-passage frequency. These fluctuations

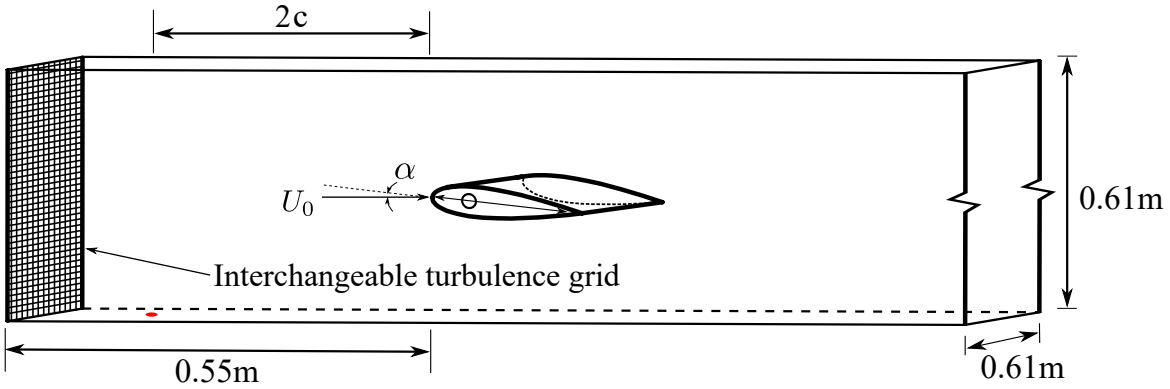

Figure 3.2: Sketch of the test section arrangement. The red circle represents the location of the free-stream static pressure tap.

persist when the grids are inserted but become progressively less significant as a result of the increasing velocity fluctuations introduced into the flow by the grids. It should also be noted that this frequency is about an order of magnitude below the frequencies of interest in the investigated separation bubbles.

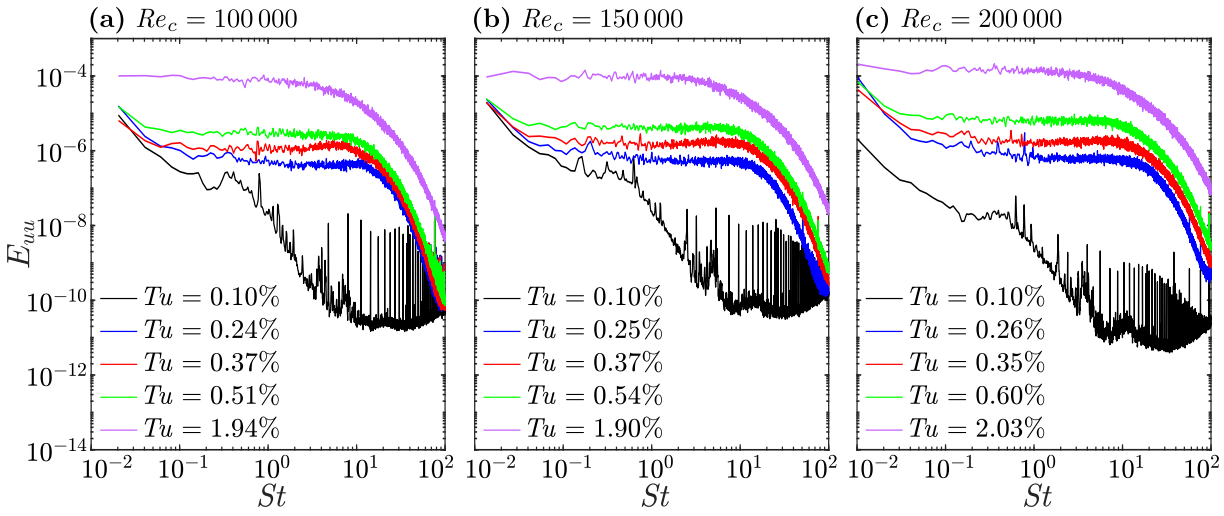

Figure 3.3: Spectra of free-stream velocity fluctuations.

3.1.2 Airfoil Model

The airfoil model used for all experiments was designed by Gerakopulos [150] and constructed from aluminum with a NACA 0018 profile. The model has a chord length and span of 0.2 m and 0.6 m, respectively. The model is equipped with ninety-five pressure taps, 0.4 mm in diameter, as well as an array of twenty-five microphones, embedded under the airfoil surface and exposed to the flow through taps 0.8 mm in diameter. A sketch of the model is shown in Fig. 3.4, along with the definitions of the chord based, and surface attached coordinate systems. The chord based system has the X coordinate aligned along the

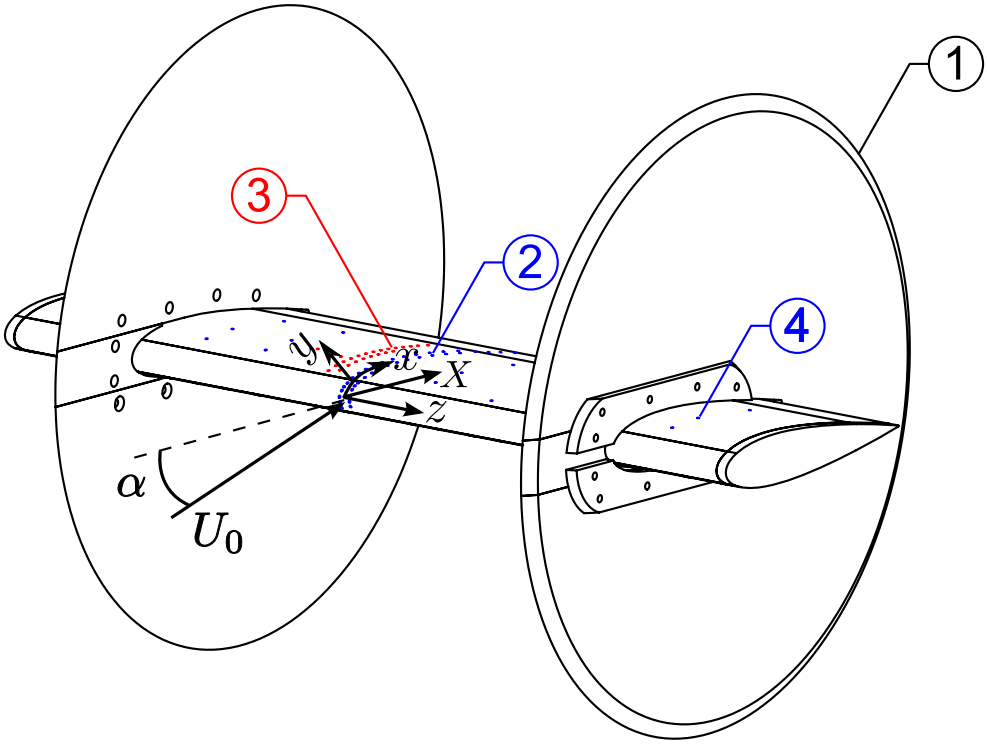

Figure 3.4: Airfoil model, after Boutilier and Yarusevych [10]. ① End plates, ② streamwise pressure tap rows, ③ surface embedded microphones, ④ spanwise pressure tap rows.

airfoil chord length, while the surface attached coordinate system has the x coordinate aligned in the streamwise direction along the airfoil surface and the y coordinate normal to the airfoil surface. The z coordinate is aligned along the airfoil span and is shared by

both coordinate systems. Sixty-five of the pressure taps are split between the suction and pressure sides of the airfoil, in two staggered rows about the midspan plane. The remaining thirty pressure taps are distributed in three spanwise rows across the suction side of the airfoil at $X/c = 0.15$, 0.30, and 0.60. All of the microphones are located on the suction side of the airfoil with twenty-two placed in staggered streamwise rows around $z/c \approx -0.2$. The remaining three microphones form a spanwise row at $X/c = 0.21$. For further details of the model design as well as the internal circuitry for the microphones, the reader is referred to the work of Gerakopulos [150]. All pressure taps are fed out of the model and test section via flexible tubing while the microphone signals are carried by coaxial cables. The angle of attack of the airfoil was set to within 0.16° using a digital protractor. Prior to experiments, the aerodynamic zero angle of attack was determined by finding the angle of attack at which the airfoil generates zero lift, *i.e.*, 0° for a symmetric airfoil [1]. Since measuring a zero quantity is challenging, the linearity of the lift curve of a NACA 0018 airfoil at low angles of attack was exploited. First, the airfoil was set to a zero angle of attack relative to the test section by eye. Then, lift was computed for small positive and negative angles of attack relative to this position. A least squares linear regression was applied to the resulting lift values, and the aerodynamic zero reference was determined. A lift value was computed at this determined angle of attack in order to verify that the lift was zero to within the experimental uncertainty.

For the parametric study, the airfoil was fitted with circular end plates having diameters of $2.25c$ and a spanwise spacing of $2c$ (see Fig. 3.4), as per the recommendation of Boutilier and Yarusevych [156]. The solid blockage ratios were within the range of 7.4% to 12.8%. In this range of blockage ratios, blockage corrections [157, 158] can be applied below the stall angle of attack [156], however, the corrections perform poorly in the post-stall regime and, therefore, for consistency, no blockage corrections were applied to the results of this investigation.

For the PIV measurements, no end plates were used in order to allow for better optical access to the measurement plane. In order to minimize end effects, measurements were performed at the midspan plane of the airfoil. At this location, surface pressure distributions are approximately two-dimensional at low angles of attack [156]. In these experiments, performed at an angle of attack of 4°, the estimated solid blockage ratio is 5.9% and no solid blockage corrections were applied. In order to prevent tonal noise emission [159–161] which has been shown to develop a feedback loop with the suction side LSB [162], a pressure side boundary layer trip was applied to the airfoil for the PIV experiments. The trip was made out of a 10 mm wide strip of randomly distributed roughness elements, approximately 0.5 mm in diameter, placed across the entire span of the airfoil at $X/c \approx 0.3$, so as to be upstream of the pressure side separation point.

3.2 Measurement Techniques

3.2.1 Surface Pressure Measurements

Mean surface pressure distributions were measured at the midspan plane of the airfoil using the streamwise rows of pressure taps as depicted in Fig. 3.4. All measurements were referenced against the mean free-stream static pressure, measured two chord lengths upstream of the airfoil with a pressure tap in the floor of the test section (see Fig. 3.2). Flexible tubing from the pressure taps routed the pressures from the taps, through the model, to two mechanical Scanivalve units mounted outside of the tunnel test section. Using a LabView program developed by Boutilier [151], the pressure taps were mechanically multiplexed to two Setra Model 239 pressure transducers allowing for two simultaneous measurements. For each measurement, when the multiplexer was indexed to the next measurement location, a settling time of at least 25 s was used to ensure that the pressure in the tubing had equalized. A total of 10^4 samples were then recorded at 1 kHz using a National Instruments USB-6259 data acquisition unit. For all experiments, a transducer with a full-scale range of ± 250 Pa was used to measure the surface pressures on the pressure side of the airfoil, with an associated uncertainty of less than 3% of the free-stream dynamic pressure. For the suction side pressure measurements, a transducer with a full-scale range of ± 620 Pa was used for the parametric study, while a transducer with a full-scale range of ± 250 Pa was used for experimental conditions investigated in the PIV campaign. The larger range was required for the parametric study in order to cover the higher range of pressures attained at higher angles of attack. The associated uncertainties in the suction side pressure measurements for the two studies are less than 5% and 3% of the free-stream dynamic pressure, respectively.

Fluctuating surface pressures were measured using the surface embedded microphones as shown in Fig. 3.4. These measurements can be used to infer the behaviour of disturbances in the separated shear layer, following similar methodology employed in previous studies [136, 159, 163, 164]. Prior to the experiments, the microphone responses were calibrated over a range of frequencies between 100 Hz and 5000 Hz against a Brüle and Kjær 4192 microphone. Details of the calibration procedure and sample microphone responses are provided in Appendix D. The signals from the microphones were simultaneously sampled at 40 kHz, and low-pass filtered at 20 kHz, for a total of 2^{20} samples using two National Instruments 9220 data acquisition modules held in a National Instruments CompactDAQ chassis. A custom breadboard unit was used to connect the 25 coaxial cables running from the microphones into a single 32-pin connector required of the data acquisition modules. The uncertainty in the root-mean-square of the measured surface pressure fluctuations is

estimated as the measured noise floor plus 20% of the measurement. Details are provided in Appendix A following the methodology discussed by Boutilier [151].

3.2.2 Particle Image Velocimetry Measurements

Particle Image Velocimetry (PIV) was employed in order to describe the effects of free-stream turbulence intensity on the spatio-temporal flow development within the laminar separation bubble. Both side and top view arrangements, as sketched in Fig. 3.5, were used in order to assess the streamwise and spanwise flow development, respectively. For the side view configuration, the laser sheet was placed at the midspan of the airfoil and allowed for the assessment of the streamwise flow development within the laminar separation bubble. For the top view configuration, the laser sheet was positioned above the airfoil such that it passed through the upper portion of the separated shear layer rollers, as informed by the side view PIV measurements, and therefore allowed for the characterization of the spanwise flow development. In this way, as reflected in Fig. 3.6, the top view measures the velocity components in the spanwise and chordwise directions, whereas the side view measures streamwise and wall-normal components of velocity in the surface attached coordinate system.

For all PIV measurements, the flow was seeded with a water-glycol based fog produced with a Rosco Vapour fog machine and having a mean particle diameter of 4 µm. For the side view, two PIV systems were used: 1) a two-camera, time-resolved system, and 2) a single camera, non time-resolved system. The time-resolved system was used to characterize the spatio-temporal flow development, while the low speed system employed a higher-resolution camera in order to measure higher resolution mean fields. The first system, the high-speed system, consisted of two 1024 px × 1024 px Photron SA4 cameras, equipped with 200 mm Nikon lenses. The magnification was adjusted so as to capture the entire separation bubble with adequate spatial resolution, while maintaining an overlap region between the two images of approximately 10% in order to stitch the final vector fields together. The flow was illuminated by a Photonics DM20-527 high repetition rate Nd:YLF laser. For the second system, the low-speed system, a single 1600 px × 1200 px LaVision Pro-X camera equipped with a 200 mm Nikon lens was employed. The camera was placed on a 3-axis traverse and five overlapping 18 mm × 13 mm flow regions were imaged by traversing the camera in the streamwise direction, over the full extent of the separation bubble. Flow illumination was provided by an EverGreen 70 Nd:YAG laser. In both configurations, the laser beam was introduced into the test section downstream of the airfoil and conditioned into a sheet by a series of optical devices mounted to a breadboard, as depicted in Fig. 3.5a. The breadboard and optics were confirmed to have no significant effect on the flow development over the

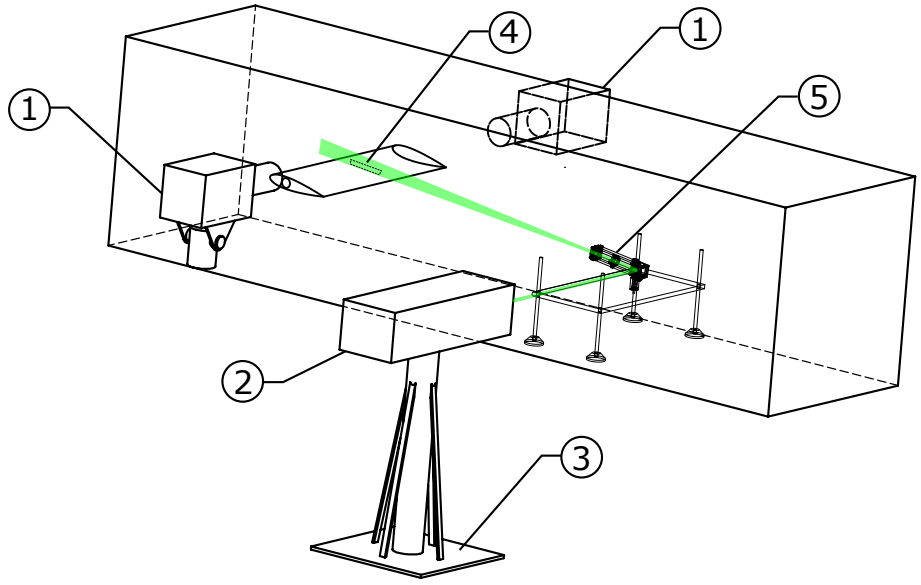

(a) Side view.

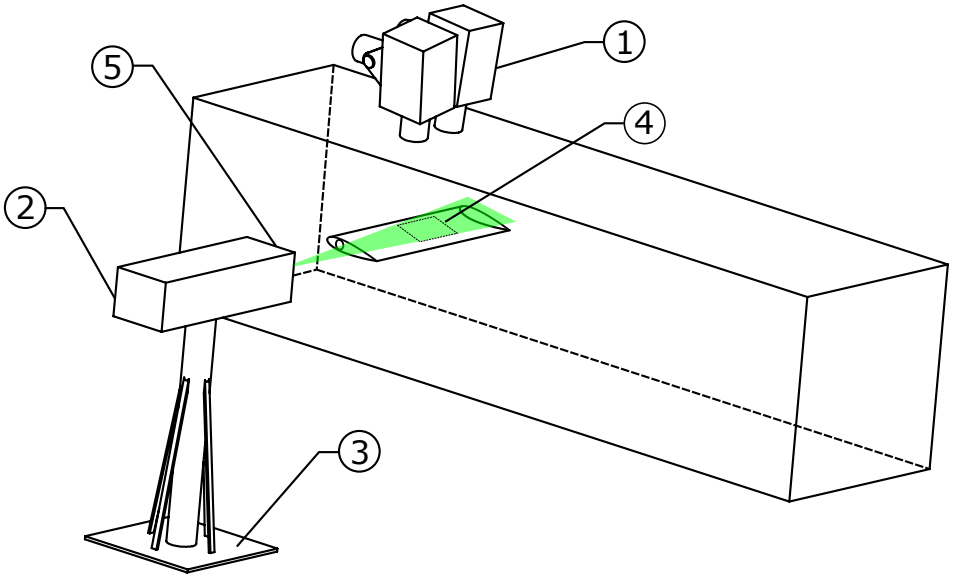

(b) Top view.

Figure 3.5: PIV arrangements. ① High-speed cameras, ② laser, ③ stepper motor stand, ④ PIV field-of-view, ⑤ laser sheet forming optics.

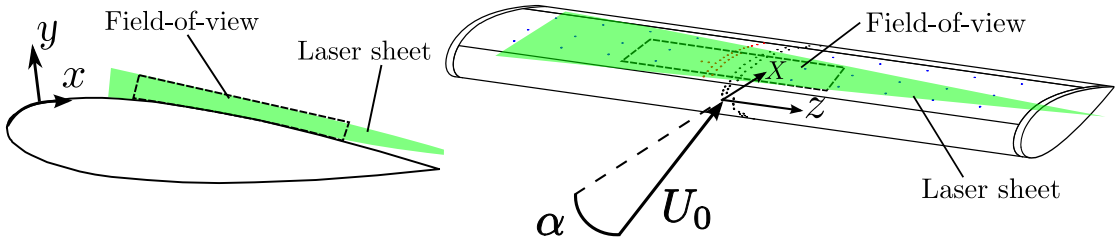

(a) Side view. **(b)** Top view.

Figure 3.6: Sketch of PIV fields-of-view and coordinate systems relevant to the measurements.

airfoil through a comparison of mean surface pressure distributions. The beam was first turned upstream by a 90° turning mirror, and then conditioned into a sheet approximately 1 mm thick by a spherical lens with a focal length of 1000 mm, a cylindrical lens with a focal length of −200 mm, and a variable focal length lens from LaVision.

For the top view, the same time-resolved system used in the side view arrangement was employed, and the two Photron SA4 cameras were equipped with 105 mm focal length Nikon lenses. Due to the size of the camera bodies, one of the cameras had to be tilted by approximately 10° so that an overlap region between the two camera images could be attained. In order to correct for the tilt, a Scheimpflug adapter was affixed to the camera lens in order to project the plane of the laser sheet onto the camera sensor focal plane. The laser was introduced directly above the airfoil with all sheet forming optics affixed to the laser head, as depicted in Fig. 3.5b. The beam was conditioned into a sheet approximately 1 mm thick using a −20 mm focal length cylindrical lens and the same variable focal length lens from LaVision used in the side view arrangement.

For all PIV measurements, particle images were captured in double-frame mode with the cameras and laser synchronized using a LaVision timing unit controlled through LaVision's DaVis 8 software. The images were processed in DaVis 8 using a multi-pass cross-correlation algorithm with window deformation. The final window size was 16 × 16 pixels, with 75% overlap. The final vector fields were stitched together using a cosine blending scheme in the image overlap region. For the side view, the final vector fields were then transformed into the surface attached coordinate system, as shown in Fig. 3.6a. The methodology used in determining the uncertainty in the PIV measurements is discussed in Appendix A, and is estimated to be less than 5% and 6% of the free-stream velocity for instantaneous side and top view measurements, respectively. A summary of the important side and top view PIV parameters are provided in Table 3.3 and Table 3.4, respectively.

Table 3.3: Summary of important side view PIV parameters for the low-speed (LS) and time-resolved (TR) systems.

	LS side-view		TR side-view		Unit
Parameter	$Re_c = 80\,000$	125 000	80 000	125 000	
Sampling rate	15		3000	3200	Hz
Number of samples	1000		5000		
Frame separation	23	14	80[1] 60[2]	36	μs
Camera lens focal length	200		200		mm
Magnification factor	0.34		0.66[1] 0.49[2]	0.49	
Combined field of view	0.4×0.06		0.35×0.06[1] 0.30×0.06[2]	0.3×0.06	c
Final window size	16×16		16×16		px
Vector pitch	0.05		0.17[1] 0.12[2]	0.12	mm

[1] Cases i) & ii) in Table 3.2
[2] Cases iv) & v) in Table 3.2

Table 3.4: Summary of important top view PIV parameters.

	Top view		
Parameter	$Re_c = 80\,000$	125 000	Unit
Sampling rate	1.95		kHz
Number of samples	2500		
Frame separation	110	60	μs
Camera lens focal length	105		mm
Magnification factor	0.34		
Combined field of view	0.3×0.6		c
Final window size	16×16		px
Vector pitch	0.25		mm

Chapter 4

Low Reynolds Number Flow Over an Airfoil and the Effects of Turbulence Intensity

This chapter presents results from an exhaustive data set containing mean surface pressure distributions, sectional lift coefficients, suction side laminar separation bubble characteristics, and fluctuating surface pressure measurements. All measurements were made on a NACA 0018 airfoil for angles of attack between 0° and 20°, chord Reynolds numbers between 100 000 and 200 000, and free-stream turbulence intensities between 0.09% and 2.03%. One of the main objectives of the chapter is to shed light on the interdependence between angle of attack, chord Reynolds number, and free-stream turbulence intensity on the flow development over a low Reynolds number airfoil. Mean surface pressure measurements are used to identify changes in the airfoil sectional lift (Section 4.1) and mean bubble topology (Sections 4.2 and 4.3), while fluctuating surface pressure measurements are used to infer changes to the transition process in the separated shear layer (Section 4.4). Due to the relatively large test matrix, a portion of the results is presented in order to highlight key trends in the data. A more detailed discussion of the transition process will be presented in Chapter 5 but the measurements presented in this chapter allow for the identification of trends in transition process characteristics with varying operating conditions. All results presented in this chapter are in the chord based coordinate system defined in Fig. 3.4.

4.1 Airfoil Lift

The effects of free-stream turbulence intensity on the flow over the airfoil are first examined via the sectional lift coefficient. The sectional lift coefficient is calculated by numerically integrating the mean surface pressure distribution measured at the airfoil midspan (see Fig. 3.4). The angle of attack and local surface curvature were both considered in the calculation. Further, since the furthest downstream pressure tap is at $X/c = 0.95$, an additional integration point was added at the airfoil trailing edge ($X/c = 1$), and assigned a mean pressure value equal to the average of the taps at $X/c = 0.95$ on the suction and pressure sides of the airfoil. All computed values have an associated uncertainty of less than 2% of the free-stream dynamic pressure (details of the calculation method are provided in Appendix A). The lift coefficients computed for all investigated cases are plotted in Fig. 4.1.

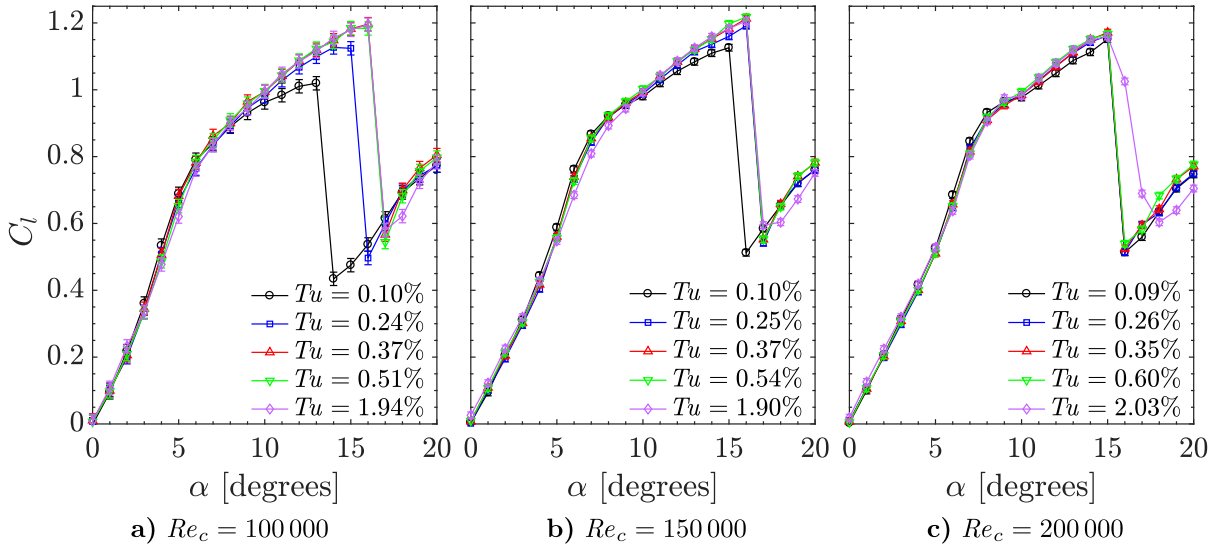

a) $Re_c = 100\,000$ **b)** $Re_c = 150\,000$ **c)** $Re_c = 200\,000$

Figure 4.1: Sectional lift coefficients.

The results at the baseline level of Tu are in good agreement with previous investigations that reported the lift generated by a NACA 0018 airfoil in low disturbance environments [10, 41, 165]. The data for all Reynolds numbers and Tu levels can generally be divided into three distinct regions: (i) 'low angles of attack', $\alpha \lesssim 6°$, where C_l increases approximately linearly with increasing angle of attack; (ii) 'pre-stall angles of attack', from $\alpha \approx 7°$ to stall, where C_l increases with increasing angle of attack, but the slope as compared to lower

angles of attack is checked, and (iii) 'post-stall angles of attack', where C_l recovers with increasing angle of attack after the large loss in lift at stall.

At low angles of attack ($\alpha \lesssim 3°$), the results at all Reynolds numbers show no significant variation in C_l with increasing Tu. As the angle of attack is increased further towards the pre-stall range (*i.e.*, $4° \lesssim \alpha \lesssim 6°$), slightly higher lift is generated at lower Tu levels. The upper limit of the low angle of attack range, and thus the onset of the pre-stall range, shifts to higher angles of attack with increaasing Reynolds number, namely, $\alpha = 6°$, 7°, and 8° for $Re_c = 100\,000$, 150 000, and 200 000, respectively. Below these angles of attack, at a given Tu level, the rate of increase of C_l with respect to α increases with increasing angle of attack, similar to the trend reported by Boutilier and Yarusevych [10]. In the pre-stall angle of attack range, the lift curves show significant variations with increasing Tu level. As the level of Tu is increased, the local lift slope is increased and, in general, higher lift is generated at a given angle of attack. This effect becomes checked as either Tu or Re_c is increased. For example, at $Re_c = 100\,000$ (Fig. 4.1a), the slope of the lift curve is increased significantly when Tu is increased from 0.10% to 0.24%, but further increases result in notably smaller changes, with no significant variation in lift seen for $Tu \gtrsim 0.37\%$. Similarly, when Re_c is increased to 200 000 (Fig. 4.1c), the slopes of the lift curves are approximately equal for all levels of Tu investigated, and the relative effect of increasing Tu on the lift coefficient diminishes.

The results in Fig. 4.1 show that airfoil stall tends to be delayed at higher Tu levels, with the effect saturating at higher levels of Tu and higher Re_c. For example, at $Re_c = 100\,000$ (Fig. 4.1a) the airfoil stalls at $\alpha = 14°$ at the baseline level of Tu. The stall angle is increased to $\alpha = 16°$ at $Tu = 0.24\%$ and $\alpha = 17°$ for all further increases in Tu. When the chord Reynolds number is increased to $Re_c = 150\,000$ (Fig. 4.1b), the airfoil stall angle is increased from $\alpha = 16°$ to 17° by increasing Tu from the baseline level to all elevated levels of Tu investigated. At $Re_c = 200\,000$ (Fig. 4.1c), the effect of Tu on the stall angle falls within the resolution of the test matrix (*i.e.*, 1°) and the airfoil stalls at $\alpha = 16°$ for all Tu levels investigated. For $Re_c \leq 150\,000$, the stall of the airfoil is sudden, and there is a decrease in C_l of approximately 0.5 over a 1° increase in the angle of attack for all Tu levels investigated. At $Re_c = 200\,000$, the behvaiour is similar, except for $Tu = 2.03\%$ where the stall is more gradual, and lift decreases in the range of $16° < \alpha \leq 18°$. This result is similar to the findings of Cao *et al.* [39], who reported a more gradual decrease in the lift of an S1223 airfoil in post-stall conditions at a high Tu level. An analysis of mean and fluctuating surface pressure distributions for this case indicate that the behaviour can be attributed to bi-stable oscillations between an attached and stalled state for these flow conditions. Similar behaviour has also been reported in the investigation of Zaman *et al.* [56] who measured low frequency fluctuations over the suction side of an airfoil at an

elevated level of Tu. At fully stalled angles of attack, C_l increases at a similar rate for all Tu levels investigated for a given chord Reynolds number.

A summary of the effects of Tu and Re_c on the maximum lift coefficients for all flow conditions is shown in Fig. 4.2. Since Tu varies slightly across the Reynolds numbers, the legend shows the averaged value for a given turbulence generating grid (or the baseline condition) across all Reynolds numbers investigated. In general, increases in either Tu

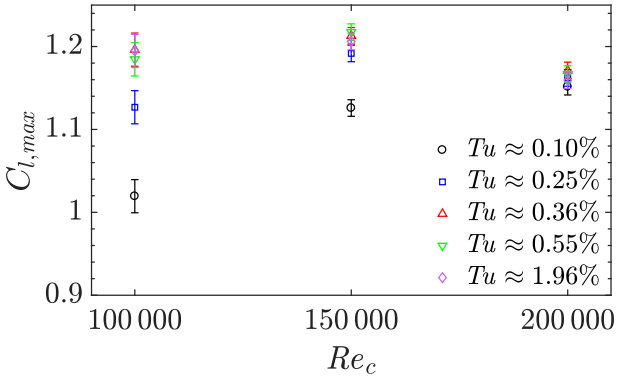

Figure 4.2: Maximum sectional lift coefficients.

or Re_c result in an increase in $C_{l,max}$. For example, at $Re_c = 100\,000$, the maximum lift coefficient is increased by approximately 17% by increasing Tu from the baseline level to the highest level investigated. Similarly, at the baseline level of Tu, $C_{l,max}$ is increased by approximately 10% and 13% by increasing Re_c from 100 000 to 150 000 and 200 000, respectively. As has been noted above, as either Tu or Re_c is increased, the effect of the other parameter is reduced. For example, at $Re_c = 200\,000$, $C_{l,max}$ is increased by approximately 1% by increasing Tu from the baseline level to the highest level investigated as compared to approximately 17% at $Re_c = 100\,000$. At all elevated levels of Tu (*i.e.*, $Tu > 0.10\%$), $C_{l,max}$ decreases when Re_c is increased from 150 000 to 200 000. This is a result of the delay in stall with increasing Tu at $Re_c = 150\,000$ (Fig. 4.1b), whereas at $Re_c = 200\,000$ there is no discernible effect on the stall angle with increasing Tu (Fig. 4.1c). The result is higher overall $C_{l,max}$ values at $Re_c = 150\,000$. This result is note-worthy as is indicates that the generally accepted trend of increasing C_l with increasing Re_c for low Reynolds number airfoil flows [10] can be altered at elevated levels of Tu.

4.2 Surface Pressure Distributions and Mean Bubble Topology

To investigate the effects of free-stream turbulence intensity on the laminar separation bubble formed over the suction side of the airfoil, and explain the observed differences in C_l with increasing Tu noted in Section 4.1, mean surface pressure distributions over the suction and pressure sides of the airfoil are presented in Fig. 4.3 for all Reynolds numbers investigated. The presented angles of attack represent the different regions of angle of attack identified above, namely low, pre-stall, and post-stall angles of attack. In addition, an angle of attack in between the low and pre-stall angles is presented and represents the transition between these two regions. Additional angles of attack are included in Appendix E. Mean surface pressure distributions are commonly used in identifying the presence and extent of a laminar separation bubble (LSB), which can be characterized by a region of nearly constant surface pressure downstream of the suction peak [6, 7, 9, 10]. The results show that below the stall angle of attack (Figs. 4.3a–i), separation bubbles can be identified in the range of $0.1 \lesssim X/c \lesssim 0.7$, except for at low angles of attack and the highest Tu level investigated. Beyond stall, the surface pressure distributions show that the magnitude of the suction peak is greatly diminished as compared to the pre-stall angles (*e.g.*, compare Figs. 4.3g and 4.3j) and the surface pressure is nearly constant over the majority of the suction surface (Figs. 4.3j–l). Throughout Fig. 4.3, marginal differences in the pressure side C_P distributions are observed for all angles of attack and Reynolds numbers investigated, and thus the discussion will focus on the suction side results.

For cases where a separation bubble can be identified on the suction side of the airfoil, the beginning of the region of nearly constant surface pressure corresponds to the location of mean flow separation, X_S. The subsequent region of rapid pressure recovery indicates the aft portion of the separation bubble, with the beginning of this region marking the approximate location of mean transition, X_T, and the end roughly corresponding to the location of mean flow reattachment, X_R [9]. These locations are estimated using a method discussed by Boutilier and Yarusevych [10], which is illustrated graphically in Fig. 4.4 for two representative cases. The method involves approximating the mean surface pressure distribution around the pressure plateau with four lines, shown as the dashed lines in Fig. 4.4. The three intercepts of these lines serve to estimate the locations of mean separation, transition, and reattachment, as shown by the filled diamond markers in Fig. 4.4. These locations were determined for all cases for which a separation bubble could be identified and the results are summarized in Fig. 4.5, while the variation in separation bubble length is shown in Fig. 4.6.

At low angles of attack ($\alpha \lesssim 4°$), the mean separation location rapidly advances upstream

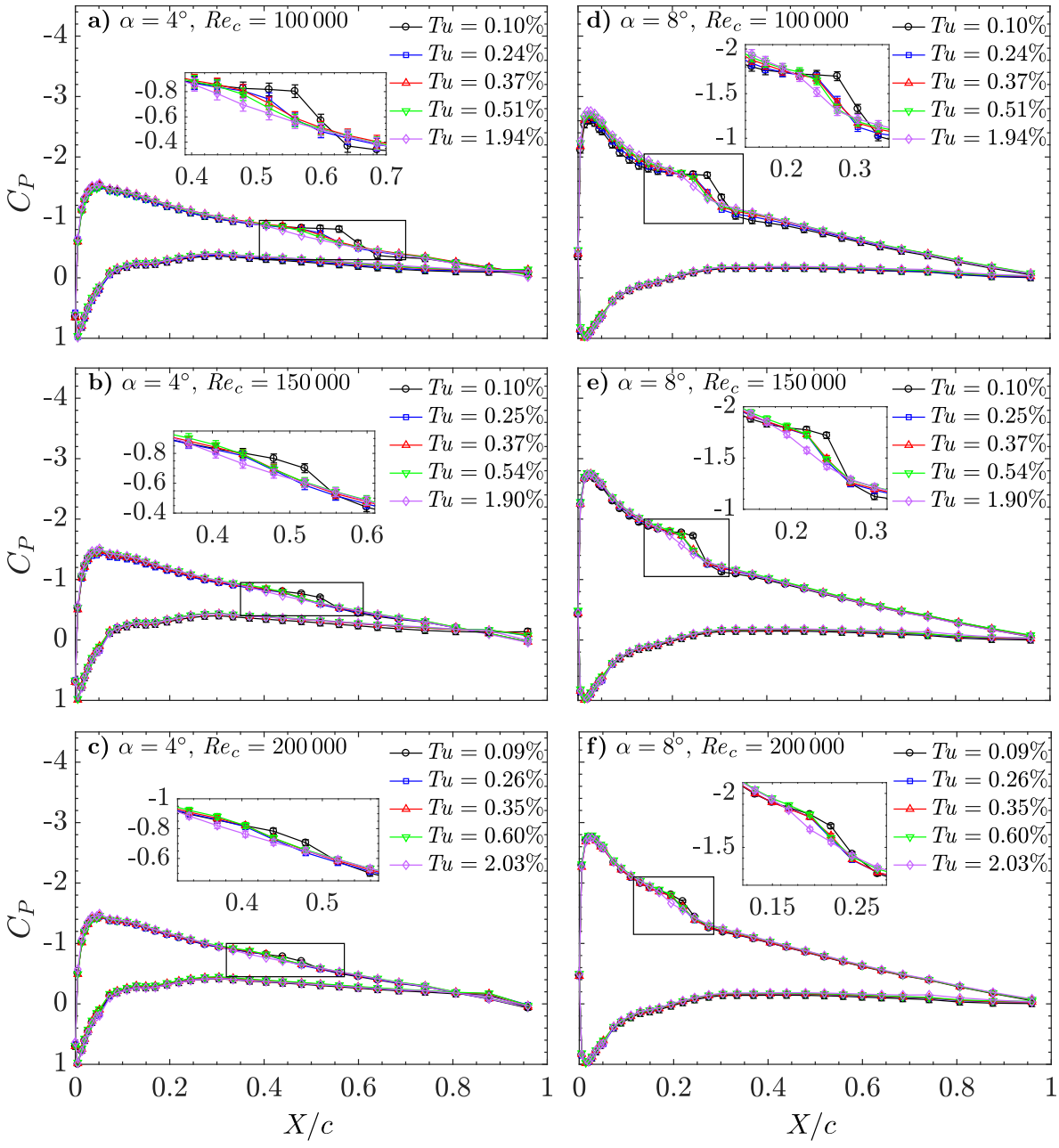

Figure 4.3: Mean surface pressure distributions. Error bars shown in inset plots.

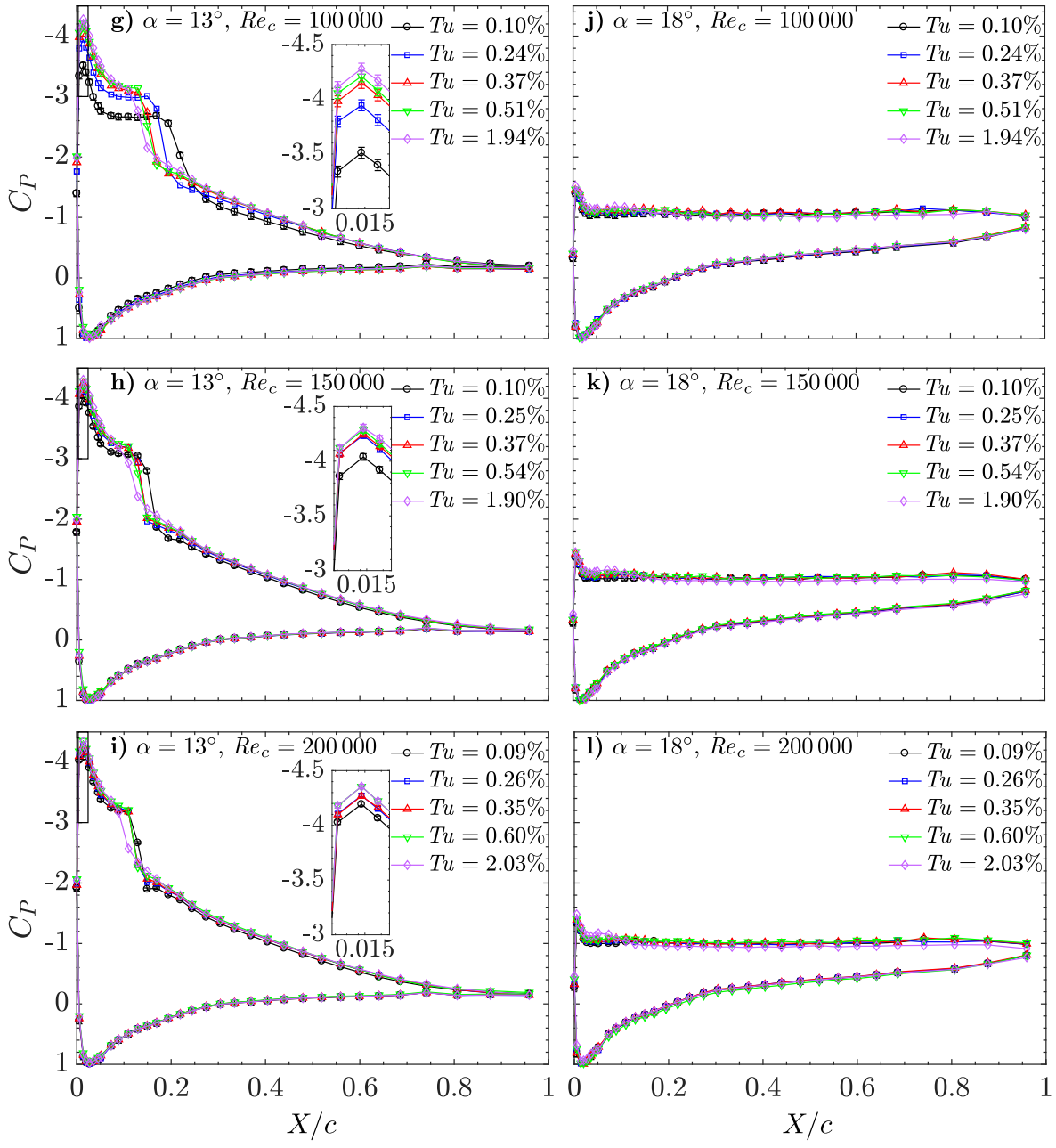

Figure 4.3 (cont.): Mean surface pressure distributions. Error bars shown in inset plots.

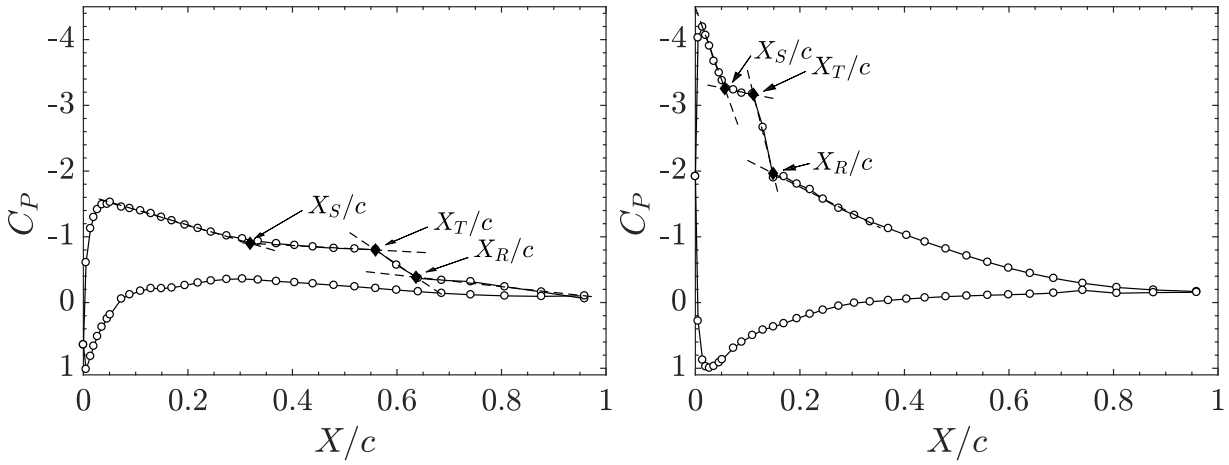

(a) $\alpha = 4°$, $Re_c = 100\,000$ **(b)** $\alpha = 13°$, $Re_c = 200\,000$

Figure 4.4: Sketch of the method used to determine the locations of mean separation, transition, and reattachment for (a) a relatively large, and (b) a relatively small separation bubble. For both surface pressure distributions $Tu = 0.10\%$.

as the angle of attack is increased (Fig. 4.5), but the overall length of the bubble remains relatively constant in this range of angles of attack (Fig. 4.6). Increasing the level of Tu leads to a decrease in the overall separation bubble length (Fig. 4.6), which can be attributed primarily to the earlier onset of mean transition and, consequently, earlier mean reattachment (Fig. 4.5). This is reflected in the upstream advancement of the rapid pressure recovery region in the aft portion of the separation bubble, as seen in the inset plots in Figs. 4.3a–c. For $Re_c \geq 150\,000$ and the highest Tu level investigated, separation appears to be suppressed on the suction side of the airfoil, with no evidence of a separation bubble in Figs. 4.3b–c. The net reduction in separation bubble length with increasing Tu is particularly significant at lower Reynolds numbers (Fig. 4.6a). For example, at $Re_c = 100\,000$ and $\alpha = 6°$, ℓ_b is reduced by approximately 13% and 40% by increasing Tu from the baseline level to 0.24% and 1.94%, respectively. This observed reduction in separation bubble length with increasing Tu level is similar to that noted by Olson *et al.* [34] for an SD7003 airfoil at $20\,000 \leq Re_c \leq 40\,000$ and comparable angles of attack. In their investigation, for a chord Reynolds number of 25 000 and an angle of attack of 6°, an increase in Tu from 0.3% to 0.9% resulted in a 35% reduction in the suction side separation bubble length. Olson *et al.* [34] found that this reduction was the result of a small downstream shift in the location of mean separation and a larger upstream shift in the location of mean reattachment by using estimates from Molecular Tagging Velocimetry measurements. The upstream shift in

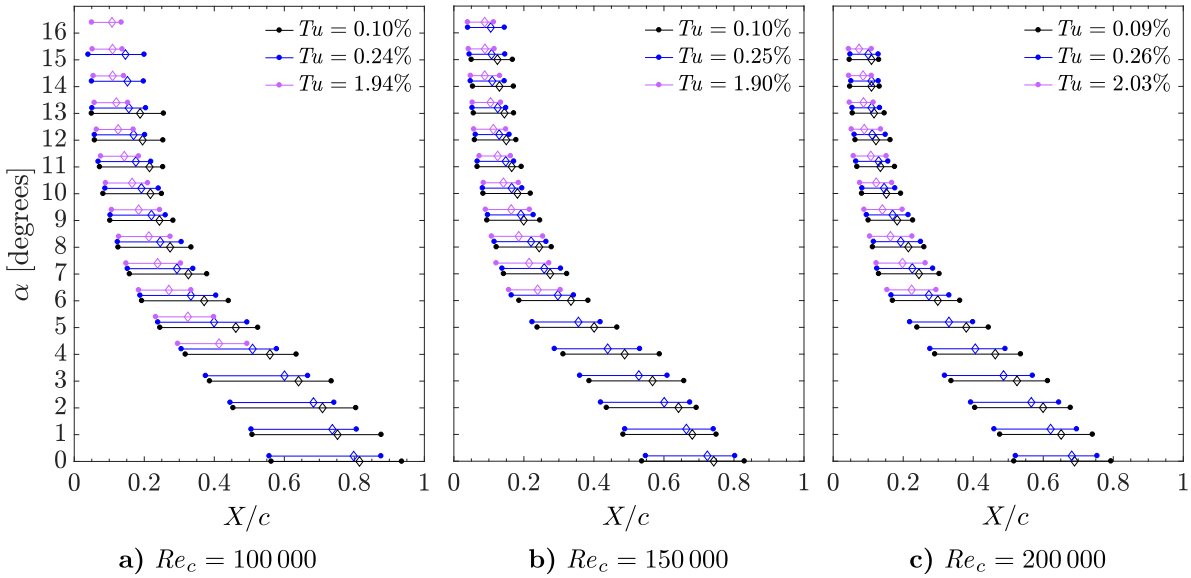

Figure 4.5: Summary of mean separation bubble topology. Filled circles represent mean separation and reattachment locations while diamond markers represent mean transition. The width of the diamond markers is approximately equal to the uncertainty in each of the locations. Plots at equal angles of attack are offset slightly in the vertical direction for clarity.

mean reattachment is consistent with the results of this investigation (Fig. 4.5), however, the observed changes in mean separation fall within the experimental uncertainty of the present investigation and therefore cannot be quantified. The results in Figs. 4.5 and 4.6 show that the effect of Tu on the size and position of the separation bubble become less pronounced as the Reynolds number is increased, consistent with the results presented in Fig. 4.1. For example, at $Re_c = 200\,000$ and $\alpha = 6°$, the length of the separation bubble is decreased by 27% by increasing Tu from the baseline level to the highest level investigated, as compared to a 40% reduction at $Re_c = 100\,000$ for the same angle of attack and increase in Tu. At low angles of attack, the separation bubble forms over the aft portion of the airfoil (Fig. 4.5), far downstream of the suction peak (Figs. 4.3a–c). Thus, when the level of Tu is increased and the separation bubble length is decreased, there is no appreciable effect on the magnitude of the suction peak (Figs. 4.3a–c). However, the reduction in local suction associated with the pressure plateau leads to a slight reduction in lift for increasing Tu levels, as seen in Fig. 4.1 at low angles of attack.

As the angle of attack is increased above $\alpha \approx 4°$, the separation bubble on the suction

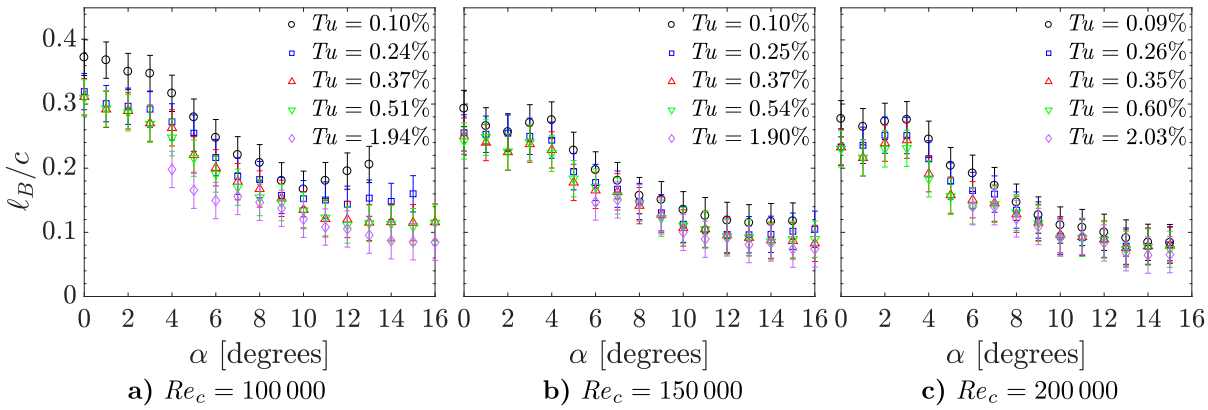

a) $Re_c = 100\,000$ **b)** $Re_c = 150\,000$ **c)** $Re_c = 200\,000$

Figure 4.6: Variation of mean separation bubble length.

side of the airfoil continues to move upstream (Fig. 4.5), but at a reduced rate as compared to that at the low angles of attack, consistent with the trend reported by Boutilier and Yarusevych [10]. At the same time, the length of the bubble decreases rapidly (Fig. 4.6) due to the rapid upstream advancement of the mean transition and reattachment locations Fig. 4.5. As a result of the upstream motion of the bubble, it begins to form closer to the suction peak and starts to affect its magnitude, as can be seen in Figs. 4.3d–f and Figs. 4.3g–i for $\alpha = 8°$ and 13°, respectively. For increasing Tu levels, earlier transition occurs (Fig. 4.5) and reduces the size of the separation bubble (Fig. 4.6), thereby reducing the adverse effect of the bubble on the magnitude of the suction peak (Figs. 4.3d–i). With the bubble forming near the suction peak, the curvature of the streamlines around the leading edge of the airfoil is reduced, thereby reducing flow acceleration and increasing mean surface pressure. When the bubble size is reduced, streamline curvature is increased, thereby increasing flow acceleration around the leading edge and decreasing mean surface pressure (*i.e.*, increasing the magnitude of the suction peak). At $Re_c = 100\,000$ and $\alpha = 8°$ (Fig. 4.3d), the magnitude of the suction peak is increased by approximately 6% when the level of Tu is increased from 0.10% to 1.94%. This effect becomes stronger as the angle of attack is increased further and the bubble continues to move upstream towards the location of the suction peak (Fig. 4.5). For example, at $Re_c = 100\,000$ and $\alpha = 13°$ (Fig. 4.3g), the magnitude of the suction peak is increases by approximately 22% by increasing Tu from 0.10% to 1.94% as compared to 6% at $\alpha = 8°$ for the same increase in Tu. As a consequence, increasing Tu leads to an overall increase in C_l at pre-stall angles of attack (Fig. 4.1a). A similar increase in the magnitude of the suction peak with increasing Tu is also seen in the results of O'Meara and Mueller [9] for pre-stall angles of attack and comparable experimental conditions. The relative effect of increasing Tu on the magnitude

of the suction peak is reduced as Re_c is increased, due to the smaller bubble that initially forms at the baseline Tu level at higher Reynolds numbers. At $Re_c = 200\,000$ and $\alpha = 13°$, increasing Tu from the baseline level to the highest level investigated results in an increase of about 1% in the magnitude of the suction peak as compared to 22% at $Re_c = 100\,000$. As a consequence, there is a diminishing influence of Tu on C_l for a given pre-stall angle of attack as Re_c is increased (Fig. 4.1).

As the angle of attack is increased through the pre-stall angles of attack (*i.e.*, from $\alpha \approx 7°$ to the stall angle), the rate of upstream shift in the separation bubble location is decreased significantly (Fig. 4.5) and the rate of decrease in the bubble size diminishes (Fig. 4.6). At lower Reynolds numbers or Tu levels, the decrease in the size of the separation bubble with increasing angle of attack is checked, and, in some cases, an increase in the bubble length is observed prior to stall. This effect is most pronounced at the baseline Tu level for $Re_c = 100\,000$ and angles of attack above 10° (Fig. 4.5a), where the separation bubble lengthens by approximately 23% before the airfoil stalls (Fig. 4.6). For these flow conditions and angles of attack, the chordwise distance between the mean separation and transition locations remains approximately constant (Fig. 4.5a), while the distance between mean transition and reattachment increases with increasing angle of attack. A similar trend has been noted in previous experiments over an airfoil [9], and is a precursor to bubble bursting and stall [7]. When either the free-stream turbulence intensity or Reynolds number are increased, this effect is suppressed (Fig. 4.6). Further, consistent with the discussion presented thus far, as either parameter is increased the bubble length decreases, and the relative effect of the other parameter diminishes. Beyond stall, the effects of Tu on the surface pressure distributions are confined to the first 15% of the chord length on the suction side of the airfoil, in the immediate vicinity of the suction peak (Figs. 4.3j–l). However, the changes in the surface pressure distributions with increasing Tu do not result in appreciable changes in lift at post-stall angles of attack (Fig. 4.1), with the exception of the stall behaviour at $Re_c = 200\,000$ for the highest Tu level investigated, as discussed in Section 4.1.

The relation between the effects of free-stream turbulence intensity on mean separation bubble characteristics and the resulting changes in airfoil lift can be summarized as follows. First, for all cases examined, increasing the Tu level leads to a reduction in the length of the suction-side separation bubble (Fig. 4.6), which is largely the result of an upstream shift in the locations of mean transition and, consequently, reattachment (Fig. 4.5). This effect becomes checked as the chord Reynolds number is increased. At small angles of attack, relatively long bubbles form over the aft portion of the airfoil suction side, relatively far downstream from the suction peak. When Tu is increased, the decrease in separation bubble length has no appreciable affect on the suction peak but leads to a reduction in

local suction at the location of the separation bubble, thereby slightly decreasing lift at low angles of attack (Fig. 4.1). At larger angles of attack where the separation bubble forms further upstream, there is a notable decrease in maximum suction due to the presence of the separation bubble. As the level of Tu is increased and the bubble shrinks, the adverse influence on the suction peak is reduced and lift increases. Hence, for large pre-stall angles of attack where the bubble forms near the suction peak, smaller bubbles formed at high levels of Tu lead to higher lift coefficients, whereas at low angles of attack, larger bubbles forming at low levels of Tu lead to higher lift coefficients due to the larger pressure plateau. At moderate angles of attack, there is a balance between these competing effects, with the main determining factors being the relative size of the separation bubble and its proximity to the suction peak.

4.3 Reynolds Number Effects

Previous discussions showed that the effects of free-stream turbulence intensity on airfoil lift (Section 4.1) and mean bubble topology (Section 4.2) are reduced as the chord Reynolds number is increased. This section provides a quantitative characterization of the effect of Reynolds number on airfoil lift and the underlying changes to the mean separation bubble characteristics at different levels of free-stream turbulence intensity. Results are presented for the baseline case and two elevated Tu levels (cases i), ii), and v) in Table 3.2). Since the actual measured free-stream turbulence intensity varies slightly with Re_c for a given condition, the averaged levels of Tu across the investigated Reynolds numbers are used to refer to the data corresponding to a given screen configuration, namely, $Tu \approx 0.10\%$, 0.25%, and 1.96% for cases i), ii), and v), respectively. Fig. 4.7 highlights the effect of Reynolds number on the sectional lift coefficient. At low angles of attack and a given level of Tu, increasing the chord Reynolds number results in a decrease in the sectional lift coefficient. At higher angles of attack and the baseline Tu level, increasing the Reynolds number leads to an increase in lift, similar to the trend reported by Boutilier and Yarusevych [10] in a low disturbance environment. However, this effect diminishes at higher levels of Tu. By comparing Figs. 4.1 and 4.7, it can be seen that for a given angle of attack similar changes in lift are produced by increasing either the Reynolds number or the level of Tu and holding the other constant.

Similarly to the discussion provided in Section 4.2, the effects of increasing Reynolds number on lift can be linked to changes in separation bubble characteristics on the suction side of the airfoil. Surface pressure distributions for the same angles of attack presented in Fig. 4.3 are shown in Fig. 4.8, while mean bubble topology and separation bubble lengths are summarized in Figs. 4.9 and 4.10, respectively. At the baseline Tu level, the

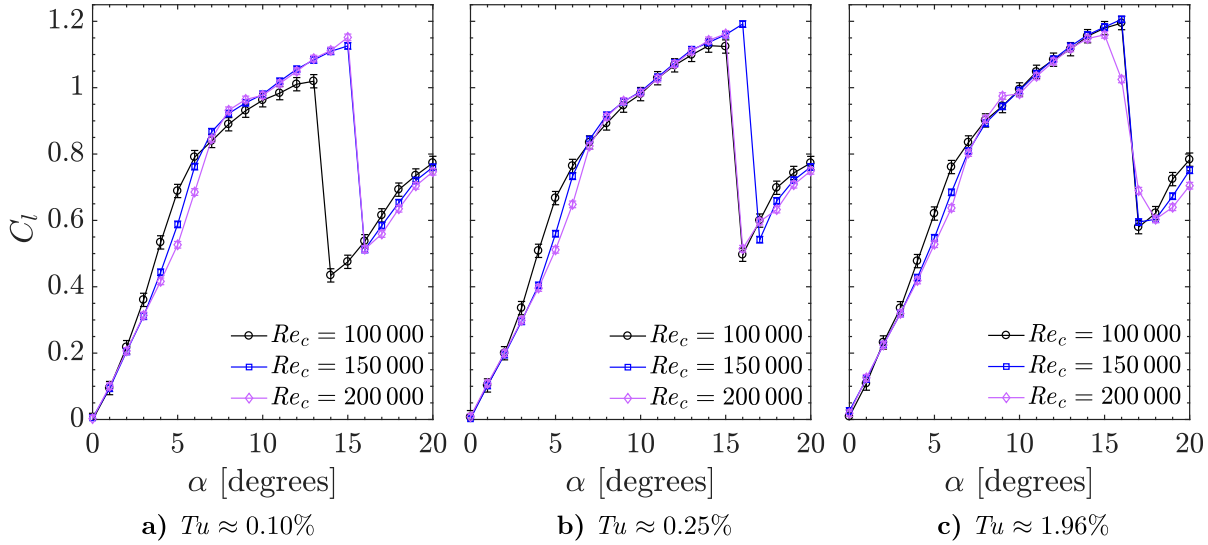

Figure 4.7: Effect of Reynolds number on sectional lift coefficients.

separation bubble shifts upstream slightly (Fig. 4.9a), and decreases in length (Fig. 4.10a) with increasing chord Reynolds number. The latter is largely the result of an upstream shift in the location of mean transition, and as a result mean reattachment (Fig. 4.9a), consistent with the results of previous investigations in low disturbance environments [10, 41]. This upstream shift can also be observed as the upstream shift of the aft portion of the separation bubble shown in the inset plots of Figs. 4.8a and 4.8d. As the level of free-stream turbulence intensity is increased, similar decreases in separation bubble length with increasing Re_c are observed (Figs. 4.10b–c), also as a result of upstream shifts in the locations of mean transition and reattachment (Figs. 4.9b–c), but the changes are notably smaller than at the baseline Tu level. This decreasing influence of Re_c on the separation bubble and thus mean surface pressure distributions at elevated levels of Tu is similar to the opposite case (*i.e.*, decreasing influence of Tu at higher Re_c) discussed in Section 4.2.

The mean surface pressure distributions show that at low angles of attack (Figs. 4.8a–c), the formed separation bubble has no measureable influence on the suction peak magnitude and thus when Re_c is increased, the magnitude of the suction peak remains constant. The decrease in local suction produced by this change then leads to the lower levels of lift at higher Reynolds numbers noted in Fig. 4.7. However, for pre-stall angles of attack (Figs. 4.8g–i), the bubble forms near the suction peak (Fig. 4.9) and thus the magnitude of the suction peak is adversely affected by its presence. As Re_c is increased and the bubble size deceases, the impact of the bubble is reduced and there is a net increase in

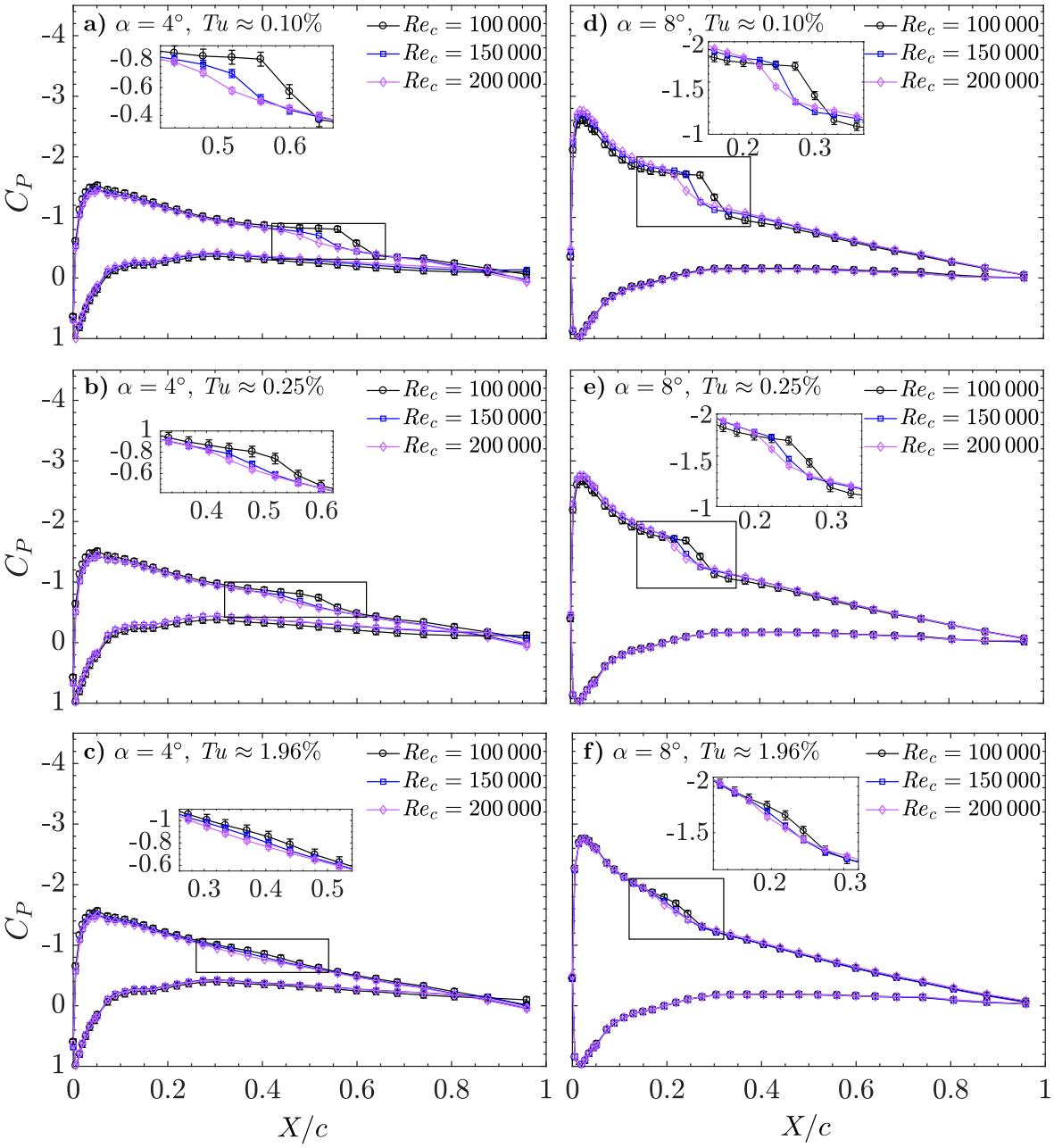

Figure 4.8: Effect of Reynolds number on mean surface pressure distributions. Error bars shown in inset plots.

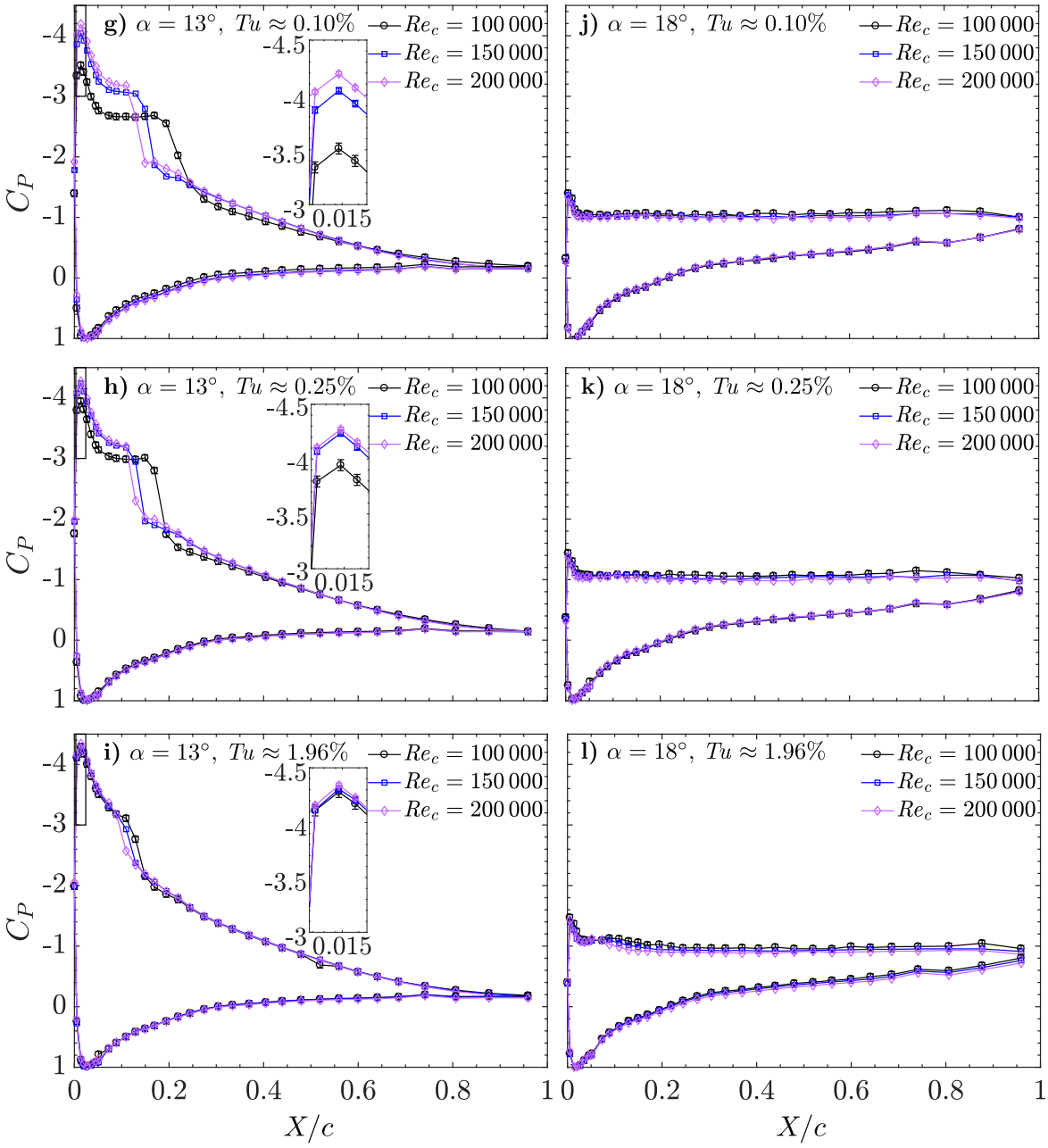

Figure 4.8 (cont.): Effect of Reynolds number on mean surface pressure distributions. Error bars shown in inset plots.

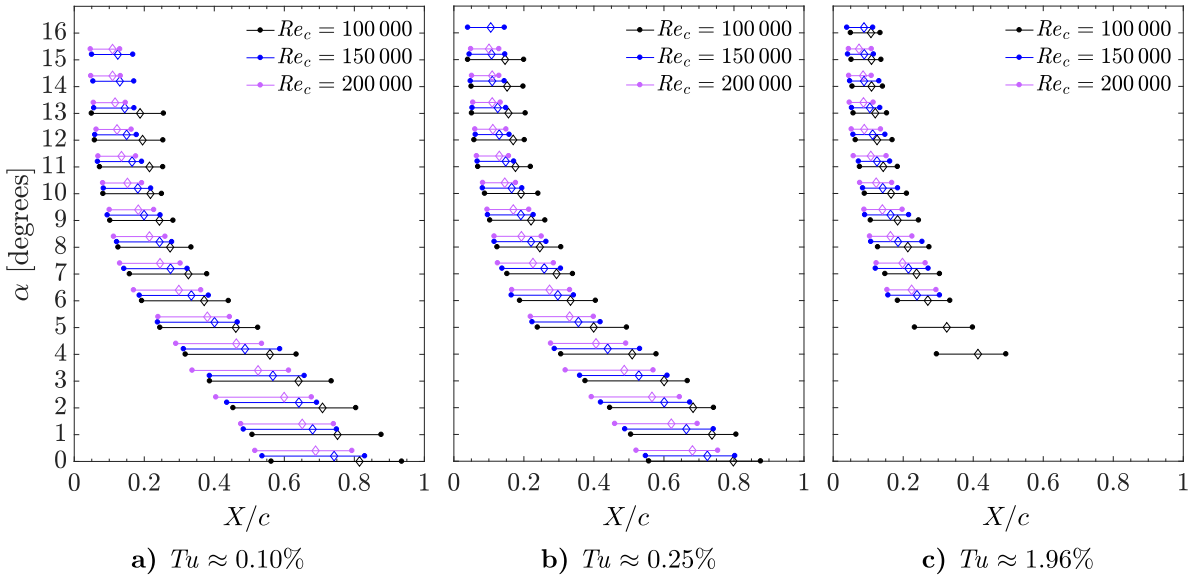

Figure 4.9: Effect of Reynolds number on mean separation bubble topology. Filled circles represent mean separation and reattachment locations. Diamond markers represent mean transition and whose widths are approximately equal to the uncertainty of each location. Plots at equal angles of attack are offset slightly in the vertical direction for clarity.

lift (Fig. 4.7). At an intermediate angle of attack of $\alpha = 8°$ (Figs. 4.8d–f), both effects are present, particularly for $Tu \approx 0.10\%$, and as a result there is a transition from decreased to increased lift with increasing Re_c in the range of $6° \lesssim \alpha \lesssim 10°$. Both of these effects become notably less significant at higher levels of free-stream turbulence intensity. From a comparison of Figs. 4.3 and 4.8, it is clear that increases in either Tu or Re_c result in similar changes to the mean surface pressure distributions. Moreover, the influence of either parameter on the mean flow is reduced as the other is increased since both affect the length of the separation bubble. In their investigation, O'Meara and Mueller [9] noted the similarity of the effects of these two parameters on mean surface pressure distributions which led them to describe the effect of increased Tu as being similar to an 'effective' Reynolds number increase. While the results of this investigation support this concept, it will be shown in Section 4.4 that the underlying physics which lead to the observed changes in mean bubble topology and sectional lift differ significantly depending on whether one increases Tu or Re_c.

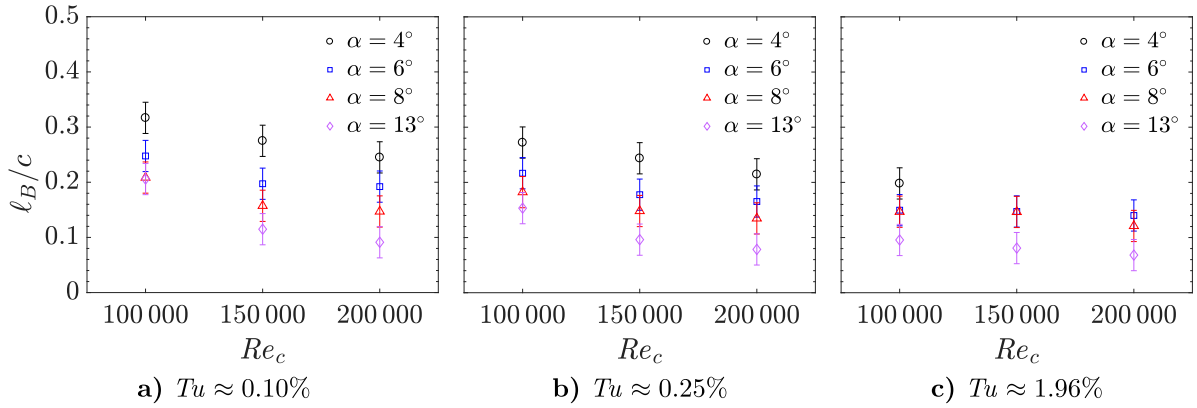

Figure 4.10: Effect of Reynolds number on mean separation bubble length.

4.4 Separated Shear Layer Transition

The results presented in Section 4.2 showed that the observed changes in mean bubble topology at elevated Tu levels are related to an upstream shift in the location of mean transition (*e.g.*, Fig. 4.5). An analysis of the flutuating surface pressure measurements is thus performed in order to characterize the development of shear layer disturbances, similar to the methodology used in previous studies examining transition [136, 159, 163, 164]. A more detailed discussion of the effects of Tu on the flow development within a laminar separation bubble will be provided in Chapter 5, but the goal of this section is to highlight the effects of free-stream turbulence intensity, angle of attack, and chord Reynolds number on the separated shear layer transition characteristics.

Streamwise distributions of the root-mean-square (RMS) of fluctuating surface pressures over the suction side of the airfoil at $Re_c = 100\,000$ are shown in Fig. 4.11 for two levels of Tu and several angles of attack. The results show that, following separation, there is a region of amplification of the surface pressure fluctuations, followed by an apparent decrease in their amplitude. The initial increase in the amplitude of the pressure fluctuations is reflective of the amplification of velocity and pressure fluctuations in the separated shear layer [136], while the subsequent decrease occurs downstream of mean reattachment in the developing turbulent boundary layer and is largely due to the increasing distance from the fluctuations to the microphones [136]. Indicated locations of mean transition, as determined from the mean surface pressure distributions (*i.e.*, Fig. 4.5), correspond well with the streamwise location where significant amplification of surface pressure fluctuations is observed, with the peak pressure fluctuations, p'_{max}, typically occurring just downstream of mean transition. The upstream shift in the streamwise location of p'_{max} with increasing angle of attack is

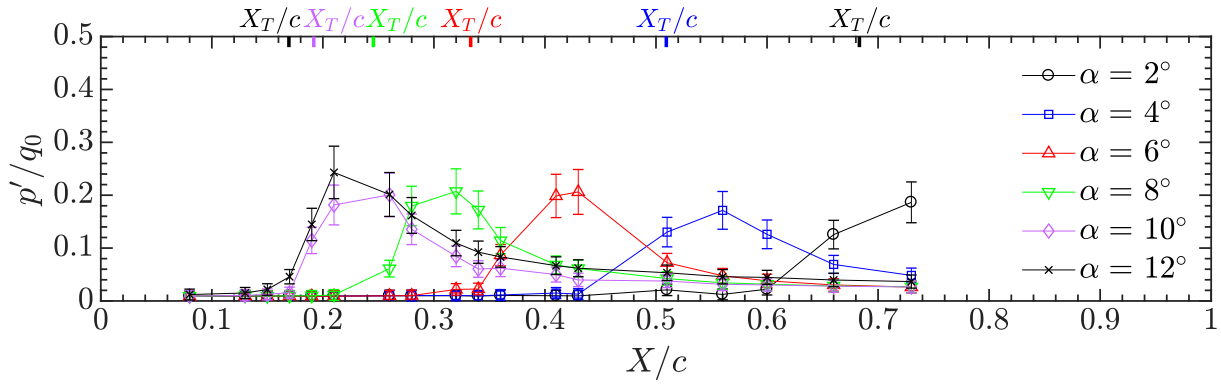

(a) $Tu = 0.10\%$

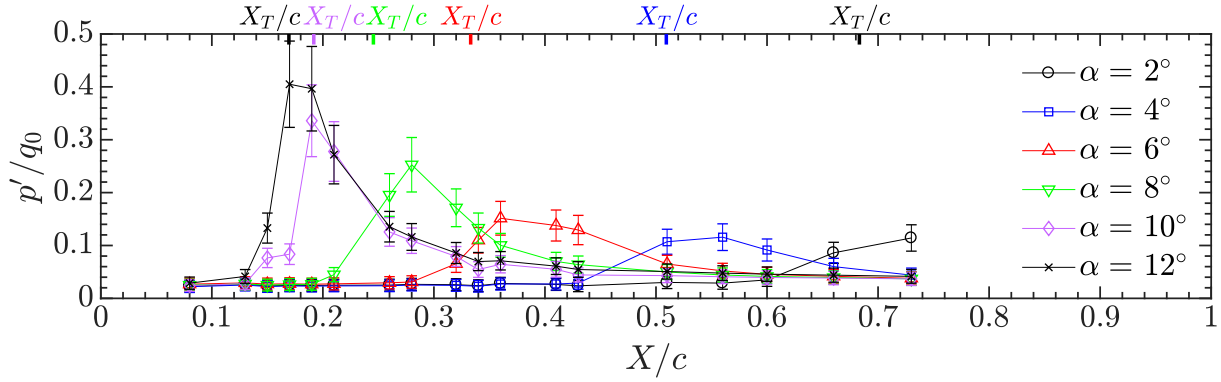

(b) $Tu = 0.24\%$

Figure 4.11: Distributions of the root-mean-square of fluctuating surface pressures at $Re_c = 100\,000$. Thick lines and labels, coloured according to the legend, indicate the mean transition locations as determined from mean surface pressure distributions.

therefore linked to the upstream shift in the locations of mean transition. Comparing the results for the two levels of Tu presented in Fig. 4.11 shows that the pressure fluctuations follow very similar behaviour at elevated Tu levels, indicating that a comparison of the RMS of fluctuating surface pressure distributions can provide insight into the effects of Tu on the transition process.

Streamwise distributions of the RMS of fluctuating surface pressures over the suction side of the airfoil for increasing levels of Tu are presented in Fig. 4.12 for $\alpha = 4°$ and 8°, representative of low and pre-stall angles of attack, respectively. As was shown in Fig. 4.11, the surface pressure fluctuations in Fig. 4.12 generally attain maximum amplitudes just downstream of the mean transition location, and the location of mean transition follows the

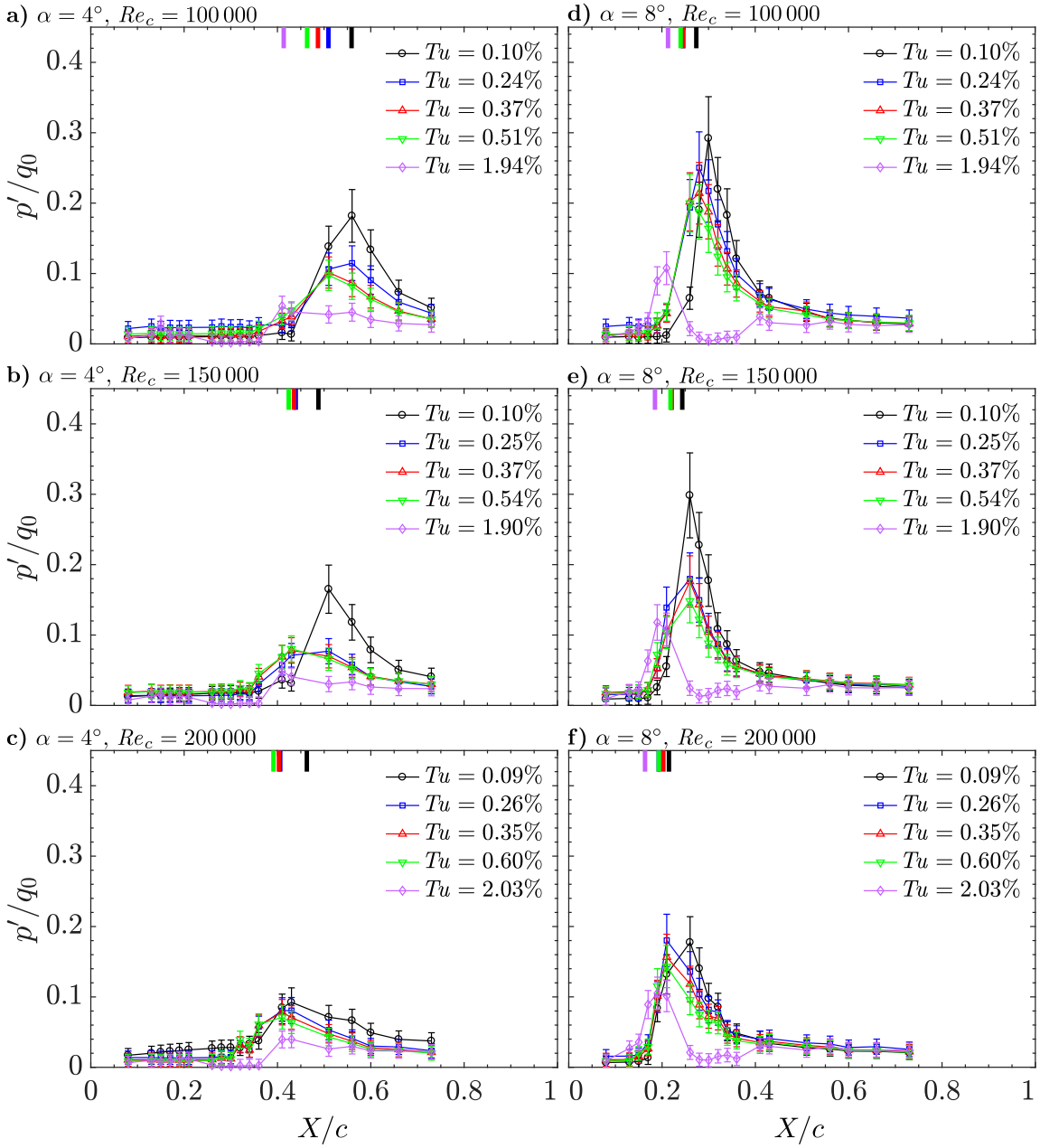

Figure 4.12: Distributions of the root-mean-square of fluctuating surface pressures. Thick lines, coloured according to the legend, indicate mean transition locations as determined from the mean surface pressure distributions.

upstream shift in the location of p'_{max} with increasing Tu. On the average, the upstream shift is also accompanied by a decrease in p'_{max}, ascribed primarily to the reduction in the magnitude of vertical velocity fluctuations in the separated shear layer, as shown by Yarusevych and Kotsonis [24] to be a result of the increased influence of the wall. At low angles of attack (Figs. 4.12a–c), the results show little-to-no amplification of the pressure fluctuations in the range of $0.35 \lesssim X/c \lesssim 0.40$ for the highest Tu level investigated. In fact, from the surface pressure distributions (Fig. 4.3), a bubble can only be detected for $Re_c = 100\,000$ (Fig. 4.12a). This finding then suggests that, for $Re_c = 100\,000$ and the highest Tu level investigated, the bubble is so small in the wall normal direction that it does not significantly influence the mean surface pressure distribution and the influence of the wall strongly inhibits wall-normal velocity fluctuations. At the higher Reynolds numbers, the results suggest that separation is suppressed (Fig. 4.5) and the transition process is likely altered such that it is not associated with strong wall-normal fluctuations (Figs. 4.12b and 4.12c). In agreement with earlier observations, the effect of Tu on the fluctuating surface pressure distributions decreases with increasing Re_c for both angles of attack shown in Fig. 4.12. Comparing the results, it can be seen that both the upstream shift and decrease in magnitude of p'_{max} with increasing Tu are decreased at higher Re_c as both parameters shift transition upstream and decrease the size of the separation bubble (Figs. 4.6 and 4.10).

The streamwise distributions of the RMS of fluctuating surface pressures can also be used to estimate spatial amplification factors of the separated shear layer disturbances as $\sigma_{p'} = (\Delta \ln(p'/q_0))/(\Delta X/c)$ [10, 136]. The maxima of these spatial amplification factors are presented in Fig. 4.13 for each Reynolds number and all Tu levels investigated. For a given Reynolds number and Tu level, maximum amplification factors increase with increasing angle of attack, explaining the associated decrease in separation bubble length (Fig. 4.6), and is consistent with the results of Boutilier and Yarusevych [10] in a low disturbance environment. In contrast, for a given Reynolds number and angle of attack, the maximum spatial amplification rate decreases with increasing Tu level, implying that the bubble becomes more stable with increasing Tu. This is similar to the findings of Dovgal *et al.* [50], who showed using analytical velocity profiles that the stability of separated shear layers increases with decreasing distance to a wall. Decreased growth rates have also been observed in separation bubbles with imposed mean flow deformations both experimentally [24] and numerically [43]. The implication in the present investigation is that since the bubble becomes more stable with increasing Tu, the upstream shift in the location of mean transition with increasing Tu (Fig. 4.5) is solely the result of larger amplitudes of the initial perturbations at elevated Tu levels.

The discussion in Section 4.3 showed that the effects of increasing chord Reynolds

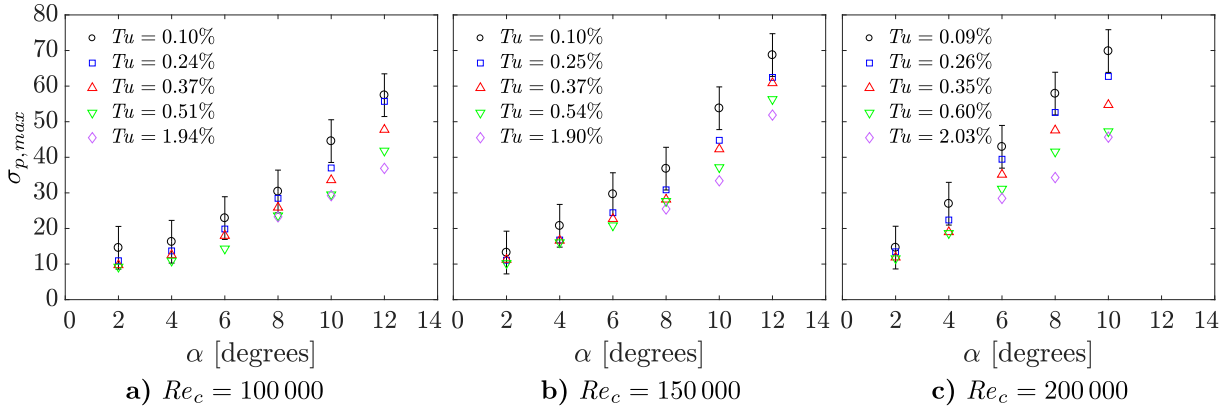

Figure 4.13: Maximum spatial amplification factors. Representative error bars are shown for the baseline level of Tu.

number on mean surface pressure distributions and separation bubble topology are similar to those of increasing Tu. Therefore, the effects of chord Reynolds number on the streamwise distribution of the RMS of fluctuating surface pressures are presented in Fig. 4.14 for the same three levels of Tu discussed in Section 4.3 (*i.e.*, $Tu \approx 0.10\%$, 0.25%, and 1.96%). The results show that as the Reynolds number is increased, p'_{max} shifts upstream and is followed by the location of mean transition as determined from the mean surface pressure distributions. The result is similar to the effects of increasing Tu presented in Fig. 4.12. Further, in general, as the chord Reynolds number is increased the magnitude of p'_{max} is decreased with increasing Reynolds number, a result of the smaller separation bubble (Fig. 4.10) having a damping effect on the velocity fluctuations [24]. The decreasing effect of Re_c on the separation bubble at higher Tu levels is evident by comparing Figs. 4.14d–f where the same increase in Reynolds number has a diminishing effect on both the upstream shift and magnitude of p'_{max} as the Tu level is increased, showing further similarities between these two parameters on separation bubbles.

The effects of Re_c on maximum spatial amplification rates are shown in Fig. 4.15 for $Tu \approx 0.10\%$, 0.25%, and 1.96%. Here, for a given angle of attack and Tu level, $\sigma_{p',max}$ increases with increasing Re_c, a trend that has also been observed by Boutilier and Yarusevych [10] in a low disturbance environment. This result is different than that for increasing Tu levels (Fig. 4.6) where $\sigma_{p',max}$ was shown to decrease with increasing Tu. Although the effects of increasing Re_c and Tu have been shown thus far to be very similar, this result highlights a key difference. While increasing either parameter at a given angle of attack leads to a reduction in separation bubble length through the upstream

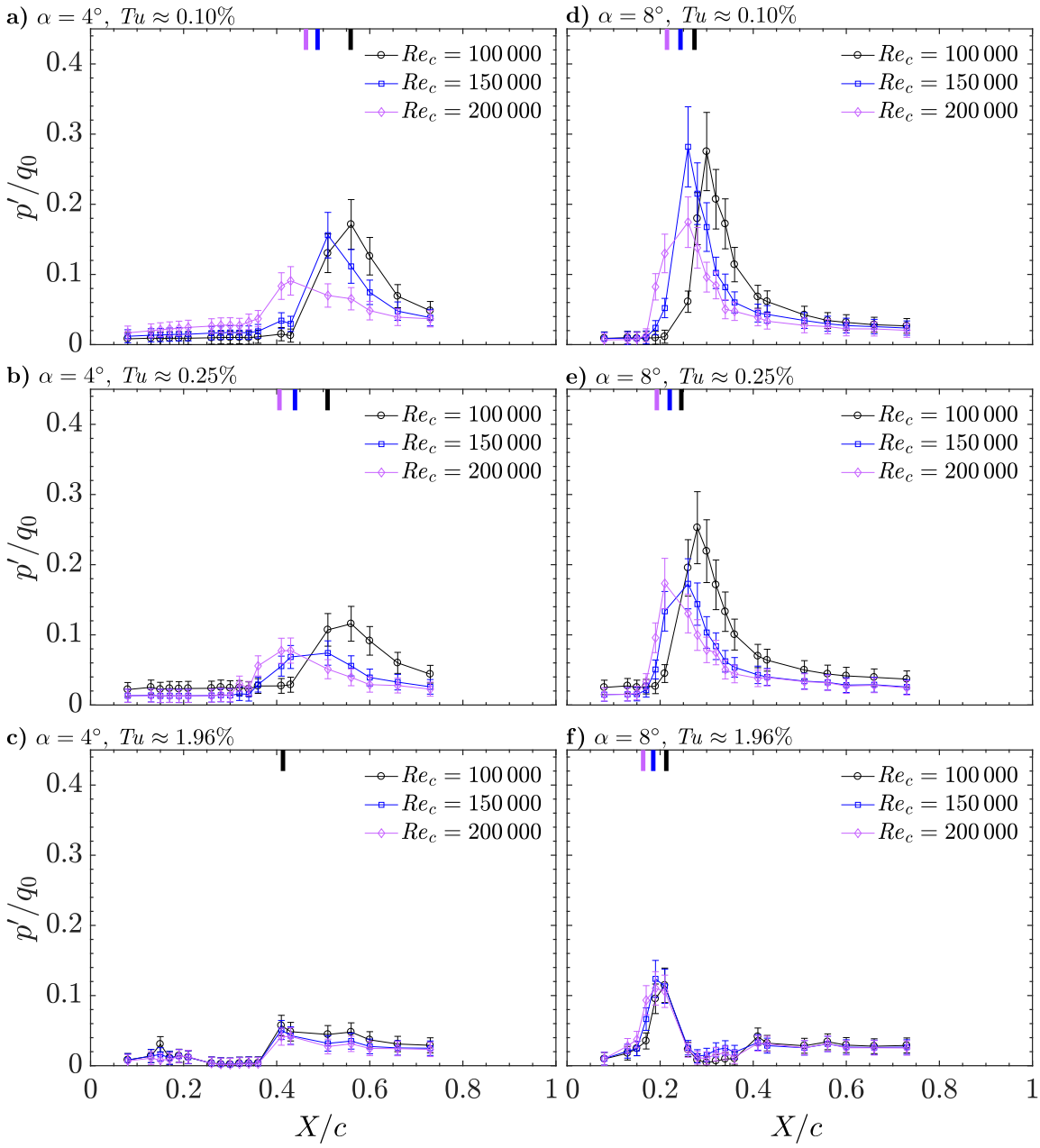

Figure 4.14: Distributions of the root-mean-square of fluctuating surface pressures. Thick lines, coloured according to the legend, indicate mean transition locations as determined from the mean surface pressure distributions.

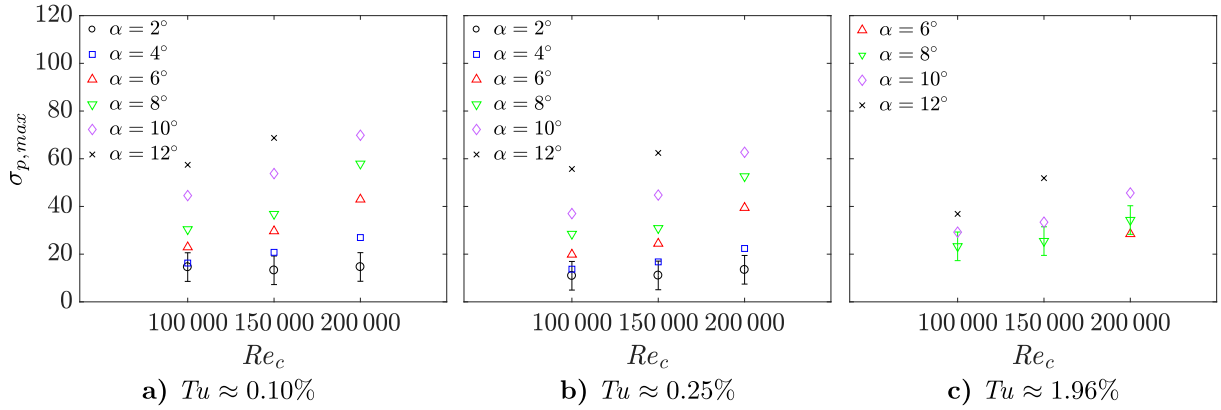

Figure 4.15: Maximum spatial amplification factors. Representative error bars are shown for a single angle of attack.

advancement of mean transition, increasing Re_c achieves this by decreasing flow stability (*i.e.*„ increasing amplification rates) while increasing Tu leads to a more stable bubble (*i.e.*„ decreased amplification rates) and achieves the upstream shift in mean transition through an increase in the initial amplitude of perturbations supplied to the separated shear layer. Therefore, although there is an 'effective' analogy between the two parameters with respect to their influence on mean surface pressure distributions and separation bubble length [9], the underlying separated shear layer transition characteristics differ significantly.

It is instructive to consider the effects of increasing Tu and Re_c on the frequency content of the separated shear layer disturbances. Spectra of the fluctuating surface pressure measurements were computed using Welch's method [155], with a resulting frequency resolution of 2.4 Hz. Example spectra for all Tu levels investigated and for several streamwise measurement locations are shown in Fig. 4.16 for $\alpha = 4°$ and 8° for $Re_c = 100\,000$ and $Re_c = 150\,000$. All frequencies have been non-dimensionalized into a chord based Strouhal number. In general, the spectra show that downstream of the approximate location of mean separation, disturbances are amplified within a band of unstable frequencies, ΔSt, centered on some central frequency, St_0. Downstream of mean transition, the energy content is re-distributed to a broader range of frequencies, and the spectra downstream of mean reattachment resemble those typical of a turbulent flow. As the level of Tu is increased, the detectable band of unstable frequencies broadens. This is a result of the more significant energy content present over a broader range of relevant frequencies in the free-stream at the higher Tu levels (Fig. 3.3), which leads to earlier detectable amplitudes of fluctuations over a broader range of frequencies in the separated shear layer. That is to say, no new

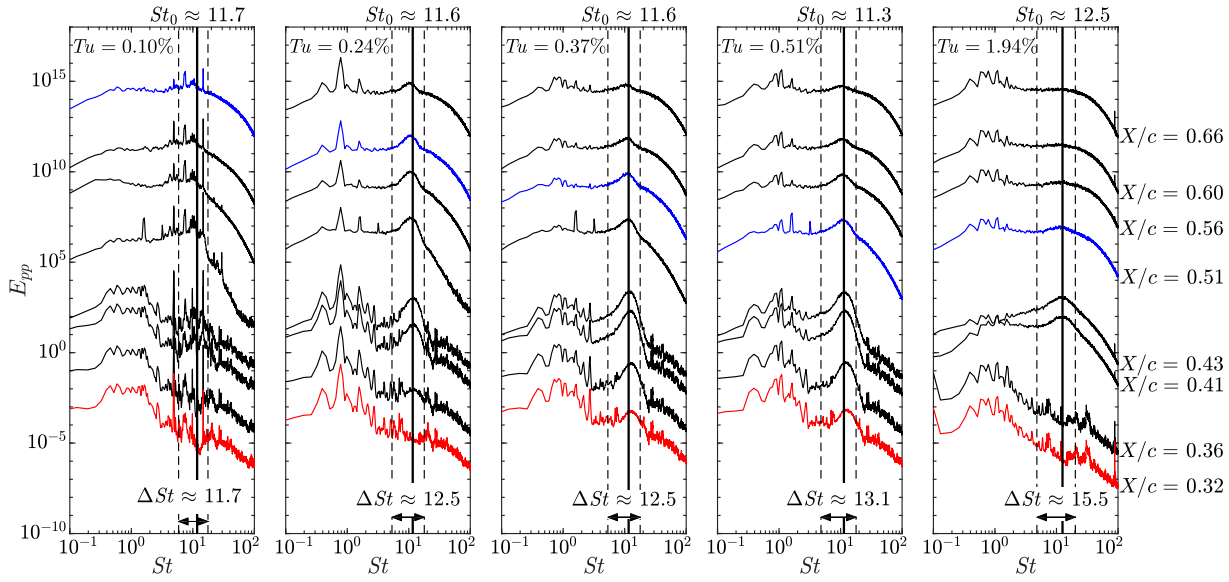

(a) $\alpha = 4°$

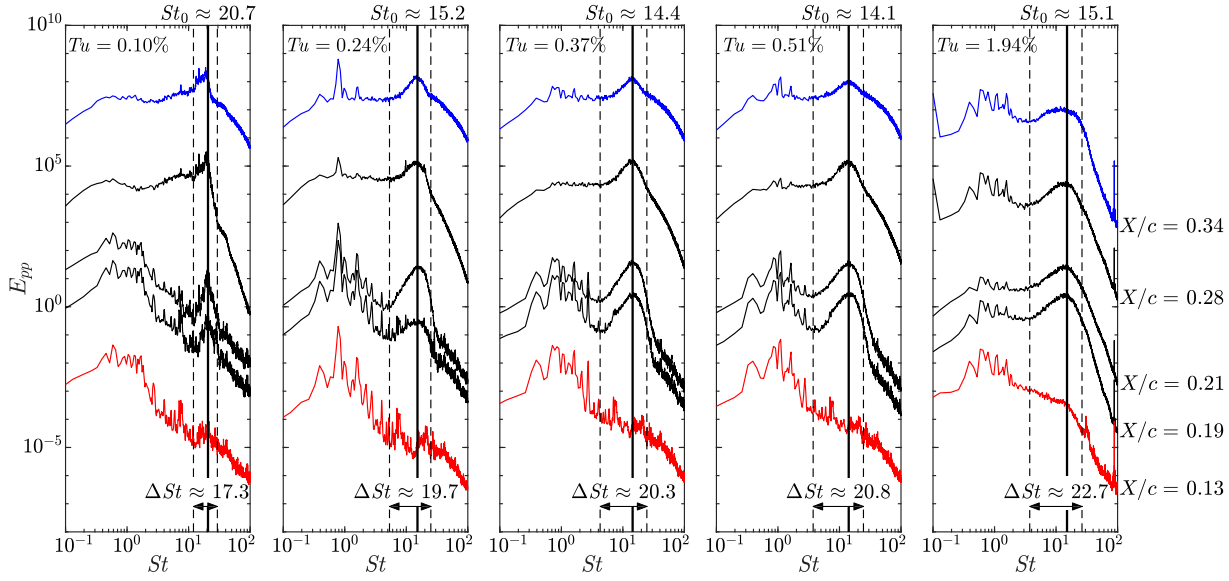

(b) $\alpha = 8°$

Figure 4.16: Spectra of fluctuating surface pressures at $Re_c = 100\,000$. All spectra are normalized by the total energy and stepped by an order of magnitude proportional to their chordwise position. Red and blue spectra indicate the approximate locations of mean separation and reattachment for each case, respectively.

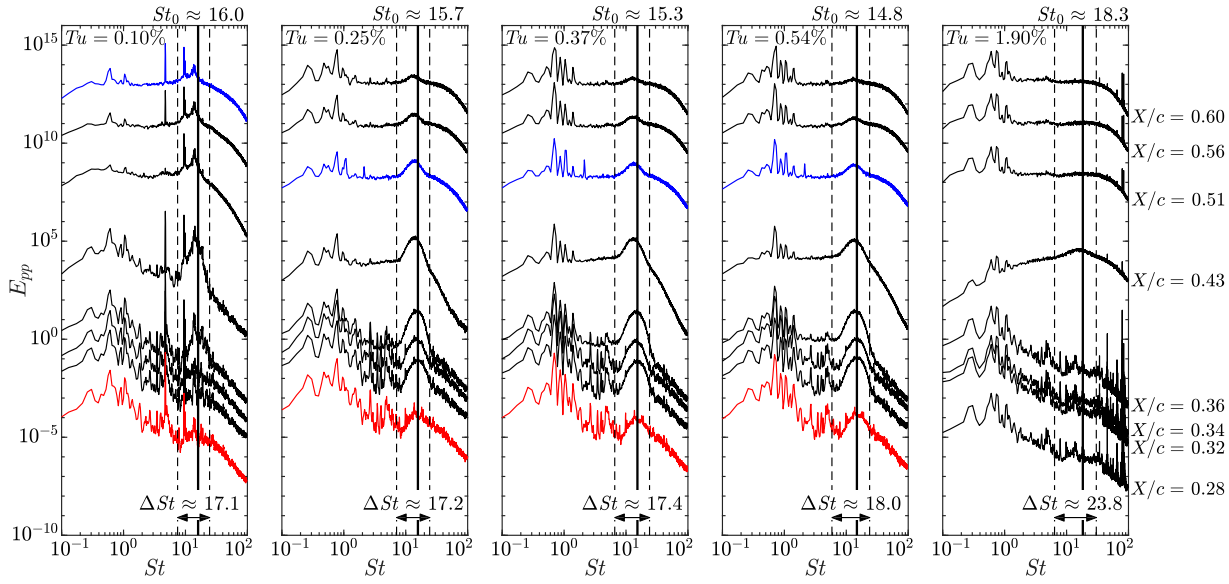

(c) $\alpha = 4°$

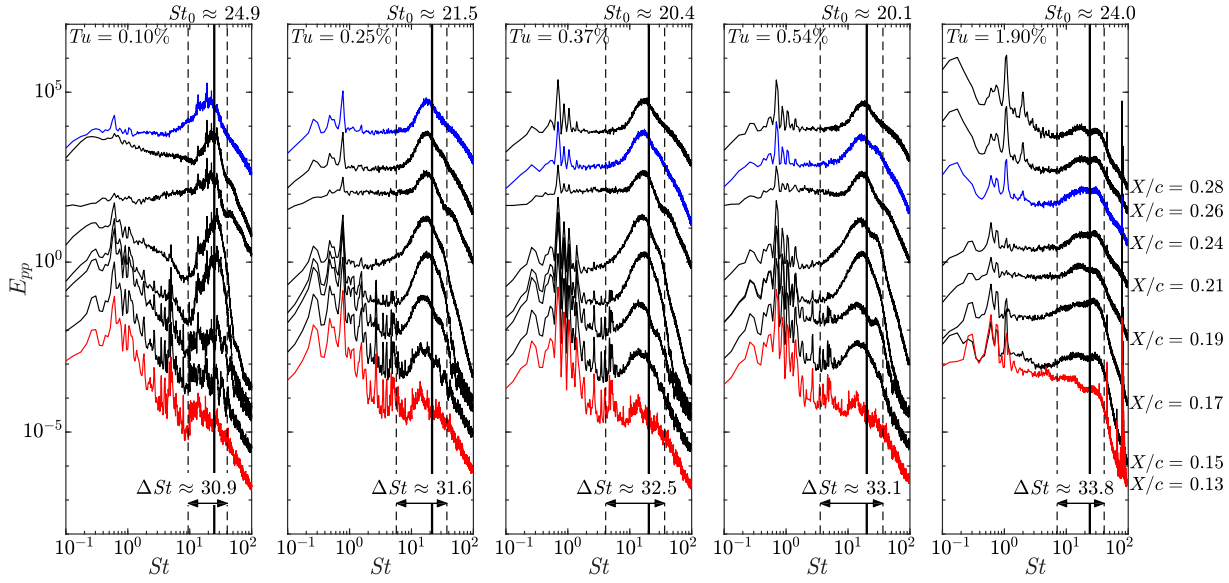

(d) $\alpha = 8°$

Figure 4.16 (cont.): Spectra of fluctuating surface pressures at $Re_c = 150\,000$. All spectra are normalized by the total energy and stepped by an order of magnitude proportional to their chordwise position. Red and blue spectra indicate the approximate locations of mean separation and reattachment for each case, respectively.

frequencies are introduced into the flow by the turbulence generating grids, but, due to their higher initial amplitudes more frequencies grow to a detectable level in the separated shear layer at the elevated levels of Tu.

The central disturbance frequencies, St_0, were estimated for several of the cases investigated in order to identify trends in the most unstable frequency of the separation bubble with increasing Tu. Even for cases where a separation bubble could not be identified (*i.e.*, $Re_c \geq 150\,000$ and the highest level of Tu investigated) a distinct band of amplified frequencies could still be identified and thus the central disturbance frequencies were recorded. The results are summarized in Fig. 4.17. For a given Tu level, the central disturbance

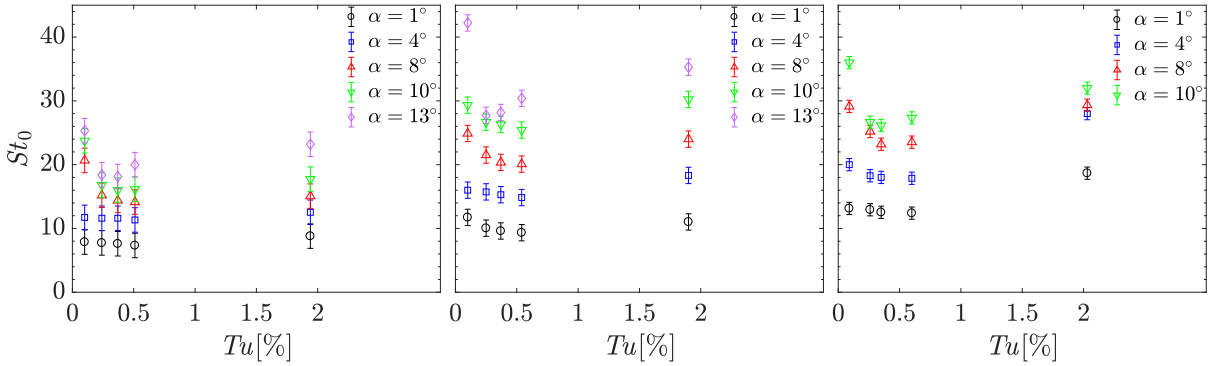

Figure 4.17: Central disturbance frequencies.

frequency increases with increases in either angle of attack or chord Reynolds number, consistent with the investigation of Boutilier and Yarusevych [10]. At low angles of attack ($\alpha \leq 4°$), the central disturbance frequency does not change significantly for $Tu \lesssim 0.60\%$ despite the large changes in mean bubble topology (Fig. 4.6), consistent with a lower effect of mean flow deformation on the frequency of the most amplified perutrbations as compared to the effect on growth rates as reported byYarusevych and Kotsonis [24] and Marxen and Rist [43]. At pre-stall angles of attack, St_0 initially decreases when Tu is increased above the baseline level, but then increases at the higher Tu levels investigated. These variations in the frequency of the most amplified disturbance increase with increasing angle of attack. The initial decrease in St_0 with increasing Tu is in line with the expected moderate decrease with decreasing bubble size, as shown by Yarusevych and Kotsonis [24] and Marxen and Rist [43] using linear stability calculations. However, the following increase in the frequency of the most amplified disturbance for higher Tu levels ($Tu \gtrsim 0.50\%$) does

not conform to the trend expected from linear stability considerations [24, 43], which hints at possible changes in the nature of the transition process. In a simulation of separation bubbles induced on a flat plate by an adverse pressure gradient at similarly high free-stream turbulence intensities, McAuliffe and Yaras [16] observed streamwise oriented streaks in the boundary layer upstream of the separation bubble. These streaks significantly altered the bubble development downstream as well as the separated shear layer transition process, as compared to the lower Tu level case they investigated. Similar streamwise oriented streaks have also been observed in boundary layer transition over flat plates subjected to high levels of free-stream turbulence intensity both experimentally [92, 94, 95] and numerically [87–90]. Evidence of these streamwise streaks is indeed observed at the highest level of Tu investigated here, and will be shown in the following chapter.

Chapter 5

Free-stream Turbulence Intensity Effects on Separation Bubble Flow Development

The objective of this chapter is to examine the effects of free-stream turbulence intensity on the spatio-temporal flow development within a laminar separation bubble. While the previous chapter presented trends in transition characteristics with increasing Reynolds number, angle of attack, and free-stream turbulence intensity, the present chapter presents a more detailed description of the transition process in a separation bubble formed over the suction side of the same NACA 0018 airfoil model. Particle Image Velocimetry (PIV) is employed in two configurations in order to assess the streamwise and spanwise flow development for an angle of attack of 4°, chord Reynolds numbers of 80 000 and 125 000, and free-stream turbulence intensities between 0.10% and 1.94%. Mean surface pressure distributions and time-averaged PIV fields are used to assess changes in mean bubble topology (Section 5.1), while time-resolved PIV measurements are used to describe separation bubble dynamics in the streamwise (Section 5.2) and spanwise (Section 5.3) directions.

5.1 Mean Bubble Topology

Although the effects of free-stream turbulence intensity on mean bubble topology were discussed in Chapter 4, it is worthwhile to compare mean bubble topology as measured using Particle Image Velocimetry (PIV) to that as determined from mean surface pressure

distributions. PIV offers a direct measurement of the separation bubble, while estimates from mean surface pressure distributions are an indirect method, though both methods have their own associated challenges and uncertainties. Mean surface pressure distributions for both Reynolds numbers and all levels of Tu investigated are shown in Fig. 5.1. It should be noted that these pressure distributions have been transformed into the surface attached coordinate system (see Fig. 3.6a) in order to be readily compared to the following PIV results. As discussed in the previous chapter, the presence of a separation bubble on the

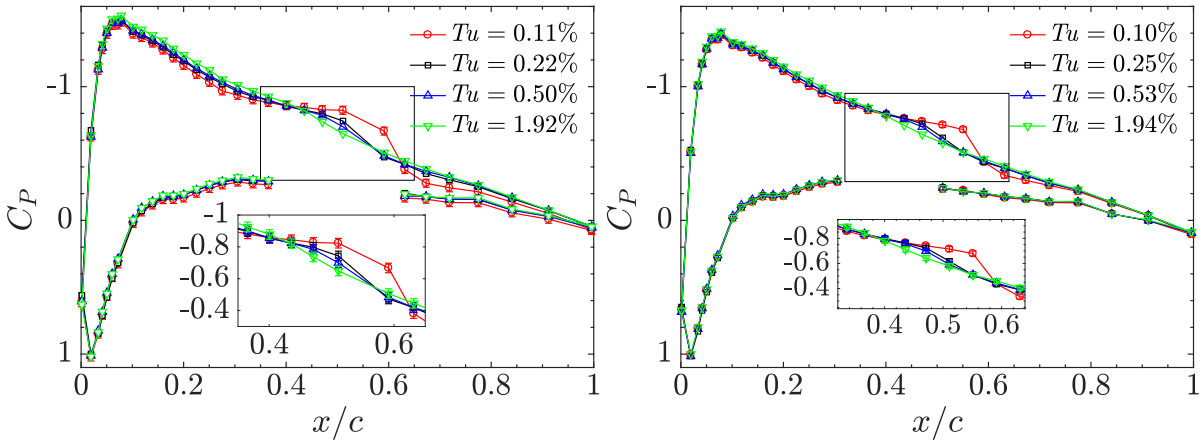

(a) $Re_c = 80\,000$ **(b)** $Re_c = 125\,000$

Figure 5.1: Mean surface pressure distributions for $\alpha = 4°$. Data points corresponding to the location of the pressure side boundary layer trip have been removed.

suction side is characterized by a pressure plateau downstream of the suction peak, with bubbles identifiable in the range of $0.3 \lesssim x/c \lesssim 0.7$ for both Reynolds numbers presented in Fig. 5.1. Following the same method used in the previous chapter (*i.e.*, Fig. 4.4), the locations of mean separation, transition, and reattachment were determined for all cases investigated and are summarized in Table 5.1. For $Re_c = 125\,000$ and the highest level of Tu investigated, a separation bubble could not be identified from the surface pressure distributions. Since the level of Tu varies slightly across the investigated chord Reynolds numbers, the averaged value for a given turbulence generating grid is used to compare the results. The results for a given chord Reynolds number show that while there is no significant influence of Tu on the mean separation location, both the mean transition and reattachment locations shift upstream with increasing Tu, resulting in shorter separation bubble lengths, consistent with the results presented in the previous chapter. Further, comparing the results for a given level of turbulence intensity, the bubble shifts upstream

Table 5.1: Summary of mean bubble topology as determined from mean surface pressure distributions.

	$Re_c = 80\,000$				$Re_c = 125\,000$			
Tu [%]	x_S/c^1	x_T/c^1	x_R/c^1	ℓ/c^2	x_S/c^1	x_T/c^1	x_R/c^1	ℓ/c^2
≈ 0.11	0.32	0.57	0.64	0.32	0.31	0.54	0.62	0.31
≈ 0.24	0.32	0.50	0.60	0.28	0.31	0.47	0.57	0.26
≈ 0.52	0.32	0.47	0.59	0.27	0.31	0.46	0.54	0.23
≈ 1.93	0.30	0.42	0.55	0.25	-	-	-	-

[1] Uncertainty is ± 0.02
[2] Uncertainty is ± 0.03

slightly and decreases in length with increasing chord Reynolds number, consistent with the previous chapter and previous investigations [10]. Since the investigated angle of attack is relatively low and the bubble forms over the aft portion of the airfoil, the decrease in separation bubble length with increasing Tu has no notable effect on the magnitude of the suction peak (Fig. 5.1).

In order to determine mean bubble topology from the PIV measurements, contours of mean streamwise velocity, as measured with the low-speed system, are presented in Fig. 5.2 for both Reynolds numbers and all turbulence intensity cases investigated. The vector fields have been transformed into the surface attached coordinate system as defined in Fig. 3.6a. At the baseline Tu level and both chord Reynolds numbers investigated, the results show a relatively large, elongated region of reverse flow adjacent to the airfoil surface, identifying the presence of a separation bubble. The thick black line traces the contour of zero mean velocity, outlining the time-averaged structure of the separation bubble. The upstream and downstream intersections of this line with the airfoil surface represent the locations of mean separation and reattachment, as shown by the square and diamond markers, respectively. At $Re_c = 80\,000$ (Fig. 5.2a), as the level of Tu is increased the length of the separation bubble is decreased, resulting from a downstream shift in the location of mean separation and an upstream shift in mean reattachment. At the highest level of Tu investigated, a reverse flow region can no longer be resolved. However, the topology of the mean streamwise velocity contours is similar to that presented at the lower Tu levels, and thus suggests that a small separation bubble is still present. For all elevated levels of Tu at $Re_c = 125\,000$ (Fig. 5.2b), a reverse flow region indicative of a separation bubble cannot be resolved. However, for these cases the topology of the velocity contours again suggest that a small separation bubble may still be present, and is supported by the estimation of a separation bubble

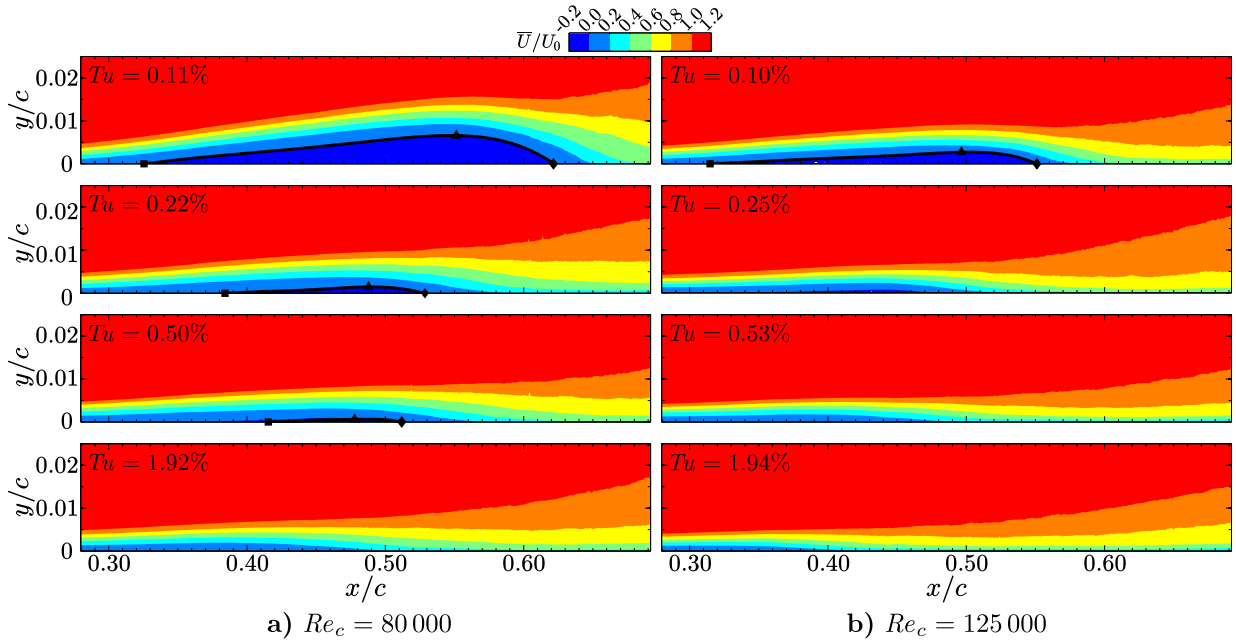

Figure 5.2: Contours of mean streamwise velocity for all levels of Tu investigated.

for $Tu = 0.25\%$ and 0.53% using the mean surface pressure distributions (Fig. 5.1b). A discussion of integral boundary layer parameters later in this section will provide further evidence of a separation bubble for the cases where a reverse flow region is not resolved.

Determining the location of mean transition from PIV measurements is not as clear as determining the locations of mean separation and reattachment, as there have been a couple of methods proposed in the literature. Some investigators cite the location of mean transition to be the streamwise location at which the Reynolds stress reaches $0.001U_0^2$ [31–33], while others use the location at which velocity fluctuation growth deviates from an exponential trend [47]. An additional definition, which is utilized in the present investigation, is to cite the location of mean transition as the streamwise location at which the boundary layer displacement thickness reaches a maximum [15]. This location is shown by the triangular markers in Fig. 5.2 for cases where a reverse flow region is identified, though it can also be determined for cases for which a reverse flow region is not identified, and will be discussed later. Similarly to the results presented in the previous chapter, and those in Table 5.1 based on estimates from mean surface pressure distributions, the location of mean transition shifts upstream with increasing Tu (Fig. 5.2a), leading to the upstream shift in mean reattachment. A summary of mean bubble topology as determined from the

PIV measurements is provided in Table 5.2. The results show that for cases where a reverse flow region is not identified in the mean fields (Fig. 5.2), the location of mean transition continues to shift upstream with increasing Tu, highlighting its importance to the flow over the suction side of the airfoil.

Table 5.2: Summary of mean bubble topology as determined from the low-speed PIV measurements.

	Tu [%]	x_S/c	x_T/c	x_R/c	ℓ/c
$Re_c = 80\,000$	0.11	0.33 ± 0.09	0.55 ± 0.01	0.62 ± 0.01	0.31 ± 0.1
	0.22	0.38 ± 0.09	0.49 ± 0.01	0.53 ± 0.02	0.15 ± 0.1
	0.50	0.42 ± 0.1	0.48 ± 0.01	0.51 ± 0.02	0.09 ± 0.1
	1.92	-	0.41 ± 0.01	-	-
$Re_c = 125\,000$	0.10	0.31 ± 0.07	0.50 ± 0.01	0.55 ± 0.01	0.24 ± 0.07
	0.25	-	0.44 ± 0.01	-	-
	0.53	-	0.40 ± 0.01	-	-
	1.94	-	0.35 ± 0.01	-	-

A comparison of mean bubble topology as determined from estimates using mean surface pressure distributions as well as PIV measurements is shown in Fig. 5.3 for $Re_c = 80\,000$. Since a separation bubble is only resolved at the baseline Tu level at $Re_c = 125\,000$ using the PIV measurements, the present discussion is focused solely on the results for $Re_c = 80\,000$. The results in Fig. 5.3a show that at the baseline Tu level, the estimates of mean bubble topology as determined from the mean surface pressure distributions and PIV measurements are in good agreement, resulting in similar estimates of separation bubble length (Fig. 5.3b). As the level of Tu is increased, the agreement of mean bubble topology as determined from each measurement technique deteriorates. For example, when the level of free-stream turbulence intensity is increased from the baseline level to $Tu = 0.50\%$, the PIV measurements show a downstream shift of $0.09c$ in the location mean separation, whereas the estimates of mean separation from the surface pressure distributions show no measurable effect on the location of mean separation. Both methods predict an upstream shift in the location of mean reattachment for the same increase in Tu, but the PIV measurements estimate an upstream shift of $0.11c$, while the surface pressure measurements estimate an upstream shift of $0.05c$. In all, the agreement of mean separation and reattachment locations is within 6% of the estimated bubble length ($0.02c$) at the baseline Tu level, whereas at $Tu = 0.50\%$ differences of up to the bubble length (*i.e.*, the length predicted by

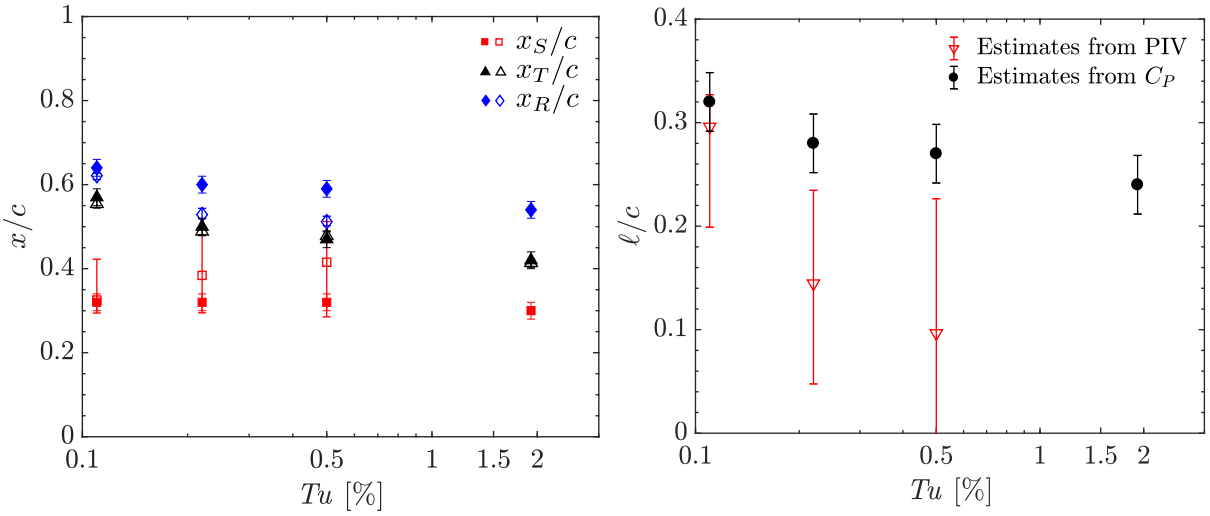

(a) Mean separation bubble topology

(b) Mean separation bubble length

Figure 5.3: Summary of mean bubble topology. Open symbols correspond to results obtained from PIV measurements while filled symbols correspond to results from the mean surface pressure distributions.

the PIV measurements) are observed.

The relatively smaller changes in mean separation and reattachment determined using estimates based on the surface pressure distributions as compared to the PIV measurements result in notable larger estimates of bubble length, as shown in Fig. 5.3b. These differences are to be expected as the uncertainty in each of the estimation methods of bubble topology increases as the level of Tu is increased and the bubble size decreases. On the other hand, the locations of mean transition as determined using each method remain in good agreement for all levels of Tu investigated. This is a result of the well defined location of mean transition in the mean surface pressure distributions (Fig. 5.1) and that the estimate from the PIV measurements is based on an integral boundary layer parameter, namely the streamwise location of the maximum displacement thickness.

As the level of Tu is increased, the separation bubble size decreases, as shown by both methods in Fig. 5.3b. This decrease in bubble size poses two significant challenges in estimating mean separation bubble topology using either PIV measurements or mean surface pressure distributions. First, the decrease in bubble size with the fixed spatial resolutions of the two methods (velocity vectors in the PIV measurements and the number of pressure taps for the pressure based estimates) means that fewer measurements will be within the separation bubble, thus increasing uncertainty in determining mean bubble

topology. Second, the decrease in bubble size is accompanied by a decreased effect on the mean surface pressure distribution (Fig. 5.1), as well as lower reverse flow velocities within the separation bubble, and thus measurement uncertainty has an increasing effect on the determination of mean bubble topology as the bubble length decreases. The uncertainty in the surface pressure based estimates is particularly affected by the decrease in the effect of the bubble on the mean surface pressure distribution. Since the method of determining mean bubble topology relies on finding the intersections of the lines used to estimate the pressure distribution around the location of the pressure plateau, as the bubble size decreases with increasing Tu and the slopes of the lines become more similar, their intersection locations become less defined. In fact, it is this issue which prevents a bubble from being detected at the highest Tu level for $Re_c = 125\,000$ (Fig. 5.1b). The uncertainty in the PIV estimate of separation is relatively large since the reverse flow velocities near separation are small, and thus the estimate of the zero velocity contour is significantly impacted by the PIV uncertainty. Additionally, the wall-normal resolution of the measurements results in fewer vectors falling within the separation bubble, thus posing a challenge in estimating the zero velocity contour. Both of these issues are discussed by Olson *et al.* [34], who attempt to determine the mean separation location of a separation bubble formed over an airfoil using molecular tagging velocimetry. At reattachment, both issues are still present but the reverse flow velocities are generally much greater and the bubble thicker, so the uncertainty in the estimate of mean reattachment is smaller as compared to that of mean separation.

A comparison of mean bubble topology using the two methods discussed here is also shown by Kurelek and Yarusevych [166]. In their investigation, acoustic excitation was used to excite a separation bubble formed over the same airfoil used in the present investigation, resulting in a decrease in separation bubble size. The authors noted that the decrease in bubble size was a result of a downstream shift in mean separation and an upstream shift in mean reattachment, similar to the results presented here. Similarly to the present results, Kurelek and Yarusevych [166] noted that these shifts were much more significant when estimated using the zero velocity contour line measured using PIV as compared to that estimated from mean surface pressure distributions. In fact, no change in the separation location could be detected in their investigation with the mean surface pressure distributions, despite a downstream shift in mean separation of about $0.03c$ measured with the PIV estimates. This is similar to the downstream shift in mean separation measured here using PIV at $Re_c = 80\,000$ when Tu is increased from 0.11% to 0.22% (Table 5.2) with no change noted in the estimates from the mean surface pressure distributions (Table 5.1). Since the PIV results provide a direct measurement of mean bubble topology and are related to the results which will be presented throughout the remainder of this chapter, the estimates of the mean bubble topology from the PIV measurements will be used herein.

In the discussion of Fig. 5.2, it was suggested that a bubble forms for the highest level of Tu at $Re_c = 80\,000$, and for $Tu \geq 0.25\%$ at $Re_c = 125\,000$, despite no reverse flow region being resolved in the PIV measurements. To provide some quantitative evidence of the formation of a separation bubble, an analysis of integral boundary layer parameters is performed, with the displacement thickness, δ^*, momentum thickness, θ, and shape factor, H, shown in Fig. 5.4, for both chord Reynolds numbers investigated. At the baseline Tu

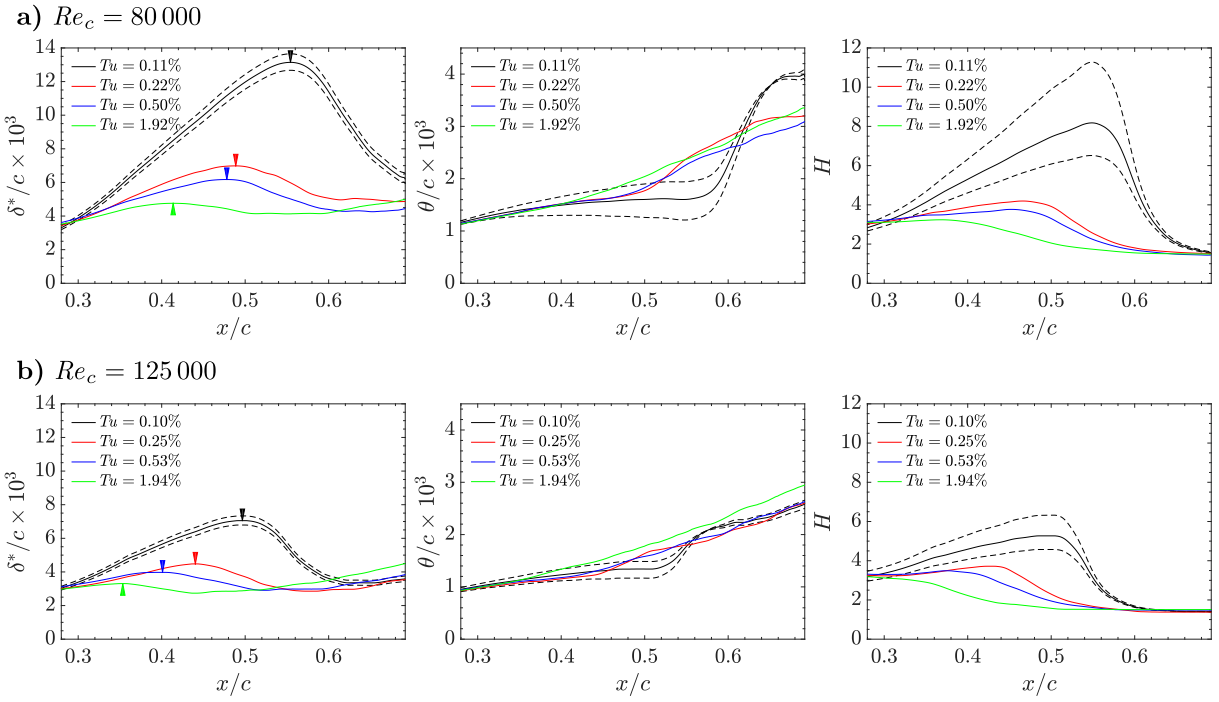

Figure 5.4: Boundary layer parameters. Dashed lines indicate uncertainty bounds for the baseline Tu level.

level for both Reynolds numbers investigated, the displacement thickness increases within $0.29 \lesssim x/c \lesssim 0.55$ (*i.e.*, the fore portion of the separation bubble as shown in Fig. 5.2a), reaches a peak, and subsequently decreases. The initial increase is the result of the increasing wall-normal extent of the separated region, while the subsequent decrease occurs due to the redirection of the mean flow towards the wall as a result of the laminar-to-turbulent transition process in the separated shear layer. The streamwise location of the peaks in the displacement thickness, previously used in identifying the locations of mean transition (Fig. 5.2), are shown by the arrowheads.

The streamwise locaion of the peak in δ^* coincides with the streamwise location at which the momentum thickness begins to grow more rapidly, and thus with the peak in shape factor which is the ratio of the two parameters (*i.e.*, $H = \delta^*/\theta$). The rapid increase in the momentum thickness indicates a rapid rise in skin friction in the aft portion and downstream of the separation bubble, and is evidenced by the large wall-normal gradients in mean streamwise velocity downstream of the separation bubble location (Fig. 5.2). As the level of free-stream turbulence intensity is increased, the streamwise location of the peak in the displacement thickness and shape factor shifts upstream, and decreases in magnitude. The upstream shift was seen previously as the peaks in δ^* were used to determine the locations of mean transition (Fig. 5.2), while the decrease in the magnitude of these variables is the result of the decreased vertical vertical extent of the separation bubble with increasing Tu (Fig. 5.2). For all cases examined, the shape factor at the most upstream location is approximately $H = 3$, similar to the value of 2.59 expected for a laminar flat-plate boundary layer [65], implying that the flow upstream of separation is in a laminar state. As the flow undergoes transition to turbulence, a turbulent boundary layer develops and is evidenced by the asymptotic levelling of the shape factor towards a value of 1.6 for all cases examined, similar to the range of 1.3-1.4 expected for a turbulent flat-plate boundary layer [65].

The similarity of the trends across all Tu levels at $Re_c = 80\,000$ suggests that a separation bubble does form over the suction side of the airfoil for $Tu = 1.92\%$. At $Re_c = 125\,000$, the conclusion for the highest level of Tu investigated is less clear. While there is a discernible peak in the displacement thickness, it is much less distinct than at the lower levels of Tu or even at the highest level of Tu for the lower Reynolds number investigated. Further, the momentum thickness increases at an elevated rate (as compared to the other Tu levels) from the most upstream location of the PIV measurements, which results in no discernible peak in the shape factor, as the shape factor decreases within the entire measurement region for this flow condition. The conclusion then is that transition certainly occurs for these flow conditions, as indicated by the shape factor transitioning between values expected for a laminar and turbulent boundary layer, and that a small separation bubble is likely forming. However, the formed separation bubble is so small as to be almost inconsequential to the mean surface pressure distribution (Fig. 5.1b), and the results in Sections 5.2 and 5.3 will show that the dynamics of the transition process have been altered significantly for these flow conditions.

It is of interest to note that the streamwise location of mean transition at $Re_c = 80\,000$ seems to exhibit an exponential relation with Tu, as can be seen from the semi-log plot in Fig. 5.3a. Further, for the PIV results, similar relations also seem to hold for the locations of mean separation and reattachment, a finding which has also been oberved in earlier studies [24, 44]. By applying controlled disturbances to a laminar separation

bubble, Yarusevych and Kotsonis [24] and Marxen and Henningson [44] showed that the resulting mean bubble deformation tended to follow an exponential relation with increasing amplitude of disturbances. However, if such relations were to hold for the mean separation and reattachment locations in the present investigation, and hence the separation bubble length, the PIV results show that no separation bubble would form for $Tu \gtrsim 1\%$. At the same time, the discussion of the boundary layer parameters put forth clear evidence of a separation bubble forming for $Re_c = 80\,000$ and $Tu = 1.92\%$. If applied to the locations of mean separation and reattachment as determined from the mean surface pressure distributions, the relations suggest the formation of separation bubbles at unreasonably large levels of Tu, likely a result of the method not being sensitive enough to changes in the relatively small separation bubbles at the higher Tu levels (Fig. 5.3a). These observations suggest that, while the exponential dependence of mean transition on Tu seems to hold over the entire range of Tu investigated here, such a trend does not hold for the separation and/or reattachment locations at higher levels of free-stream turbulence intensity. It is speculated from the results presented in Fig. 5.3a that the actual downstream shift in the location of mean separation with increasing Tu should be smaller than that which is determined from the PIV measurements.

Reviewing relevant work in the literature seems to support this speculation. In other experimental studies performed over an airfoil, a downstream shift in the location of mean separation is observed with increasing Tu [31, 33, 34] but the shift is generally much less significant than shown here. Specifically, using molecular tagging velocimetry with a higher resolution in determining the location of mean separation, Olson *et al.* [34] note a downstream shift in the location of mean separation of 3% of the chord for a 0.6% increase in Tu as compared to a downstream shift of approximately 9% of the chord length observed in the present investigation when Tu is increased from 0.11% to 0.50%. Interestingly, in both numerical [16] and experimental [37, 38] studies of separation bubbles formed over a flat plate and subjected to increasing levels of Tu, little-to-no variation in the location of mean separation is observed. This result is highlighted in the work of Lardeau *et al.* [37] who simulated a separation bubble both on a flat plate with an imposed adverse pressure gradient as well as a compressor blade and subjected both to elevated levels of Tu. The authors only noted a downstream shift in mean separation over the compressor blade whereas the location of mean separation over the flat plate remained constant with the increase in Tu. The indication here is that the downstream shift in the location of mean separation with increasing Tu may have some dependence on the global pressure distribution around the airfoil which is eliminated in flat plate studies.

5.2 Streamwise Flow Development

The results presented in the previous section supported the findings of the previous chapter, showing that the reduction in separation bubble length with increasing Tu is largely due to an upstream shift in the location of mean transition, which leads to an upstream shift in mean reattachment. The current section examines the streamwise flow development within the separation bubble, with the aim of describing the effects of increasing Tu on separation bubble flow dynamics, as well as the transition process within the separated shear layer. Results will be presented from both the low-speed and high-speed PIV systems in the surface attached coordinate system defined in Fig. 3.6a.

The effects of Tu on the flow development within a laminar separation bubble are first examined via time-averaged statistics of the velocity fluctuations as measured with the low-speed PIV system, shown in Fig. 5.5. At the baseline Tu level and both Reynolds numbers investigated, the contours of u' show three distinct peaks (Figs. 5.5a and 5.5b), consistent with previous investigations of transition over an airfoil at low Reynolds numbers in a low disturbance environment [15]. The location of the middle peak agrees well with the wall-normal location of the displacement thickness, which is also approximately the wall-normal location of the core of the separated shear layer. The outer peak agrees well with the boundary layer thickness, while the inner peak remains within the height of the separation bubble, consistent with the discussion presented by Dovgal *et al.* [50]. In contrast, the contours of v' exhibit only a single peak near the wall-normal location of the displacement thickness, which is associated with the shear layer roll-up vortices [18, 31]. The same topology persists in both the u' and v' contours when the level of Tu is increased to the first two elevated levels investigated (*i.e.*, $Tu \leq 0.50\%$) at $Re_c = 80\,000$, and for the first elevated Tu level (*i.e.*, $Tu = 0.25\%$) for $Re_c = 125\,000$.

At the highest level of Tu investigated, the topology of the u' contours in Fig. 5.5 is altered significantly for both Reynolds numbers investigated. For these flow conditions, there are significant velocity fluctuations at the most upstream location of the PIV field-of-view. The implication is that there are significant velocity fluctuations in the streamwise direction present in the boundary layer upstream of the PIV field-of-view, and therefore upstream of the location at which a separation bubble likely forms for these flow conditions. These contours are similar to the contours of $\overline{uu}$ presented by McAuliffe and Yaras [16] who modeled a separation bubble induced on a flat plate at levels of Tu comparable to the highest level investigated here. The authors linked the large fluctuations to streamwise oriented streaks originating in the boundary layer upstream of the separation bubble. The formation of these streaks will be discussed again later in this section as well as in Section 5.3.

For a given Reynolds number, the results in Fig. 5.5 show that both u' and v' generally

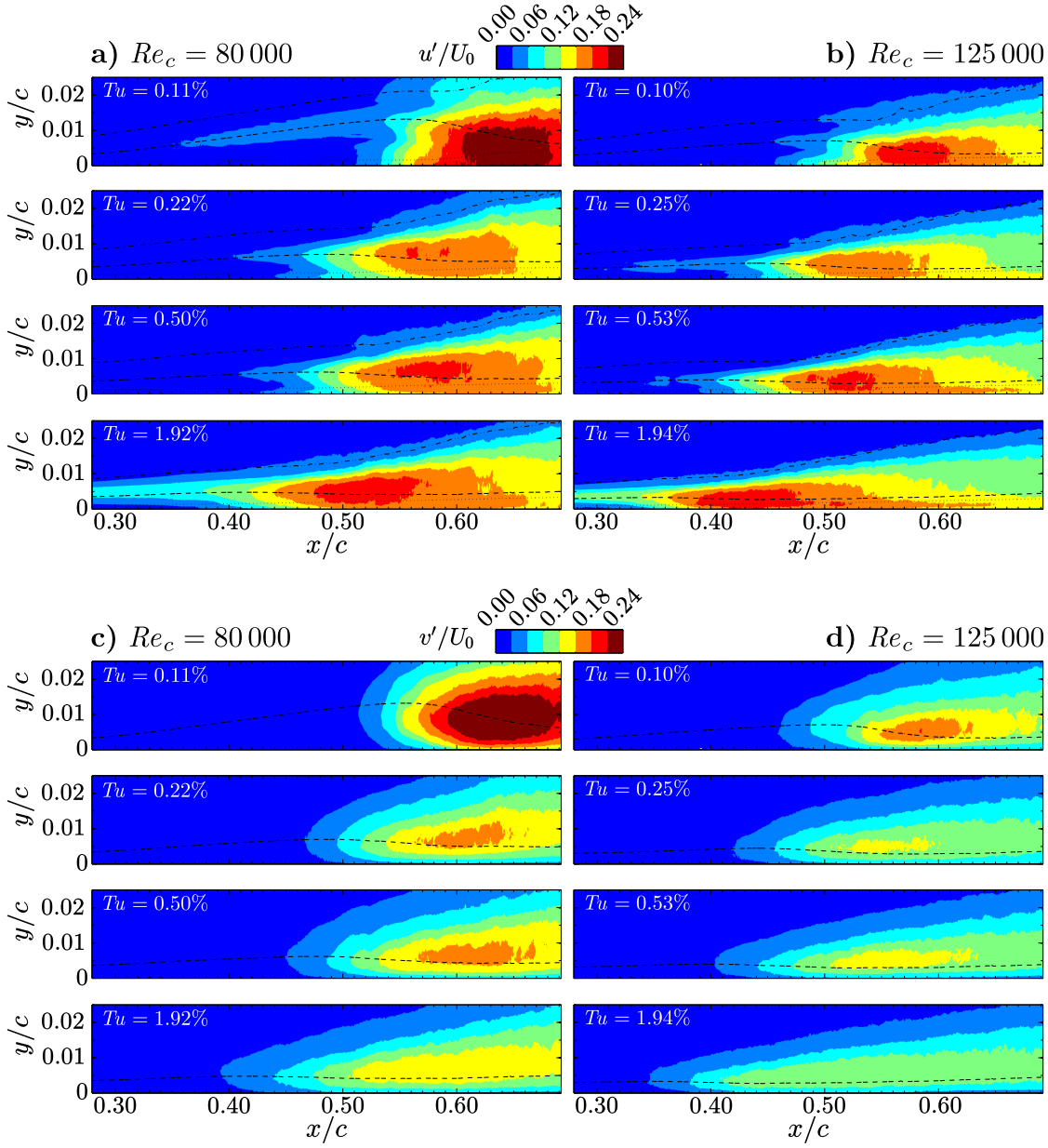

Figure 5.5: Contours of the root-mean-square of (a),(b) streamwise and (c),(d) wall-normal velocity fluctuations. Dashed lines indicate the boundary layer displacement thickness while the dotted and dotted-dashed lines indicate the momentum thickness and boundary layer thickness, respectively.

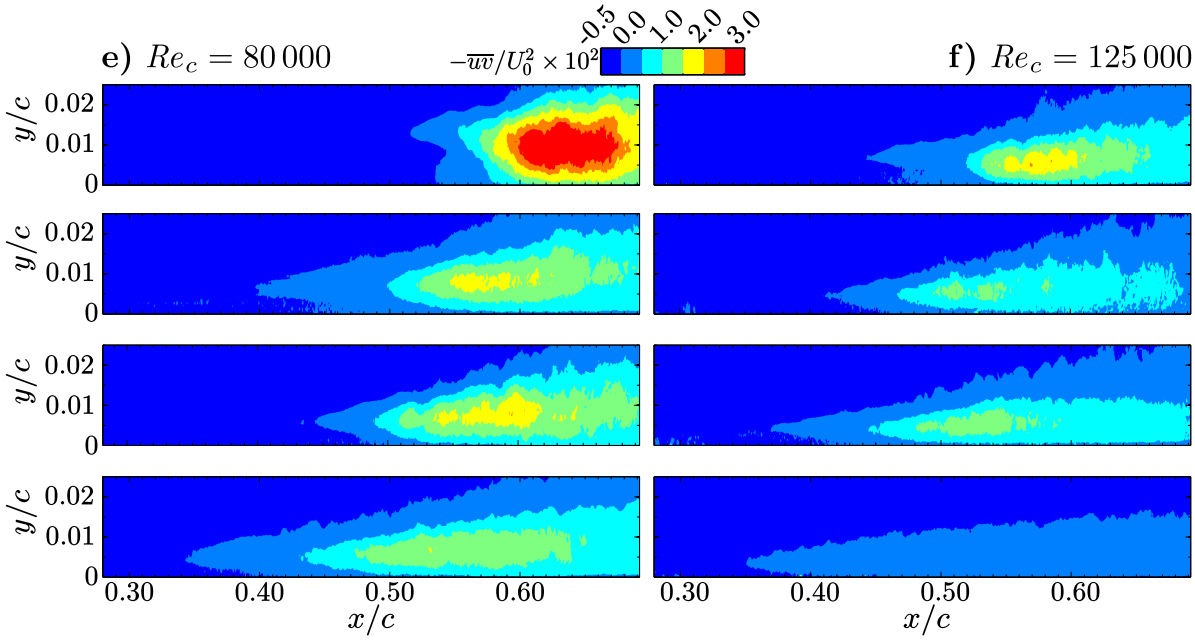

Figure 5.5 (cont.): Contours of Reynolds shear stress.

reach higher amplitudes earlier upstream with increasing Tu. This is best seen by locating the upstream extent of the green coloured contour (*i.e.*, the fourth contour level representing $0.12 \leq u'/U_0 \leq 0.15$) as this location is generally reflective of the location of mean flow transition (cf. Fig. 5.4). By comparing these locations with increasing Tu, it can be seen that this contour level shifts upstream, thus the larger velocity fluctuations attained earlier upstream ultimately lead to the upstream shift in the location of mean transition (Fig. 5.4). For both Reynolds numbers, the maximum amplitude attained in v' generally decreases as the level of Tu is increased (Figs. 5.5c and 5.5d). This is consistent with the findings of Yarusevych and Kotsonis [24] who attribute decreased wall-normal velocity fluctuations in smaller separation bubbles to the increasing influence of the wall. This result is also in good agreement with the decrease in p'_{max} with increasing Tu observed in the previous chapter.

Contours of the Reynolds stress are shown in Figs. 5.5e and 5.5f. Since the wall-normal gradient in U is positive (Fig. 5.2), the contours of negative Reynolds stress give a measure of the transport of streamwise momentum towards the surface of the airfoil. That is to say, since $\partial\overline{U}/\partial y > 0$, a fluid element at a given point with a negative v' fluctuation will be associated with a positive u' fluctuation as it is moving to a region of lower $\overline{U}$. Similarly, if that fluid element has a positive v' fluctuation, it will be associated with a negative u'

fluctuation as it is moving to a region of higher U. In both cases, when time-averaged, $\overline{u'v'} < 0$ and this quantity represents high-momentum fluid being transported towards the wall (or low-momentum fluid away from the wall). At $Re_c = 80\,000$ and the baseline Tu level, the contours of Reynolds stress show significant amplitudes beginning around the location of mean transition ($x_T/c = 0.55$) and attaining maximum amplitudes just downstream of mean reattachment ($x_R/c = 0.62$). Similar results have been reported in previous investigations [31], and the location of the onset of significant growth of the Reynolds stress as well as the location of the maxima correspond well with the locations of shear layer roll-up and breakdown, respectively. In addition, it is the transport of high momentum fluid towards the airfoil surface induced by the shear layer rollers that has been shown to lead to mean flow reattachment [18]. As the level of Tu is increased, the streamwise location of the onset of the increase in the amplitude of the Reynolds stress shifts upstream, consistent with the locations of mean transition (Fig. 5.2).

At $Re_c = 125\,000$, a similar behaviour of the Reynolds stress amplitudes is observed (Fig. 5.5f), with generally lower maximum amplitudes observed at the higher chord Reynolds number for a given level of Tu. As the maximum wall-normal velocity fluctuation amplitudes decrease with increasing either Tu or Re_c (Figs. 5.5c and 5.5d), so do the maximum amplitudes of the Reynolds stress (Figs. 5.5e and 5.5f). At $Re_c = 125\,000$ and $Tu = 1.94\%$, the contours of Reynolds stress show very small amplitudes across most of the PIV measurement field-of-view, thus indicating that there is very little transport of high streamwise momentum towards the wall. These contours however support the assertion discussed above that a very small separation bubble forms as there is a transport of higher momentum fluid towards the wall, but the small amplitudes suggest that the bubble is very small.

It is of interest to note that, at the baseline Tu level and the lower chord Reynolds number investigated, the contours of u' (Fig. 5.5a) show the presence of small-amplitude fluctuations in the fore portion of the separation bubble which are not seen in v'. Similar results have been noted by previous investigators and are attributed to bubble 'flapping' [30, 32, 48, 133], which is an unsteady up-and-down motion of the separated shear layer. Since the wall-normal gradient in U is large, the small up-and-down motion of the shear layer results in significant temporal variations in U at a given wall-normal location. It is this temporal variation that produces the elevated levels of u' in the fore portion of the separation bubble (Fig. 5.5a). The up-and-down motion is characterized by frequencies significantly lower than those of the dominant disturbances in the separated shear layer, and are also significantly less energetic than the shear layer rollers [30, 133]. This was made clear by Lengani and Simoni [133] who showed that a flow reconstuction using the first two modes of a Proper Orthogonal Decomposition (POD) could not account for the observed bubble

flapping, as the first two modes described the shear layer rollers and thus the flapping must be described by a lower energy mode. When either Tu or Re_c are increased, bubble flapping appears to be suppressed (Figs. 5.5a and 5.5b), supporting previous reports that flapping is confined primarily to low Reynolds number flows with very low disturbance environments [32, 50, 133]. In low disturbance environments, flapping may also be suppressed via artificial forcing of the boundary layer upstream of separation with small amplitude disturbances [47].

To quantify the amplification of disturbances in the separated shear layer, the values of u' and v' along the boundary layer displacement thickness, *i.e.*, the dashed black line in Figs. 5.5a–d, are plotted in Fig. 5.6 for both Reynolds numbers and all levels of Tu investigated. The results show that there is significant amplification of both velocity components within the separation bubble, followed by the saturation of their growth downstream of the mean transition location (denoted by the arrow heads in Fig. 5.6). In general, larger amplitudes of fluctuations are detected earlier upstream as Tu is increased, leading to the upstream shift in mean transition. The saturation level of velocity fluctuations in the wall-normal direction decreases with increasing Tu (Figs. 5.6b and 5.6d), a result which is observed in Figs. 5.5c and 5.5d and consistent with the findings of Yarusevych and Kotsonis [24]. On the other hand, the streamwise fluctuations do not exhibit the same behaviour, and saturate at similar amplitudes for all levels of Tu investiated for a given Reynolds number. These findings are consistent with those of Simoni *et al.* [38] who note a decrease in the saturation amplitude of wall-normal velocity fluctuations in separation bubbles induced on a flat plate with increasing Tu level, while the saturation amplitude of the streamwise fluctuations remains relatively constant.

Spatial amplification factors can be computed from the velocity fluctuations, similar to those calculated using p' in the previous chapter. Here, spatial amplification factors are computed using both the streamwise and wall-normal velocity fluctuations as $\sigma_{u'} = (\Delta \ln(u'/U_0))/(\Delta x/c)$ and $\sigma_{v'} = (\Delta \ln(v'/U_0))/(\Delta x/c)$, respectively. In general, the most significant amplification of velocity fluctuations occurs just upstream of mean transition, as shown by the data points used to compute the maximum of these amplification factors in Fig. 5.6. The results are summarized in Table 5.3 for all cases investigated. For a given Reynolds number, maximum spatial amplification factors of both components of velocity generally decrease with increasing Tu, in good agreement with the spatial amplification factors presented in the previous chapter based on fluctuating surface pressure measurements (Fig. 4.13). As was discussed earlier, this result indicates that the sole reason for the upstream shift in the location of mean transition with increasing Tu is due to the larger initial amplitudes of perturbations present at the elevated Tu levels. The observed increase in bubble stability with decreasing bubble size is consistent with the findings of

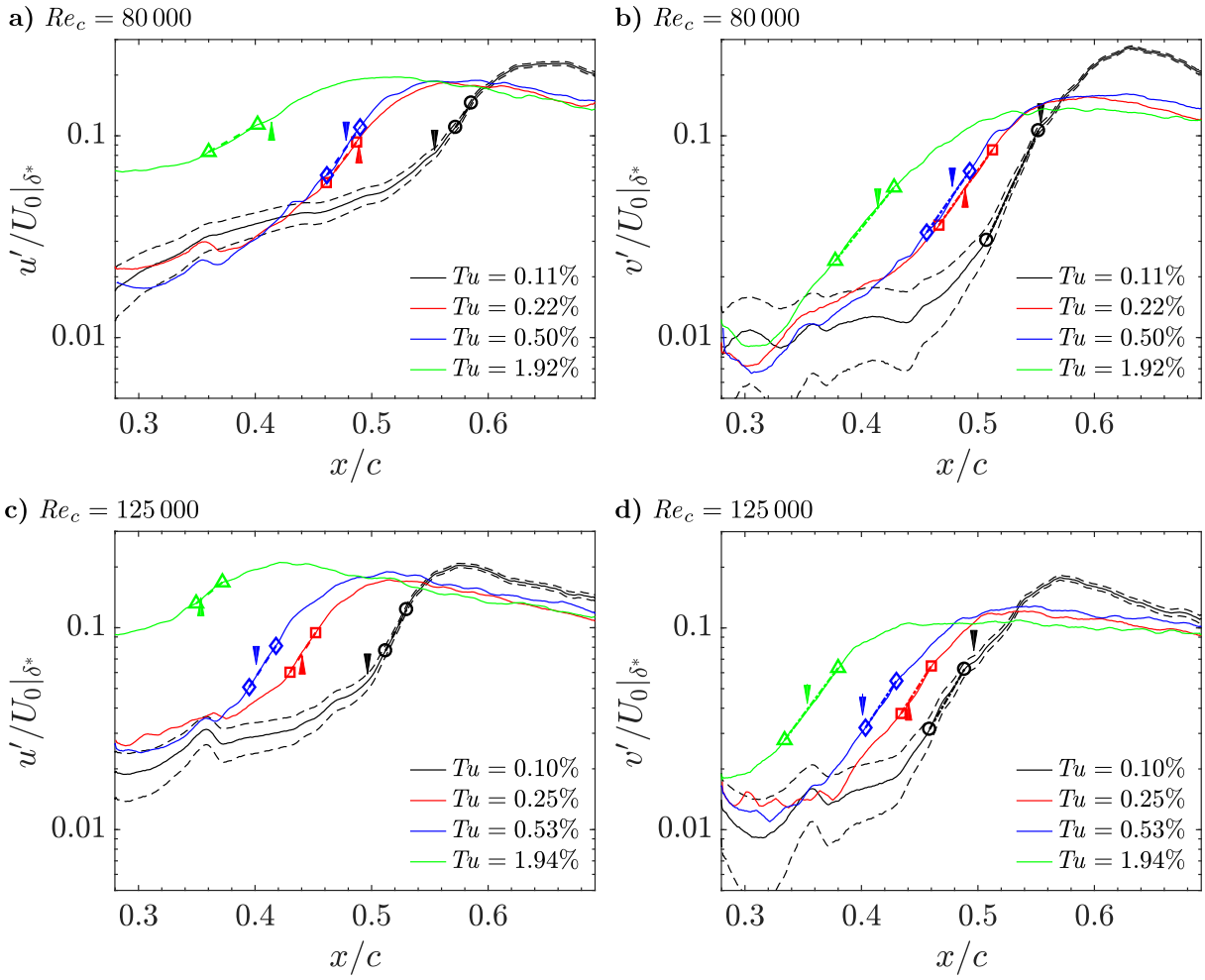

Figure 5.6: Root-mean-square of (a),(c) streamwise and (b),(d) wall-normal velocity fluctuations along the boundary layer displacement thickness. Arrow heads, coloured according to the legend, indicate the locations of mean transition. Dashed black lines represent the uncertainty interval for the baseline turbulence intensity case. Dotted dashed lines and makers in (b),(d) represent the data points used to compute the maximum of sigma.

Yarusevych and Kotsonis [24], who used plasma actuators to excite a separation bubble and observed a decrease of approximately 40% in the maximum disturbance growth rate when the separation bubble length was approximately halved. This compares favourably with the decrease in $\sigma_{v',max}$ of approximately 30% in the present study at $Re_c = 80\,000$ when Tu is increased from 0.11% to 0.50% and the bubble length is approximately halved (Fig. 5.3b). In an experimental investigation of separation bubbles induced on a flat plate, Simoni *et al.* [38] found that increasing levels of Tu had little-to-no influence on the spatial growth rate of v'. While this finding is in contrast to the observed decrease in the present investigation, the authors make the same conclusion made here that the upstream shift in mean transition must be solely the result of the larger initial amplitude of disturbances at elevated Tu levels. Simoni *et al.* [38] suggest that the spatial amplification rate is only significantly affected when the displacement thickness at separation is altered, for which Tu has no effect in their investigation. This result uncovers a dfference between the present investigation and those performed over a flat plate with an imposed adverse presure gradient, as the displacement thickness in the fore portion of the separation bubble does indeed change with increasing Tu (Fig. 5.4). As discussed at the end of the last section, flat plate studies appear to 'fix' the separation location which limits the effects of Tu on the upstream portion of the separation bubble, whereas in the present investigation a downstream shift in the location of mean separation is observed with increasing Tu (Fig. 5.2). Therefore, the mean deformation of the fore portion of the separation bubble leads to a decrease in the spatial amplifcation factors for a given Reynolds number, consistent with previous investigations [23, 43], which is not observed in the flat plate study of Simoni *et al.* [38] where the fore portion of the

Table 5.3: Summary of wall-normal velocity fluctuation characteristics. Uncertainty intervals for each parameter are summarized in Appendix A.

Reynolds number	Tu [%]	$\sigma_{u',max}$	$\sigma_{v',max}$	$\sigma_{p',max}$	St_0	ΔSt	$U_c/U_e\|_s$	λ_x
80 000	0.11	20.6	28.1	26.6	11.2	8.1	0.46	0.057
	0.22	17.8	18.7	22.8	11.2	12.4	0.46	0.056
	0.50	19.2	18.9	10.5	11.2	16.2	0.49	0.060
	1.92	7.4	16.6	9.7	12	17.3	0.56	0.065
125 000	0.10	26.1	22.8	36.1	15.5	10.3	0.44	0.039
	0.25	20.5	20.9	27.1	14.5	12.7	0.48	0.046
	0.53	20.4	20.1	17.6	14.5	16.4	0.49	0.047
	1.94	10.7	17.9	12	16.2[1]	20.4[1]	0.55	0.047

[1] Estimated from fluctuating surface pressure measurements

bubble is unaffected by increasing Tu.

The results in Table 5.3 show that by increasing the chord Reynolds numbers, larger spatial amplification rates are generally measured for a given level of Tu, implying a decrease in bubble stability with increasing Reynolds number, consistent with previous investigations [10, 38]. However, at the baseline Tu level, the spatial amplification rate of the wall-normal velocity fluctuations actually decreases with the increase in Reynolds number. By comparing Fig. 5.6b with Fig. 5.6d, it can be seen that at the lower chord Reynolds number the wall-normal velocity fluctuations attain notably higher maximum amplitudes. This is expected behaviour as the bubble size is larger [24], but it is speculated that since the spatial resolution of the PIV measurements is limited, the amplification factor at the baseline level of Tu for $Re_c = 80\,000$ may be skewed to a higher value. The amplification factors computed from the streamwise velocity fluctuations do in fact increase with increasing Reynolds number for all Tu levels investigated, in line with previous investigations [15, 38].

Further support for the increase in spatial amplification rates with increasing chord Reynolds number is provided by analyzing distributions of the fluctuating surface pressure measurements. Distributions of p' for the baseline level of Tu are shown for both Reynolds numbers in Fig. 5.7. Here, it is clear that the location of p'_{max} shifts upstream with the increase in Re_c, and in turn results in an upstream shift of mean transition, as expected. More importantly for this discussion, $\sigma_{p',max}$ increases from 26.6 to 36.1 with the increase in Re_c, though the estimates are based on two points and the corresponding uncertainty is relatively high. A summary of $\sigma_{p',max}$ for all investigated Tu levels is shown in Table 5.3, and the value increases with increasing Re_c for all levels of Tu investigated, while it decreases with increasing Tu for a given Reynolds number. Therefore, in combination with the other two spatial amplification factors presented, it is clear that bubble stability indeed increases with increasing Tu but decreases with increasing Re_c for all flow conditions investigated.

By employing the time-resolved PIV system, insight into the dynamics within the separation bubble with increasing Tu levels may be gained. In order to ensure the same separation bubble was being studied after the PIV systems were changed, the mean fields as measured with both systems were compared and show good agreement to within the experimental uncertainty. Spectra of the wall-normal velocity fluctuations, sampled along the displacement thickness, are presented in Fig. 5.8 using a non-dimensional frequency, St, based on the airfoil chord length. Spectra for all Tu levels and both Reynolds numbers investigated are normalized by a common reference value in order to easily compare the distributions of energy. Since the magnification factor was varied between the different Tu levels for $Re_c = 80\,000$, the PIV fields-of-view differ slightly and as such, for regions where no measurements were taken, hatching is used so that the results may be presented over the same extent of the streamwise coordinate. At the baseline Tu level for both chord

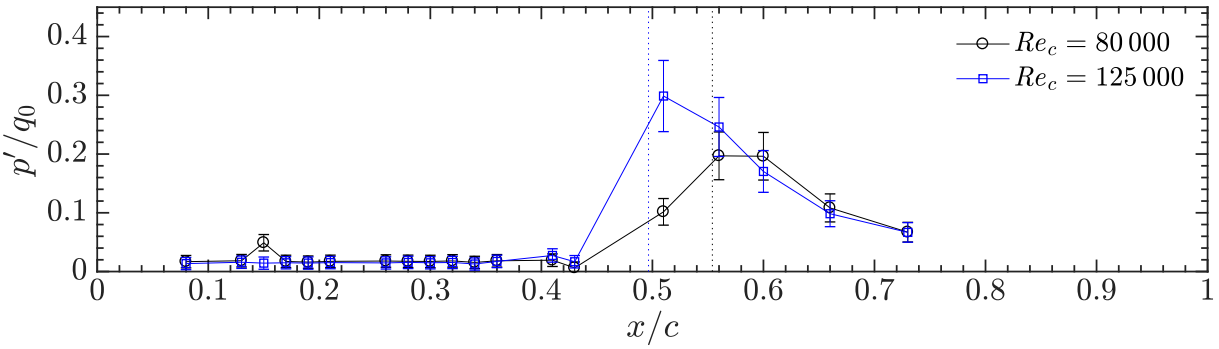

Figure 5.7: Streamwise distribution of the root-mean-square of fluctuating surface pressures at the baseline level of Tu.

Reynolds numbers, the spectra reveal streamwise amplification of disturbances within a band of unstable Strouhal numbers, ΔSt, centered on some central Strouhal number, St_0. Downstream of the location of mean transition, the energy content within the amplified band of frequencies is redistributed over a wider range of frequencies, indicating the later stages of transition where the shear layer rollers begin to breakup. The results show a similar trend when the Tu level is increased. A summary of ΔSt and St_0 is provided is Table 5.3 for all cases investigated. At $Re_c = 125\,000$ and the highest Tu level investigated, the spectral energy is spread over such a broad range that no central frequency nor unstable band can be identified from the PIV results (Fig. 5.8b). However, an analysis of spectra of the fluctuating surface pressures revealed clearer results, as the most significant amplification occured just upstream of the PIV field-of-view (at approximately $x/c = 0.28$) and these values are summarized in Table 5.3. A comparison of the spectra computed using the fluctuating surface pressures and wall-normal velocites was conducted for the other flow conditions investigated and the results were in good agreement.

At $Re_c = 80\,000$, the central Strouhal number does not change appreciably with increasing Tu, however, the width of the detectable band of frequencies increases with increasing Tu. This increase in ΔSt is attributed to the increase in energy over a broader range of frequnecies in the free-stream with increasing Tu (Fig. 3.3), leading to velocity fluctuations reaching detectable levels earlier upstream in the separated shear layer. This was also observed over a much larger range of flow conditions in the previous chapter using fluctuating surface pressure measurements. The relatively small changes in the separation bubble central frequency, despite significant mean bubble deformation, is consistent with the results of Yarusevych and Kotsonis [24] who induced a mean bubble deformation by exciting a separation bubble with controlled disturbances. Small changes to the central disturbance frequnecy of a separation bubble despite significant mean changes due to increasing Tu levels

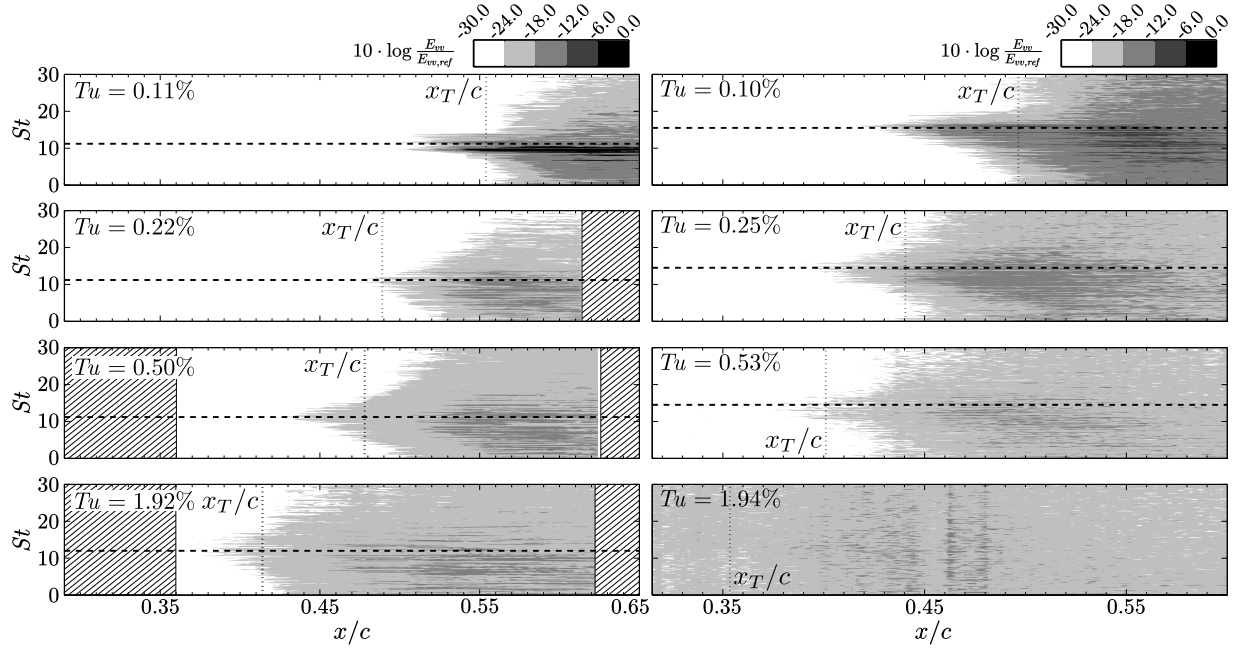

Figure 5.8: Spectra of wall-normal velocity fluctuations along the boundary layer displacement thickness. The dashed line corresponds to the central disturbance Strouhal number while the dotted-dashed lines indicate the unstable band of Strouhal numbers.

have also been reported previously in experiments [31, 38]. For $Tu \leq 0.50\%$ and $Re_c = 80\,000$ there is no change in the shedding frequnecy of the bubble while at $Re_c = 125\,000$ there is a slight decrease for increases in Tu up to $Tu = 0.53\%$, though the change is within the experimental uncertainty (± 1.5). For both Reynolds numbers and the highest Tu level investigated, there is an increase in the central disturbance frequency, within the experimental uncertainty. This increase is consistent with the results presented in the previous chapter, and the investigation of Simoni *et al.* [38] who studied a bubble formed over a flat plate with an imposed adverse pressure gradient and subject to increasing Tu.

Spatial information from the time-resolved PIV measurements may be used to compute a two-dimensional wavenumber-frequency spectrum from the wall-normal velocity fluctuations. These spectra are computed along the boundary layer displacement thickness (*i.e.*, the same locations used to compute the frequency spectra in Fig. 5.8) and are presented in Fig. 5.9 for both Reynolds numbers and all Tu levels investigated. All spectra shown in Fig. 5.9 have been normalized by their maximum values. At the baseline Tu level, the results show

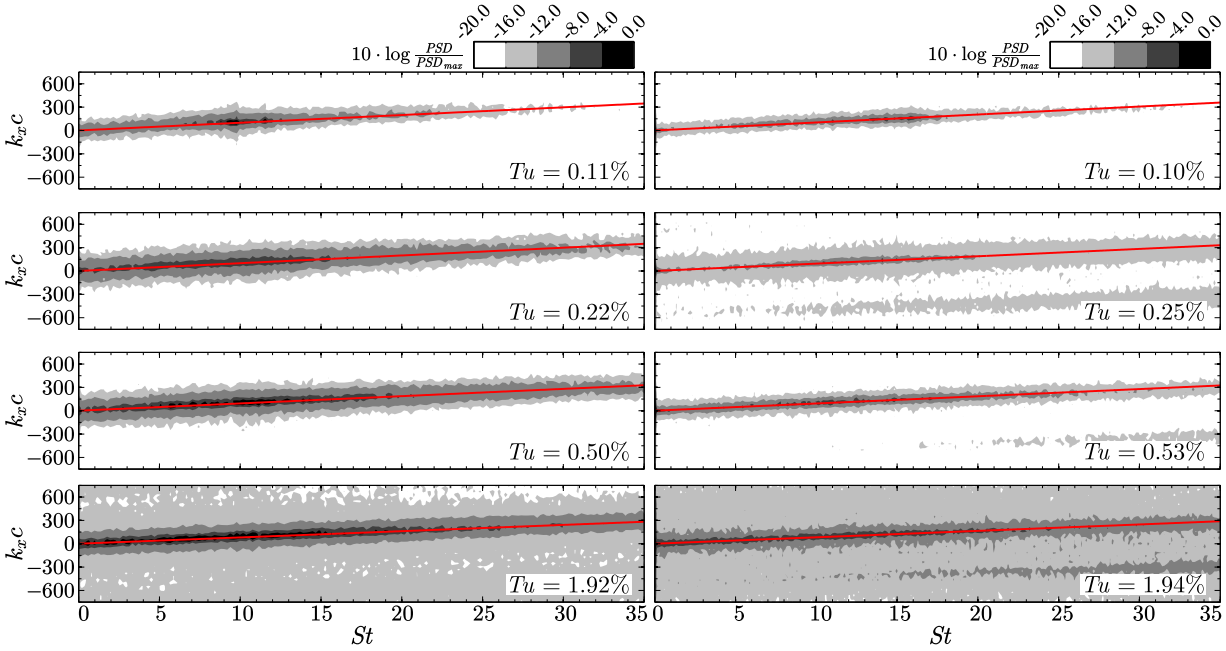

Figure 5.9: Wavenumber-frequency spectra computed along the boundary layer displacement thickness.

that the spectral energy is concentrated around a relatively narrow convective ridge [167], highlighted by the solid red line. When the level of Tu is increased, the results in Fig. 5.9 show that energy is distributed over a broader range of wavenumbers and frequencies. It should be noted that, at the higher chord Reynolds number and elevated Tu levels, there is a second convective ridge at negative wavenumbers which is attributed to aliasing from the PIV velocity signal.

By rearranging the wave equation, the average convective velocity of disturbances in the separated shear layer can be calculated from the convective ridge in Fig. 5.9 using $U_c = 2\pi f/k_x$. Since the convective ridge is linear between frequency and wavenumber, this velocity represents an average for all disturbance frequencies in the separated shear layer. The computed convective velocities are normalized by the boundary layer edge velocity at separation, and are summarized in Table 5.3. The edge veloicty is estimated as $U_e = U_0 \cdot \sqrt{1 - C_P|_S}$ where $C_P|_S$ is the mean surface pressure at the location of mean separation, as determined from the mean surface pressure distirbutions (Table 5.1). For $Re_c = 125\,000$ and the highest level of Tu investigated where separation could not be

detected, the mean separation location at the baseline Tu level was used in order to find $C_P|_S$. The results at the baseline Tu level are in good agreement with the expected range of convective velocities previously reported over an airfoil in a low disturbance environment [26]. The computed convective velocities (Table 5.3) show that the average convective speed of separated shear layer disturbances increases with increasing Tu. This increase in U_c with increasing Tu is in agreement with the results of Simoni *et al.* [38], and reflects the increase of the average separated shear layer velocity due to the decrease in the height of the separation bubble (Fig. 5.2) and in turn a reduction in the reverse flow velocities near the wall.

In addition to average convective speeds, streamwise wavelengths of the shear layer rollers can also be estimated from the two-dimensional wavenumber-frequnecy spectra presented in Fig. 5.9. For each investigated case, the wavenumber at the frequency of the most amplified disturbance (determined from Fig. 5.8) is identified as the intersection with the convective ridge, shown by the red line. Then, the streamwise wavelength was computed using the equation $\lambda_x = 2\pi/k_x$, with the results summarized in Table 5.3. The results for $Re_c = 125\,000$ and the baseline level of Tu are in good agreement with the findings of Kurelek *et al.* [18] for the same airfoil and flow conditions. The results show that as the level of Tu is increased, the average wavelength of the shear layer rollers increases. For both Reynolds numbers, increasing the level of Tu from the baseline level to the highest level investigated results in an increase in the wavelength of the rollers of approximately 20%. In an investigation of the effects of Tu on separation bubbles formed over a flat plate, Simoni *et al.* [38] characterize the streamwise wavelength of the shear layer rollers using POD and note an increase in the streamwise wavelength of approximately 10% for a similar increase in Tu. The notably smaller influence of Tu on λ_x in their study suggests that bubble dynamics are different over a flat plate versus those observed here for an airfoil. In the present investigation, since the central disturbance frequency of the bubble does not change significantly with increasing Tu (Fig. 5.8), and the average convection speed of the disturbances increases (Table 5.3), the result is an increase in the average wavelength of disturbances (Table 5.3) in the separated shear layer. For all levels of Tu, increasing the chord Reynolds number leads to a decrease in the average wavelength of disturbances, which is related to the observed increase in the central disturbance frequency with increasing chord Reynolds number (Table 5.3), an increase which has also been noted in previous investigations [10].

The dynamics within the laminar separation bubble are illustrated using consecutive snapshots of instantaneous spanwise vorticity in Figs. 5.10 and 5.11 for $Re_c = 80\,000$ and 125 000, respectively, for each Tu level investigated. Hatching is used for the elevated Tu levels at $Re_c = 80\,000$ since the magnification factors were different, thus allowing for the

results to be presented on the same streamwise scale. To aid in the identification of vortical structures, namely the shear layer rollers, contours of the λ_2 criterion [146] are shown for all Tu levels investigated. The λ_2 criterion defines vortex cores by finding pressure minima that are the result of fluid rotation. More specifically, vortices may be identified within regions where the second eigenvalue of the tensor defined by the sum of the rate-of-rotation and rate-of-strain tensors is negative. These contours show that at $Re_c = 80\,000$ and the baseline Tu level (Fig. 5.10a), a distinct shear layer roller can be seen at $x/c \approx 0.56$ with another roller forming just upstream at $x/c \approx 0.52$. A third roller is undergoing breakup downstream of $x/c = 0.60$. Based on the presented series of snapshots, it can be seen that roll-up of the structures tends to occur upstream of mean transition ($x_T/c = 0.55$), while the breakdown of these structures generally occurs downstream of mean reattachment ($x_R/c = 0.62$), agreeing well with previous investigations of separation bubbles [18, 31]. As the level of Tu is increased, the shear layer roll-up location shifts upstream, closely agreeing with the location of mean transition in all cases. In addition, the size and coherence of the rollers generally decreases with increasing Tu, which agrees with the increasing distribution of energy of associated velocity fluctuations over broader time and length scales (Fig. 5.9). In comparing the streamwise development of the structures, it can be seen that, at elevated Tu levels, the shear layer rollers appear to lose their coherence sooner after initial roll-up, a finding which will be explored further in Section 5.3. The thick black lines in Fig. 5.10 trace the approximate centres of the shear layer rollers between consecutive snapshots to aid in tracking the structures from frame to frame. The spacing of the lines is therefore representative of the streamwise wavelength of the shear layer rollers while their slope is proportional to their convective velocity. By comparing the slopes of the dashed lines for each of the Tu levels investigated, it can be seen that the slopes generally increase slightly with increasing Tu, indicating an increase in the mean convection speed which is consistent with the results summarized in Table 5.3.

At the higher chord Reynolds number investigated, roll-up of the separated shear layer follows a similar progression as compared to that discussed for $Re_c = 80\,000$, with consecutive snapshots shown for all Tu levels in Fig. 5.11. At the baseline Tu level (Fig. 5.11a), the shear layer rolls-up at approximately $x/c = 0.44$, which is upstream of the location of mean transition ($x_T/c = 0.50$). In comparing this result to that at the lower Re_c investigated (Fig. 5.10a), it is observed that roll-up occurs further upstream, consistent with the upstream shift in the location of mean transition with the increase in chord Reynolds number (Table 5.2). However, the structures are notably smaller and form much closer to the airfoil surface, a result of the smaller separation bubble size at the higher chord Reynolds number (Fig. 5.2). Similarly to the results at the lower Reynolds number, as the level of Tu is increased, the roll-up location shifts upstream with the location of mean

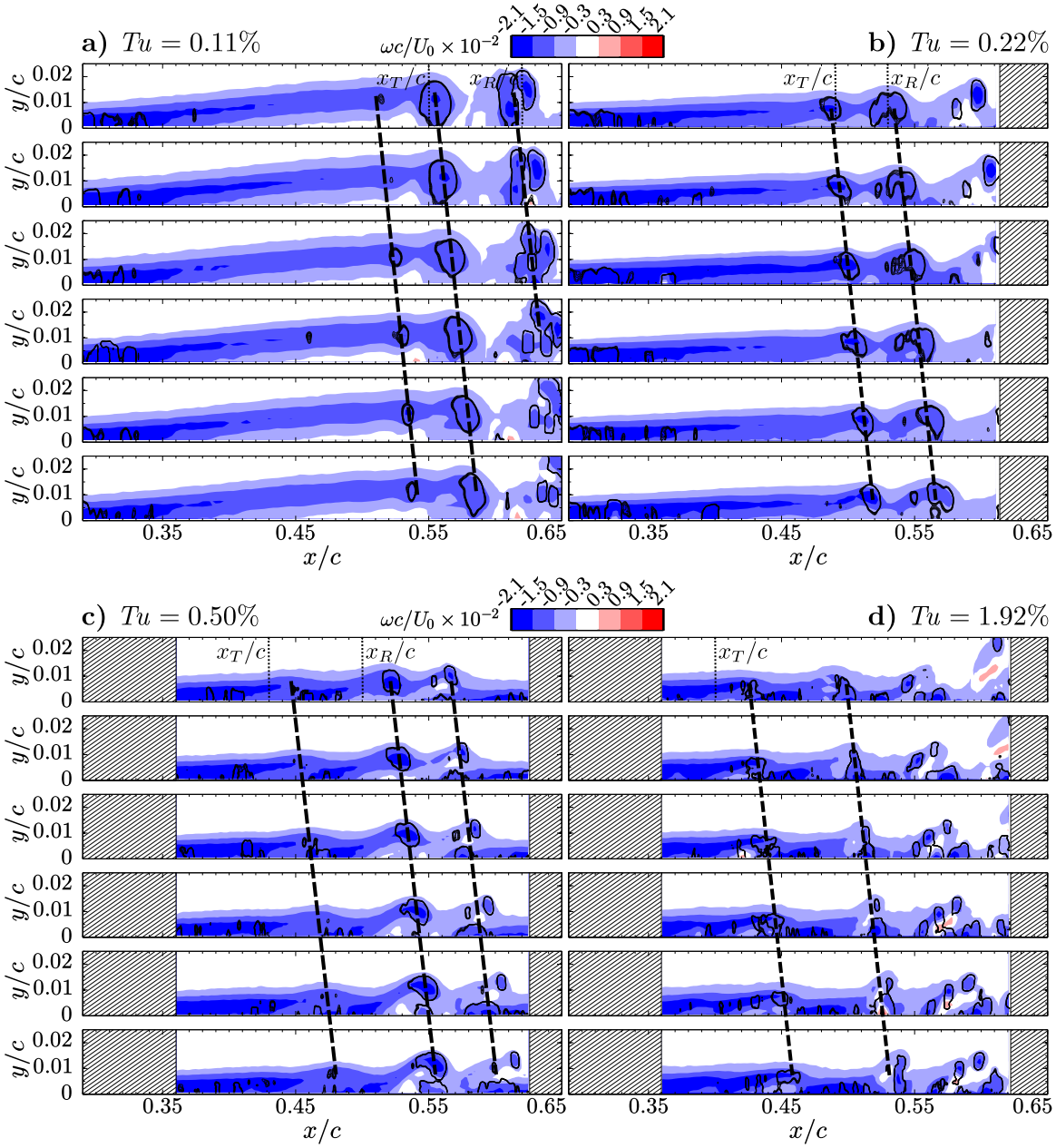

Figure 5.10: Contours of instantaneous spanwise vorticity for $Re_c = 80\,000$. Consecutive snapshots are separated by 0.33 ms. Thin black lines represent contours of the λ_2 criterion [146] while thick dashed lines trace the approximate centres of vortices.

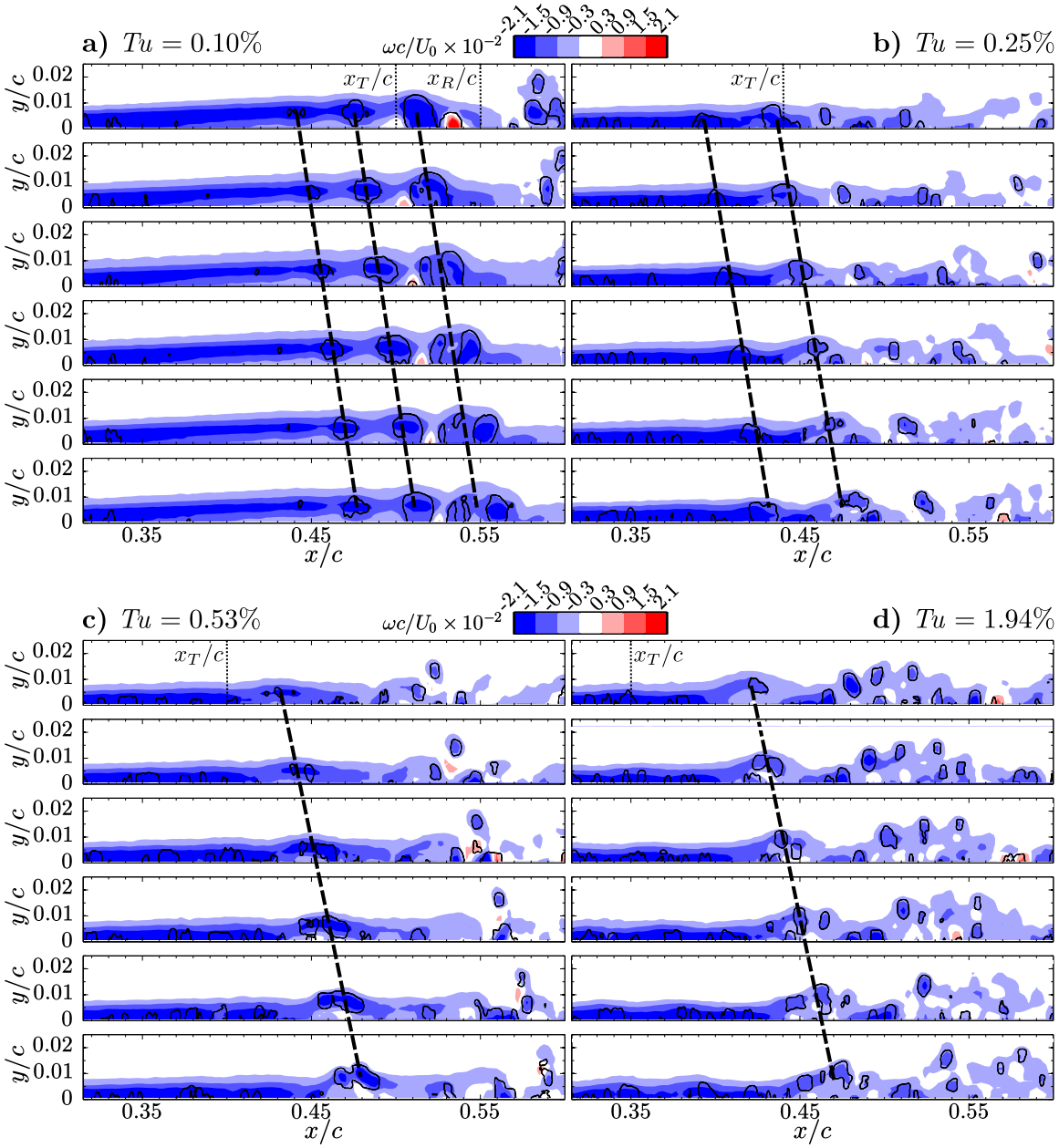

Figure 5.11: Contours of instantaneous spanwise vorticity for $Re_c = 125\,000$. Consecutive snapshots are separated by 0.28 ms. Thin black lines represent contours of the λ_2 criterion [146] while thick dashed lines trace the approximate centres of vortices.

transition, the size of the rollers generally decreases, and the their coherence decreases. At the highest Tu level investigated, structures that resemble shear layer rollers are present, suggesting that the flow does indeed separate and shear layer roll-up occurs, supporting the discussion in Section 5.1 based on the boundary layer parameters that a separation bubble does form for this flow condition, despite no reverse flow region being resolved (Fig. 5.2). However, these structures are relatively small and have notably less coherence than the lower Tu levels, suggesting that the dynamics of the transition process are altered. Since the PIV field-of-view for this Reynolds number covers a more significant downstream distance from mean reattachment for $Tu \gtrsim 0.25\%$ (based on mean surface pressure distribution estimates) than at the lower Reynolds number, the break-up of the shear layer rollers to smaller scales is more clear and it can be seen that there are no large scale structures in the downstream portion of the PIV field-of-view for any of the elevated Tu cases.

In order to gain further insight into structures within the flow, a Proper Orthogonal Decomposition (POD) was applied to the fluctuating velocity fields as measured by the high-speed PIV system. This type of analysis was introduced to the fluids community by Lumley [168] and has since been used extensively in analyzing turbulent and transitional flows (*e.g.*, Refs. [23, 38, 133, 169–171]). The methodology of POD is outlined in detail by Berkooz *et al.* [169] but, the method used in this investigation is based on the snapshot method as discussed by Sirovich [172]. This method involves first building a velocity matrix in which rows contain the fluctuating velocities of both components of velocity measured by the PIV, and each column represents a snapshot in the time sequence of measurements. Then, eigenvectors, and corresponding eigenvalues, are computed for the autocovariance matrix of this velocity matrix. The resulting eigenvalues represent the relative energy content of the modes, while the modes themselves are computed as the products of each eigenvector with the original velocity matrix, divided by the norm of the resulting quantity. The resulting POD modes are typically sorted in descending eigenvalue order such that the most important (in terms of energy) modes can be easily identified. Since the POD is computed on the velocity fluctuations, the relative energies are representative of the turbulent kinetic energy (with the note that the third component of velocity is not included here). The time coefficients of a given POD mode may be computed as the product of the mode itself with each instantaneous velocity snapshot. Therefore, if time-resolved data is used, temporal information about a given mode can be determined. Typically, the quantity of interest in the temporal sense is the frequency content of the mode fluctuations as this can be used to relate the modes to observed structures in the flow. The results from the POD of the fluctuating velocity fields as measured by the high-speed PIV system are shown in Figs. 5.12–14 for $Re_c = 80\,000$ and all Tu levels investigated. Figure 5.12 shows the relative and cumulative modal energies while the first six spatial modes in both

the streamwise and wall-normal directions are shown in Fig. 5.13. Finally, spectra of the temporal coefficients for the first six modes are shown in Fig. 5.14.

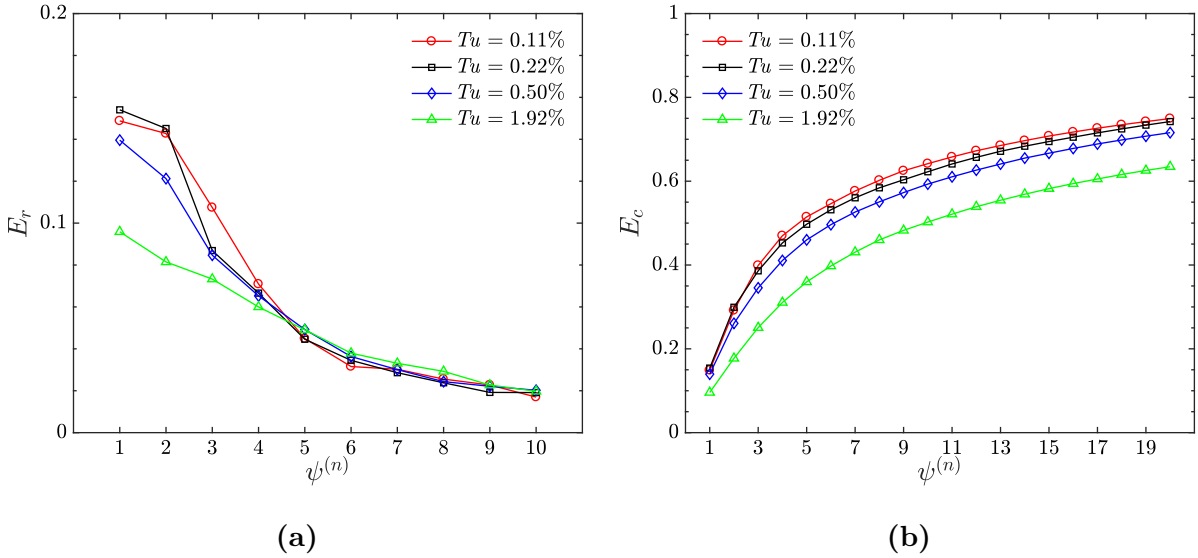

(a) **(b)**

Figure 5.12: (a) relative and (b) cumulative POD eigenvalues from the POD computed on the side view data for $Re_c = 80\,000$.

For the baseline level of Tu, the results in Fig. 5.12a show that the first two POD modes contain a similar amount of relative energy, while an inspection of the spatial distributions of the first two POD modes (Fig. 5.13a), reveals that the modes have a similar topology, but have a phase shift of approximately $\pi/2$ for both ψ_u and ψ_v. This similarity of the relative energy content and observed phase shift in the spatial distributions of the first two modes signifies mode pairing, which has been observed in previous studies involving convective amplification of periodic disturbances [23, 52, 133]. Spectral content of the temporal coefficients for these two modes (Fig. 5.14a) shows that they are associated with a frequency near that of the most amplified disturbance frequency that was detected in the separated shear layer velocity fluctuations. Therefore, these two modes represent the velocity fluctuations that are associated with the convection of the shear layer rollers shed from the aft portion of the separation bubble (Fig. 5.10a). The spatial distributions of energy for these two modes also show that the energy is concentrated in the aft portion of the PIV field-of-view, where the shear layer rollers are observed (Fig. 5.10a), with a characteristic wavelength similar to that identified from the wavenumber-frequnecy spectra (Table 5.3). The remaining four modes (ψ_3 to ψ_6) presented in Fig. 5.13a do not show

similar relative energy contents (Fig. 5.12a), but the spatial distributions of the modes and frequency content of the temporal coefficients suggest that the energy contained in these modes is also associated with the development of shear layer rollers. The spectra of the temporal coefficients for $\psi^{(3)}$ and $\psi^{(4)}$ (Fig. 5.14a) show additional peaks near the subharmonic of the most amplified frequency in the bubble, suggesting that the mode is also linked to subharmonic amplification of the fundamental frequency. This may be related to vortex paring [55], which was confirmed to occur occasionally in the aft portion of the bubble.

The POD results for $Tu = 0.22\%$ and 0.50% show some similarities and differences with the baseline Tu level. In general, inspecting spectra of the temporal coefficients in Fig. 5.14 shows that the dominant energy content of the most energetic modes shifts to lower frequencies as Tu increases. Although characterized by frequencies lower than the fundamental frequency, for these Tu levels the first two POD modes remain paired, as shown by the spatial distributions presented in Figs. 5.13b and 5.13c. The results are most clear in the distributions of the wall-normal POD modes and thus will be the focus of this discussion. For both of these elevated Tu levels (0.22% and 0.50%), spectra of the temporal coefficients (Figs. 5.14b and 5.14c) for the first two POD modes show that there is a concentration of energy near the subharmonic of the central disturbance frequency, which is reflected in the increased characteristic length scale in the corresponding spatial modes in Figs. 5.13b and 5.13c. On the other hand, spectra of the temporal coefficients for the third and fourth modes contain significant energy near the central disturbance frequency of the bubble (Figs. 5.14b and 5.14c), and the spatial modes are characterized by smaller characteristic wavelengths (Figs. 5.13b and 5.13c) than the first and second modes. Comparing the spatial distributions of the first and second modes to the third and fourth modes for $Tu = 0.22\%$ and 0.50% (Figs. 5.13b–c), it can be seen that the third and fourth modes contain more significant energy further upstream, consistent with the observed roll-up locations (Fig. 5.10), thus leading to the detected velocity fluctuations at the bubble shedding frequency in these modes. The present results therefore indicate that as the level of turbulence intensity is increased, the energy of the velocity fluctuations at the fundamental frequency of the shear layer rollers become less significant, however, are still present and show the most upstream amplification in the separated shear layer (Fig. 5.8). Additionally, the most energetic modes are still clearly associated with the shedding phenomenon of the bubble, but are characterized by lower frequencies.

On the average, as the level of Tu is increased, the relative energy content of the first two modes decreases (Fig. 5.12a), together accounting for approximately 30% of the energy at the baseline Tu level, and decreasing to approximately 17% at the highest Tu level investigated. Close inspection of the relative energy content also shows that the difference

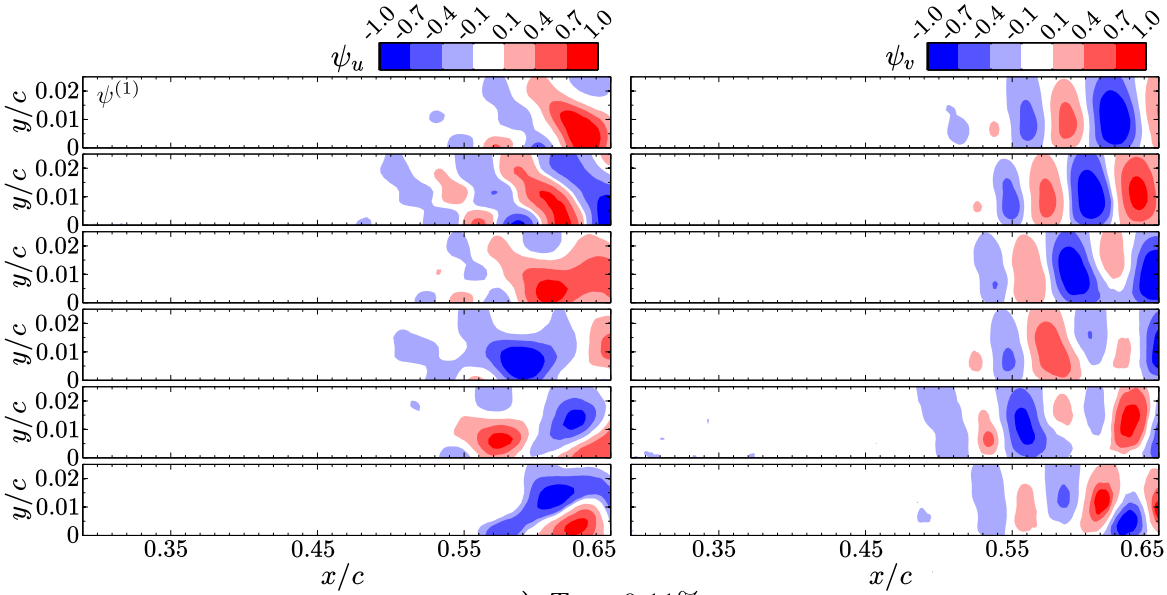

a) $Tu = 0.11\%$

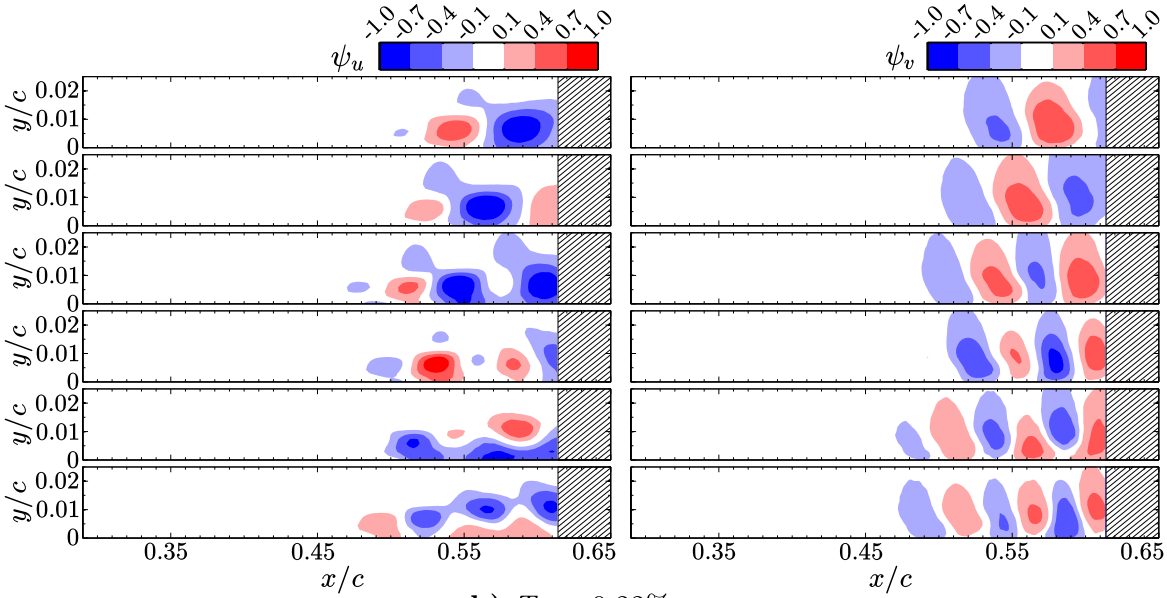

b) $Tu = 0.22\%$

Figure 5.13: Contours of the streamwise and wall-normal components of the first six POD eigenfunctions for the side view data at $Re_c = 80\,000$. All distributions have been normalized by the maximum absolute value.

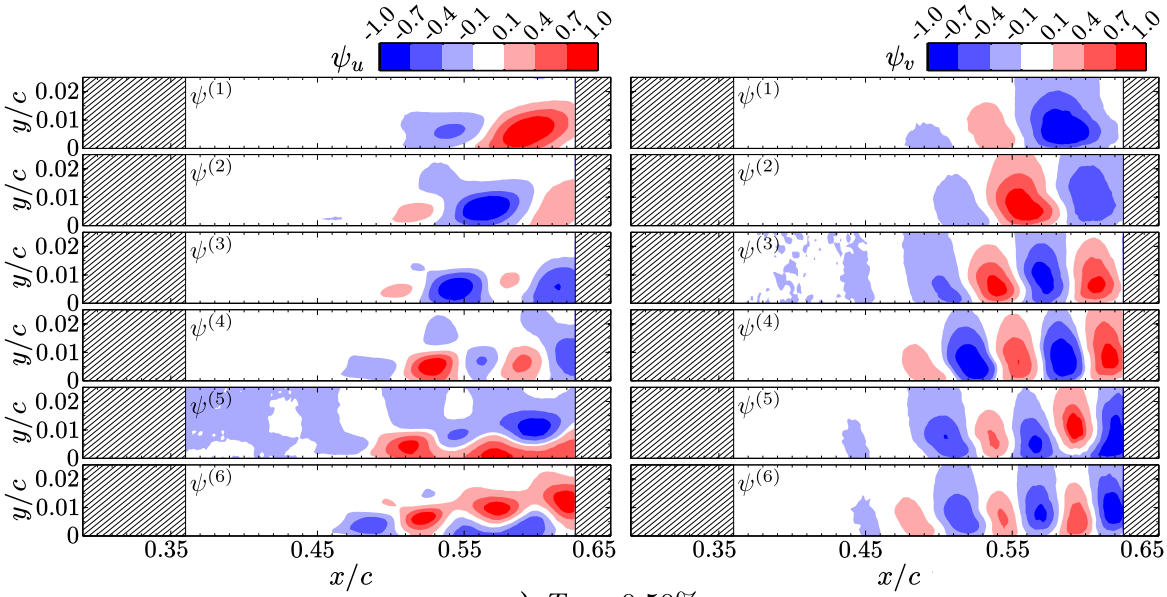

c) $Tu = 0.50\%$

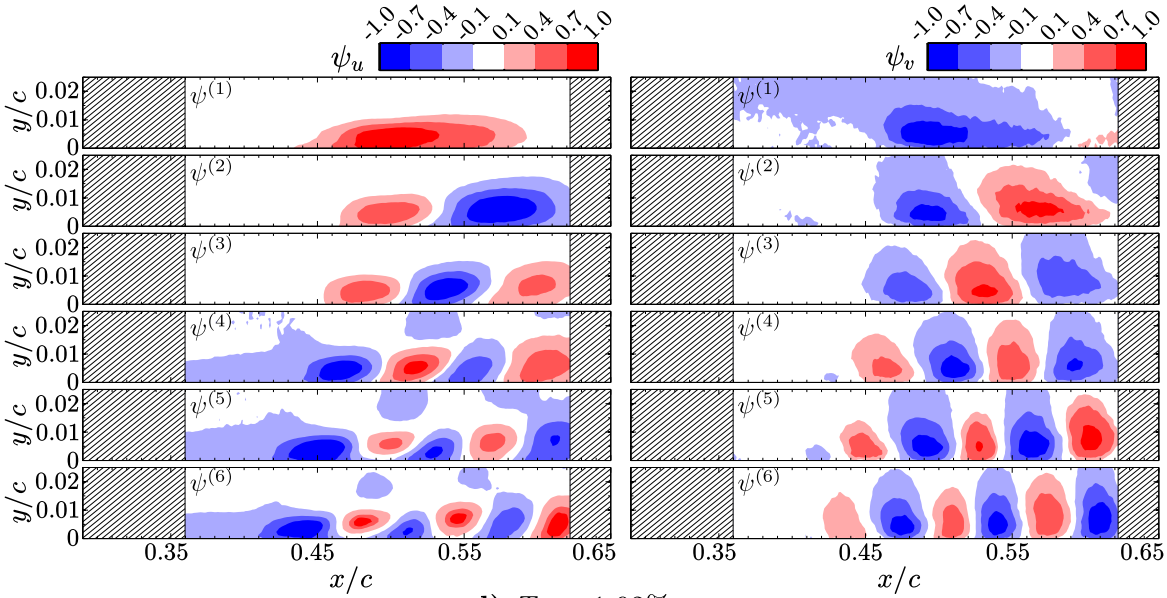

d) $Tu = 1.92\%$

Figure 5.13 (cont.)

in energy of the first and second modes increases. At $Tu = 1.92\%$, the energy content of the second mode becomes more closely aligned with that of the third mode. This result can be confirmed by the spatial distributions of the POD modes, where the first two modes indeed remain paired for $Tu = 0.22\%$ and 0.50% (Figs. 5.13b and 5.13c). However, at $Tu = 1.92\%$ the first mode is clearly unpaired from the second POD mode, as seen in both the streamwise and wall-normal components (Fig. 5.13d). Instead, the second and third modes become paired. The decrease in the combined relative energy content of the mode pair associated with shedding is consistent with the decrease in coherence of the shear layer rollers with increasing Tu (Figs. 5.10 and 5.11). Therefore, an increasing number of modes is required in order to describe the velocity fluctuations in the flow. In other words, for a given number of modes, less of the total fluctuating energy is represented as the level of Tu is increased. For example, the relative energy content contained within the first twenty modes (Fig. 5.12b)) is approximately 75%, 74%, 71%, and 63% in order of increasing turbulence intensity, thus highlighting the distribution of energy to a larger number of modes with increasing Tu.

The spatial distribution of energy associated with the first mode at $Tu = 1.92\%$ shows that the energy is distributed over a large area in the PIV field-of-view. The distribtuion of energy in this mode is qualitatively similar to the first POD mode presented by Lengani and Simoni [133] as well as Simoni *et al.* [38], who investigated the effects of Tu on the flow over a compressor blade and flat plate, respectively, at similar levels of Tu investigated here. Both of these investigations suggested that the topology of this mode was due to the presence of streamwise streaks in the flow, though they were not shown explicitly. The spectrum of the first temporal coefficient contains no significant peaks and is dominated by low frequencies (Fig. 5.14d), which is to be expected based on the relatively large characteristic wavelength in the corresponding spatial mode (Fig. 5.13d). In their POD analysis at high Tu levels, Simoni *et al.* [38] also note that the first POD mode has a large characteristic wavelength and a temporal coefficient dominated by low frequencies. The presence of streaks will be explored further in Section 5.3.

Though pairing of the higher modes becomes less clear in terms of relative energy contents (Fig. 5.12a), the spatial distributions indicate that $\psi^{(2)}$ and $\psi^{(3)}$ are indeed paired, as well as $\psi^{(4)}$ and $\psi^{(5)}$ ($\psi^{(6)}$ is also paired with $\psi^{(7)}$ which is not shown here). An analysis of the frequency content of the corresponding temporal coefficients (Fig. 5.14d) also supports this observation as these pairs contain similar spectral content. The second and third modes show significant peaks near the subharmonic frequency, while the sixth (and seventh) mode shows a significant peak at the central disturbance frequency. In comparing the spatial distributions of these modes, it can be seen that the characteristic wavelength of the POD modes decreases with increasing mode numbers, where the wavelength of the

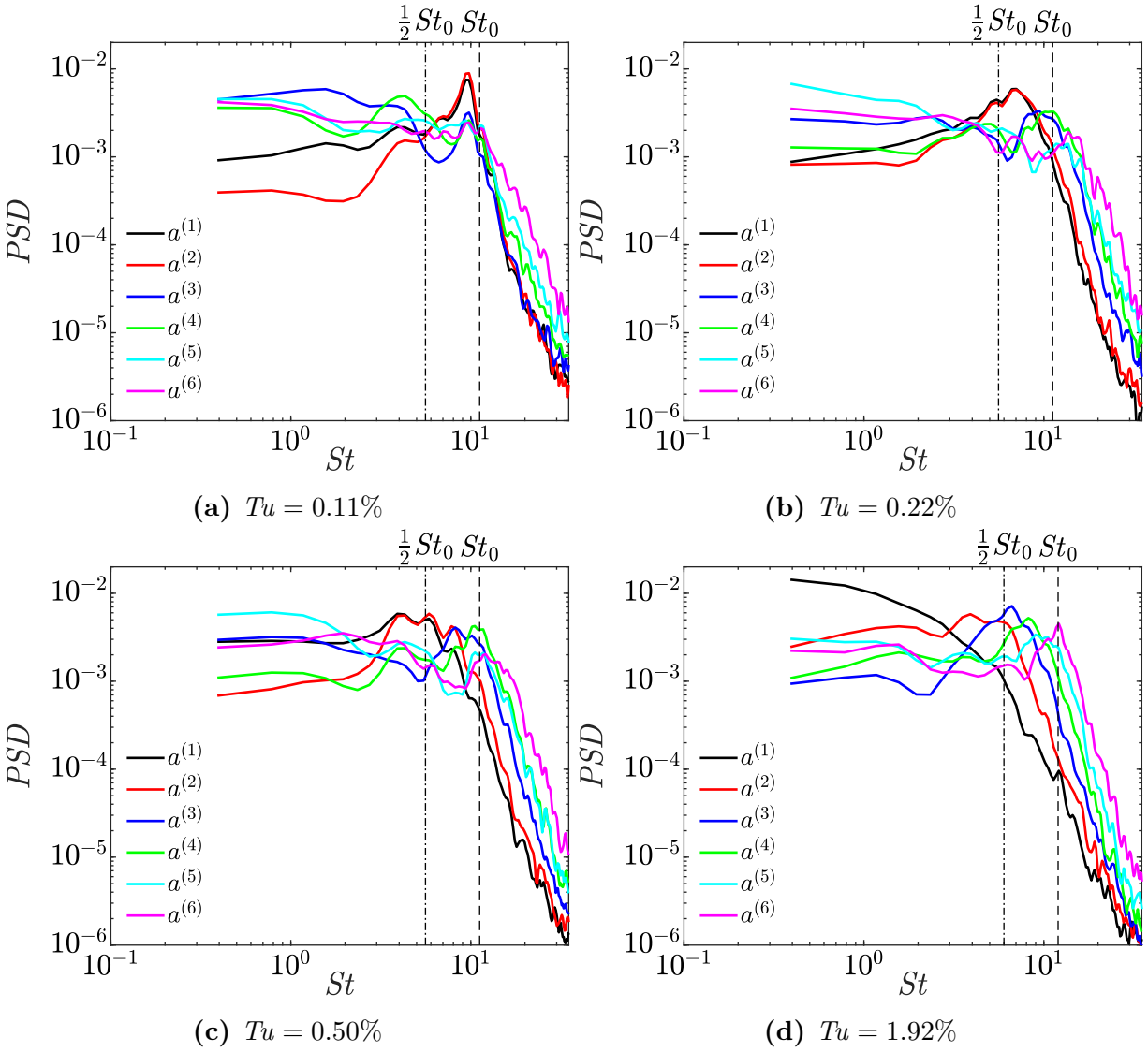

(a) $Tu = 0.11\%$ **(b)** $Tu = 0.22\%$

(c) $Tu = 0.50\%$ **(d)** $Tu = 1.92\%$

Figure 5.14: Frequency spectra of the time coefficients for the first six POD modes for each Tu level investigated at $Re_c = 80\,000$. Spectra for each mode are normalized by the total energy in the signal. The central disturbance frequency and its subharmonic were determined from wall-normal velocity fluctuations and are summarized in Table 5.3.

energy contained within the sixth mode is on the order of the wavelength of the dominant streamwise wavelength (Table 5.3). In agreement with the results for $Tu = 0.22\%$ and 0.50%, the implication here is that the velocity fluctuations associated with the fundamental frequency of the shear layer rollers become less important in terms of the total fluctuating energy. However, instead of all higher modes still being associated with the shear layer rollers, the first mode is now clearly unrelated to these structures.

The results of the POD on the fluctuating velocity fields at the higher chord Reynolds number investigated are presented in Figs. 5.15–17. In general, the results follow similar trends with increasing Tu as compared to those at the lower chord Reynolds number, but the increase in Reynolds number has further shifted the dominant frequencies of the most energetic modes to lower values. For the lowest three Tu levels investigated (*i.e.*, $Tu \leq 0.53\%$), inspection of the relative modal energies (Fig. 5.15a) and spatial distributions (Figs. 5.16a–c) suggest that the first six modes form three modal pairs (*i.e.*, $\psi^{(1)}$ and $\psi^{(2)}$, $\psi^{(3)}$ and $\psi^{(4)}$, and $\psi^{(5)}$ and $\psi^{(6)}$), all of which are associated with the shedding phenomenon. However, spectra of the temporal coefficients show that energy associated with the first two modes is associated with frequencies near the subharmonic of the most amplified disturbances for all Tu levels (Figs. 5.17a–c.

The frequency of the dominant energy contained in the modes increases with increasing mode number (Figs. 5.17a–c), and the modes which fluctuate near the most amplified frequency for $Re_c = 125\,000$, are the fifth and sixth modes for $Tu = 0.10\%$ and the sixth and seventh modes for $Tu = 0.25\%$ and 0.53%. The spatial distributions of these modes are characterized by wavelengths that are in good agreement with those estimated form the wavenumber-frequency spectra results summarized in Table 5.3. Similarly to the results presented at $Re_c = 80\,000$, the shift of the modes describing the separated shear layer roller fluctuations to higher mode numbers with increasing Tu indicates that the energy associated with these fluctuations decreases with increasing Tu, though the shedding is still represented in the more energetic modes.

At the highest Tu level investigated, the first two modes are unpaired (Fig. 5.16d), and the first set of paired modes involves the third and fourth modes. At $Tu = 1.94\%$, the first POD mode contains significantly more energy than the first mode at $Tu = 0.25\%$ and 0.53%, however, the following modes contain less energy than the corresponding modes at $Tu = 0.25\%$ and 0.53% and thus the cumulative energy of the modes at $Tu = 1.94\%$ falls below that of the lower two Tu levels by the third POD mode. The large relative energy content in the first mode is associated with a large characteristic wavelength (Fig. 5.16d), dominated by low frequencies (Fig. 5.17d), as was observed for the highest Tu level at $Re_c = 80\,000$. The large relative energy content of this mode suggests that these structures are notably stronger at this chord Reynolds number, and thus dominate the flow development.

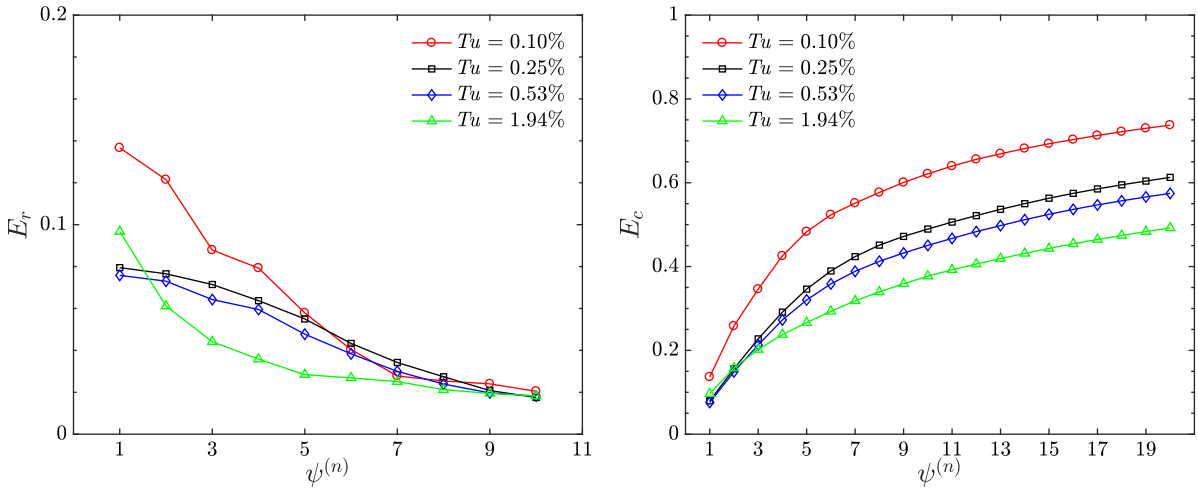

(a) **(b)**

Figure 5.15: (a) relative and (b) cumulative POD eigenvalues from the POD computed on the side view data for $Re_c = 125\,000$.

At this level of Tu, the spatial distributions of the POD modes, frequency content of their temporal coefficients, and characteristic wavelengths do not match those expected of the separated shear layer rollers (Table 5.3) until the tenth and eleventh modes, further showing that the energy of velocity fluctuations associated with the shear layer rollers decreases with increasing Tu.

The cumulative modal energies across the first twenty modes at $Re_c = 125\,000$ are 74%, 61%, 57%, and 49% in order of increasing Tu level. In general, less cumulative energy is recovered for a given number of POD modes at the same Tu level for $Re_c = 125\,000$ as compared to 80 000. The decrease in cumulative energy over a given number of modes shows that the energy is distributed over a wider range of modes, consistent with the observed decrease in coherence of the shear layer rollers at a given level of Tu (Figs. 5.10 and 5.11).

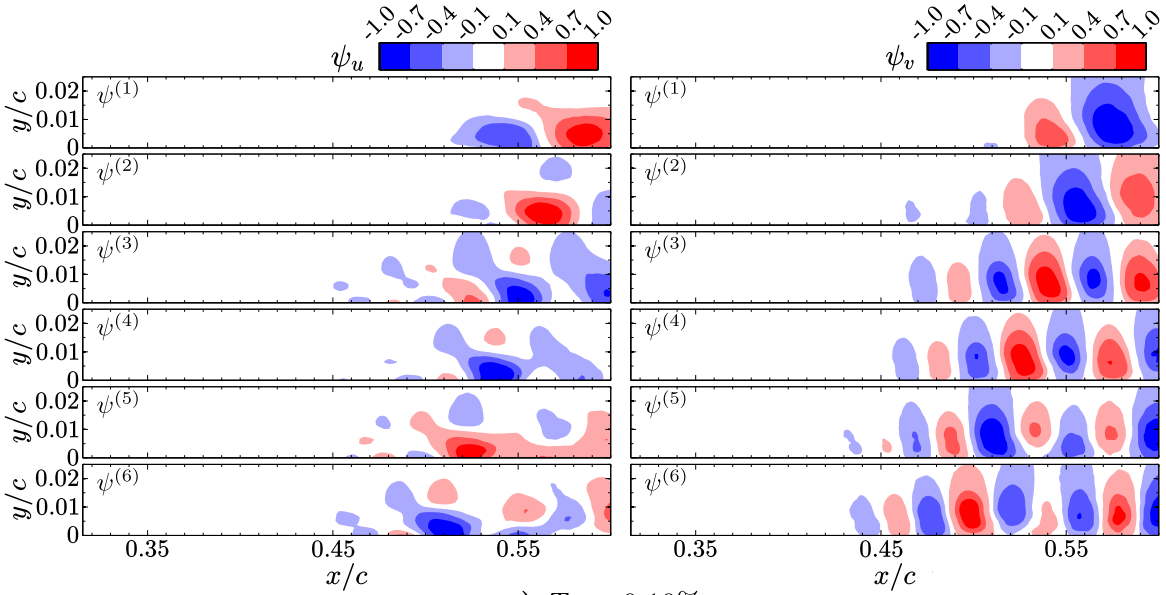

a) $Tu = 0.10\%$

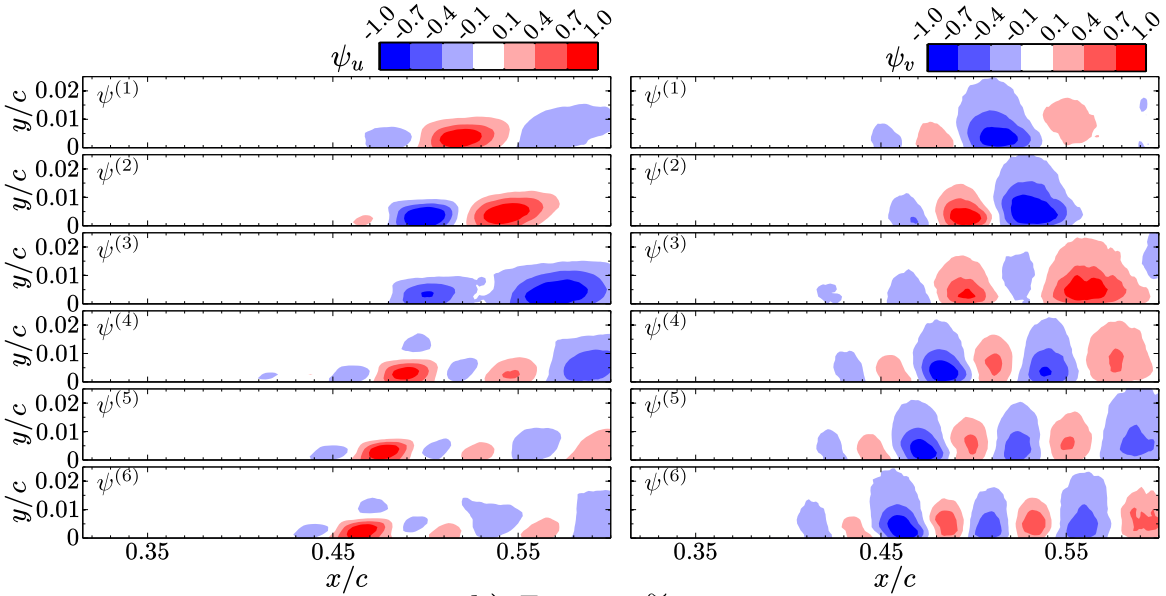

b) $Tu = 0.25\%$

Figure 5.16: Contours of the streamwise and wall-normal components of the first six POD eigenfunctions for the side view data at $Re_c = 125\,000$. All distributions have been normalized by the maximum absolute value.

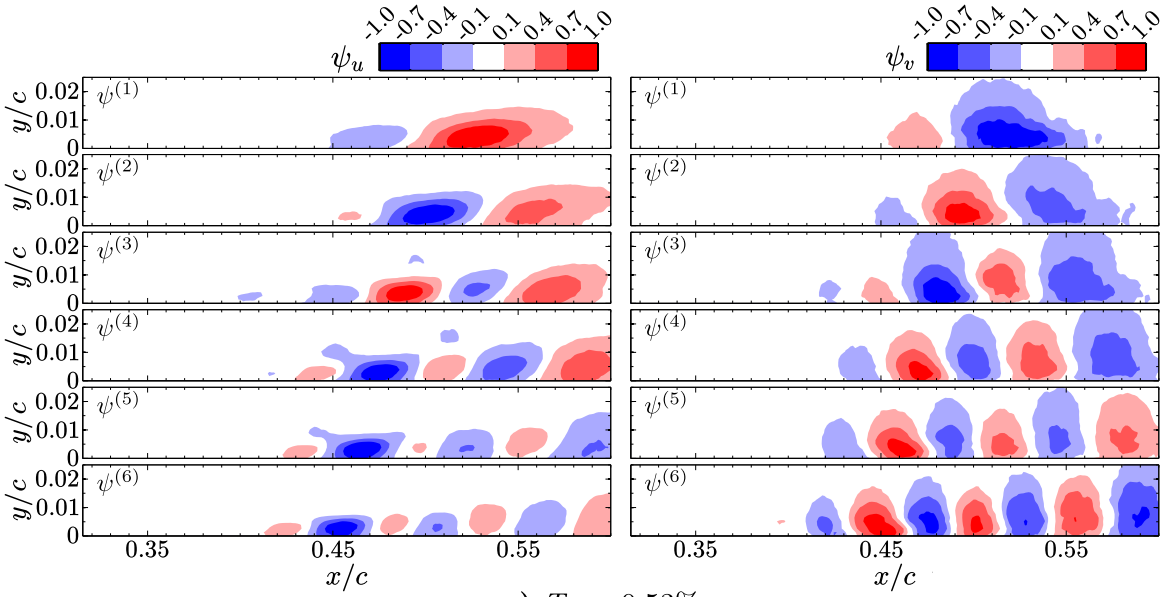

c) $Tu = 0.53\%$

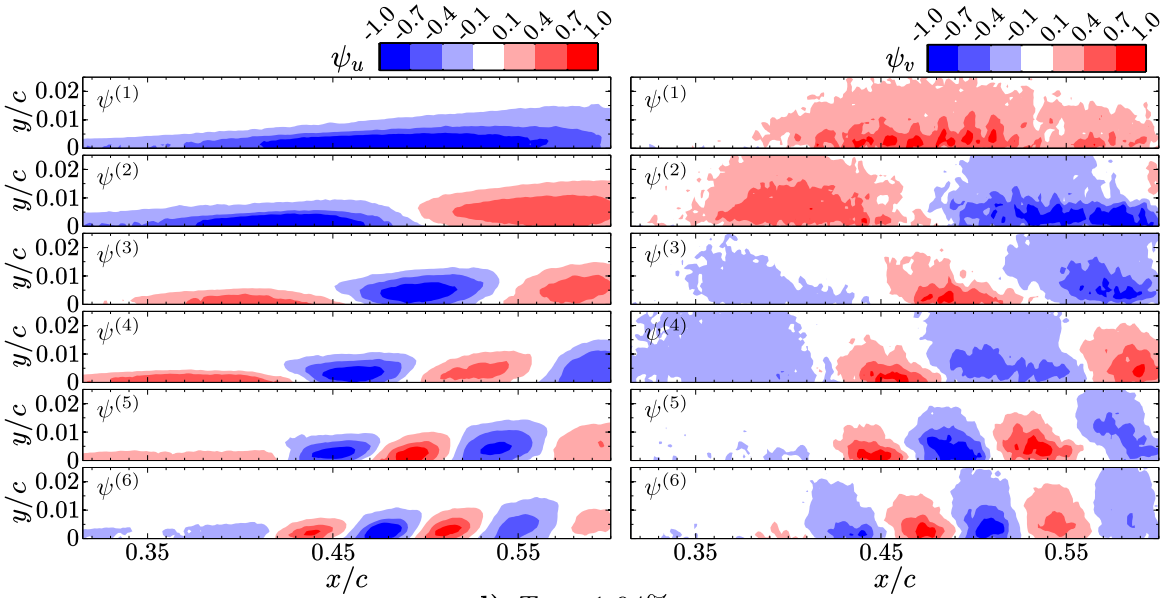

d) $Tu = 1.94\%$

Figure 5.16 (cont.)

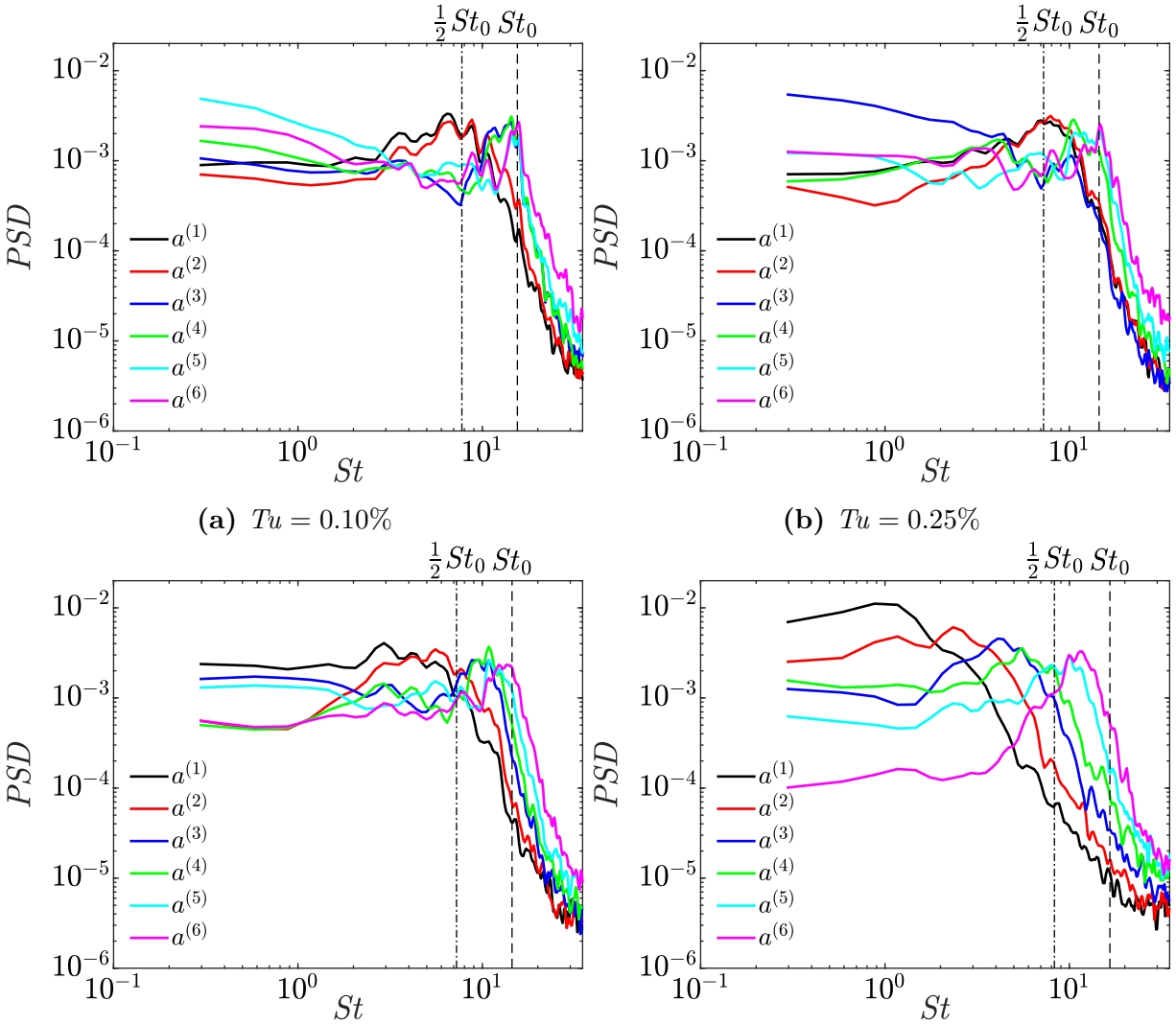

(a) $Tu = 0.10\%$ **(b)** $Tu = 0.25\%$

(c) $Tu = 0.53\%$ **(d)** $Tu = 1.94\%$

Figure 5.17: Frequency spectra of the time coefficients for the first six POD modes for each Tu level investigated at $Re_c = 125\,000$. Spectra for each mode are normalized by the total energy in the signal. The central disturbance frequency and its subharmonic were determined from wall-normal velocity fluctuations and are summarized in Table 5.3.

5.3 Spanwise Flow Development

Spanwise flow development over the suction side of the airfoil was characterized using time-resolved PIV measurements in the top view configuration, as depicted schematically in Fig. 3.5b, with the field-of-view and coordinate system shown in Fig. 3.6b. For all measurements, the laser sheet was placed above the surface of the airfoil such that it cut through the top halves of the shear layer rollers, as informed by the flow measurements in the xy plane (*i.e.*, using the results presented in Figs. 5.10 and 5.11). The streamwise location of the field-of-view was set to capture the roll-up location of the shear layer rollers and their development downstream. In this configuration, the exact location of the laser sheet from the surface of the airfoil is difficult to measure along the streamwise extent of the measurement region, and as such it is not trivial to transform the results into the surface attached coordinate system used in Sections 5.1 and 5.2. Since the laser sheet was relatively closely aligned with the chord of the airfoil for all cases investigated, results in this section are presented in the chord attached coordinate system (Fig. 3.6b), with the spanwise axis matching that of the surface attached coordinate system. This section will focus on the instantaneous results to describe the bubble dynamics, but, for completeness, time-averaged quantities are presented in Appendix E.

In order to investigate the spanwise flow development over the suction side of the airfoil, representative sequences of instantaneous chordwise velocity are presented in Fig. 5.18 and Fig. 5.19 for $Re_c = 80\,000$ and $Re_c = 125\,000$, respectively, for all Tu levels investigated. Since the laser sheet was positioned to pass through the upper halves of the shear layer rollers, the rollers can be identified as bands of elevated chordwise velocity. The locations of mean transtion were determined from the locations of maximum displacement thickness (Table 5.2) and then transformed into the chord based coordinate system location. At the baseline Tu level (Fig. 5.18a), a nearly two-dimensional roller can be identified in the first snapshot at approximately $X/c = 0.55$, just downstream of the location of mean transition. In addition, the early formation of a roller can be observed upstream at approximately $X/c = 0.50$. Downstream of mean transition, the rollers develop spanwise deformations, as has been observed in previous experiments [18, 31], and numerical simulations [17, 42]. These spanwise deformations grow with increasing streamwise distance, leading to a reorientation of the spanwise vorticity into the streamwise direction, and the eventual breakdown of the shear layer rollers [18]. The breakdown of a roller can be observed by tracking the chordwise progression of the roller located at approximately $X/c = 0.60$ in the first frame of Fig. 5.18a. As this structure convects downstream, the spanwise unsteadiness grows in amplitude and in the last frame the filament is beginning to break-up and has lost significant coherence at $z/c \approx 0.10$. The chordwise location of this break-up ($X/c \approx 0.65$) agrees well with

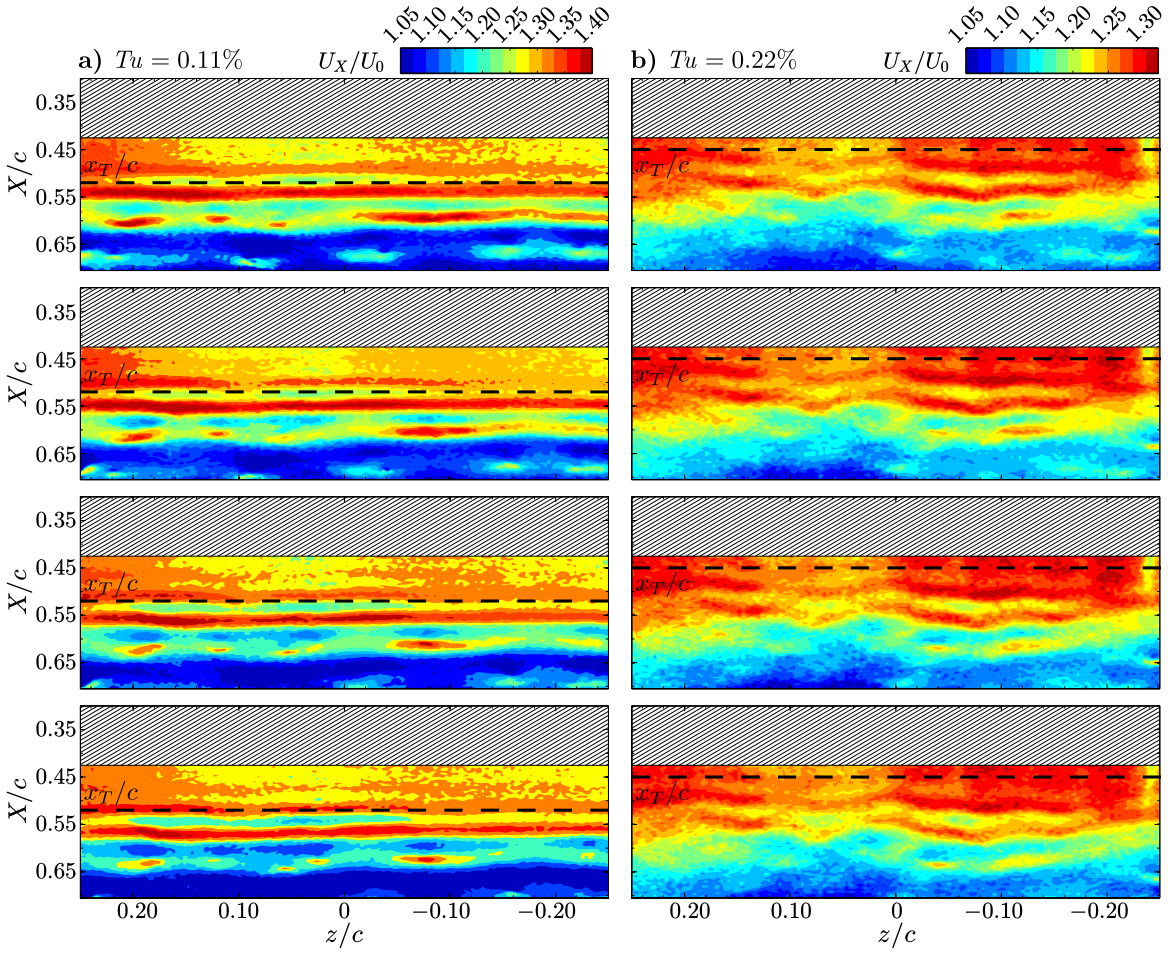

Figure 5.18: Contours of instantaneous chordwise velocity for $Re_c = 80\,000$. Consecutive snapshots are separated by 0.51 ms. Dashed black lines mark the locations of mean transition as determined from the displacement thickness.

the observed loss of coherence of the structures downstream of mean reattachment in the snapshots of instantaneous spanwise vorticity (Fig. 5.10a).

As the level of Tu is increased to 0.22% and 0.50%, the shear layer rollers are observed to form further upstream, in agreement with the upstream shift in mean transition. More notably, the rollers are characterized by more significant spanwise deformations at the location of roll-up, similar to the structures observed in the experiments of Burgmann and Schröder [31]. They performed PIV measurements of a laminar separation bubble formed over an airfoil in a water tunnel characterized by a free-stream turbulence intensity of

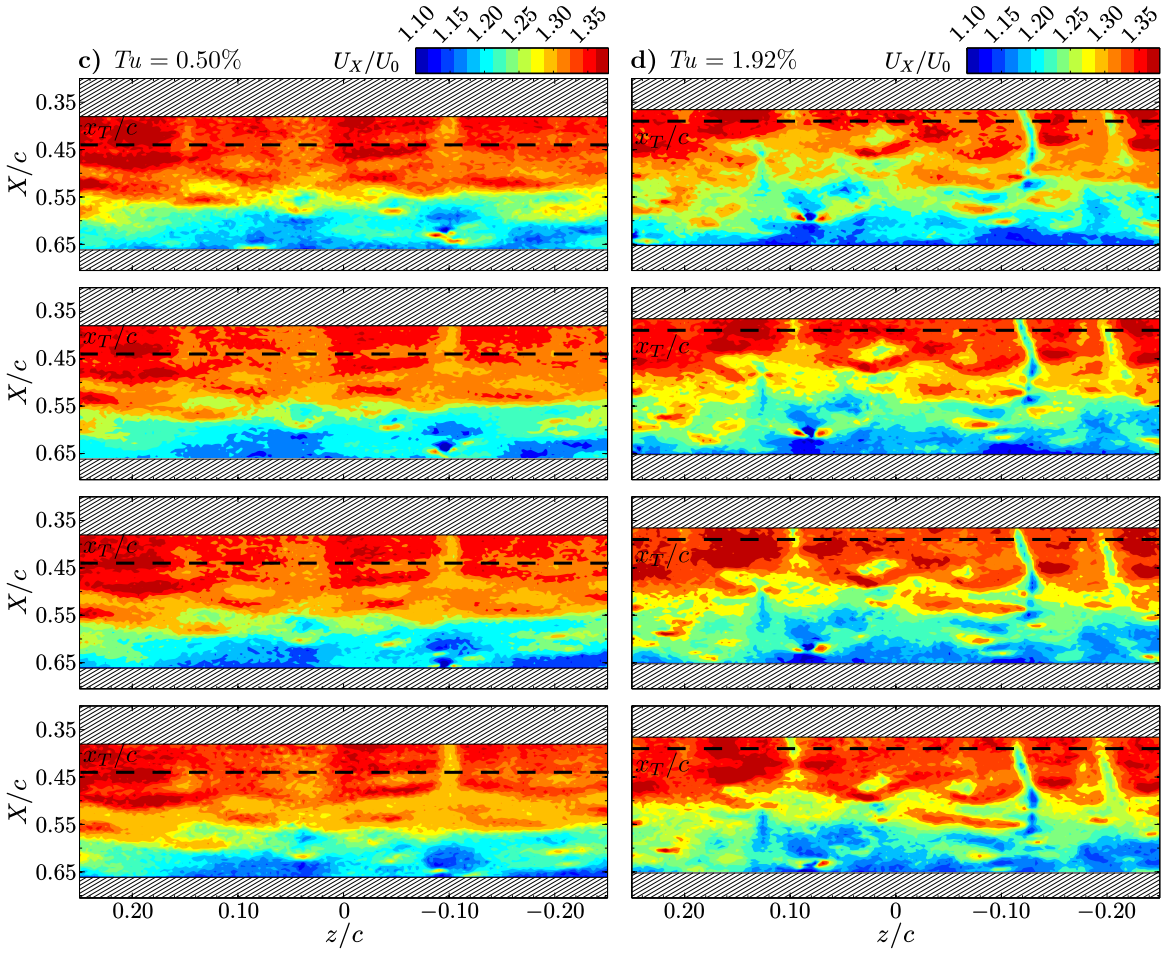

Figure 5.18 (cont.)

approximately 1%, thus suggesting that the elevated Tu level is responsible for the increased undulations at roll-up. This decrease in spanwise coherence is also similar to the results of Kurelek [20], who observed a notable decrease in the spanwise coherence of shear layer rollers when subjected to broadband acoustic excitation. This form of excitation can be seen as analogous to the increase in free-stream turbulence intensity in this investigation, as the increase here is a result of an increase of energy over a broad range of frequencies (Fig. 3.3). The sequence of instantaneous chordwise velocity snapshots at $Tu = 0.50\%$ (Fig. 5.18c) shows that roll-up occurs just upstream of $X/c = 0.45$, around the location of mean transition. Just downstream of the roll-up location, the rollers have significant spanwise undulations that were not yet present at the baseline Tu level and a similar

downstream distance from the location of roll-up (Fig. 5.18a). In tracking the chordwise progression of the roller located at $X/c \approx 0.53$ in the first frame at $Tu = 0.50\%$ (Fig. 5.18c), it can be seen that the structure begins to break-up in the second frame at $X/c \approx 0.54$ and $z/c \approx -0.10$. By the last frame in Fig. 5.18c, this structure has almost completely broken down and is characterized by a lower velocity than the rest of the structure at this spanwise location ($z/c = -0.10$). Therefore, the chordwise length between roll-up ($X/c \approx 0.45$) and break-up ($X/c \approx 0.55$) over which the roller persisted at $Tu = 0.50\%$ is approximately 10% of the chord length. This is in comparison to approximately 15% of the chord length that the rollers persist at the baseline Tu level (from $X/c \approx 0.50$ to $X/c \approx 0.65$). Therefore, the results show that the chordwise extent over which the rollers exist decreases as the level of Tu is increased, confirming the observed results in Fig. 5.10. The decrease in the chordwise extent over which the rollers persist can be attributed to an increase in the amplitude of the spanwise undulations of the shear layer rollers at the location of roll-up for elevated levels of Tu. These undulations then amplify rapidly, leading to breakdown and shorter overall bubbles (Fig. 5.2).

At the highest level of Tu investigated (Fig. 5.18d), the signature of the shear layer rollers is still present, however, these structures are highly deformed in the spanwise direction and are interacting with streamwise oriented streaks of lower velocity fluid. One streak can be observed in the first frame of Fig. 5.18d at $z/c \approx -0.10$. On average, the chordwise velocity of fluid within the streamwise streaks is approximately $0.2U_0$ less than the velocity within the upper halves of the shear layer rollers (within the measurement plane). Similar streaks have been previously observed and studied in flat plate boundary layers subjected to high levels of free-stream turbulence intensity [87, 91, 94]. The presence of these streaks results in the increase in u' upstream of the separation bubble in the time-averaged statistics presented in Fig. 5.5a. Further, it is the presence of these streaks which lead to the change in the topology of the first POD mode at this level of Tu in the side view POD results (Figs. 5.13d and 5.16d). Additionally, it is likely that the presence of similar streaks lead to the similar side view POD mode presented by Simoni *et al.* [38] at a similar level of Tu, for which the authors did not perform top-view measurements to confirm their presence. Careful inspection of the results at $Tu = 0.50\%$ shows the presence of these streaks (also at $z/c \approx -0.10$), however they are much weaker and therefore do not have a significant influence on the flow development.

The results at the highest Tu level investigated show qualitative agreement with the numerical results of McAuliffe and Yaras [16], who simulated a separation bubble induced on a flat plate and subjected to elevated Tu levels. The authors noted that the shear layer still rolled up via an instability similar to that observed at a low level of Tu, but was significantly impacted by three-dimensionality that was induced by streamwise oriented

streaks originating upstream of the bubble. The influnece of the streaks on the shear layer roll-up in the present investigation can be observed qualitatively in the presented sequence of spanwise vorticity (Fig. 5.10d). The results, and analysis of a larger sequence, show that the periodicity and coherence of the roll-up and shedding of the rollers is decreased as compared to the lower Tu levels investigated. The appearance of streaks at this Tu level suggests that the boundary layer forming over the fore portion of the suction side of the airfoil is beginning to transition via a bypass mode [91]. Similarly, at $Tu = 0.50\%$, there is evidence of the onset of bypass transition in the boundary layer upstream producing the streaks, though they do not grow enough to significantly impact the formed separation bubble. Therefore, as evidenced in the POD modes of the streamwise velocity fluctuations (Fig. 5.13d), the conclusion for the flow development at $Tu = 1.92\%$ is that the transition mechanism of the separation bubble formed over the suction side of the airfoil is altered from that observed at the lower Tu levels. In particular, the appearance of the streamwise streaks results in a strongly three-dimensional flow in the fore portion of the bubble, thus breaking the assumption of initially two-dimensional disturbances amplified in the separated shear layer during the early stages of the transition process [15, 42].

Sequences of instantaneous chordwise velocity at the higher chord Reynolds number investigated are presented in Fig. 5.19 for all Tu levels investigated. In general, the results with increasing Tu are similar to those presented at the lower chord Reynolds number (Fig. 5.18). At the baseline Tu level (Fig. 5.19a), a nearly two-dimensional roller can be identified at $X/c \approx 0.50$. It should be noted that due to the smaller separation bubble size at this Reynolds number, it was difficult to capture the shear layer rollers at the roll-up location of $X/c \approx 0.42$ (Fig. 5.11a). Therefore, the laser sheet was positioned so as to capture them further downstream where the structures are larger and thus easier to measure. In general however, the rollers form further upstream than at the baseline Tu level at $Re_c = 80\,000$, consistent with the upstream shift in mean transition (Table 5.2). At the baseline Tu level, the rollers begin to break-up at approximately $X/c = 0.60$, upstream of the observed breakup location of approximately $X/c = 0.65$ at $Re_c = 80\,000$. The upstream shift in the chordwise location of breakup is consistent with the upstream shift in mean reattachment with increasing Reynolds number (Table 5.2), as well as the upstream shift in the observed break-up in the sequences of instantaneous contours of spanwise vorticity (*i.e.*, compare Figs. 5.10a and 5.11a). At the higher chord Reynolds number, break-up of the rollers occurs more rapidly, with the rollers persisting for approximately 10% of the chord length (from approximately $X/c = 0.50$ to $X/c = 0.60$) as compared to approximately 15% at $Re_c = 80\,000$. This decrease in the chordwise extent of the structures is consistent with the shorter separation bubble lengths (Table 5.2), and arises from the increased deformations across the span of the flow at the higher Reynolds number (compare Figs. 5.18a and 5.19a).

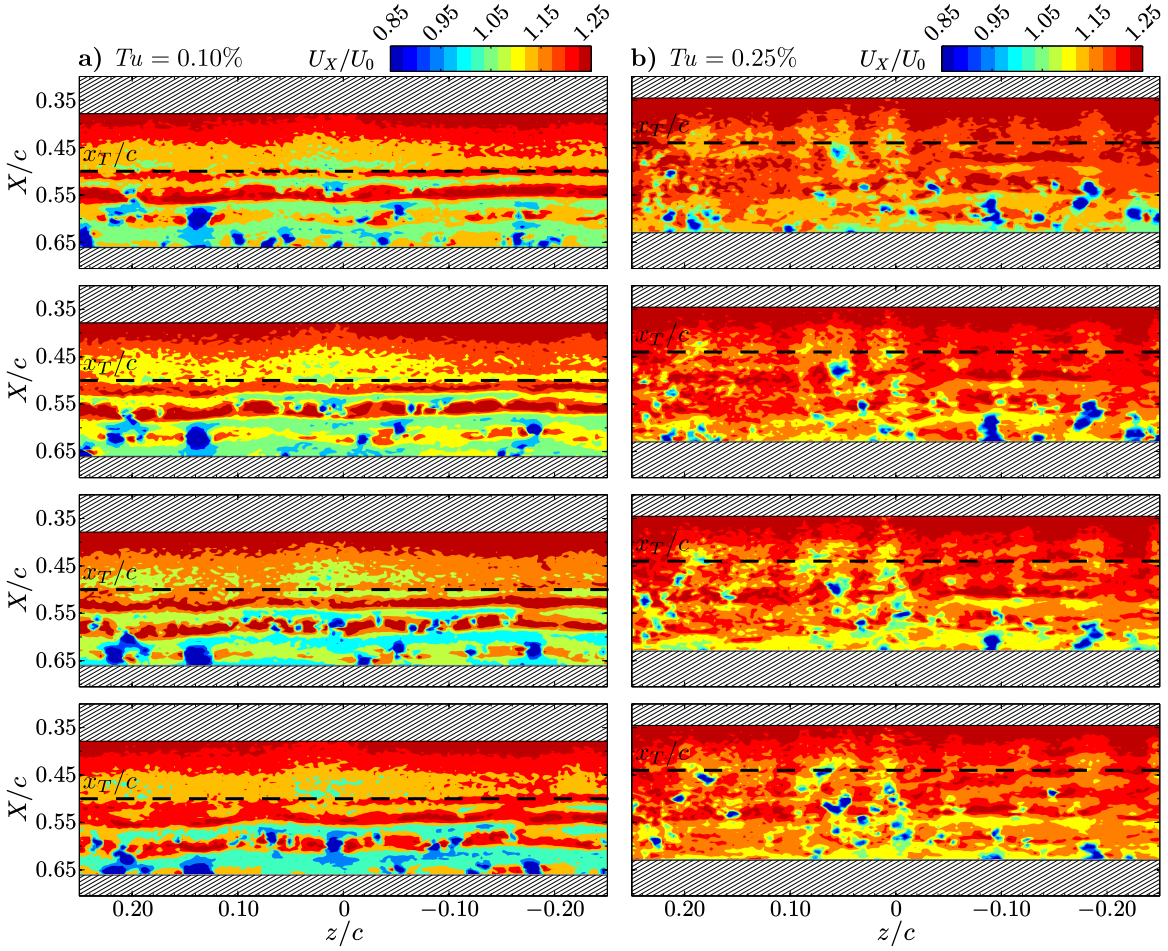

Figure 5.19: Contours of instantaneous chordwise velocity for $Re_c = 125\,000$. Consecutive snapshots are separated by 0.51 ms. Dashed black lines mark the locations of mean transition as determined from the displacement thickness.

For increasing levels of Tu at $Re_c = 125\,000$, the shear layer rollers become increasingly deformed at roll-up and also more difficult to identify, consistent with the results at $Re_c = 80\,000$ (Fig. 5.18). At the highest Tu level, the flow is dominated by several streamwise oriented streaks, and identification of the shear layer rollers becomes challenging. The dominance of the streaks at the highest level of Tu is similar to that observed at the lower Reynolds number, but here appear larger and lead to the highly energetic first mode of the side view POD characterized by a large streamwise wavelength (Fig. 5.13d).

The results in Figs. 5.18 and 5.19 show that, for all cases investigated, shear layer rollers

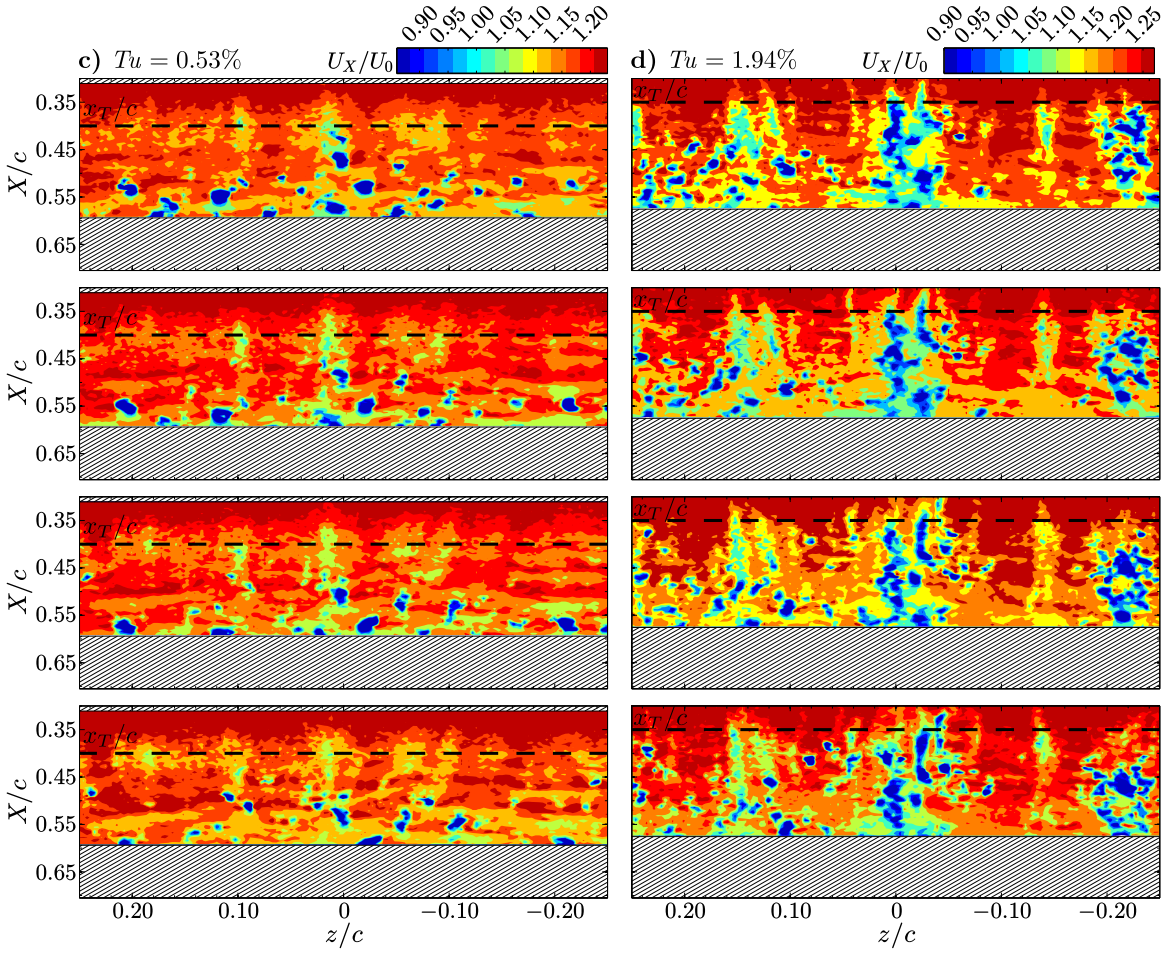

Figure 5.19 (cont.)

are identifiable but their spanwise coherence is significantly affected by both Tu and Re_c. In order to compare the spanwise coherence of these structures, coherence length estimates across the span of the PIV measurements are computed for all streamwise locations, as per the method discussed by Kurelek [20]. Specifically, spanwise correlation coefficients of the chordwise velocity signals are computed along the span at a givent streamwise location. An exponential fit is then applied to these correlation coefficients, and is integrated from zero to infinity to yield an estimation of the spanwise coherence length at that given streamwise location. The results for all streamwise locations and all cases investigated are presented in Fig. 5.20. It should be noted that the resolution of the PIV vectors in this configuration is equivalent to $\ell_z/c \approx 10^{-3}$, and thus the results in Fig. 5.20 below approximately $\ell_z/c \approx 10^{-2}$

become increasingly affected by the sparse data. In addition, as discussed by Kurelek [20], upstream of the mean transition location, velocity fluctuations are characterized by relatively low amplitudes (Fig. 5.6), and thus the correlations are significantly affected by measurement uncertainty. Therefore, the coherence length estimates upstream of the location of mean transition are shown by dashed lines in Fig. 5.20. The flow condition of $Re_c = 125\,000$ and $Tu = 0.10\%$ is the same as that studied by Kurelek [20], and the results computed here are in good agreement with his reported results.

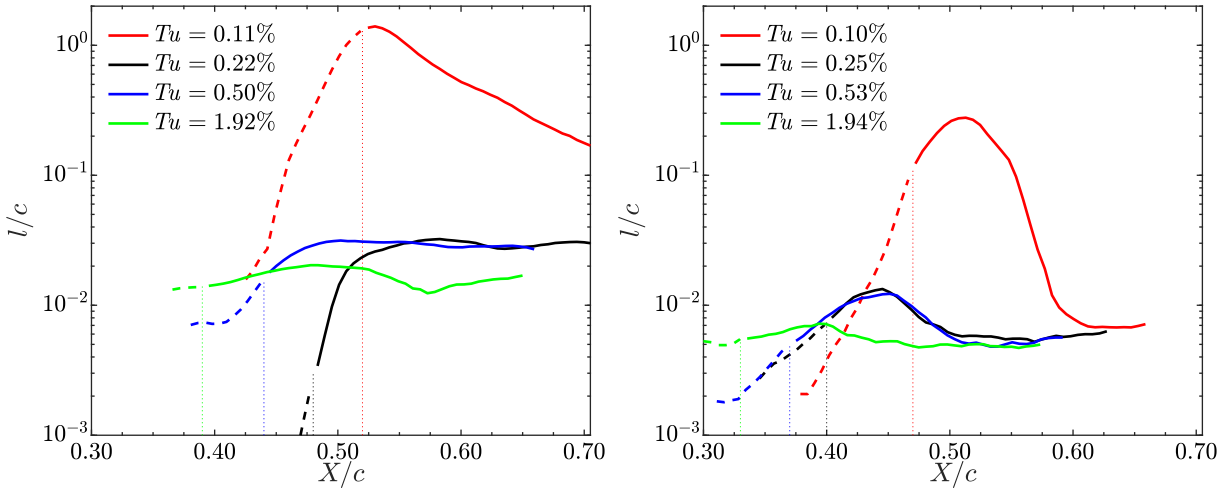

(a) $Re_c = 80\,000$ **(b)** $Re_c = 125\,000$

Figure 5.20: Spanwise coherence lengths. Dotted lines correspond to the locations of mean transition.

At $Re_c = 80\,000$ (Fig. 5.20a), the results show that, at the baseline Tu level, the maximum coherence length is on the order of the airfoil chord length, consistent with the strong coherence observed at roll-up in Fig. 5.18a. For this Reynolds number, the maximum estimated coherence length decreases by an order of magnitude when the level of Tu is increased from the baseline level to $Tu = 0.22\%$. Notably smaller reductions in the maximum of the coherence length estimates are observed for the increases in Tu to 0.50% and 1.92%. The maximum coherence length estimates for all Tu levels and both chord Reynolds numbers investigated are summarized in Table 5.4. The results for the higher Reynolds number show a similar trend to the lower Reynolds number, with a decrease in the maximum coherence length of approximately an order of magnitude for increasing Tu from 0.10% to 0.25%. The decrease in coherence length maximum can be attributed to the

increase in the spanwise deformations of the shear layer rollers at the location of roll-up, as observed in Figs. 5.18 and 5.19. The results in Fig. 5.20 also show that the streamwise location of the maximum coherence length shifts upstream, following the location of mean transition and, therefore, that of the shear layer roll-up location. Comparing the results for a given Tu level, it is observed that the maximum coherence length decreases with increasing Reynolds number for all Tu levels investigated. The observed decrease in spanwise coherence is consistent with the increase in initial spanwise deformations at the higher Reynolds numbers, as observed by comparing the contours of instantaneous streamwise velocity at the two Reynolds numbers for a given level of Tu (Figs. 5.18 and 5.19).

In order to compute a spanwise wavelength of the dominant spanwise deformations of the rollers, a methodology discussed by Michelis *et al.* [137] was followed. Due to the limited spanwise extent of the PIV field-of-view, this method makes use of a wavelet analysis, using a Morlet wavelet at the base function. For all cases, the chordwise velocity signal at the chordwise location of mean transition was taken to be the signal on which the spatial wavelet analysis was performed. Then, for each snapshot in the PIV sequence, the wavelength corresponding to the maximum wavelet coefficient returned by the wavelet analysis was recorded. The average of these wavelengths was computed and taken to be the dominant wavelength of the spanwise deformations, with the results summarized in Table 5.4. The result for the baseline Tu level at $Re_c = 80\,000$ is in good quantitative agreement with observations in the consecutive snapshots of instantaneous chordwise velocity presented in Fig. 5.18a. For example, in the second frame, the roller at $X/c \approx 0.62$ has a spanwise wavelength of approximately 0.15 which is in good agreement with the estimate of 0.125 from the wavelet analysis (Table 5.4). At $Tu = 0.22\%$, the wavelength of the spanwise deformations is notably smaller than at the baseline Tu level (compare Figs. 5.18a and 5.18b), and is reflected by the decrease in the estimated wavelength from the wavelet analysis. As the level of Tu is increased further, comparing the wavelet results to the contours of instantaneous chordwise velocity becomes more challenging. In considering the ratio of the spanwise wavelength to the streamwise wavelength (λ_z/λ_x), the results at $Re_c = 80\,000$ generally fall within the range of $1.8 \lesssim \lambda_z/\lambda_x \lesssim 2.2$, which is in reasonable agreement with previous investigations of separation bubbles [18, 44, 137]. The results at the higher chord Reynolds number are in good agreement at the baseline Tu level, but are difficult to compare to the contours of instantaneous velocity for all elevated Tu levels. However, for all Tu levels, the ratio of the spanwise wavelength of the rollers to the streamwise wavelength remains in reasonable agreement with the range expected from previous investigations of separation bubbles [18, 44, 137].

Similarly to the streamwise flow development analysis in Section 5.2, a POD can be performed on the fluctuating velocity fields as measured using the top view PIV system.

This type of analysis aids in providing a description of the flow structures associated with the most significant amount of fluctuating velocity energy. For all Tu levels investigated at $Re_c = 80\,000$, relative and cumulative modal energies are shown in Fig. 5.21, while the spatial distributions of a select number of the eigenfunctions are shown in Fig. 5.22, with spectra of the temporal coefficients for the first six modes shown in Fig. 5.23. Here, the first six modes are made up of three sets of paired modes (*i.e.*, $\psi^{(1)}$ and $\psi^{(2)}$, $\psi^{(3)}$ and $\psi^{(4)}$, and $\psi^{(5)}$ and $\psi^{(6)}$), and, therefore, for conciseness only the spatial distributions of the first, third, and fifth modes are presented in Fig. 5.22.

At the baseline Tu level, the first two POD modes are paired, evidenced by the similar energy content (Fig. 5.21a) and the similarity of the spatial distributions of the eigenfunctions, which have a $\pi/2$ phase shift (the second mode is not shown here). The spatial distributions of these modes show good qualitative agreement with the shear layer rollers visualized in the consecutive snapshots of instantaneous chordwise velocity (Fig. 5.18a), and spectra of the temporal coefficients for these two modes show a peak at the central disturbance frequency of the separation bubble. These findings therefore indicate that these two modes describe the convection of the shear layer rollers. Modes 3 and 4, as well as 5 and 6, also form modal pairs and contain significant energy near the central frequency of the separation bubble, as well as at the subharmonic frequency (Fig. 5.23a). The streamwise wavelength of the energy within the spatial distribution of the third mode ($\psi^{(3)}$) increases with increasing X (Fig. 5.22a). At the most upstream location of the energy within the mode, the wavelength is on the order of the shear layer rollers (*i.e.*, similar to the characteristic wavelength in mode 1). Downstream, the wavelength increases and is approximately twice the initial wavelength at the most downstream portion of the PIV

Table 5.4: Summary of transition characteristics. Uncertainty intervals are summarized in Appendix A.

Reynolds number	Tu [%]	$l/c\|_{max}$	λ_z/c	λ_z/λ_x
80 000	0.11	$1.419 \pm 6\%$	0.125	2.19
	0.22	$0.033 \pm 6\%$	0.100	1.79
	0.50	$0.032 \pm 6\%$	0.105	1.75
	1.92	$0.021 \pm 6\%$	0.134	2.06
125 000	0.10	$0.278 \pm 6\%$	0.124	3.18
	0.25	$0.014 \pm 6\%$	0.144	3.13
	0.53	$0.013 \pm 6\%$	0.144	3.06
	1.94	$0.008 \pm 6\%$	0.060	1.28

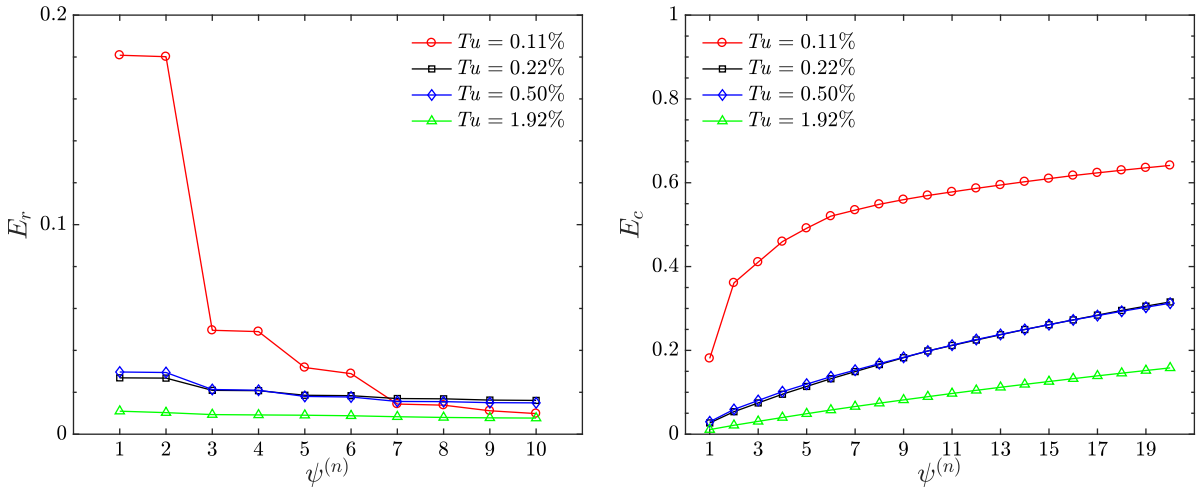

(a) **(b)**

Figure 5.21: (a) relative and (b) cumulative modal energy of the top view POD eigenvalues for $Re_c = 80\,000$.

field-of-view. Therefore, this result suggests that the third and fourth POD modes describe merging of the shear layer rollers, since the merging events typically occur in the aft portion or downstream of the bubble, where the wavelength of the energy is doubled.

As the level of free-stream turbulence intensity is increased to $Tu = 0.25\%$ and 0.53%, similar pairing within the first six POD modes is observed, as indicated in Fig. 5.21a and confirmed by a comparison of the spatial distributions of the modes. In general, the spatial distributions of these first six modes (Figs. 5.22b and 5.22c) reflect the increase in spanwise non-uniformity observed in the shear layers rollers at the location of roll-up in the consecutive snapshots of instantaneous chordwise velocity (Fig. 5.18). For both Tu levels, spectra of the temporal coefficients for the first six modes are characterized by a relatively broad peak near the central disturbance frequency of the separation bubble, with no discernible peaks at the subharmonic frequency, suggesting that vortex merging contributes much less of the fluctuating energy at these Tu levels.

Consistent with the side view POD results, the cumulative energy distributions of the POD modes from the top view show that the fluctuating energy becomes distributed over a greater number of modes as the level of Tu is increased (Fig. 5.21b). At $Tu = 0.11\%$, the first twenty modes capture approximately 64% of the fluctuating velocity energy. As the level of Tu is increased, the relative energy content of the first twenty modes is decreased to 32% for $Tu = 0.22\%$ and 0.50%, and to 16% for $Tu = 1.92\%$. In addition, the relative

energy content of the first two modes, the paired modes associated with the shear layer rollers, decreases significantly with increasing Tu (Fig. 5.21a). This result is also consistent with the side view POD results (Fig. 5.12a), where the energy associated with the shear layer rollers is contained in progressively higher mode numbers with increasing Tu.

At the highest Tu level investigated, a significant change in the spatial distributions of the first two POD modes is observed (Fig. 5.22d). For this Tu level, the first two modes are paired, unlike the side view results where the first POD mode was unpaired, but now represent the streamwise streaks which were observed in Fig. 5.18d. This change in topology of the first two POD modes highlights the change in bubble dynamics at the highest Tu level. The spatial distributions of ψ_1 and ψ_2 are characterized by elongated chordwise distributions of energy in both the u_X and w components. Additionally, spectra of the temporal coefficients for these two modes are dominated by low frequency activity with no distinct peaks observed at any frequency (Fig. 5.23d). Therefore, it can be concluded that the first two modes represent the streamwise oriented streaks (Fig. 5.18d) which are associated with a large characteristic streamwise wavelength. If cut in a streamwise plane, representing the side view PIV measurements, these modes would yield a mode topology similar to that of ψ_1 in Fig. 5.13d. Therefore, the results presented here suggest that the similar side view POD mode presented by Simoni *et al.* [38] at a high level of Tu does likely represent streaks, though the authors did not show this explicitly. At this Tu level, spectra of the temporal coefficients for $\psi^{(3)}$, $\psi^{(4)}$, and $\psi^{(5)}$ show peaks near the central disturbance frequency of the bubble, indicating that they are representative of the shear layer rollers. The spatial distributions for $\psi^{(3)}$ and $\psi^{(5)}$ at this elevated Tu level (Fig. 5.22d) highlight the drastic reduction in the spanwise coherence of the shear layer rollers, as was observed in Fig. 5.18d.

A POD analysis was also performed for the higher chord Reynolds number, but is not presented here for the sake of brevity. Very similar trends are observed in the data with increasing Tu, but the modes become less clear at the higher Tu levels, and specifically at the highest Tu level investigated. The modes are however included in Appendix E for completeness.

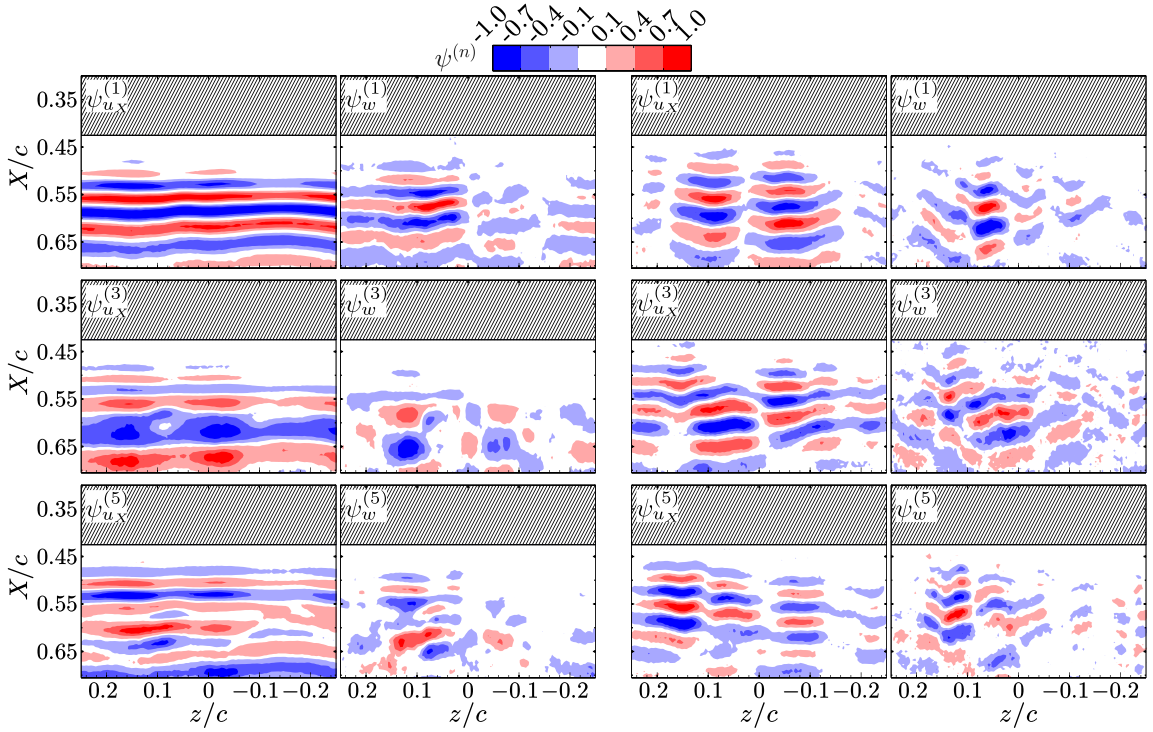

a) $Tu = 0.11\%$ **b)** $Tu = 0.22\%$

Figure 5.22: Contours of the streamwise and wall-normal components of the spatial POD modes at $Re_c = 80\,000$.

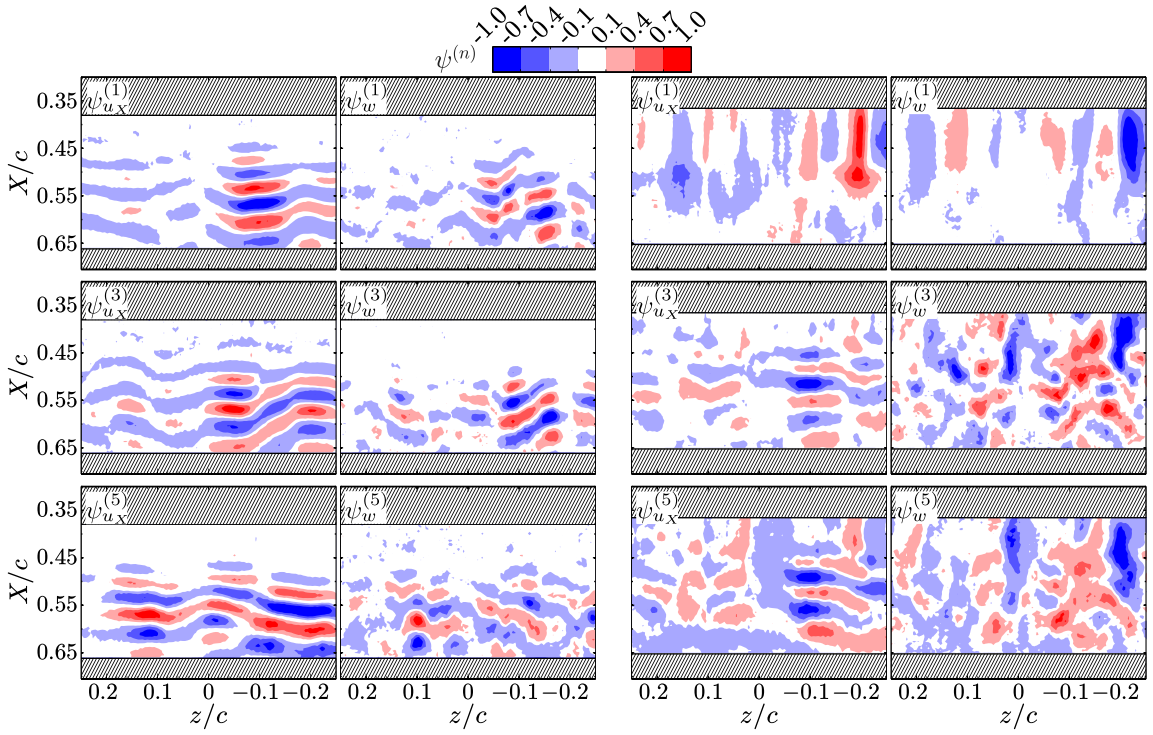

c) $Tu = 0.50\%$ **d)** $Tu = 1.92\%$

Figure 5.22 (cont.)

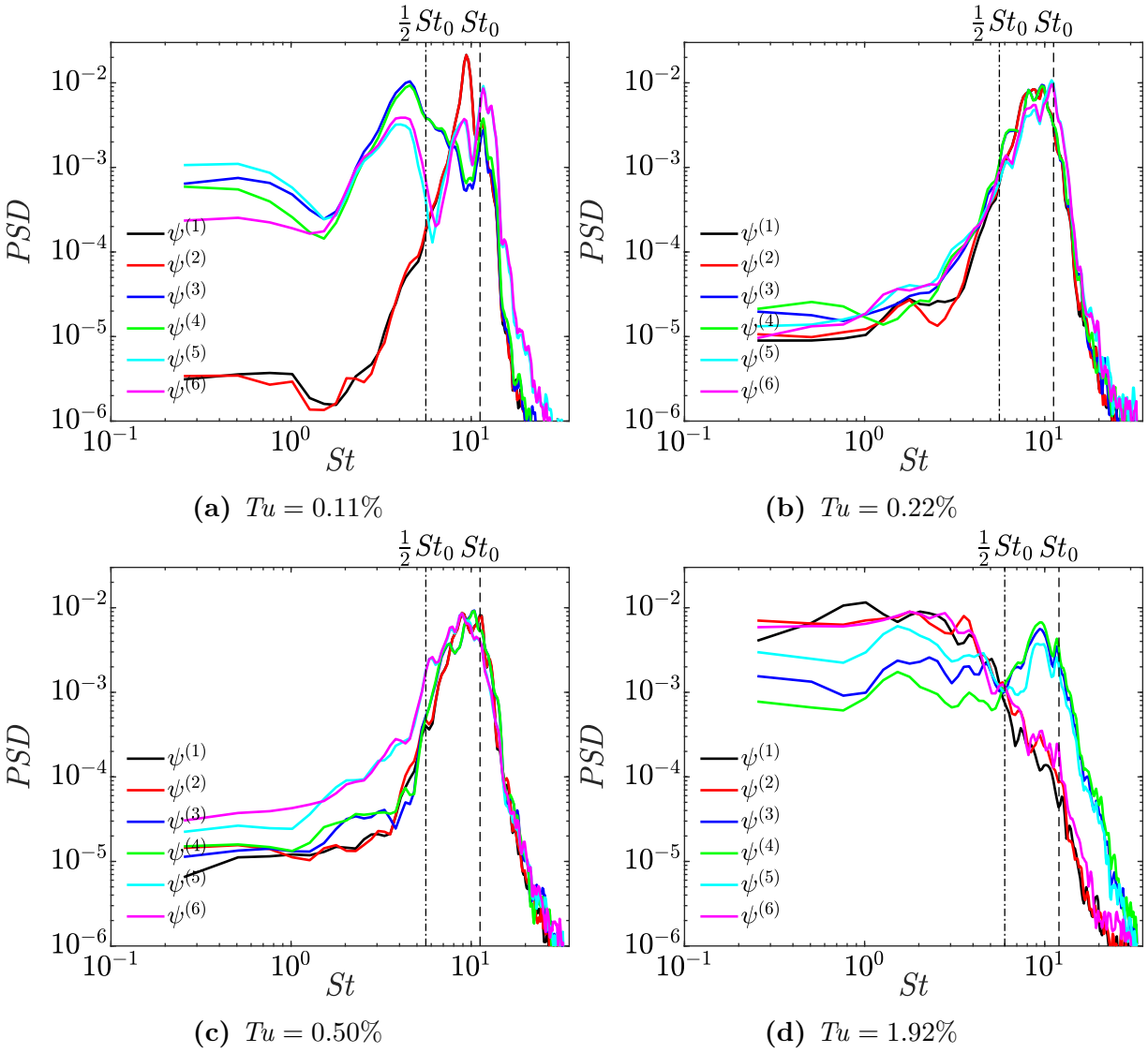

(a) $Tu = 0.11\%$ **(b)** $Tu = 0.22\%$

(c) $Tu = 0.50\%$ **(d)** $Tu = 1.92\%$

Figure 5.23: Frequency spectra of time coefficients corresponding to the first six POD modes at $Re_c = 80\,000$. Spectrum for each mode are normalized by the total energy within the signal. The central disturbance frequency and its subharmonic were determined from wall-normal velocity fluctuations and are summarized in Table 5.3.

Chapter 6

Conclusions

The effects of free-stream turbulence intensity on the flow over a NACA 0018 airfoil were studied experimentally in a wind tunnel facility. Chapter 4 presented results from a parametric study performed for chord Reynolds numbers from 100 000 to 200 000, angles of attack from 0° to 20°, and free-stream turbulence intensities from 0.09% to 2.03% using mean and fluctuating surface pressure measurements. The results revealed the effects of each parameter on suction side laminar separation bubble topology and separated shear layer transition characteristics, as well as the attendant changes in airfoil lift. In Chapter 5, results from flow field measurements made using Particle Image Velocimetry (PIV) were presented in order to assess the spatio-temporal flow development in both the streamwise and spanwise directions within a laminar separation bubble. Measurements were made for an angle of attack of 4°, Reynolds numbers of 80 000 and 125 000, and free-stream turbulence intensities ranging from 0.10% to 1.94% in order to distinguish between Reynolds number and turbulence intensity effects.

6.1 Low Reynolds Number Flow Over an Airfoil and the Effects of Turbulence Intensity

Results from the parametric study show that increasing the level of free-stream turbulence intensity leads to a reduction in separation bubble length, largely due to an upstream shift in mean transition and, consequently, mean reattachment. At low angles of attack, the reduction in separation bubble length leads to a slight reduction in airfoil lift due to the reduction in local suction over the airfoil. However, at pre-stall angles of attack, the reduction in separation bubble length alleviates the loss of suction at the location of the

suction peak, thereby increasing lift, and can delay stall. The main factors in determining airfoil lift are the length of the separation bubble and its location on the surface of the airfoil in relation to the suction peak. At higher chord Reynolds numbers, the effects of increasing free-stream turbulence intensity are reduced, as increases in either parameter have similar effects on mean bubble topology. While the effects of these two parameters on mean bubble topology and airfoil lift are similar, the underlying effects on the separated shear layer transition process differ substantially.

An analysis of fluctuating surface pressure measurements shows that at elevated levels of free-stream turbulence intensity, disturbances reach maximum values earlier upstream, leading to the upstream shift in the location of mean transition. The results also show that spatial amplification rates are decreased at higher turbulence intensity levels, attributed to the decreased bubble size. Despite the increased stability, mean transition shifts upstream, which is therefore solely a result of the larger initial amplitude of perturbations at the elevated levels of free-stream turbulence intensity. In contrast, the decrease in mean bubble size resulting from increased chord Reynolds numbers is due to an increase in spatial amplification rates, *i.e.*, due to a less stable bubble. This difference is a key in differentiating the effects of increased turbulence intensity from those of increased chord Reynolds number on formed separation bubbles.

Frequency spectra of the fluctuating surface pressures show that, as the level of free-stream turbulence intensity is increased, the band of detectable amplified frequencies in the separated shear layer broadens. This broadening is the result of a higher energy content over a broader range of frequencies in the free-stream at the higher levels turbulence intensity, leading to earlier detectable levels of perturbations in the separated shear layer over a broader range. An initial decrease in the most amplified disturbance frequency is observed for increasing the free-stream turbulence intensity to moderate levels ($Tu \leq 0.50\%$), in agreement with flow stability considerations reported in previous studies on laminar separation bubbles. At the higher turbulence intensity levels investigated, an increase in the most unstable frequency of the bubble is observed, in addition to an apparent suppression of separation at lower angles of attack. The combination of these results suggest that the transition process over the suction side of the airfoil is altered at elevated levels of free-stream turbulence intensity, which is shown to be due to bypass transition taking place in the boundary layer upstream of separation by detailed PIV measurements.

6.2 Free-stream Turbulence Intensity Effects on Separation Bubble Flow Development

Flow field measurements with PIV are compared to mean surface pressure distributions for $Re_c = 80\,000$ in order to compare estimations of mean bubble topology using the two methods. The results show that estimations of mean separation, transition, and reattachment using both methods are within $\pm 0.02c$ (6% of the predicted separation bubble length) at the baseline level of free-stream turbulence intensity. When the level of turbulence intensity is increased to 0.50% and the length of the separation bubble decreases, both methods are impacted by increasing measurement uncertainty, and the agreement of the mean separation and reattachment locations falls to be within $\pm 0.09c$. This uncertainty corresponds to about the length of the bubble estimated with the PIV measurements, or about half of that estimated with the mean surface pressure measurements. The estimation of mean transition remains within $\pm 0.02c$. Therefore, while it is difficult to quantify which method gives a more accurate representation of the bubble topology with increasing Tu, both methods estimate a decrease in separation bubble length, as well as an accurate estimation of mean transition.

Velocity fluctuations along the boundary layer displacement thickness reveal that larger velocity fluctuation amplitudes are detected earlier upstream as the level of turbulence intensity or Reynolds number are increased. This leads to the upstream shift in mean transition, as was discussed in Section 6.1 based on fluctuating surface pressure measurements. In addition, significant streamwise velocity fluctuations are detected upstream of the separation bubble at the highest level of turbulence intensity investigated. Spatial amplification rates computed using velocity fluctuation amplitudes decrease with increasing turbulence intensity and increase with increasing Reynolds number, consistent with the conclusions drawn using fluctuating surface pressure measurements (Section 6.1). Therefore, the upstream shift in mean transition with increasing turbulence intensity is a result of larger initial amplitudes of perturbations at the elevated turbulence intensity levels, while it is associated with decreased bubble stability at higher Reynolds numbers. Two-dimensional wavenumber-frequency spectra of the velocity fluctuations along the boundary layer displacement thickness show that the energy associated with the velocity fluctuations becomes more broadband in both time and space with increasing turbulence intensity, extending the conclusion of disturbances becoming more broadband in time discussed in Section 6.1. Average streamwise wavelengths and convective velocities of disturbances increase with increasing free-stream turbulence intensity, with the latter ascribed to the increase in the average separated shear layer velocity as the bubble size is reduced. As a result, the fundamental disturbance frequency of the separation bubble is relatively constant for moderate

increases in the free-stream turbulence intensity, despite significant changes in mean bubble topology. The dominant streamwise wavelength of disturbances and central disturbance frequency both increase with increasing chord Reynolds number.

Roll-up of the separated shear layer becomes less coherent across the span of the airfoil as the level of free-stream turbulence intensity is increased, showing similarities with previous investigations performed in elevated disturbance environments. As the rollers convect downstream, the spanwise deformations are amplified and ultimately lead to the breakdown of the structures. This breakdown occurs sooner at elevated levels of turbulence intensity due to the initial deformation of the structures at roll-up. Increasing the chord Reynolds number also increases the initial amplitude of the spanwise undulations, leading to sooner vortex breakdown. Average wavelengths of the spanwise deformations are found to be in good agreement with previous investigations of separation bubbles for all turbulence intensity levels investigated. At elevated levels of turbulence intensity streamwise streaks of low speed fluid are observed, originating in the boundary layer upstream of the separation bubble, with the streaks most notable at the highest level of turbulence intensity investigated.

A Proper Orthogonal Decomposition (POD) performed on the fluctuating velocity fields measured in both the side and top view PIV configurations shows that, as the level of turbulence intensity is increased, the energy of the velocity fluctuations is spread over a larger number of modes, consistent with the observed decrease in shear layer roller coherence. At the baseline turbulence intensity level, the two most energetic modes in both PIV configurations are paired, and are shown to represent the velocity fluctuations associated with the shear layer rollers. As the level of turbulence intensity is increased, the modes associated with the shear layer rollers shift to higher mode numbers, indicating that they represent less fluctuating velocity energy. At the highest turbulence intensity level investigated, the most energetic mode in the side view POD is characterized by a large wavelength, dominated by low frequencies in the spectra of the POD temporal coefficient. In the top view POD, the first two modes at the highest level of turbulence intensity investigated are paired and represent the streamwise streaks. Increasing the Reynolds number does not significantly change the topology of the POD modes, but does lead to a shift in the modes describing the shear layer rollers to higher mode numbers.

At the highest turbulence intensity level investigated, the sum of the side and top view results show that while a separation bubble does still form, the dynamics are altered significantly from those observed at lower turbulence intensity levels. Notably, streamwise streaks form upstream of the separation bubble, as a result of bypass transition in the boundary layer, and lead to significant streamwise velocity fluctuations upstream of the separation bubble, and alter the flow dynamics within the bubble itself, and ultimately leading to changes in the transition characteristics of the separated shear layer.

Chapter 7

Recommendations

From the conclusions of the present investigation, the following recommendations for continued work are made:

1. The results in this thesis clearly demonstrate that the effects of free-stream turbulence intensity must be considered in engineering designs employing low Reynolds number airfoils. Specifically, the lift was shown to decrease at low angles of attack and increase at pre-stall angles of attack with increasing free-stream turbulence intensity, a finding which must be considered by designers. In addition, the transition process in the separated shear layer is affected by increasing free-stream turbulence intensity, and thus care should be taken in simulations to properly model expected free-stream turbulence intensities.
2. Employing a form of a controllable turbulence generating grid could offer the possibility of studying transient effects of free-stream turbulence intensity on separation bubbles and the attendant changes in airfoil performance, thus being representative of gusts and atmospheric turbulence. Coupled with force balance measurements enabling time-resolved force measurements, this experimental configuration would give the investigator the ability to measure performance over a range of free-stream and operating conditions.
3. Determining the level of free-stream turbulence intensity at which laminar separation is suppressed would also be of practical interest. At this high level of free-stream turbulence intensity, the flow would be turbulent beginning near the leading edge of the airfoil and would therefore be comparable to flow at high Reynolds numbers.
4. The focus of this investigation was on the effects of free-stream turbulence intensity on separation bubbles, and thus the effects of the length scale of the turbulence for a given level of intensity should be investigated. While some previous investigations

have considered this problem and suggest that the effects of the turbulent length scale are less significant than those of the intensity [39, 53], it would be worthwhile to revisit the problem with more powerful measurements techniques such as PIV.

5. A stability analysis of the mean fields measured in the present investigation should be completed and compared to other investigations which induce a mean flow deformation via controlled disturbances. This analysis will enable a comprehensive comparison of stability characteristics of separation bubbles subjected to different forms of forcing. Specifically, comparisons to other forms of broadband forcing would be insightful.
6. Due to the increasing three-dimensionality of the flow with increasing free-stream turbulence intensity, further insight into separation bubble dynamics at elevated levels of free-stream turbulence intensity would benefit greatly from three-dimensional measurements or simulations. The planar measurements of the current investigation are insightful but measurements with tomographic PIV for example would enable a more complete characterization of the separation bubble flow development.
7. Clear evidence of streamwise streaks forming at the higher levels of free-stream turbulence intensity was observed, with these streaks originating upstream of the separation bubble. Boundary layer measurements over the fore portion of the airfoil could provide quantification of these streaks, but would also provide insight into fluctuations present in the boundary layer at all other levels of free-stream turbulence intensity investigated. These measurements could be made via hot-wire anemometry and would give some insight into the receptivity process at the airfoil leading edge, as well as how the perturbations develop within the boundary layer upstream of the separation bubble.
8. Performing a similar experimental campaign as the PIV investigation here, but over a different airfoil geometry would be of benefit. A good candidate airfoil should have a notably different pressure distribution over the suction side, resulting in different separation bubble dynamics. This will help to shed light on the effect of the pressure gradient on separation bubble dynamics, and the influence of free-stream turbulence intensity.

Letter of Copyright Permission

UNIVERSITY OF WATERLOO

FACULTY OF ENGINEERING | Mechanical and Mechatronics Engineering
519-888-4567, ext. 33328 | fax 519-888-4351
mme.uwaterloo.ca

July 26, 2017

Dear Mark Istvan,

This letter serves as permission for you to publish content from the following papers, in full or in part, in your MASc thesis:

1. M.S. Istvan, J. Kurelek, and S. Yarusevych, "Effects of free-stream turbulence intensity on laminar separation bubbles," 46th AIAA Fluid Dynamics Conference, 2016.

2. M.S. Istvan and S. Yarusevych, "Effects of free-stream turbulence intensity on transition within a laminar separation bubble," 10th International Symposium on Turbulence and Shear Flow Phenomena, 2017.

3. M.S. Istvan and S. Yarusevych, "Free-stream turbulence effects on transition within a laminar separation bubble," 47th AIAA Fluid Dynamics Conference, 2017.

Sincerely yours,

Serhiy Yarusevych, Ph.D., P.Eng.,

Associate Professor
Department of Mechanical and Mechatronics Engineering
University of Waterloo
200 University Avenue West
Waterloo, On, Canada, N2L 3G1
Phone: (519) 888-4567 x35442
Fax: (519) 885-5862
E-mail: syarus@uwaterloo.ca
Web: http://www.fmrl.uwaterloo.ca

References

[1] E. N. Jacobs and A. Sherman. Airfoil Section Characteristics as Affected by Variations of the Reynolds Number. Technical report. NACA, 1937. URL. ↩

[2] I. H. Abbott, A. E. von Doenhoff, and L. S. J. Stivers. Summary of airfoil data. Technical report. National Advisory Committee for Aeronautics, 1945. URL. ↩

[3] B. H. Carmichael. Low Reynolds number airfoil survey, volume 1. Technical report. NASA, 1981. URL. ↩

[4] P. B. S. Lissaman. Low-Reynolds-Number airfoils. *Annu. Rev. Fluid Mech.*, 15(1):223–239, 1983. DOI. ↩

[5] P. Owen and L. Klanfer. On the Laminar Boundary Layer Separation from the Leading edge of a Thin Aerofoil. Technical report. Aeronautical Research Council, 1953. URL. ↩

[6] I. Tani. Low-speed flows involving bubble separations. *Prog. Aerosp. Sci.*, 5:70–103, 1964. DOI. ↩

[7] M. Gaster. The Structure and Behaviour of Laminar Separation Bubbles. Technical report. Aeronautical Research Council, 1967. URL. ↩

[8] H. Horton. Laminar Separation Bubbles in Two and Three Dimensional Incompressible Flow. PhD thesis. Queen Mary College, 1968. ↩

[9] M. M. O'Meara and T. J. Mueller. Laminar separation bubble characteristics on an airfoil at low Reynolds numbers. *AIAA J.*, 25(8):1033–1041, 1987. DOI. ↩

[10] M. S. Boutilier and S. Yarusevych. Parametric study of separation and transition characteristics over an airfoil at low Reynolds numbers. *Exp. Fluids*, 52(6):1491–1506, 2012. DOI. ↩

[11] G. B. McCullough and D. E. Gault. Examples of three representative types of airfoil-section stall at low speed. Technical report. NACA, 1951. URL. ↩

[12] W. S. Saric, H. L. Reed, and E. J. Kerschen. Boundary-Layer Receptivity to Freestream Disturbances. *Annu. Rev. Fluid Mech.*, 34(1):291–319, 2002. DOI. ↩

[13] O. Marxen, M. Lang, U. Rist, and S. Wagner. A Combined Experimental/Numerical Study of Unsteady Phenomena in a Laminar Separation Bubble. *Flow, Turbul. Combust.*, 71(1):133–146, 2003. DOI. ↩

[14] L. E. Jones, R. D. Sandberg, and N. D. Sandham. Stability and receptivity characteristics of a laminar separation bubble on an aerofoil. *J. Fluid Mech.*, 648:257–296, 2010. DOI. ↩

[15] M. S. Boutilier and S. Yarusevych. Separated shear layer transition over an airfoil at a low Reynolds number. *Phys. Fluids*, 24(8):084105, 2012. DOI. ↩

[16] B. R. McAuliffe and M. I. Yaras. Transition Mechanisms in Separation Bubbles Under Low- and Elevated-Freestream Turbulence. *J. Turbomach.*, 132(1):011004, 2010. DOI. ↩

[17] O. Marxen, M. Lang, and U. Rist. Vortex formation and vortex breakup in a laminar separation bubble. *J. Fluid Mech.*, 728:58–90, 2013. DOI. ↩

[18] J. W. Kurelek, A. R. Lambert, and S. Yarusevych. Coherent Structures in the Transition Process of a Laminar Separation Bubble. *AIAA J.*, 54(8):2295–2309, 2016. DOI. ↩

[19] S. Yarusevych, P. E. Sullivan, and J. G. Kawall. Effect of Acoustic Excitation Amplitude on Airfoil Boundary Layer and Wake Development. *AIAA J.*, 45(4):760–771, 2007. DOI. ↩

[20] J. W. Kurelek. Transition in a Laminar Separation Bubble and the Effect of Acoustic Excitation. MASc. University of Waterloo, 2016. URL. ↩

[21] D. V. Roupassov, A. A. Nikipelov, M. M. Nudnova, and A. Y. Starikovskii. Flow Separation Control by Plasma Actuator with Nanosecond Pulsed-Periodic Discharge. *AIAA J.*, 47(1):168–185, 2009. DOI. ↩

[22] M. L. Post and T. C. Corke. Separation Control Using Plasma Actuators: Dynamic Stall Vortex Control on Oscillating Airfoil. *AIAA J.*, 44(12):3125–3135, 2006. DOI. ↩

[23] S. Yarusevych and M. Kotsonis. Effect of Local DBD Plasma Actuation on Transition in a Laminar Separation Bubble. *Flow, Turbul. Combust.*, 98(1):195–216, 2017. DOI. ↩

[24] S. Yarusevych and M. Kotsonis. Steady and transient response of a laminar separation bubble to controlled disturbances. *J. Fluid Mech.*, 813:955–990, 2017. DOI. ↩

[25] M. A. Feero, S. D. Goodfellow, P. Lavoie, and P. E. Sullivan. Flow Reattachment Using Synthetic Jet Actuation on a Low-Reynolds-Number Airfoil. *AIAA J.*, 53(7):2005–2014, 2015. DOI. ↩

[26] S. Yarusevych, P. E. Sullivan, and J. G. Kawall. On vortex shedding from an airfoil in low-Reynolds-number flows. *J. Fluid Mech.*, 632:245–271, 2009. DOI. ↩

[27] G. Schubauer and H. Skramstad. Laminar-boundary-layer oscillations and transition on a flat plate. Technical report. NACA, 1943, pages 251–292. URL. ↩

[28] T. J. Mueller, P. Conigliaro, and B. J. Jansen. The influence of free-stream disturbances on low Reynolds number airfoil experiments. *Exp. Fluids*, 1(1):3–14, 1983. DOI. ↩

[29] L. L. Pauley, P. Moin, and W. C. Reynolds. The structure of two-dimensional separation. *J. Fluid Mech.*, 220:397–411, 1990. DOI. ↩

[30] P. G. Wilson and L. L. Pauley. Two- and three-dimensional large-eddy simulations of a transitional separation bubble. *Phys. Fluids*, 10(11):2932–2940, 1998. DOI. ↩

[31] S. Burgmann and W. Schröder. Investigation of the vortex induced unsteadiness of a separation bubble via time-resolved and scanning PIV measurements. *Exp. Fluids*, 45(4):675–691, 2008. DOI. ↩

[32] R. Hain, C. Kähler, and R. Radespiel. Dynamics of laminar separation bubbles at low-Reynolds-number aerofoils. *J. Fluid Mech.*, 630:129–153, 2009. DOI. ↩

[33] M. V. Ol, B. R. McAuliffe, E. S. Hanff, U. Scholz, and C. Kähler. Comparison of Laminar Separation Bubble Measurements on a Low Reynolds Number Airfoil in Three Facilities. In *35th AIAA Fluid Dyn. Conf. Exhib.* Toronto, Ontario, 2005. DOI. ↩

[34] D. A. Olson, A. W. Katz, A. M. Naguib, M. M. Koochesfahani, D. P. Rizzetta, and M. R. Visbal. On the challenges in experimental characterization of flow separation over airfoils at low Reynolds number. *Exp. Fluids*, 54(2):1470–1480, 2013. DOI. ↩

[35] J. P. Gostelow, A. R. Blunden, and G. J. Walker. Effects of Free-Stream Turbulence and Adverse Pressure Gradients on Boundary Layer Transition. *J. Turbomach.*, 116(3):392–404, 1994. DOI. ↩

[36] R. E. Walraevens and N. A. Cumpsty. Leading Edge Separation Bubbles on Turbomachine Blades. *J. Turbomach.*, 117(1):115–125, 1995. DOI. ↩

[37] S. Lardeau, M. Leschziner, and T. A. Zaki. Large Eddy Simulation of transitional separated flow over a flat plate and a compressor blade. *Flow, Turbul. Combust.*, 88(1):19–44, 2012. DOI. ↩

[38] D. Simoni, D. Lengani, M. Ubaldi, P. Zunino, and M. Dellacasagrande. Inspection of the dynamic properties of laminar separation bubbles: free-stream turbulence intensity effects for different Reynolds numbers. *Exp. Fluids*, 58(6):66, 2017. DOI. ↩

[39] N. Cao, D. S.-K. Ting, and R. Carriveau. The Performance of a High-lift Airfoil in Turbulent Wind. *Wind Eng.*, 35(2):179–196, 2011. DOI. ↩

[40] W. B. Roberts. The Effect of Reynolds Number and Laminar Separation on Axial Cascade Performance. *J. Eng. Power*, 97(2):261–273, 1975. DOI. ↩

[41] W. Timmer. Two-dimensional low-Reynolds number wind tunnel results for airfoil NACA 0018. *Wind Eng.*, 32(6):525–537, 2008. DOI. ↩

[42] L. E. Jones, R. D. Sandberg, and N. D. Sandham. Direct numerical simulations of forced and unforced separation bubbles on an airfoil at incidence. *J. Fluid Mech.*, 602:175–207, 2008. DOI. ↩

[43] O. Marxen and U. Rist. Mean flow deformation in a laminar separation bubble: separation and stability characteristics. *J. Fluid Mech.*, 660:37–54, 2010. DOI. ↩

[44] O. Marxen and D. S. Henningson. The effect of small-amplitude convective disturbances on the size and bursting of a laminar separation bubble. *J. Fluid Mech.*, 671:1–33, 2011. DOI. ↩

[45] P. Bagade, S. Krishnan, and T. Sengupta. DNS of Low Reynolds Number Aerodynamics in the Presence of Free Stream Turbulence. *Front. Aerosp. Eng.*, 4(1):20–34, 2015. DOI. ↩

[46] J. H. Watmuff. Evolution of a wave packet into vortex loops in a laminar separation bubble. *J. Fluid Mech.*, 397:119–169, 1999. DOI. ↩

[47] M. Lang, U. Rist, and S. Wagner. Investigations on controlled transition development in a laminar separation bubble by means of LDA and PIV. *Exp. Fluids*, 36(1):43–52, 2004. DOI. ↩

[48] P. R. Spalart and M. K. Strelets. Mechanisms of transition and heat transfer in a separation bubble. *J. Fluid Mech.*, 403:329–349, 2000. DOI. ↩

[49] U. Maucher, U. Rist, M. Kloker, and S. Wagner. DNS of Laminar-Turbulent Transition in Separation Bubbles. In *High Perform. Comput. Sci. Eng. '99*, 2000, pages 279–294. DOI. ↩

[50] A. V. Dovgal, V. V. Kozlov, and A. Michalke. Laminar boundary layer separation: Instability and associated phenomena. *Prog. Aerosp. Sci.*, 30(1):61–94, 1994. DOI. ↩

[51] U. Rist and U. Maucher. Investigations of time-growing instabilities in laminar separation bubbles. *Eur. J. Mech.*, 21(5):495–509, 2002. DOI. ↩

[52] D. Lengani, D. Simoni, M. Ubaldi, and P. Zunino. POD analysis of the unsteady behavior of a laminar separation bubble. *Exp. Therm. Fluid Sci.*, 58:70–79, 2014. DOI. ↩

[53] R. Hillier and N. J. Cherry. The effects of stream turbulence on separation bubbles. *J. Wind Eng. Ind. Aerodyn.*, 8(1):49–58, 1981. DOI. ↩

[54] M. Kiya and K. Sasaki. Structure of a turbulent separation bubble. *J. Fluid Mech.*, 137:83–113, 1983. DOI. ↩

[55] A. R. Lambert and S. Yarusevych. Characterization of Vortex Dynamics in a Laminar Separation Bubble. *AIAA J.*, 2017. DOI. ↩

[56] K. B. M. Q. Zaman, D. J. McKinzie, and C. L. Rumsey. A natural low-frequency oscillation of the flow over an airfoil near stalling conditions. *J. Fluid Mech.*, 202:403–442, 1989. DOI. ↩

[57] P. Freymuth. On transition in a separated laminar boundary layer. *J. Fluid Mech.*, 25(4):683–704, 1966. DOI. ↩

[58] G. L. Brown and A. Roshko. On density effects and large structure in turbulent mixing layers. *J. Fluid Mech.*, 64(4):775–816, 1974. DOI. ↩

[59] C. D. Winant and F. K. Browand. Vortex pairing: the mechanism of turbulent mixing-layer growth at moderate Reynolds number. *J. Fluid Mech.*, 63(2):237–255, 1974. DOI. ↩

[60] C. M. Ho and L.-S. Huang. Subharmonics and vortex merging in mixing layers. *J. Fluid Mech.*, 119:443–473, 1982. DOI. ↩

[61] G. M. Corcos and F. S. Sherman. The mixing layer: deterministic models of a turbulent flow. Part 1. Introduction and the two-dimensional flow. *J. Fluid Mech.*, 139:29–65, 1984. DOI. ↩

[62] E. N. Fales. A New Laboratory Technique for Investigation of the Origin of Fluid Turbulence. *J. Franklin Inst.*, 259(6):491–515, 1955. DOI. ↩

[63] P. Klebanoff, K. Tidstrom, and L. Sargent. The three-dimensional nature of boundary-layer instability. *J. Fluid Mech.*, 12(1):1–34, 1962. DOI. ↩

[64] T. Herbert. Secondary instability of plane channel flow to subharmonic three-dimensional disturbances. *Phys. Fluids*, 26(4):871–874, 1983. DOI. ↩

[65] H. Schlichting and K. Gersten. *Boundary-layer theory*. Springer, 8th edition, 2000. DOI. ↩

[66] D. P. Rizzetta and M. R. Visbal. Numerical Investigation of Plasma-Based Control for Low-Reynolds-Number Airfoil Flows. *AIAA J.*, 49(2):411–425, 2011. DOI. ↩

[67] O. Reynolds. An Experimental Investigation of the Circumstances Which Determine Whether the Motion of Water Shall be Direct or Sinuous, and the Law of Resistance in Parallel Channels. *Proc. R. Soc. London*, (35):84–99, 1883. URL. ↩

[68] I. Tani. Boundary-Layer Transition. *Annu. Rev. Fluid Mech.*, 1(1):169–196, 1969. DOI. ↩

[69] L. Prandtl. On the motion of a fluid with very small viscosity. In *Third Int. Congr. Math.* Heidelberg, 1904, pages 484–491. ↩

[70] H. Blasius. The boundary layers in fluids with little friction. Technical report. NACA, 1908. URL. ↩

[71] W. M. Orr. The Stability or Instability of the Steady Motions of a Perfect Liquid and of a Viscous Liquid. Part I: A Perfect Liquid. In *Proc. R. Irish Acad. Sect. A Math. Phys.* Volume 27, 1907, pages 9–68. URL. ↩

[72] A. Sommerfeld. Ein Beitrag zur hydrodynamischen Erklarung der turbulenten Flussigkeitsbewegungen. In *Atti del 4. Congr. Internat. dei Mat.* Volume 3. Roma, 1908, pages 116–124. ↩

[73] W. Tollmien. Über die Eintstehung der Turbulenz. *Nach. Ges. Wiss. Göttingen, Math. Phys. Klasse*:21–44, 1928. DOI. ↩

[74] H. Schlichting. Zur Enstehung der Turbulenz bei der Plattenströmung. *Nachr. Ges. Wiss. Göttingen, Math. Phys. Klasse*:182–208, 1933. URL. ↩

[75] F. R. Hama, J. D. Long, and J. C. Hegarty. On Transition from Laminar to Turbulent Flow. *J. Appl. Phys.*, 28:388–394, 1957. DOI. ↩

[76] B. J. Bayly and S. A. Orszag. Instability Mechanisms in Shear-Flow Transition. *Annu. Rev. Fluid Mech.*, 20(1):359–391, 1988. DOI. ↩

[77] M. Head and P. Bandyopadhyay. New aspects of turbulent boundary-layer structure. *J. Fluid Mech.*, 107:297–338, 1981. DOI. ↩

[78] T. Herbert. Secondary Instability Of Boundary Layers. *Annu. Rev. Fluid Mech.*, 20(1):487–526, 1988. DOI. ↩

[79] Y. S. Kachanov and V. Y. Levchenko. The resonant interaction of disturbances at laminar-turbulent transition in a boundary layer. *J. Fluid Mech.*, 138:209–247, 1984. DOI. ↩

[80] P. R. Spalart and K.-S. Yang. Numerical Simulation of Boundary Layers : Part 2. Ribbon-Induced Transition in Blasius Flow. Technical report. NASA, 1986. DOI. ↩

[81] C. Knapp and P. Roache. A Combined Visual and Hot-Wire Anemometer Investigation of Boundary-Layer Transition. *AIAA J.*, 6(1):29–36, 1968. DOI. ↩

[82] F. P. Bertolotti. Linear and Nonlinear Stability of Boundary Layers with Streamwise Varying Properties. PhD. Ohio State University, 1991. ↩

[83] H. Emmons. The Laminar-Turbulent Transition in a Boundary Layer - Part I. *J. Aeronaut. Sci.*, 18(7):490–498, 1951. DOI. ↩

[84] G. Schubauer and P. Klebanoff. Contributions on the Mechanics of Boundary-Layer Transition. Technical report. NACA, 1956. URL. ↩

[85] G. Taylor. The spectrum of turbulence. In *R. Soc. London. Ser. A, Math. Phys. Sci.* 1937. DOI. ↩

[86] M. V. Morkovin. *On the many faces of transition*. C. Wells, editor. Springer, US, 1969, pages 1–31. DOI. ↩

[87] R. G. Jacobs and P. Durbin. Simulations of bypass transition. *J. Fluid Mech.*, 428:185–212, 2001. DOI. ↩

[88] Y. Liu, T. A. Zaki, and P. Durbin. Boundary-layer transition by interaction of discrete and continuous modes. *J. Fluid Mech.*, 604:199–233, 2008. DOI. ↩

[89] T. A. Zaki and P. Durbin. Mode interaction and the bypass route to transition. *J. Fluid Mech.*, 531:85–111, 2005. DOI. ↩

[90] T. A. Zaki and P. Durbin. Continuous mode transition and the effects of pressure gradient. *J. Fluid Mech.*, 563:357–388, 2006. DOI. ↩

[91] T. A. Zaki. From Streaks to Spots and on to Turbulence: Exploring the Dynamics of Boundary Layer Transition. *Flow, Turbul. Combust.*, 91(3):451–473, 2013. DOI. ↩

[92] K. J. A. Westin, A. V. Boiko, B. G. B. Klingmann, V. V. Kozlov, and P. H. Alfredsson. Experiments in a boundary layer subjected to free stream turbulence. Part 1. Boundary layer structure and receptivity. *J. Fluid Mech.*, 281:193–218, 1994. DOI. ↩

[93] A. V. Boiko, K. J. A. Westin, B. G. B. Klingmann, V. V. Kozlov, and P. H. Alfredsson. Experiments in a boundary layer subjected to free stream turbulence. Part 2. The role of TS-waves in the transition process. *J. Fluid Mech.*, 281:219–245, 1994. DOI. ↩

[94] M. Matsubara and P. H. Alfredsson. Disturbance growth in boundary layers subjected to free-stream turbulence. *J. Fluid Mech.*, 430:149–168, 2001. DOI. ↩

[95] J. H. M. Fransson, M. Matsubara, and P. H. Alfredsson. Transition induced by free-stream turbulence. *J. Fluid Mech.*, 527:1–25, 2005. DOI. ↩

[96] J. H. M. Fransson, L. Brandt, A. Talamelli, and C. Cossu. Experimental study of the stabilization of Tollmien-Schlichting waves by finite amplitude streaks. *Phys. Fluids*, 17(5):054110, 2005. DOI. ↩

[97] P. Durbin and X. Wu. Transition Beneath Vortical Disturbances. *Annu. Rev. Fluid Mech.*, 39:107–128, 2007. DOI. ↩

[98] J. Hunt and P. Durbin. Perturbed vortical layers and shear sheltering. *Fluid Dyn. Res.*, 24(6):375–404, 1999. DOI. ↩

[99] L. Brandt, P. Schlatter, and D. S. Henningson. Transition in boundary layers subject to free-stream turbulence. *J. Fluid Mech.*, 517:167–198, 2004. DOI. ↩

[100] S. Hosseinverdi and H. F. Fasel. Numerical Investigation of the Interaction of Active Flow Control and Klebanoff Modes. In *47th AIAA Fluid Dyn. Conf.* Denver, 2017, pages 1–17. DOI. ↩

[101] C. E. Grosch and H. Salwen. The continuous spectrum of the Orr-Sommerfeld equation. Part 1. The spectrum and the eigenfunctions. *J. Fluid Mech.*, 87(1):33–54, 1978. DOI. ↩

[102] L. Brandt and D. S. Henningson. Transition of streamwise streaks in zero-pressure-gradient boundary layers. *J. Fluid Mech.*, 472:229–261, 2002. DOI. ↩

[103] C. M. Ho and P. Huerre. Perturbed free shear layers. *Annu. Rev. Fluid Mech.*, 16(1):365–424, 1984. DOI. ↩

[104] R. T. Pierrehumbert and S. E. Widnall. The two- and three-dimensional instabilities of a spatially periodic shear layer. *J. Fluid Mech.*, 114:59–82, 1982. DOI. ↩

[105] A. Michalke. Vortex formation in a free boundary layer according to stability theory. *J. Fluid Mech.*, 22(2):371–383, 1965. DOI. ↩

[106] F. K. Browand and P. D. Weidman. Large scales in the developing mixing layer. *J. Fluid Mech.*, 76(1):127–144, 1976. DOI. ↩

[107] F. K. Browand and T. R. Troutt. A note on spanwise structure in the two-dimensional mixing layer. *J. Fluid Mech.*, 97(4):771–781, 1980. DOI. ↩

[108] F. K. Browand. An experimental investigation of the instability of an incompressible, separated shear layer. *J. Fluid Mech.*, 26(2):281–307, 1966. DOI. ↩

[109] A. Michalke. On spatially growing disturbances in an inviscid shear layer. *J. Fluid Mech.*, 23(3):521–544, 1965. DOI. ↩

[110] P. A. Monkewitz and P. Huerre. Influence of the velocity ratio on the spatial instability of mixing layers. *Phys. Fluids*, 25(7):1137–1143, 1982. DOI. ↩

[111] G. M. Corcos and S. J. Lin. The mixing layer: deterministic models of a turbulent flow. Part 2. The origin of the three-dimensional motion. *J. Fluid Mech.*, 139:67–95, 1984. DOI. ↩

[112] R. W. Metcalfe, S. A. Orszag, M. E. Brachet, S. Menon, and J. J. Riley. Secondary instability of a temporally growing mixing layer. *J. Fluid Mech.*, 184:207–243, 1987. DOI. ↩

[113] L.-S. Huang and C. M. Ho. Small-scale transition in a plane mixing layer. *J. Fluid Mech.*, 210:475–500, 1990. DOI. ↩

[114] P. C. Patnaik, F. S. Sherman, and G. M. Corcos. A numerical simulation of Kelvin-Helmholtz waves of finite amplitude. *J. Fluid Mech.*, 73(2):215–240, 1976. DOI. ↩

[115] D. R. Williams and F. R. Hama. Streaklines in a shear layer perturbed by two waves. *Phys. Fluids*, 23(3):442–447, 1980. DOI. ↩

[116] M. A. Hernan and J. Jimenez. Computer analysis of a high-speed film of the plane turbulent mixing layer. *J. Fluid Mech.*, 119:323–345, 1982. DOI. ↩

[117] R. W. Miksad. Experiments on the nonlinear stages of free-shear-layer transition. *J. Fluid Mech.*, 56(4):695–719, 1972. DOI. ↩

[118] C. Chandrsuda, R. D. Mehta, A. D. Weir, and P. Bradshaw. Effect of free-stream turbulence on large structure in turbulent mixing layers. *J. Fluid Mech.*, 85(4):693–704, 1978. DOI. ↩

[119] R. Breidenthal. Structure in turbulent mixing layers and wakes using chemical reaction. *J. Fluid Mech.*, 109:1–24, 1981. DOI. ↩

[120] L. P. Bernal. The Coherent Structure of Turbulent Mixing Layers I. Similarity of the Primary Vortex Structure II. Secondary Streamwise Vortex Structure. PhD dissertation. California Institue of Technology, 1981. URL. ↩

[121] D. Benney and C. Lin. On the Secondary Motion Induced by Oscillations in a Shear Flow. *Phys. Fluids*, 3(4):656–657, 1960. DOI. ↩

[122] S. J. Lin and G. M. Corcos. The mixing layer: deterministic models of a turbulent flow. Part 3. The effect of plane strain on the dynamics of streamwise vortices. *J. Fluid Mech.*, 141:139–178, 1984. DOI. ↩

[123] L. P. Bernal and A. Roshko. Streamwise vortex structure in plane mixing layers. *J. Fluid Mech.*, 170:499–525, 1986. DOI. ↩

[124] J. C. Lasheras, J. S. Cho, and T. Maxworthy. On the origin and evolution of streamwise vortical structures in a plane, free shear layer. *J. Fluid Mech.*, 172:231–258, 1986. DOI. ↩

[125] A. Michalke. A note on spatially growing three-dimensional disturbances in a free shear layer. *J. Fluid Mech.*, 38(4):765–767, 1969. DOI. ↩

[126] J. H. Konrad. An Experimental Investigation of Mixing in Two-Dimensional Turbulent Shear Flows with Applications to Diffusion-Limited Chemical. PhD dissertation. California Institue of Technology, 1977. URL. ↩

[127] P. Bradshaw. The effect of initial conditions on the development of a free shear layer. *J. Fluid Mech.*, 26(2):225–236, 1966. DOI. ↩

[128] J. Jimenez, R. Martinez-Val, and M. Rebollo. On the Origin and Evolution of Three Dimensional Effects in the Mixing Layer. Technical report. Univ. Politec. Madrid, 1979. URL. ↩

[129] I. Wygnanski, D. Oster, H. Fiedler, and B. Dziomba. On the perseverance of a quasi-two-dimensional eddy-structure in a turbulent mixing layer. *J. Fluid Mech.*, 93(2):325–335, 1979. DOI. ↩

[130] S. Mohammadian, M. Saiy, and S. Peerless. Fluid Mixing With Unequal Free-Stream Turbulence Intensities. *J. Fluids Eng.*, 98(2):229–235, 1976. DOI. ↩

[131] N. K. Pui and I. S. Gartshore. Measurements of the growth rate and structure in plane turbulent mixing layers. *J. Fluid Mech.*, 91(1):111–130, 1979. DOI. ↩

[132] S. S. Diwan and O. N. Ramesh. On the origin of the inflectional instability of a laminar separation bubble. *J. Fluid Mech.*, 629:263–298, 2009. DOI. ↩

[133] D. Lengani and D. Simoni. Recognition of coherent structures in the boundary layer of a low-pressure-turbine blade for different free-stream turbulence intensity levels. *Int. J. Heat Fluid Flow*, 54:1–13, 2015. DOI. ↩

[134] M. Alam and N. D. Sandham. Direct numerical simulation of 'short' laminar separation bubbles with turbulent reattachment. *J. Fluid Mech.*, 403:223–250, 2000. DOI. ↩

[135] J. Serna and B. J. Lazaro. On the laminar region and the initial stages of transition in transitional separation bubbles. *Eur. J. Mech. B/Fluids*, 49:171–183, 2015. DOI. ↩

[136] R. Gerakopulos and S. Yarusevych. Novel Time-Resolved Pressure Measurements on an Airfoil at a Low Reynolds Number. *AIAA J.*, 50(5):1189–1200, 2012. DOI. ↩

[137] T. Michelis, M. Kotsonis, and S. Yarusevych. On the origin of spanwise vortex deformations in laminar separation bubbles. *J. Fluid Mech.*, (Under Review). ↩

[138] E. Lamballais, J. Silvestrini, and S. Laizet. Direct numerical simulation of a separation bubble on a rounded finite-width leading edge. *Int. J. Heat Fluid Flow*, 29(3):612–625, 2008. DOI. ↩

[139] E. Lamballais, J. Silvestrini, and S. Laizet. Direct numerical simulation of flow separation behind a rounded leading edge: Study of curvature effects. *Int. J. Heat Fluid Flow*, 31(3):295–306, 2010. DOI. ↩

[140] M. Langari and Z. Yang. Numerical study of the primary instability in a separated boundary layer transition under elevated free-stream turbulence. *Phys. Fluids*, 25(7):074106, 2013. DOI. ↩

[141] T. Yap, M. Abdullah, Z. Husain, Z. Mohd Ripin, and R. Ahmad. The Effect of Turbulence Intensity on the Aerodynamic Perfromance of Airfoils. In *4th Int. Conf. Mech. Eng.* 2001, pages 31–36. ↩

[142] J. A. Hoffmann. Effects of freestream turbulence on the performance characteristics of an airfoil. *AIAA J.*, 29(9):1353–1354, 1991. DOI. ↩

[143] M. Kiya and K. Sasaki. Free-stream turbulence effects on a separation bubble. *J. Wind Eng. Ind. ...*, 14(1):375–386, 1983. DOI. ↩

[144] R. J. Butler, A. R. Byerley, K. VanTreuren, and J. W. Baughn. The effect of turbulence intensity and length scale on low-pressure turbine blade aerodynamics. *Int. J. Heat Fluid Flow*, 22(2):123–133, 2001. DOI. ↩

[145] J. Hunt, A. Wray, and P. Moin. Eddies, streams, and convergence zones in turbulent flows. Technical report. NASA, 1988, pages 193–208. URL. ↩

[146] J. Jeong and F. Hussain. On the identification of a vortex. *J. Fluid Mech.*, 285:69–94, 1995. DOI. ↩

[147] G. Comte-Bellot and S. Corrsin. The use of a contraction to improve the isotropy of grid-generated turbulence. *J. Fluid Mech.*, 25(4):657–682, 1966. DOI. ↩

[148] P. E. Roach. The generation of nearly isotropic turbulence by means of grids. *Int. J. Heat Fluid Flow*, 8(2):82–92, 1987. DOI. ↩

[149] E. M. Laws and J. L. Livesey. Flow Through Screens. *Annu. Rev. Fluid Mech.*, 10(1):247–266, 1978. DOI. ↩

[150] R. Gerakopulos. Investigating flow over an airfoil at low Reynolds numbers using novel time-resolved surface pressure measurements. MASc thesis. University of Waterloo, 2011. URL. ↩

[151] M. S. Boutilier. Experimental Investigation of Transition over a NACA 0018 Airfoil at a Low Reynolds Number. MASc. University of Waterloo, 2011. URL. ↩

[152] T. M. Kirk. The Later Stages of Transition over a NACA0018 Airfoil at a Low Reynolds Number by. MASc. University of Waterloo, 2014. URL. ↩

[153] A. R. Lambert. Vortex Dynamics within the Laminar Separation Bubble over a NACA 0018 Airfoil at Low Reynolds Numbers. MASc. University of Waterloo, 2015. URL. ↩

[154] G. K. Batchelor and A. Townsend. Decay of isotropic turbulence in the initial period. *R. Soc. London. Ser. A, Math. Phys. Sci.*, 193(1035):539–558, 1948. DOI. ↩

[155] P. D. Welch. The Use of Fast Fourier Transform for the Estimation of Power Spectra: A Method Based on Time Averaging Over Short, Modified Periodograms. *IEEE Trans. audio Electroacoust.*, 15(2):70–73, 1967. DOI. ↩

[156] M. S. Boutilier and S. Yarusevych. Effects of End Plates and Blockage on Low-Reynolds-Number Flows Over Airfoils. *AIAA J.*, 50(7):1547–1559, 2012. DOI. ↩

[157] G. S. West and C. Apelt. The effects of tunnel blockage and aspect ratio on the mean flow past a circular cylinder with Reynolds numbers between 104 and 105. *J. Fluid Mech.*, 114:361–377, 1982. DOI. ↩

[158] Y. Kubo, M. Miyazaki, and K. Kato. Effects of end plates and blockage of structural members on drag forces. *J. Wind Eng. Ind. Aerodyn.*, 32(3):329–342, 1989. DOI. ↩

[159] R. W. Paterson, P. G. Vogt, M. R. Fink, and C. L. Munch. Vortex Noise of Isolated Airfoils. *J. Aircr.*, 10(5):296–302, 1973. DOI. ↩

[160] H. Arbey and J. Bataille. Noise generated by airfoil profiles placed in a uniform laminar flow. *J. Fluid Mech.*, 134:33–47, 1983. DOI. ↩

[161] S. Pröbsting, J. Serpieri, and F. Scarano. Experimental investigation of aerofoil tonal noise generation. *J. Fluid Mech.*, 747:656–687, 2014. DOI. ↩

[162] S. Pröbsting and S. Yarusevych. Laminar separation bubble development on an airfoil emitting tonal noise. *J. Fluid Mech.*, 780:167–191, 2015. DOI. ↩

[163] D. G. Mabey. Analysis and Correlation of Data on Pressure Fluctuations in Separated Flow. *J. Aircr.*, 9(9):642–645, 1972. DOI. ↩

[164] N. J. Cherry, R. Hillier, and M. E. M. P. Latour. Unsteady measurements in a separated and reattaching flow. *J. Fluid Mech.*, 144:13–46, 1984. DOI. ↩

[165] R. Gerakopulos, M. S. Boutilier, and S. Yarusevych. Aerodynamic Characterization of a NACA 0018 Airfoil at Low Reynolds Numbers. In *40th AIAA Fluid Dyn. Conf.* Chicago, Illinois, 2010. DOI. ↩

[166] J. W. Kurelek and S. Yarusevych. The effect of acoustic excitation on the later stages of transition in a laminar separation bubble. In *46th AIAA Fluid Dyn. Conf.* Washington, D.C., 2016. DOI. ↩

[167] M. S. Howe. *Acoustics of fluid-structure interactions*. Cambridge University Press, 1998. DOI. ↩

[168] J. L. Lumley. The structure of inhomogeneous turbulent flows. *Atmos. Turbul. radio wave Propag.*, 1967. ↩

[169] G. Berkooz, P. Holmes, and J. L. Lumley. The proper orthogonal decomposition in the analysis of turbulent flows. *Annu. Rev. Fluid Mech.*, 25(1):539–575, 1993. DOI. ↩

[170] Z. Liu, R. J. Adrian, and T. J. Hanratty. Large-scale modes of turbulent channel flow: transport and structure. *J. Fluid Mech.*, 448:53–80, 2001. DOI. ↩

[171] M. Ilak and C. W. Rowley. Modeling of transitional channel flow using balanced proper orthogonal decomposition. *Phys. Fluids*, 20(3):034103, 2008. DOI. ↩

[172] L. Sirovich. Turbulence and the dynamics of coherent structures. II. Symmetries and transformations. *Q. Appl. Math.*, 45(3):561–571, 1987. DOI. ↩

[173] R. J. Moffat. Contributions to the Theroy of Single-Sample Uncertainity Analysis. *J. Fluids Eng.*, 104(2):250–258, 1982. DOI. ↩

[174] R. J. Moffat. Describing the Uncertainties in Experimental Results. *Exp. Therm. Fluid Sci.*, 1(1):3–17, 1988. DOI. ↩

[175] J. G. Kawall, M. Shokr, and J. F. Keffer. A digital technique for the simultaneous measurement of streamwise and lateral velocities in turbulent flows. *J. Fluid Mech.*, 133:83–112, 1983. DOI. ↩

[176] M. Brendel and T. J. Mueller. Boundary-Layer Measurements on an Airfoil at Low Reynolds Numbers. *J. Aircr.*, 25(7):612–617, 1988. DOI. ↩

[177] A. Sciacchitano, F. Scarano, and B. Wieneke. PIV uncertainty quantification by image matching. *Meas. Sci. Technol.*, 24(4):045302, 2013. DOI. ↩

[178] C. Norberg. Fluctuating lift on a circular cylinder: Review and new measurements. *J. Fluids Struct.*, 17(1):57–96, 2003. DOI. ↩

Appendices

Appendix A

Experimental Uncertainty

As with any experimental investigation, it is important to quantify the uncertainty in reported values. The goal of this Appendix is to outline the methods used to compute the uncertainties of measured and derived quantities presented throughout this thesis. Throughout this Appendix, the variable Δu_ϵ will be used to denote the uncertainty in a quantity ϵ, reported over a 95% confidence interval. Further, uncertainties in a given measurement are computed using a root-sum-square approach [173, 174]:

$$\Delta u_\epsilon = \sqrt{\sum_{i=1}^{n} (\Delta u_{\epsilon_i})^2} \tag{A.1}$$

Not all quantities can be directly measured and therefore must be calculated from other measured quantities. For derived quantities such as these, uncertainties are propagated through the deriving equation based on the following:

$$\Delta u_\epsilon = \sqrt{\sum_{i=1}^{n} \left(\frac{\partial \epsilon_i}{\partial i} \Delta u_{\epsilon_i} \right)^2} \tag{A.2}$$

where the subscript i refers to variables in the equation for ϵ and represent the individual error sources. In some cases of derived quantities, the equation for the desired quantity may be too complex to apply Eq. A.2 and thus, a propagation of error method can be employed. For this method, the uncertainty in the measured variables is applied for both the high and low estimates, the derived quantity re-computed, and the results used to determine an uncertainty range of the derived quantity. A summary of all experimental uncertainties is provided in Table A.1, with details of the calculations provided in the following sections.

Table A.1: Summary of experimental uncertainties.

Quantity	Reynolds number	Uncertainty	Applies to
$C_P\|_{suction}$	100 000	± 0.05	Figs. 4.3, 4.8, and 5.1
	80 000, 150 000	± 0.03	
	125 000, 200 000	± 0.02	
$C_P\|_{pressure}$	80 000	± 0.03	Figs. 4.3, 4.8, and 5.1
	100 000, 125 000	± 0.02	
	150 000, 200 000	± 0.01	
C_l	100 000	± 0.02	Figs. 4.1, 4.2, and 4.7
	150 000, 200 000	± 0.01	
ℓ_b/c	All	0.03	Figs. 4.6 and 4.10
$l/c\|_{max}$	All	$\pm 6\%$[20]	Table 5.4
λ_x	All	± 0.024	Table 5.3 and Fig. 5.9
p'	All	$\pm\sqrt{0.01^2 + 0.2p'^2}$	Figs. 4.11, 4.12, and 4.14 Fig. 5.7
U_c	All	$\pm 13\%$	Table 5.3
X_S/c, X_T/c, X_R/c	All	± 0.02	Figs. 4.5 and 4.9
x_S/c from $\overline{U}$	All	± 0.1	Figs. 5.2 and 5.3 Table 5.2
x_T/c from $\overline{U}$	All	± 0.01	
x_R/c from $\overline{U}$	All	± 0.02	
St_0, ΔSt	80 000	± 2.4	Figs. 4.16, 4.17, and 5.8
	125 000	± 1.5	Table 5.2 and Fig. 5.9
$\overline{U}/U_0$	All	0.05	Fig. 5.2
u'/U_0, v'/U_0	All	0.03	Fig. 5.5
U_X/U_0	All	0.06	Figs. 5.18 and 5.19
$\sigma_{p',max}$	All	± 6	Figs. 4.13 and 4.15 Table 5.3
$\sigma_{u',max}$, $\sigma_{v',max}$	80 000	± 4.5	Table 5.3
	125 000	± 8.1	
q_0	All	± 0.65 Pa	
Tu	All	$\pm 0.07\%$	
U_0, Re_c	80 000	$\pm 2\%$	
	100 000, 125 000	$\pm 1\%$	
	150 000, 200 000	$\pm 0.5\%$	
α	All	$\pm 0.16°$	

A.1 Experimental Conditions

The mean free-stream velocity is determined based on the contraction pressure drop as outlined in Appendix B. The free-stream velocity uncertainty has contributions from the calibration between the contraction pressure drop and free-stream dynamic pressure, as well as Bernoulli's principle used to calculate the free-stream velocity from the free-stream dynamic pressure. First, the uncertainty from the contraction pressure drop measurement is propagated through the determined calibration relation of the form $q_0 = A \cdot \Delta P_c + B$, where A and B are the constants determined in the calibration (see Appendix B). This is done using Eq. A.2:

$$\Delta u_{q_0} = \sqrt{\frac{\partial q_0}{\partial \Delta P_c} \cdot \Delta u_{\Delta P_c}}$$

The resulting uncertainty is added to the root-mean-square error of the calibration fit using the root-sum-squared method to yield a final uncertainty in the the free-stream dynamic pressure of less than $\pm 0.65\,\mathrm{Pa}$. This uncertainty is then propagated through Bernoulli's equation to determine the uncertainty in the free-stream velocity. Error in calculating the density of air was assumed to be negligible as the ambient temperature and pressure in the laboratory were monitored regularly with devices having relatively high precision. In addition, all free-stream velocities investigated were well below the level at which compressibility effects become important. The resulting uncertainty in the free-stream velocity is less than $\pm 2\%$ for all chord Reynolds numbers investigated. Similarly, if there is negligible error in calculating the kinematic viscosity of air, the chord Reynolds number has the same uncertainty as that of the free-stream velocity.

The angle of attack of the airfoil is set using a digital protractor affixed to the axis of rotation of the airfoil with an associated accuracy of $\pm 0.1°$. To find the aerodynamic zero, the airfoil is first set to zero angle of attack by eye, then, sectional lift coefficients are computed for positive and negative angles of attack within the linear regime of the airfoil lift curve, as shown in Fig. A.1. Based on this method, an additional error in the airfoil angle of attack is introduced based on the goodness of fit of the linear regression. For this investigation, the root-mean-squared error of the linear fit is 0.13° which when combined with the resolution error yields an uncertainty in the airfoil angle of attack of $\pm 0.16°$.

The free-stream turbulence intensity was characterized by means of normal hot-wire anemometry in the empty test section. For normal hot-wire measurements, the uncertainty in U_0 and u' in flows where the turbulence intensity is below approximately 30% is less than about 5% [175]. Further, since the measurements are taken away from any walls and the probe holder is directly behind the wire, rectification errors and influences from the probe itself are negligible [175, 176]. Therefore, in this investigation where mean flow speeds are

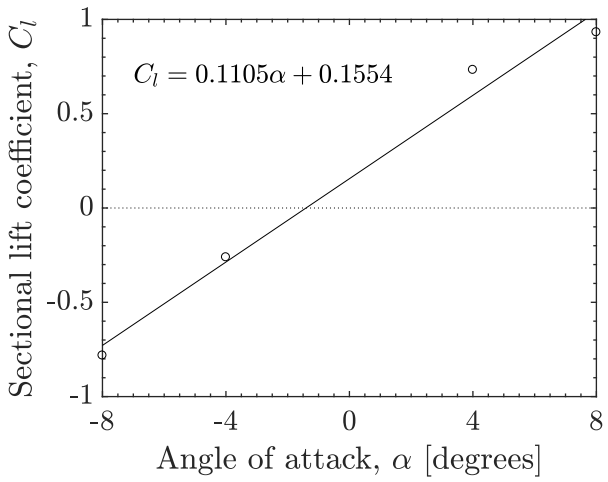

Figure A.1: Plot of method used to determine the aerodynamic zero of the airfoil. The free-stream conditions were such that $Re_c = 100\,000$ and $Tu = 0.10\%$.

relatively high and turbulence intensities are relatively low, combining these uncertainties using Eq. A.2 yields an uncertainty in Tu of approximately $\pm 0.07\%$.

A.2 Surface Pressure Measurements

The two types of surface pressure measurements made in this investigation were mean and fluctuating surface pressure measurements. The sectional lift coefficient and mean bubble topology are also derived from the mean surface pressure distributions, while spatial growth rates and disturbance frequencies are determined from the fluctuating surface pressure measurements. The calibration curves for all pressure transducers were provided by Kurelek [20]. In order to account for the sensitivity of the pressure transducers to temperature as well as the difference in experiment and calibration temperatures, a zero pressure offset was applied before every measurement.

As summarized in Table A.1, the uncertainty in the pressure coefficient depends on the chord Reynolds number, as the uncertainty magnitude is fixed based on the full-scale range of the pressure transducer and thus becomes a decreasing percentage of the free-stream dynamic pressure. The pressure coefficient is derived from the mean surface pressure measurements and is also influenced by uncertainty in the mean free-stream velocity. As discussed previously, uncertainties in the air density are assumed to be negligible, and the following equation therefore shows the derivation of the uncertainty in the pressure

coefficient:

$$\Delta u_{C_P} = \sqrt{\left(\frac{\partial C_P}{\partial U_0} \cdot \Delta u_{U_0}\right)^2 + \left(\frac{\partial C_P}{\partial \Delta P} \cdot \Delta u_{\Delta P}\right)^2}$$

For the parametric study, a transducer with a full scale range of 1250 Pa and accuracy of ±1.7 Pa was used for the suction side pressure measurements, yielding an uncertainty in the pressure coefficient of less than ±5%. All pressure side measurements, and the suction side measurements in the PIV study, were conducted with a transducer having a full scale range and accuracy of 500 Pa and ±0.7 Pa, respectively, resulting in a pressure coefficient uncertainty of less than ±3%.

To compute the sectional lift coefficient from the mean surface pressure distributions, a numerical integration scheme was employed. Here, the uncertainty in each surface pressure measurement acts on its integration window. As such, the uncertainty in the lift values was taken to be the root-sum-square of the uncertainties over each of the integration windows along the chord length of the airfoil:

$$\Delta u_{C_l} = \sqrt{\sum_{i=1}^{n} \left[\left(\Delta u_{C_{P,suction}} \cdot (\Delta x/c)\right)^2_{suction} + \left(\Delta u_{C_{P,pressure}} \cdot (\Delta x/c)\right)^2_{pressure}\right]}$$

The resulting uncertainty in the sectional lift coefficient is estimated to be less than ±0.02 per unit span.

Mean bubble topology is estimated from the surface pressure distributions by finding the intersections of the lines fit to the suction side pressure distribution (see Fig. 4.4). Therefore, the associated uncertainty is proportional to the local pressure tap spacing and has a minimum value of half of the local pressure tap spacing. This value varies along the chord length and increases toward the aft portion of the airfoil. However, since the change in slope is small near separation, particularly for low angles of attack (see Fig. 4.4), a more conservative estimate of separation would be to within the spacing of two pressure taps, or $\pm 0.02c$. On average, transition and reattachment can be estimated more precisely, to within one tap spacing, and since this occurs over the aft portion of the airfoil where the spacing is greater, is also approximately equal to $\pm 0.02c$. The separation bubble length is derived from the locations of mean separation and reattachment and therefore has an uncertainty less than $\pm 0.03c$.

The uncertainty in the root-mean-square of the fluctuating surface pressure measurements has an error associated with the calibration of the microphones as well as the noise floor of the measurements. The noise floor has contributions from ambient noise in the laboratory, fan noise, other acoustics present in the wind tunnel, and electrical noise in the data acquisition

system. Therefore, the actual noise floor was taken to be the lowest measurement of p' across all of the microphones for a given flow condition and was, on the average, approximately $\pm 0.01 q_0$. It is of interest to note that the noise floor in the facility of this investigation is about half of that estimated by Boutilier [151] in the open-return wind tunnel also located in the Fluid Mechanics Research Laboratory at the University of Waterloo. The uncertainty arising from the calibration comes from assuming a linear microphone response to varying input amplitudes, as well as an equal response across all frequencies. Boutilier [151] estimates that the total uncertainty as a result of these two sources is approximately 20% of the root-mean-square measurement. Combining these two sources of error yields a total uncertainty in p'/q_0 of less than $\pm\sqrt{0.01^2 + (0.2p'/q_0)^2}$.

Spatial amplification rates estimated from the fluctuating surface pressure measurements have an uncertainty that is dominated by the estimation of the exponential growth region. The uncertainty in the estimated spatial amplification rates is a result of the limited spatial resolution of the microphones, leading to an uncertainty in the streamwise distance over which the growth occurs, as well as the relatively large uncertainty in the root-mean-square pressure measurements, resulting in an uncertainty in the amplitude of the disturbance growth. In most cases, maximum spatial amplification rates are computed over the streamwise distance of three microphone locations ($\approx 0.05c$). The expected uncertainty in the streamwise extent of disturbance amplification is related to the spacing between microphone locations and is estimated to be $\pm 0.01c$. Growth of disturbances typically begins from the noise floor of the microphone measurements and saturates in the range of $0.2 \lesssim p'/q_0 \lesssim 0.4$. The difference between these two values is used in the calculation of the amplification factor, and has an uncertainty approximately equal to that of the measurement at the end of the amplification region. Combining these two effects using Eq. A.2, the uncertainty in the maximum amplification rate of disturbances is estimated to be approximately ± 6.

The frequency content of the fluctuating surface pressure measurements is used to determine both the unstable band of frequencies as well as the central disturbance frequency of the separated shear layer disturbances. While the calculation of the frequencies yields a resolution of 2.4 Hz, the uncertainty in St_0 and ΔSt is much larger. The unstable frequency band is determined by identifying the beginning and end of the range of amplified frequencies. The lower limit of the unstable band is taken to be the frequency at which there is an increase in the energy content of disturbances in the separated shear layer, while the end is determined as the approximate location at which the energy content of the disturbances returns to the same energy level as at the beginning of the unstable range. The central disturbance frequency is computed as the arithmetic mean of these two values. This process is best shown schematically, and is presented for an example spectrum in Fig. A.2. The

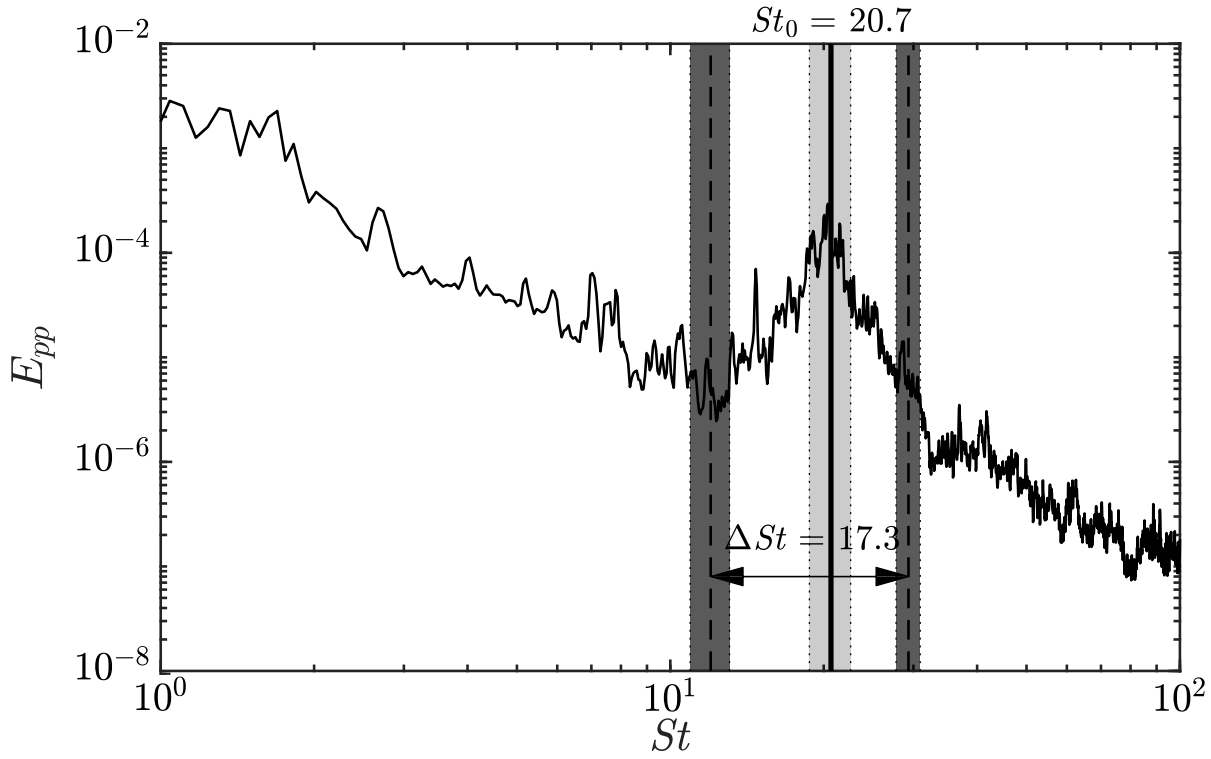

Figure A.2: Sketch of the method used to determine the unstable frequency band. The energy spectrum is taken for $Re_c = 100\,000$, $\alpha = 8°$, and $Tu = 0.10\%$. Dashed lines mark the beginning and end of the unstable frequency band while the solid line marks the central disturbance frequency. Shaded grey regions denote the uncertainty limits.

uncertainty in the frequency at beginning and end of the unstable range was found by shifting the location to higher and lower frequencies, and assessing whether it was still an accurate representation of beginning or end of the unstable band. By applying this technique to several spectra for different free-stream conditions, it was determined that, on average, the uncertainty in the frequency at the beginning of the unstable range is ±40 Hz ($St \approx 1.1$ in Fig. A.2) and ±60 Hz ($St \approx 1.6$ in Fig. A.2) at the end of the unstable range. These are shown by the shaded dark grey regions in Fig. A.2. The uncertainty in the central disturbance frequency (and unstable band width) is taken to be the root-sum-square of these values, ±72 Hz ($St \approx 2$), shown by the shaded light grey region in Fig. A.2.

A.3 PIV Measurements

Uncertainty in PIV measurements can be difficult to quantify due to the large number of factors that can influence the final velocity fields. In this investigation, estimates of the random error in PIV measurements were computed using the particle disparity method [177] built into DaVis 8. For the cases examined, the largest uncertainty in the side view measurements occurred in the separated shear layer and near the wall as a result of the large velocity gradients. Similarly, for the top view measurements, uncertainty increased with chordwise distance as the shear layer rollers grew and the flow transitioned to turbulence. On the average, the uncertainty in the mean streamwise velocity was found to be less than 5% of the mean free-stream velocity everywhere. As such, this value was used as an estimate for the uncertainty over the entire velocity field in order to determine uncertainties in derived quantities.

Uncertainty in mean bubble dimensions and location was assessed by applying the uncertainty in mean velocity to the mean fields and then propagating it to the estimated parameters. In other words, 5% of the free-stream velocity was added and subtracted from the mean fields and the topology was assessed for each case. In such a manner, the most extreme locations of the mean bubble topology would be obtained.

Similarly to the method in determining the effects of uncertainty on mean bubble topology, the effect of PIV uncertainty on integral boundary layer parameters was assessed by adding and subtracting the uncertainty from the field before computing the parameters. In this way, upper and lower bounds on the parameters could be determined.

For the root-mean-square quantities of the fluctuating velocities as measured by the low speed PIV system, the uncertainty was assessed by computing the standard deviation of the uncertainty fields as determined in the DaVis 8 software. Typical uncertainties along the displacement thickness were $0.005U_0$, and thus this value was assigned to the RMS values sampled along the displacement thickness.

Following the uncertainty of the root-mean-square velocity fields, the uncertainties in $\sigma_{u',max}$ and $\sigma_{v',max}$ were assessed by adding and subtracting the uncertainty in the root-mean-square value along the location at which the value was measured in order to find uncertainty bounds on the quantity.

Spectra of the wall-normal velocity fluctuations were computed using Welch's method [155], where the window size was selected such that the same frequency resolution as the fluctuating surface pressure spectra was retained. Then, following the methodology in Fig. A.2 similar uncertainty values in St_0 and ΔSt were obtained for all cases investigated.

To determine the average convective velocities of disturbances, as well as the streamwise wavelength of the most amplified disturbances, two-dimensional wavenumber-frequency

spectra were computed for the wall-normal velocity fluctuations along the boundary layer displacement thickness. Welch's method [155] was used to compute the spectra in both time and space, with window sizes of 2^{10} and 2^{8}, respectively, and using a 50% window overlap. The resulting resolutions in frequency and wavenumber are $\pm 2.4\,\mathrm{Hz}$ and $\pm 0.15\,\mathrm{mm^{-1}}$, respectively. The uncertainty in the wavenumber results in an uncertainty in the streamwise wavelength (λ_x/c) of $\pm 1.2 \times 10^{-4}$. The wavenumber uncertainty along the convective ridge is $\pm 0.005\,\mathrm{mm^{-1}}$, corresponding to the values used in computing the convective velocity of disturbances. The resulting uncertainty in convective velocity would then be less than 0.4% of the mean free-stream velocity. However, the root-mean-square error of the fit used to find the convective ridge is approximately $0.11\,\mathrm{mm^{-1}}$ and therefore has a greater impact on the convective velocity estimates, resulting in a final uncertainty estimate of the convective velocity of less than 13% of the free-stream velocity.

Appendix B

Wind Tunnel Characterization

B.1 Free-stream Velocity Calibration

Prior to experiments, the velocity in the empty test section was calibrated against the contraction pressure drop for all conditions investigated (*i.e.*, for each of the turbulence generating grids). Details of the turbulence generating grid geometry are provided in Appendix C. Under ideal conditions (*i.e.*, no losses) the dynamic pressure in the test section can be related to the contraction pressure drop using Bernoulli's equation and conservation of mass. For a streamline between the inlet and exit of the contraction, we can write:

$$P_i + 0.5\rho U_i^2 = P_e + 0.5\rho U_e^2$$

and conservation of mass gives,

$$\rho U_i A_i = \rho U_e A_e$$

where the subscripts i and e represent the inlet and exit of the contraction, respectively, and A represents the cross-sectional area. The geometry of the contraction gives $A_i/A_e = 9$. An expression for the test section dynamic pressure as a function of the contraction pressure drop can then be written as:

$$q_0 = 1.012(P_i - P_e) = 1.012\Delta P_c$$

This relation indicates that the relationship between the contraction pressure drop and free-stream dynamic pressure is linear. For ideal conditions (*i.e.*, no losses), this relation would hold but the true relationship must be determined experimentally and is subject to

losses in the contraction. Therefore, the general form of the calibration is represented by:

$$q_0 = A \cdot \Delta P_c - B \tag{B.1}$$

where A and B must be determined experimentally, and B represents losses.

For each free-stream condition, the calibration was conducted in an empty test section using 1 m/s intervals between 7 m/s and 16 m/s, spanning the Reynolds number range of this investigation. For each calibration point, the static pressure drop across the contraction as well as the dynamic pressure, measured at the location of the midspan of the leading edge of the airfoil, were measured using two Setra Model 239 pressure transducers having full scales ranges of ±250 Pa. The signals were simultaneously sampled at 1 kHz for 10 s using a National Instruments USB-6259 data acquisition unit. The values were averaged and converted into pressures based on the transducer calibrations, and are presented in Fig. B.1 for each of the flow conditions investigated.

B.2 Flow Conditions

Once the free-stream calibration relations were determined, the flow conditions at each of the investigated chord Reynolds numbers were characterized. This was done by means of hot-wire anemometry in the empty test section. A normal Dantec 55P11 probe, connected to a Dantec Streamline Constant Temperature Anemometry system, was placed at the location corresponding to the midspan of the airfoil leading edge. The hot-wire was calibrated in-situ against a reference Pitot-static tube placed approximately 3 cm below it. The mean free-stream velocity was determined from the mean dynamic pressure measured using a Setra Model 239 pressure transducer having a full-scale range of ±250 Pa. A total of 10^4 samples were recorded at a rate of 1 kHz and averaged. Hot-wire signals were sampled using a National Instruments PCI-4472 data acquisition card at a rate of 100 kHz for a total of 2^{23} samples. Calibration points were spaced in 1 m/s intervals between the lowest and highest free-stream velocities in this investigation. A fourth-order polynomial was then fit to the data using a least-squares approach, with the results shown in Fig. B.2.

For each flow condition, the integral length scale of the turbulence was computed from the hot-wire measurements. First, the auto-correlation function of the free-stream velocity fluctuations was computed with an example result shown in Fig. B.3. The integral length scale can be computed from this auto-correlation function by integrating the result, and then multiplying it by the mean free-stream velocity, assuming Taylor's hypothesis is valid [85]. However, since the function fluctuates around zero, an exponential curve fit is applied to the result and integrated instead in order to yield a more converged result [178].

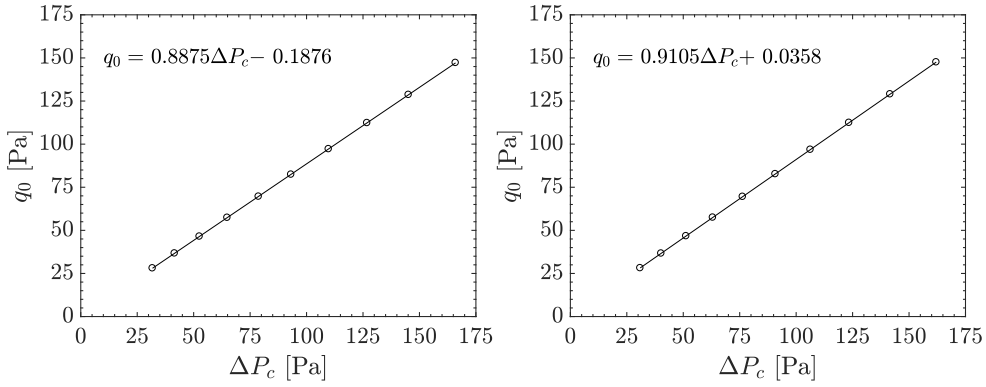

(a) No screen

(b) Fine screen

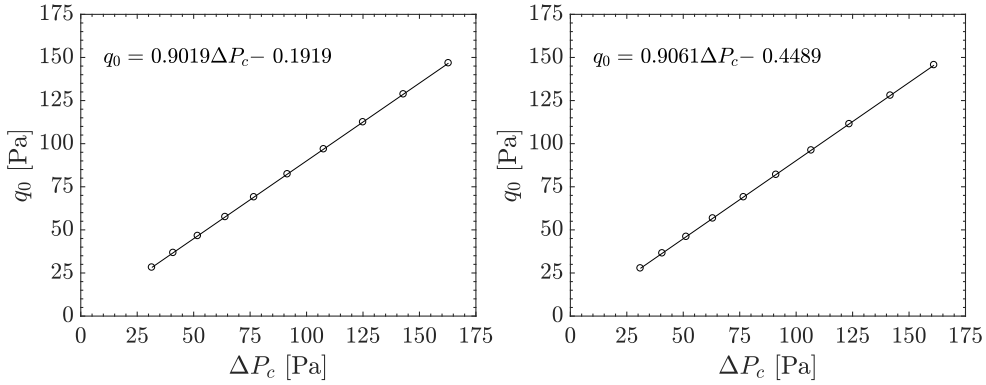

(c) Medium screen

(d) Coarse screen

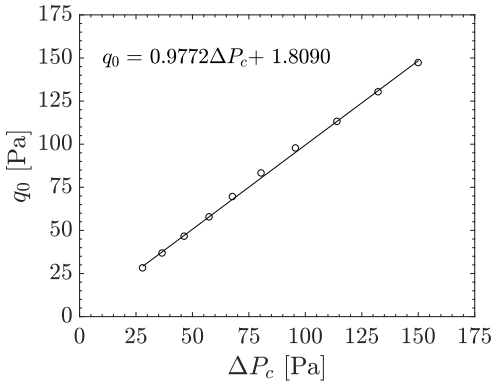

(e) Grid

Figure B.1: Free-stream dynamic pressure as a function of contraction pressure drop for each flow condition investigated. Equations for the linear fits are of the form of Eq. B.1.

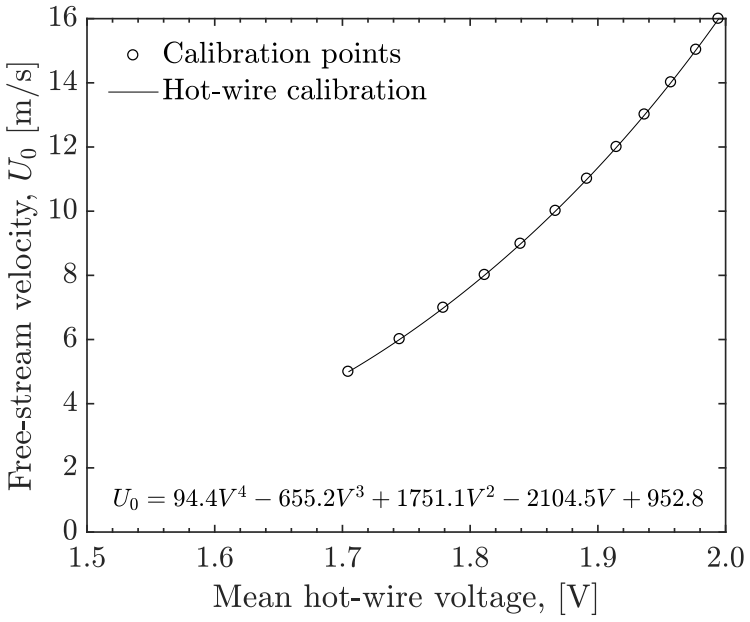

Figure B.2: Hot-wire calibration.

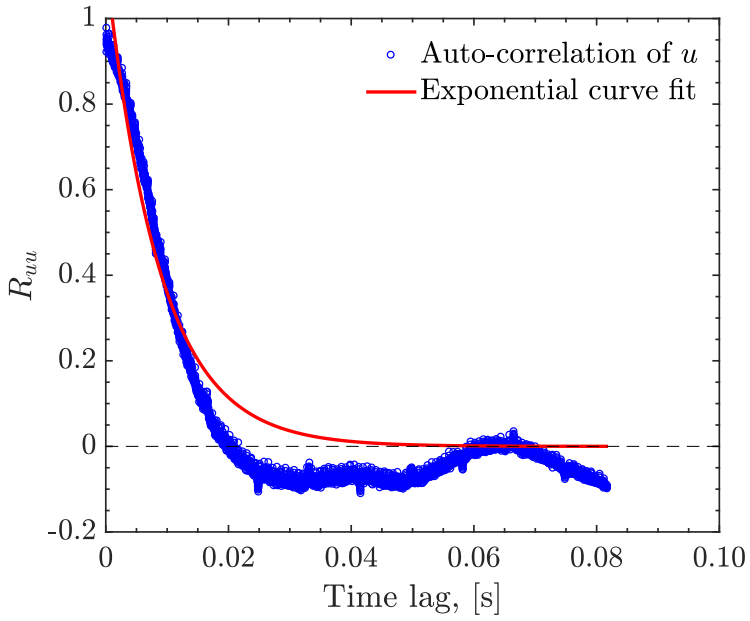

Figure B.3: Auto-correlation of u for the no screen condition at $Re_c = 100\,000$.

Appendix C

Turbulence Generating Grids

In order to increase the level of free-stream turbulence intensity in the test-section, turbulence generating grids were placed just upstream of the test section inlet, as shown in Fig. 3.2. Close-up photographs of the grids used in this study are shown in Fig. C.1. The grids were designed so as to fit in between the flanges which connect the outlet of the contraction to the inlet of the test section, as depicted in Fig. 3.1. The largest grid was a square array of rectangular elements which could be inserted directly between the two flanges. The smaller three grids however were made from woven wire mesh screens, and thus required a structure in order to hold them in place. Simple square steel frames were designed to hold the woven wire meshes in tension so that they could be inserted between the two flanges. The frames were designed to have an inner dimension equal to that of the inside dimension of the test section, and an outer dimension small enough to fit inside the bolts used to hold the test section and contraction flanges together. In this manner there would be no step or gap at the inside edge of the test section, and the same bolts could be used to tighten the flanges together, effectively sandwiching the frames in place. The frames were constructed by Rob Kraemer in the University of Waterloo's Engineering Machine Shop and a simple shop drawing is included on the following page. For the larger two woven wire screens, a pair of these frames were used and spot welded together with the screen held in tension between them. For the smallest screen, it was discovered that the spot welding would melt the wires. Therefore, for this screen, the frames were glued together while the screen was held in tension between them. Characterization of the turbulence generated by the grids when installed upstream of the test section is discussed in Appendix B.

All dimensions are in inches.

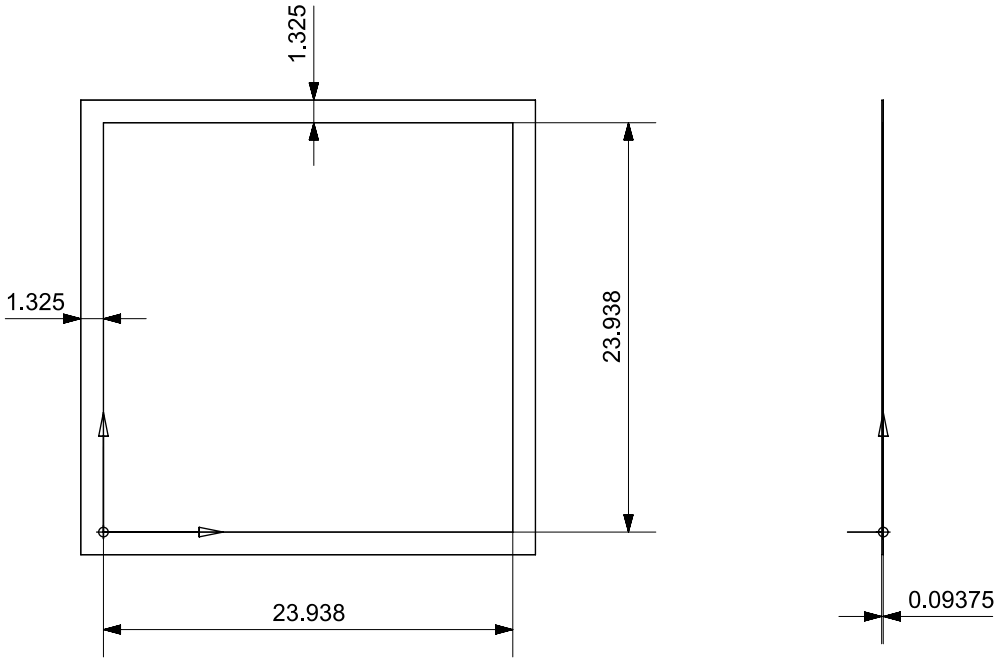

The inside dimension, 23 and 15/16 inches should be exact

Part Name	Screen Frame
Author	Mark Istvan
Material	General Purpose Steel
Page Number	1 of 1
Date	December 21, 2015

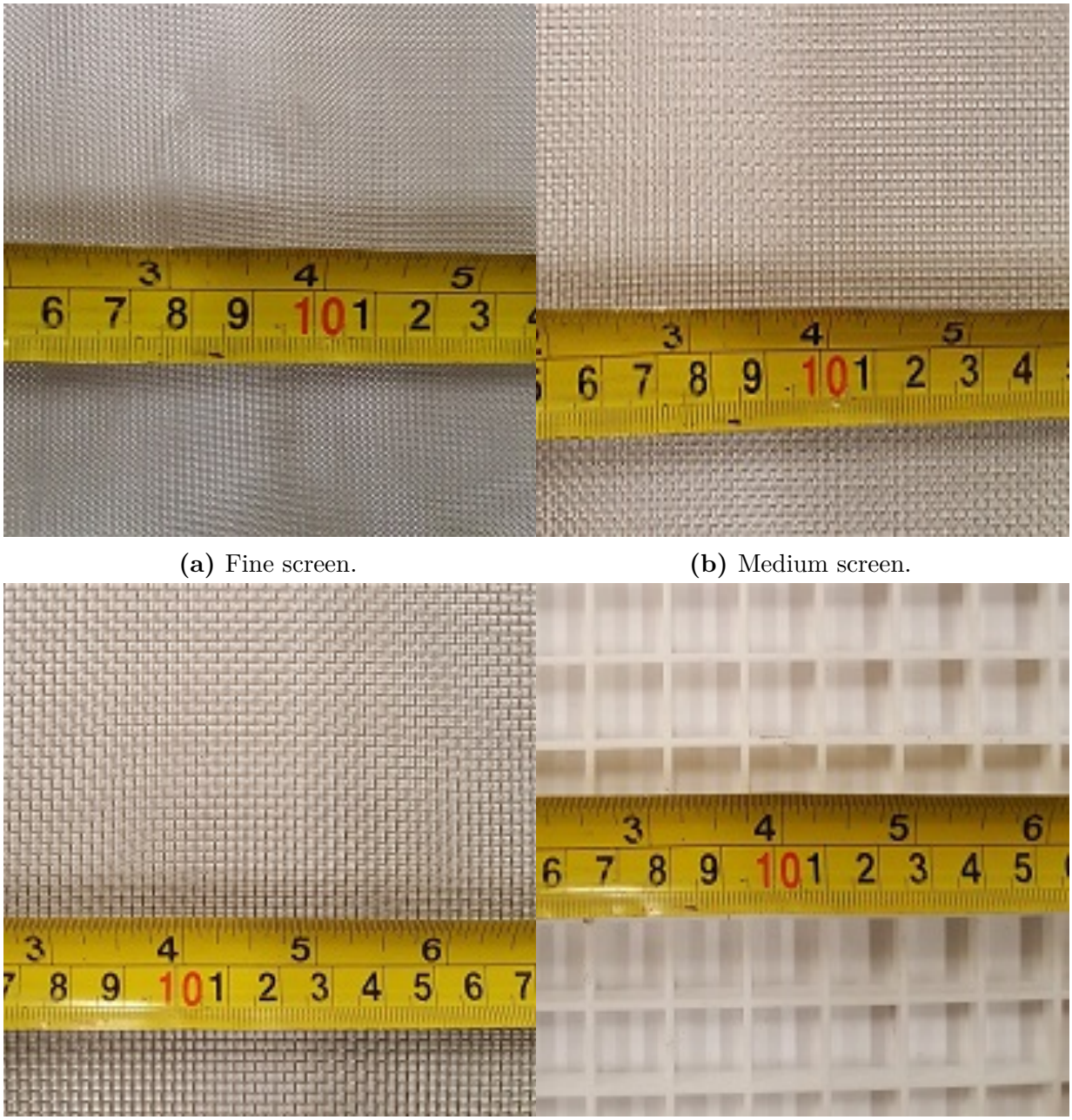

(a) Fine screen.

(b) Medium screen.

(c) Coarse screen.

(d) Square array of rectangular elements.

Figure C.1: Close-up photographs of the turbulence generating grids. Dimensions are summarized in Table 3.1.

Appendix D

Airfoil Microphone Re-Calibration

Since the microphones were installed and calibrated in the year 2011 when instrumented by Gerakopulos [150], the sensitivities of the microphones were assumed to have drifted slightly. Therefore, prior to experiments, the microphone responses were re-calibrated against a Brüle and Kjær 4192 reference microphone. The airfoil was placed in a large room away from any reflective surfaces, while the reference microphone was placed approximately 1 cm above the port of the microphone being calibrated. The calibration procedure involved playing tones through a loudspeaker in 1/3 octave bands between 100 Hz and 5000 Hz, and measuring the Sound Pressure Level (SPL) recorded by both the reference microphone and surface embedded microphone. For each tested frequency, a sound pressure level between 90 dB and 95 dB as measured by the reference microphone was targeted such that it was significantly above the background noise floor. A summary of the calibration test points is provided in Table D.1.

Table D.1: Summary of microphone calibration test matrix.

Calibration point	1	2	3	4	5	6
1/3 octave band centre [Hz]	100	125	160	200	250	315
	7	8	9	10	11	12
	400	500	630	800	1000	1250
	13	14	15	16	17	18
	1600	2000	2500	3150	4000	5000

At each tested frequency, the microphone sensitivity was computed based on the reference

microphone measurement and its known sensitivity. Then, the sensitivity value assigned to a given microphone was computed as the average sensitivity across all tested frequencies. The obtained sensitivities are provided in Table D.2, along with the values that were originally computed by Gerakopulos [150]. The results show that, on the average, the sensitivity of the microphones has decreased by approximately 9% of their original values.

The relative frequency response of the microphones was also evaluated by first normalizing the measurement at each frequency by the reference microphone measurement. Then, the response at all frequencies was normalized by the response at a frequency of 250 Hz. An example of this normalization is provided in Fig. D.1 and shows that the response of the microphone is relatively flat across the investigated frequencies.

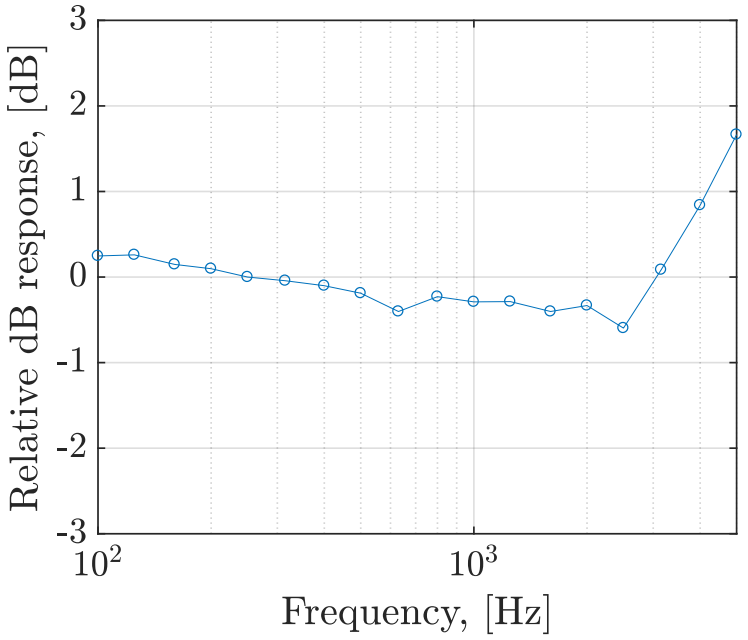

Figure D.1: Relative dB response for microphone number 1 ($X/c = 0.73$). The reference frequency is 250 Hz.

Table D.2: Summary of the microphone re-calibration.

		Sensitivity [mV/Pa]		
Microphone	Chordwise location (X/c)	Gerakopulos [150]	Current	% change
1	0.73	191.3	185.9	-2.8
2	0.66	187.1	172.2	-7.9
3	0.6	205.5	181.2	-11.8
4	0.56	193.9	177.8	-8.3
5	0.51	189.6	155.5	-18
6	0.47	197.7	181.6	-8.2
7	0.43	167.9	141.6	-15.7
8	0.41	167.3	167.8	0.3
9	0.39	193.6	203.7	5.2
10	0.36	173.4	187.7	8.3
11	0.34	159.5	150.4	-5.7
12	0.32	179.3	163.7	-8.7
13	0.3	197.5	180.5	-8.6
14	0.28	199.9	185.1	-7.4
15	0.26	150.0	130.6	-12.9
16	0.24	166.2	86.4	-48
17	0.21	193.8	182.4	-5.9
18	0.21	192.3	176.8	-8.1
19	0.21	209.9	184.7	-12
20	0.21	158.3	158.5	0.1
21	0.19	181.6	188.2	3.6
22	0.17	173.8	165.2	-5
23	0.15	156.7	147.2	-6.1
24	0.13	189.6	177.7	-6.3
25	0.08	184.2	137.0	-25.6

Appendix E

Supplementary Results

This Appendix presents results which support the discussions presented throughout this thesis but were omitted from the previous chapters for conciseness. The results are presented here for completeness of the data sets presented.

E.1 Mean Surface Pressure Distributions

In Chapter 4, mean surface pressure distributions were shown for four angles of attack in order to highlight trends in the effects of Tu on mean separation bubble topology. However, data were collected in 1° angle of attack increments between 0° and 20°, and thus a large portion of the data was not shown. Here, in Fig. E.1, six additional angles of attack are shown. The selected angles of attack were chosen to fit in the gaps left by the angles of attack presented in Chapter 4. The data show the same trends that were discussed throughout Chapter 4 and therefore no further discussion is required. All mean bubble topology from these distributions was extracted and presented in Figs. 4.5, 4.6, 4.9, and 4.10.

E.2 PIV Top View Mean Fields

While the main purpose of the top view PIV configuration was to examine the dynamics of the spanwise flow development, it is informative to assess the time-averaged statistics. For both chord Reynolds numbers and all Tu levels investigated, contours of mean chordwise and spanwise velocity are presented in Fig. E.2, while contours of the root-mean-square

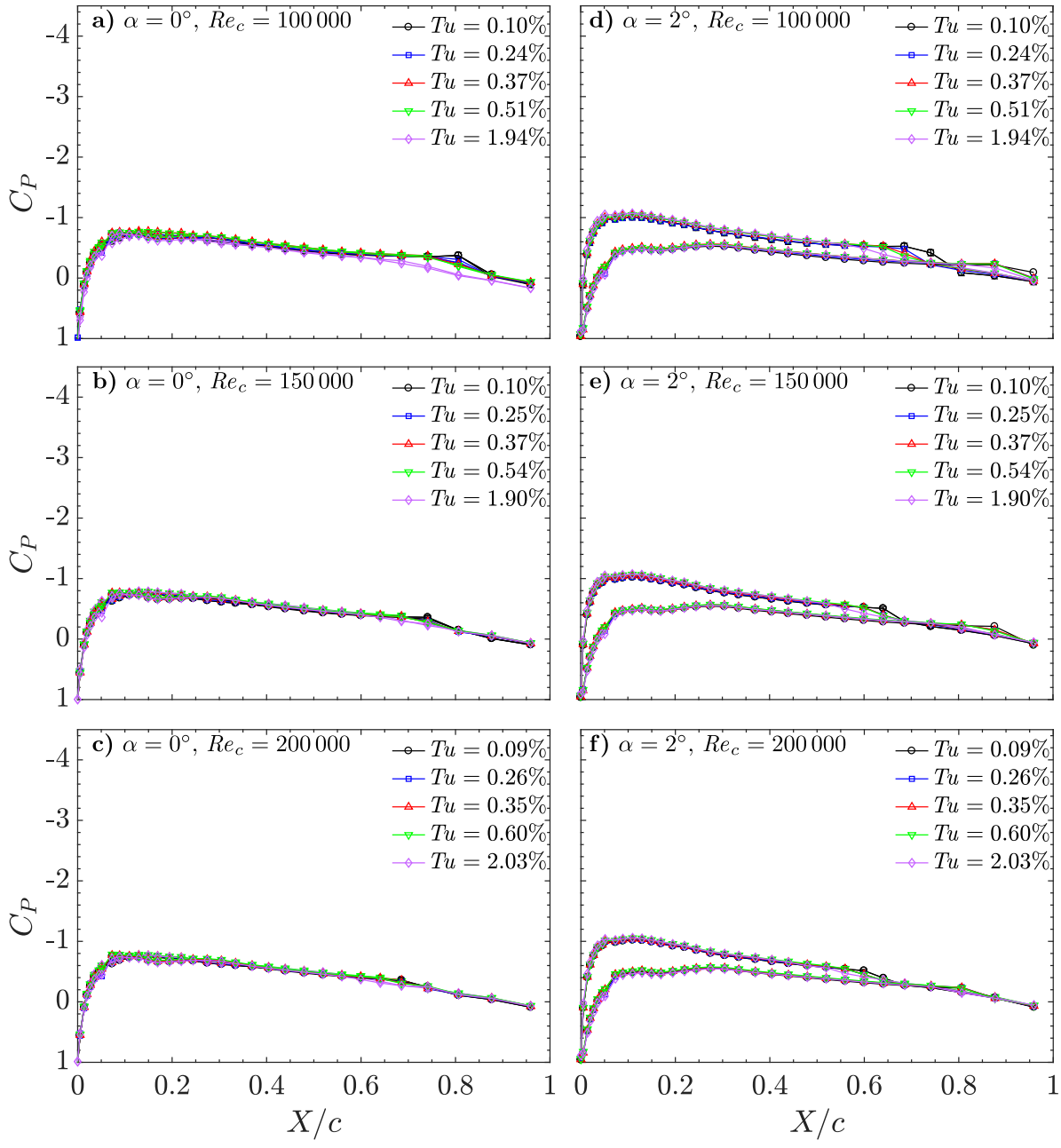

Figure E.1: Mean surface pressure distributions.

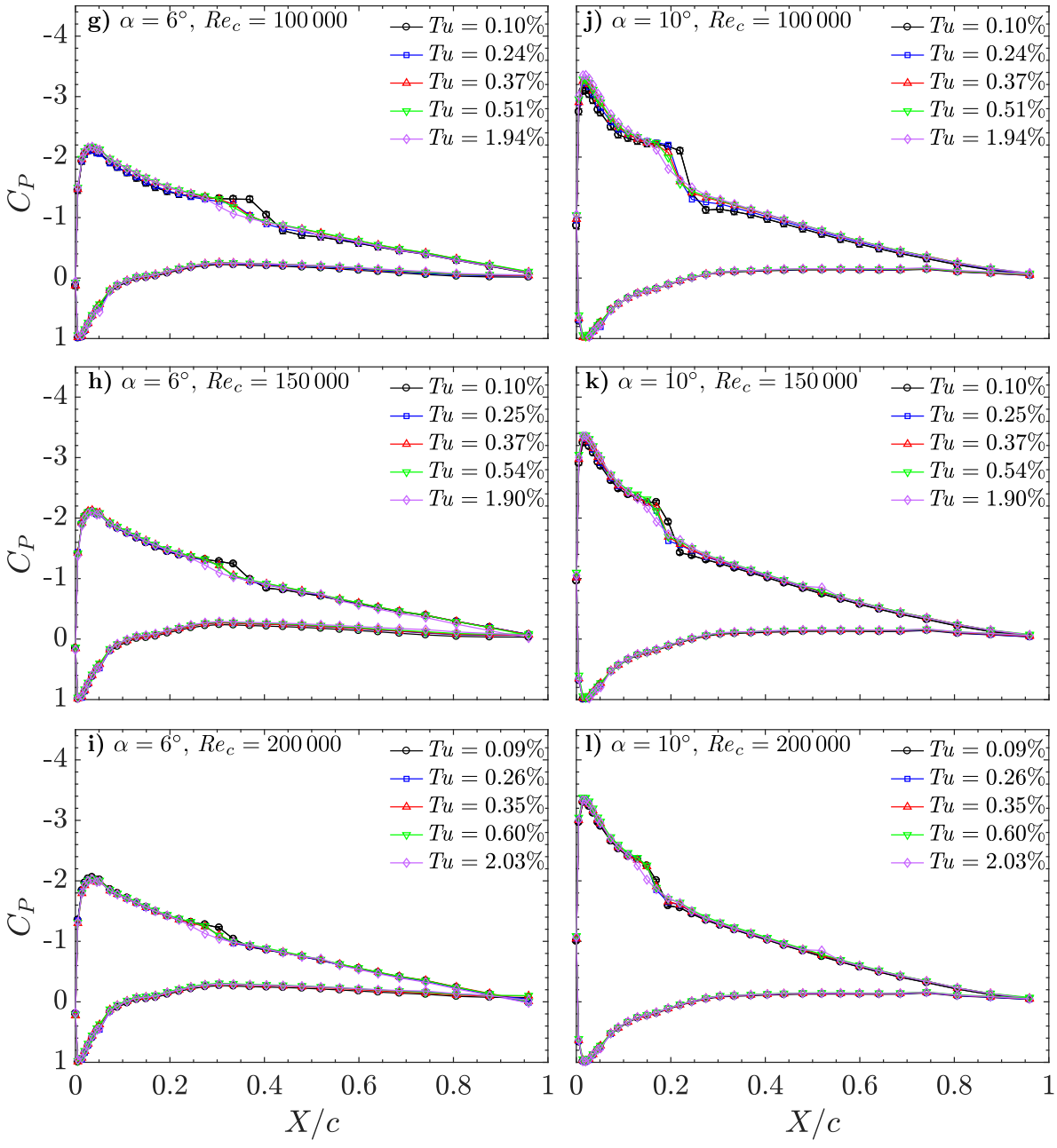

Figure E.1 (cont.): Mean surface pressure distributions.

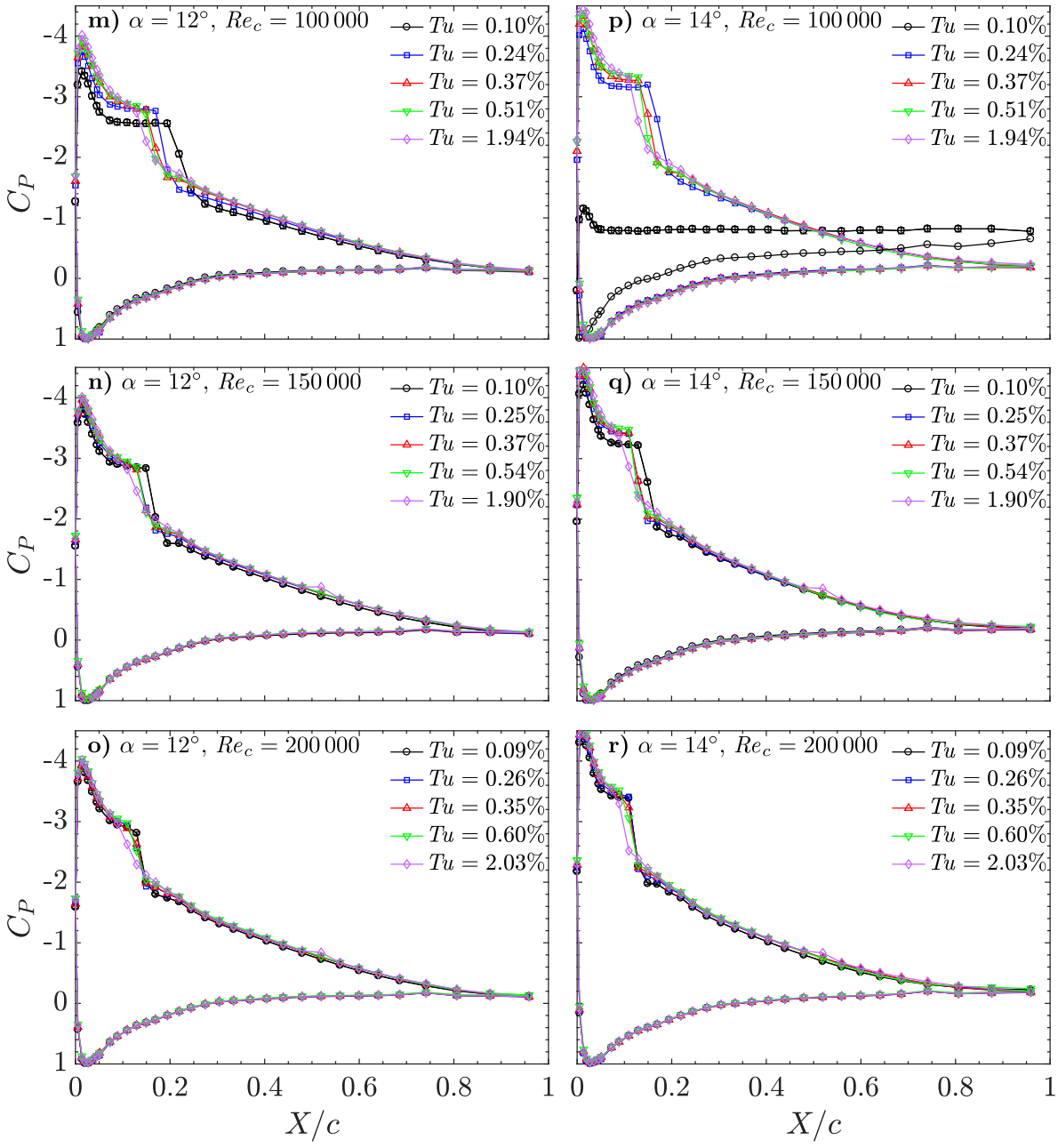

Figure E.1 (cont.): Mean surface pressure distributions.

of the chordwise and spanwise velocity fluctuations are presented in Fig. E.3. It should be noted that, in general, all presented results fall within the random error of the PIV measurements ($\pm 0.05 U_0$) and thus the following discussion is limited.

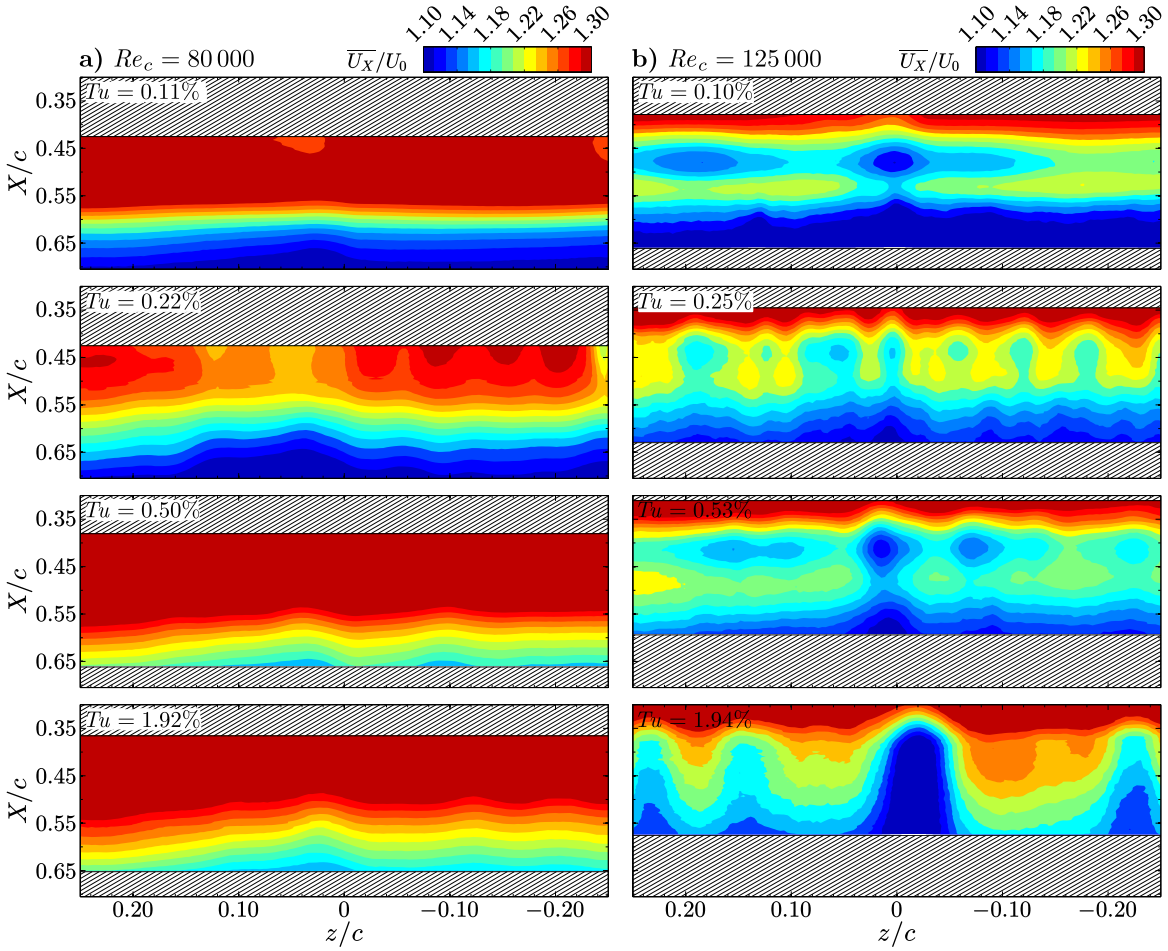

Figure E.2: Contours of mean chordwise velocity.

At the baseline level of Tu for both chord Reynolds numbers, the results show relatively spanwise uniform contours of chordwise velocity, with the exception of two low-speed regions at $Re_c = 125\,000$. However, at the higher levels of Tu, there are notable spanwise variations in the mean chordwise velocities, with variations up to $0.05 U_0$ observed across the span of the measurement region. The non-uniformity across the span is more evident in the contour plots of u'_X and w' presented in Fig. E.3, where a notable variation across the span of the

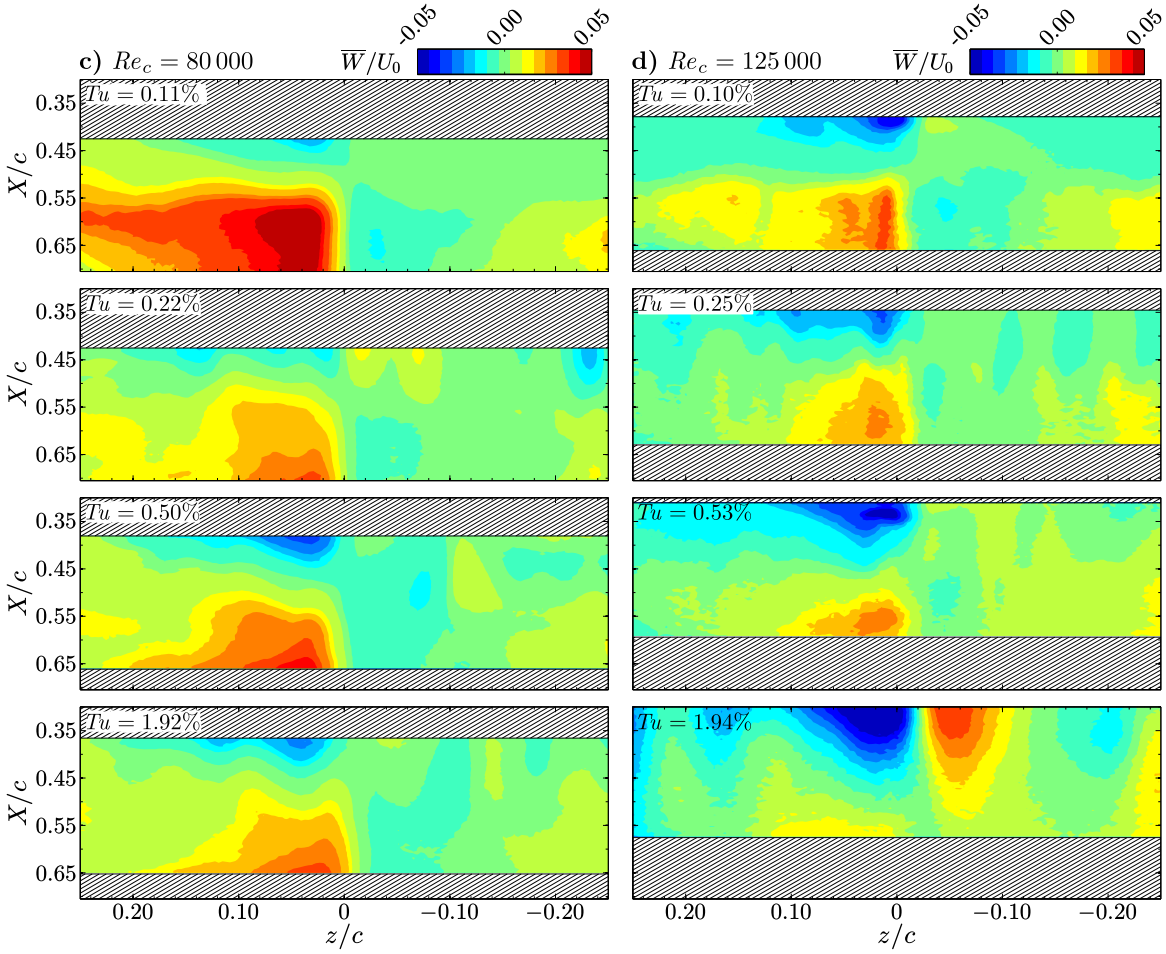

Figure E.2 (cont.): Contours of mean spanwise velocity.

PIV measurements is observed. This spanwise variation in the time-averaged quantities indicates that there is a prefered spanwise wavelength of the flow, and is consistent with the variation in mean reattachment location across the span of a separation bubble observed by Michelis *et al.* [137]. In ideal conditions, the deformation and breakdown of the shear layer rollers should occur at random spanwise locations in time, thus leading to time-averaged quantities that are uniform across the span of the airfoil. However, in experiments, the spanwise instability of the structures may lock onto some perturbation in the facility which may arise from model imperfections, non-uniformity in the flow, etc. Further, measurement uncertainty makes this uniformity difficult to accurately represent.

At the elevated Tu levels, the spanwise non-uniformity is also present (Fig. E.3) and has

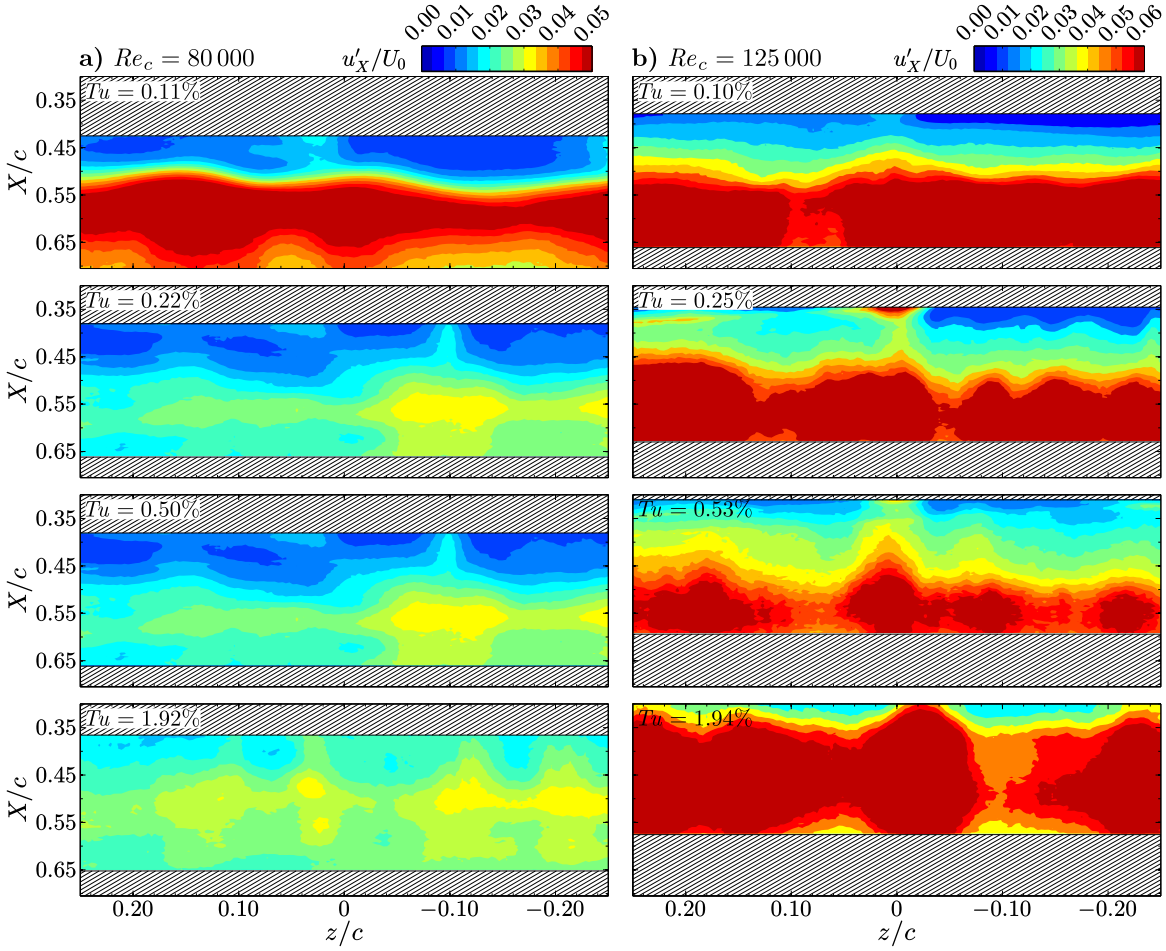

Figure E.3: Contours of the root-mean-square of the chordwise velocity fluctuations.

an increasing influence on the mean fields as Tu is increased (Fig. E.2). The non-uniformity in the mean fields is particularly evident for $Re_c = 125\,000$, where the laser sheet was placed slightly lower in the boundary layer as compared to the cases at $Re_c = 80\,000$. The laser sheet being place slightly lower in the boundary layer also results in lower measured velocities relative to the free-stream velocity.

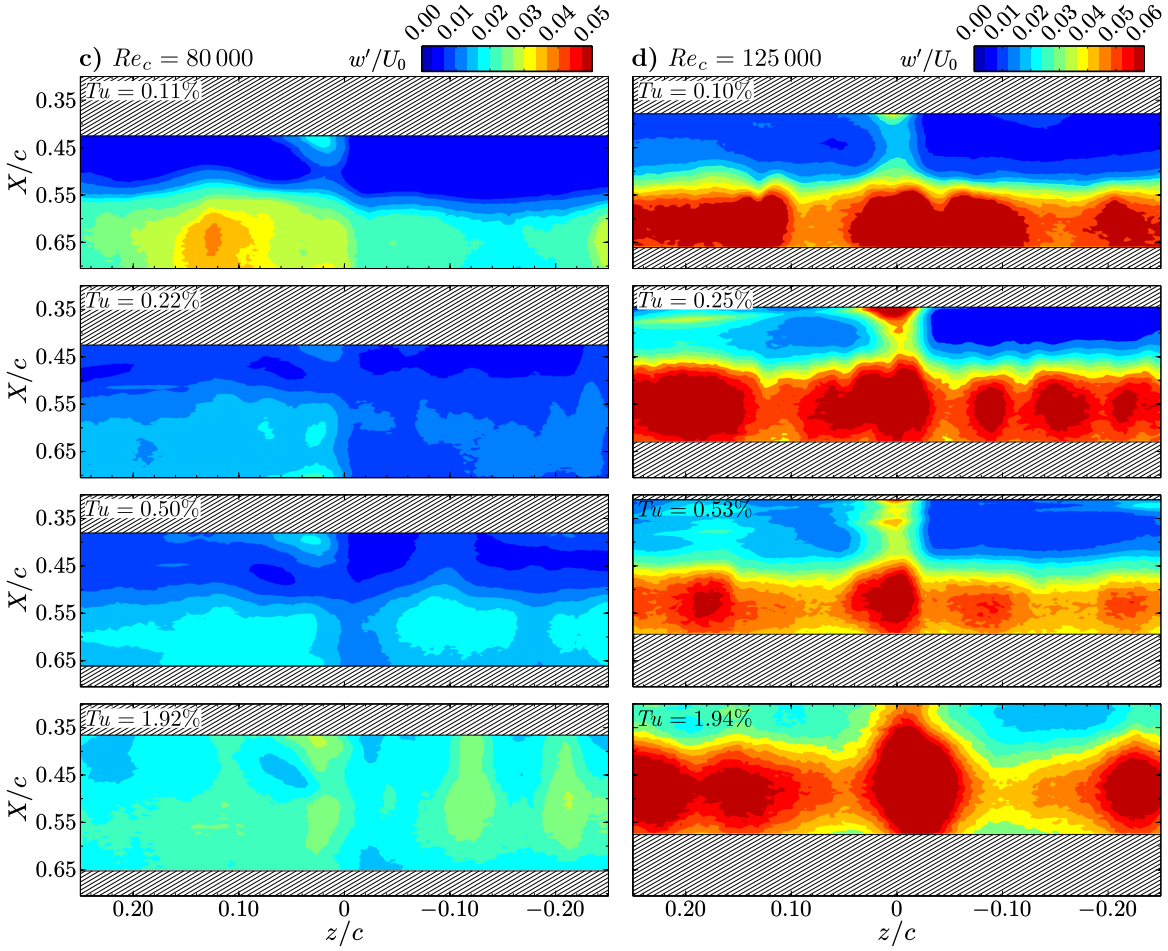

Figure E.3 (cont.): Contours of the root-mean-square of the spanwise velocity fluctuations.

E.3 Top View POD Results

The discussion of the top view POD results in Chapter 5 was limited to the lower Reynolds number for conciseness. The results for the higher chord Reynolds number, $Re_c = 125\,000$, are presented in Fig. E.4.

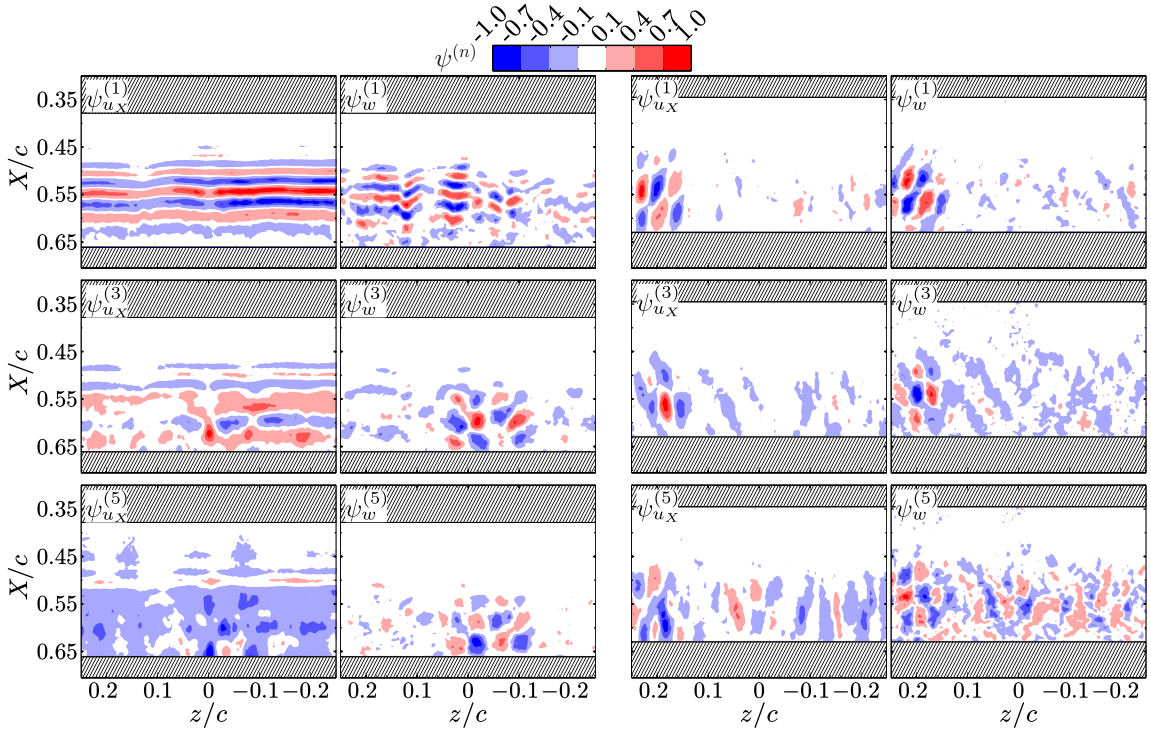

a) $Tu = 0.10\%$ **b)** $Tu = 0.25\%$

Figure E.4: Contours of the streamwise and wall-normal components of the spatial POD modes at $Re_c = 125\,000$.

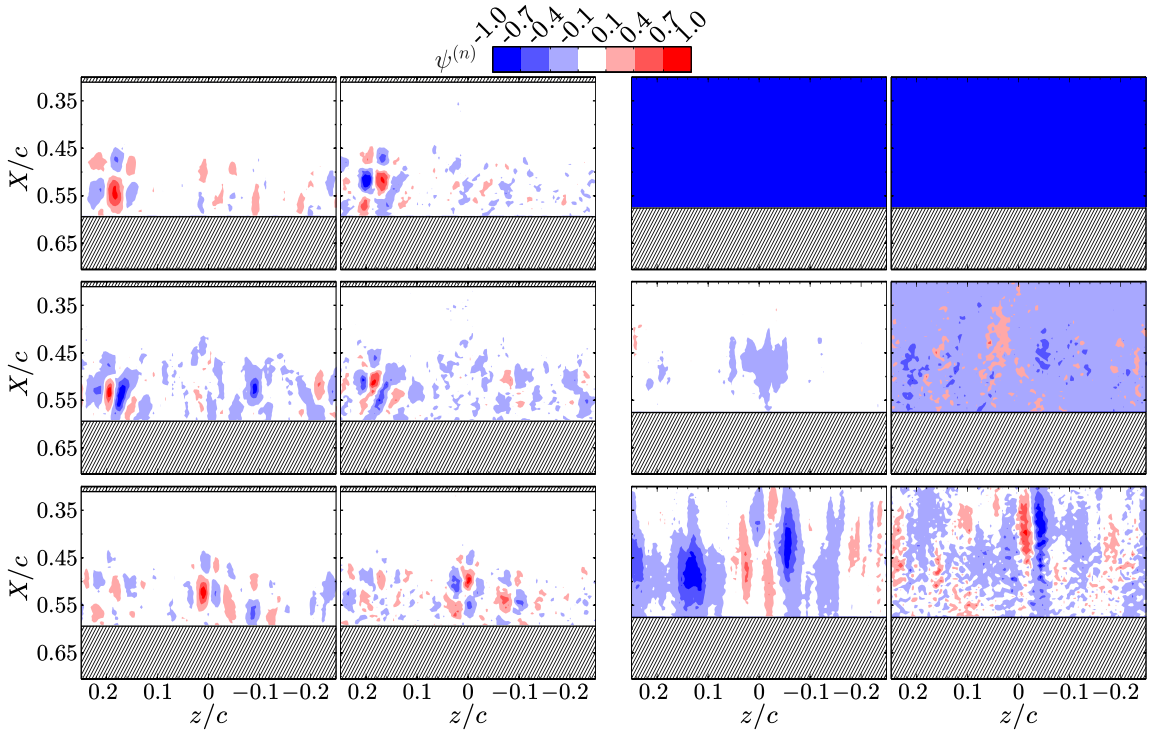

c) $Tu = 0.53\%$ **d)** $Tu = 1.94\%$

Figure E.4 (cont.)